Experimental and Numerical Perspectives on The Role of Localization and Heating in Small-Magnitude Earthquakes

Chien-Cheng Hung

Members of the dissertation committee:

Prof. dr. Giulio Di Toro
Università di Padova, Padova, Italy

Prof. dr. Martyn Drury
Utrecht University, Utrecht, The Netherlands

Prof. dr. Li-Wei Kuo
National Central University, Taoyuan, Taiwan

Prof. dr. Marie Violay
École Polytechnique Fédérale de, Lausanne, Switzerland

Prof. dr. Wenlu Zhu
University of Maryland, Maryland, United States of America

Experimental and Numerical Perspectives on The Role of Localization and Heating in Small-Magnitude Earthquakes

Experimentele en numerieke perspectieven op
de rol van lokalisatie en verwarming in kleine aardbevingen
(met een samenvatting in het Nederlands)

Proefschrift

ter verkrijging van de graad van doctor aan de Universiteit Utrecht op gezag van de
rector magnificus, prof. dr. H.R.B.M. Kummeling, ingevolge het besluit van het college
voor promoties in het openbaar te verdedigen op vrijdag 23 februari 2024
des ochtends te 10.15 uur

door

Chien-Cheng Hung

geboren op 3 mei 1993
te Taichung, Taiwan

Promotor: **Prof. dr. C.J. Spiers**

Copromotoren: **Dr. A.R. Niemeijer**

Dr. Amir Raoof

Explanation of the cover image:
The image on the front cover of this book is a thermograph snapshot of an experimentally deformed Ottawa sand quartz gouge layer captured by a high-speed infrared camera within 3 milliseconds. The circular field of view is about 8 mm in diameter. The warm colors indicate high temperature while the dark colors indicate low temperature. The gouge layer is confined between two steel pistons (top and bottom) under a normal load and is sheared at a slip velocity of 5 cm/s by imposing rotation on the bottom piston (from right to left). This image illustrates that temperature rises are significant where slip localizes, accompanied by a strong reduction in grain size at high slip velocity.

Contents

Summary

In recent years, there has been a growing focus on small-magnitude earthquakes (M < 4) owing to the global surge in human-induced seismicity, stemming from subsurface activities occurring at shallow depths (less than 5 km). These activities include hydrocarbon production, CO_2 storage, wastewater storage, and the exploitation of geothermal resources, which can lead to the seismic activation or triggering of faults cutting the reservoir system and/or neighboring lithologies, including the basement, sometimes bringing significant societal unrest. To evaluate the potential maximum moment magnitude of induced events and to mitigate the associated seismic hazard, data on the dynamic frictional sliding behavior of the fault rock materials (i.e. natural wear products known as fault gouges) are needed as input for a physics-based dynamic rupture model of the reservoir system. A comprehensive understanding of the dynamic behavior of a (gouge-filled) fault requires a full characterization of the process of slip localization and the amount of heat generation from rupture nucleation to propagation.

In this thesis, I provide both experimental and numerical perspectives on the role of slip localization and frictional heating on the mechanical evolution of quartz-rich gouge-filled faults, from earthquake rupture nucleation through to propagation and arrest. I took production-induced seismic events occurring in Europe's largest gas field, the Groningen gas field (Netherlands), as the case study for small-magnitude earthquakes that occur within gouge-filled faults at upper crustal stresses, employing (near) in-situ pore fluid pressure and chemical conditions. Laboratory friction experiments were performed on simulated fault gouges prepared by crushing drill core taken from the Slochteren sandstone (a quartz-rich rock with 72–90 vol% of quartz), which is the main reservoir lithology and hosts most induced events in the Groningen field. The results of this thesis not only address Groningen earthquakes but can also be applied to other small earthquakes occurring under conditions like Groningen and provide input for feasibility studies of future projects in the subsurface.

In **Chapter 1**, I first outline the motivation and the scope of this thesis. Then, I give an overview of natural fault zone structures as well as background knowledge on laboratory friction experiments and numerical modeling of fault dynamics. I go on to introduce the history of the induced seismicity occurring

within the Groningen gas field and associated geological background relating to the reservoir lithologies. Finally, I summarize the aims and structure of this thesis.

In **Chapter 2**, I report the results of an experimental rock friction study on shear zone evolution and localization, using the simulated, quartz-rich, Groningen fault gouges, focusing on the effects of increasing shear strain and slip velocity under conditions relevant to rupture nucleation. All the experiments were performed using a direct-shear setup confining a ~1 mm thick gouge layer under near in-situ reservoir conditions in Groningen, i.e. at an effective normal stress of 40 MPa, a pore fluid (DI water) pressure of 15 MPa, and a temperature of 100 °C. Deformed gouge samples were produced in experiments arrested at 1.3, 3.4, and 5.5 mm of shear displacement, corresponding to strain-hardening, strain-softening, and steady-state stages of deformation imposed at a slip velocity of 1, 30, and 1000 μm/s. I added a strip of pure albite powder mid-way along the gouge layer to act as a passive strain marker, thus allowing quantification of slip/shear localization using X-ray Computed Tomography (XCT). The albite layer provides a significant gray-scale intensity contrast to the quartz in XCT imaging, enabling identification of a visible boundary before and after the shearing experiment. To automatically identify localization features along the marker boundary and to quantify displacement partitioning between these features, in hundreds to thousands of XCT images, I developed a machine-learning-based boundary detection method based on the random forest approach. The automatic boundary detection method is shown to be an efficient and reliable tool to determine localization features and to quantify the displacement partitioning along R_1 and Y (including boundary B shear) shears versus homogeneous shear of the gouge body. The results show that sandstone-derived fault gouges at all tested displacement rates exhibit a similar evolution of mechanical response, localization features and partitioning of displacement. Overall, the evolution from the strain-hardening to the strain-softening, and then steady-state stages, is associated with an evolution from dominant R_1 shears to dominant Y (including B) shears, which are the two main localization features observed in the gouge layer. Ultimately, a principle (B) slip zone (i.e. PSZ) becomes better developed at either one or both sides of the gouge-host block boundary at steady state. These localization features accommodate up to 60% of the total displacement by the end of the steady-state stage. The results provide, for the first time, quantitative data on displacement partitioning between the evolving shear band structures that

form in a quartz-rich fault gouge, and have important implications for ongoing fault slip accommodation as well as heat production and weakening during accelerating slip.

In **Chapter 3**, I utilized 3-D discrete element modeling (DEM) to explore how much contrast in grain size and thickness of the principal (Y and B) slip zone (PSZ) is required for slip to be fully accommodated within the PSZ at seismic slip rates. A numerical PSZ model was developed, featuring a granular gouge pack (gouge body) plus an additional layer of finer particles, with each layer having a single-size particle size distribution (PSD). The fine-grained layer is constructed parallel to the shear plane, within the main granular layer, to mimic the presence of a Y or B type PSZ produced by localized grain size reduction. Grain interactions are elastic and frictional following the Hertz-Mindlin (HM) contact model, with no grain breakage being allowed. Four different PSZ particle sizes (0.9d, 0.75d, 0.6d, and 0.5d where $d = 250$ μm is the grain size of the gouge body layer) and four different thicknesses of the PSZ (1/8t, 1/4t, 3/8t, and 1/2t where $t = 3.75$ mm is the thickness of the gouge layer) were explored. During numerical shearing at 1 m/s, the simulated sample does not exhibit any slip-weakening behavior, while the gouge deformation pattern reveals significant shear localization in the fine-grained layers. The amount of localization is strongly dependent on the finer grain size, with up to 90% of the displacement being localized in the fine zone when the contrast ratio of the grain size is 50%. On the other hand, the amount of localization shows only a minor dependence on layer thickness contrast, with the shear displacement pattern across the whole sample evolving from being linearly distributed, at low thickness contrast, to non-linearly focused near and in the fine-grained layer (and/or its interface with the coarse-grained layer) at high thickness contrast. The results reveal that slip is prone to become focused near the grain-size contrast boundary, likely because the boundary represents a significant contrast in grain contact stiffness and grain contact force between the fine- and coarse-grained layers. I conclude that the presence of a weaker, fine-grained layer within a dense fault zone is likely to result in the self-enhanced weakening of the fault.

The above two chapters focus on shear localization and the associated fault slip distribution in experimental fault gouges and numerical granular bodies deformed at low and high slip velocities, respectively. The combined results

reveal i) the role of slip localization during the faulting process where most of the fault displacement would be localized on boundary-parallel shear bands and only a limited amount of fault displacement (a few mm) is accommodated by distributed shearing, and ii) the importance of the development of boundary-parallel shears in accommodating fault slip as well as in controlling the mechanical behavior of a fault.

In the following two chapters, I investigate the role of slip localization together with frictional heating on fault mechanical behavior, conducting medium-velocity (MV) rotary-shear friction experiments at slip velocities ranging from 0.001 m/s to 0.05 m/s. The aim was to determine the effectiveness and efficiency of flash heating and thermal pressurization (TP), the two major dynamic weakening mechanisms expected to be active within fluid-infiltrated gouge-filled faults.

Accordingly, in **Chapter 4**, I report the results of an experimental study on the characterization of flash heating, specifically on the dependence of peak flash temperature on normal stress, slip velocity, and grain size. Friction experiments were performed on gouges composed of Ottawa sand (consisting of nearly spherical quartz grains), using a range of normal stresses (1 to 7.5 MPa), slip velocities (0.001 to 0.05 m/s), and initial sand grain sizes (250–300 μm, 300–425 μm, 425–500 μm, and 500–710 μm), under room-dry and wet conditions. A high-speed (1200 Hz) infrared camera was employed, with a specific IR temperature range sensing capacity (60°C–200°C and 30°C–150°C for room-dry and wet conditions, respectively), to capture local, short-term temperature increases of flashes at asperity contacts during frictional sliding. The thermal imaging data reveal that instantaneous temperature rises of up to 220°C and 80°C can be spatially and temporally monitored and quantified in the actual shear zone for room-dry and wet gouges, respectively, with the presence of water limiting recorded flash temperature rise. Although the source of these flashes (i.e. whether they are from sliding between grain-grain or grain-window contacts) requires further testing, the measured flash temperatures do show some dependence on slip velocity and grain size, in broad agreement with theoretical predictions.

In **Chapter 5**, I explored the effects of pore fluid properties, (different thermal and hydraulic properties) on the efficiency of TP and associated TP-

induced weakening of sandstone-derived gouges, under room-dry and wet (pore fluid pressure) conditions. Four different types of pore fluid, including deionized water, synthetic brine (with a composition similar to the in-situ brine in the Groningen gas reservoir), and Dow Corning 200 silicone oils (1 and 5 centistokes), were used. Experiments with each pore fluid were conducted at an applied normal stress of 12 MPa, at a constant slip velocity of 0.05 m/s, with an initial pore fluid pressure of 0.1, 1, and 2 MPa, under undrained conditions. A total displacement of 0.75 m was imposed. All the wet gouges exhibit two stages of dynamic slip weakening following initial static peak friction, namely a first sharp weakening and a second weakening of longer duration, likely dominated by flash pressurization and bulk TP, respectively. The observed magnitude of the TP-induced weakening decreases with increased fluid viscosity, and the experimental observations are similar to theoretical predictions of TP models, when applied assuming a possible order of magnitude increase in the permeability of the shear zone for specific fluids. The feasibility of such an increase in permeability is supported by microstructural observations which showed that shear zones developed in the presence of high viscosity fluid experienced a smaller degree of grain size reduction. In addition, I showed that experiments with a high-viscosity fluid tend to generate higher temperatures without causing enhanced weakening.

Summarizing the results from the medium-velocity (MV) friction experiments presented in Chapters 4 and 5, they revealed i) strong dynamic slip weakening in the presence of fluid which is absent under room-dry conditions where a higher efficiency of flash heating is expected, ii) reduced TP-weakening and higher dynamic friction is seen in gouge-filled faults saturated with high-viscosity as opposed to low viscosity pore fluid, despite the larger thermal pressurization factor, lower hydraulic diffusivity, and higher temperature rise associated with the higher viscosity, and iii) the importance of shear zone development and associated permeability changes of the fault zone, which can potentially influence the dynamic frictional behavior of a gouge-filled fault under conditions favorable for the operation of TP. This may have implications for rupture nucleation and growth of production- or injection-induced seismicity, which involves various pore fluids with variable properties (viscosity, compressibility, etc).

In **Chapter 6**, I report the results obtained from a series of high-velocity (HV) rotary-shear experiments under displacement and velocity conditions close to those expected to occur in M3–4 earthquakes. The aim here is to identify the controlling dynamic weakening mechanism and to provide better constraints on dynamic friction utilizing more realistic earthquake conditions similar to the Groningen earthquakes. HV friction experiments were performed on conditioned sandstone-derived fault gouges confined between sandstone plates subjected to a pulse-like displacement-time function (triangular vs. modified Yoffe velocity functions) at an initial effective normal stress σ_{eff} of 4.9–16.6 MPa. I imposed a peak velocity V_{pk} up to 1.8 m/s with slip accelerations of up to 42 m/s^2 within displacements of 7.5–15 cm, using either Argon-dry or water as pore fluid (undrained, initial pore fluid pressure $P_i = 0.1$ and 1 MPa) at ambient temperature conditions. The results for all samples show that the evolution of the apparent friction coefficient μ_{app} during the seismic slip pulse is strongly velocity-dependent, with slip weakening and restrengthening occurring during the acceleration and deceleration phases, respectively. The dry gouge exhibits single and minor dynamic weakening (μ_{pk} of 0.75 drops to μ_{min} of 0.48 at a normal stress of 12 MPa), as compared to the water-saturated gouges, which show 30–70% dynamic weakening (μ_{pk} of 0.6–0.8 drops to μ_{min} of 0.25–0.41), depending on displacement, normal stress, and to some extent pre-applied shear stress. Strong dynamic weakening is absent in a wet control experiment conducted with porous steel plates. The combined results of the microstructural observations and thermo-mechanical modeling suggest that TP with a water/vapor phase transition at the shear-band scale is likely to be the controlling weakening mechanism in wet samples. Overall, the results of this chapter provide better constraints on slip-weakening parameters (e.g. dynamic friction, weakening distance, and weakening rate) for small-displacement earthquakes, which can be used as new input for physics-based dynamic rupture models to estimate the maximum possible moment magnitude of induced seismicity in the Groningen gas reservoir.

The work presented in this thesis has provided insights into the (micro)mechanics of small-displacement earthquakes on quartz-rich, gouge-filled faults under upper crustal conditions. Both experimental and numerical perspectives have been pursued regarding shear localization, frictional heating, and dynamic weakening during rupture nucleation and propagation. In **Chapter 7**, I summarize the main conclusions and provide overall implications for induced seismicity in the Groningen field, as well as broader implications for small-

displacement earthquakes. Finally, remaining questions are identified and suggestions are made for further research.

Samenvatting

De laatste jaren is er een groeiende focus op kleine aardbevingen (M < 4) als gevolg van de wereldwijde toename van seismiciteit door antropogene ondergrondse activiteiten die plaatsvinden op dieptes tot 5 km. Deze activiteiten, waaronder de productie van koolwaterstoffen, CO_2-opslag, afvalwateropslag en de exploitatie van geothermie, kunnen leiden tot seismische activatie van breuken in het reservoir en/of de omliggende gesteenten. Soms leidt dit tot aanzienlijke maatschappelijke onrust en schade. Om de potentiële maximale kracht van geïnduceerde aardbevingen te evalueren en de bijbehorende seismische gevaren te verminderen, zijn gegevens over de dynamische wrijvingseigenschappen van de breukgesteentes (breukmeel dat ontstaat wanner gesteenten over elkaar wrijven) nodig. Deze gegevens kunnen direct worden toegepast in fysische computermodellen die het dynamische gedrag van breuken in het reservoirsysteem nabootsen. Om het dynamische gedrag van (met breukmeel gevulde) breuken volledig te kunnen begrijpen, is kennis nodig over waar verplaatsing gebeurt (lokalisatie van beweging) en de hoeveelheid warmte die wordt geproduceerd gedurende de nucleatie en propagatie van aardbevingen.

In dit proefschrift bied ik zowel experimentele als numerieke perspectieven op de rol van wrijvingswarmte en de lokalisatie van beweging op de mechanische evolutie van kwarts-rijke breukgesteenten. Deze evolutie omvat de hele seismische cyclus, van nucleatie, propagatie tot het tot stilstand komen van breuken. De door gas productie geïnduceerde seismiciteit in het Groningen gasveld (Nederland) dient in dit proefschrift als casestudy voor de kleine aardbevingen die optreden bij breukbeweging in de ondiepe ondergrond. Wrijvingsexperimenten werden uitgevoerd in het laboratorium waarbij de spanningen, vloeistofdruk en temperatuur op reservoirdiepte werden nagebootst. Het breukgesteente of breukmeel in deze experimenten werd gesimuleerd door materiaal uit boorkernen afkomstig van het Slochteren zandsteen reservoir (het zandsteenreservoir in Groningen bestaande uit 72–90 vol% kwarts) fijn te malen tot een poeder. De resultaten van dit proefschrift hebben niet alleen implicaties voor de aardbevingen in het Groningen gasveld, maar zijn ook van toepassing op andere kleine aardbevingen die optreden onder omstandigheden zoals in het Groningen gasveld. Daarmee kunnen ze worden gebruikt als belangrijke input voor haalbaarheidsstudies en zogenoemde 'hazard and risk assessments' van toekomstige projecten in de ondergrond.

In **Hoofdstuk 1** geef ik eerst een overzicht van de motivatie en reikwijdte van dit proefschrift. Vervolgens geef ik een overzicht van de structuren in natuurlijke breukzones en de achtergrondkennis over wrijvingsexperimenten in het laboratorium en numerieke modellen die het dynamische gedrag van breuken beschrijven. Vervolgens introduceer ik een historisch overzicht van de geïnduceerde seismische activiteit die plaatsvond binnen het Groningen-gasveld en de bijbehorende geologische achtergrond met betrekking tot de reservoir-gesteenten. Tot slot vat ik de doelstellingen en structuur van dit proefschrift samen.

In **Hoofdstuk 2** rapporteer ik de resultaten van een experimentele studie naar de wrijvingsevolutie en lokalisatie van verplaatsing in gesimuleerd kwartsrijk breukmeel, representatief voor het materiaal in breuken in Groningen. Ik richt me op de effecten van toenemende verplaatsing en schuifsnelheid onder de omstandigheden die relevant zijn voor beginnende breukbeweging (nucleatie). Alle experimenten werden uitgevoerd op een ~1 mm dikke laag breukmeel geplaatst in een direct-shear setup waarin de condities van het Groningen reservoir kunnen worden benaderd, d.w.z. een effectieve normaalspanning van 40 MPa, een vloeistofdruk van 15 MPa en een temperatuur van 100 °C. De experimenten werden gestopt na respectievelijk 1.3, 3.4 en 5.5 mm verplaatsing. Deze verplaatsingen zijn representatief voor stadia van versterking ('strain-hardening'), verzwakking ('strain-softening') en constante sterkte ('steady-state') bij verplaatsingssnelheden van 1, 30 en 1000 µm/s. Waar de verplaatsing binnen het monster plaatsvond in deze experimenten kon worden gekwantificeerd door het toevoegen van een smalle strook poeder van albiet (een 'strain-marker'). Met behulp van deze zogenoemde 'strain-marker' en van X-ray Computed Tomography (XCT), was het mogelijk om te kwantificeren waar hoeveel verplaatsing plaatsvond, doordat albiet en kwarts contrasterende intensiteitswaarden opleveren in de XCT-beeldvorming. Ik ontwikkelde een op machine-learning gebaseerde grensdetectiemethode om de verplaatsing kwantificeren in honderden tot duizenden XCT beelden te kwantificeren. De automatische grensdetectiemethode is een efficiënt en betrouwbaar hulpmiddel gebleken om lokalisatiekenmerken te bepalen waarbij onderscheid kon worden gemaakt tussen homogene verplaatsing en gelokaliseerde verplaatsing langs zogenoemde R_1- en Y-shears. De resultaten tonen aan dat breukmeel gevormd uit zandsteen een vergelijkbare evolutie van lokalisatie en mechanische response laat

zien bij alle geteste verplaatsingssnelheden. Deze evolutie bestaat uit een stadium waarin R_1-shears actief zijn, gevolgd door een fase waarin Y-shears (en B-shears) actief worden. Uiteindelijk lokaliseert de verplaatsing zich op een of beide B-shears aan de randen van het breukmeelmonster. Deze drie fases komen overeen met de geobserveerde mechanische fases van 'strain-hardening', 'strain-softening' en 'steady-state'. Tot 60% van de totale verplaatsing word geaccommodeerd door lokalisatie van verplaatsing op R_1-, Y-, en B-shears. De resultaten leveren voor het eerst kwantitatieve gegevens op over de verdeling van verplaatsing in kwartsrijk breukmeel en hebben belangrijke implicaties voor de warmteproductie en de hiermee geassocieerde hoeveelheid verzwakking van de breuk tijdens toenemende snelheden in breukbeweging.

In **Hoofdstuk 3** heb ik 3D-discrete-elementmodellering (DEM) gebruikt om te onderzoeken hoeveel contrast in korrelgrootte en breedte van de zogenoemde principal slip zone (PSZ) nodig zijn om verplaatsing volledig te accommoderen binnen de PSZ bij seismische verplaatsingssnelheden. Een numeriek PSZ-model werd ontwikkeld, bestaande uit een laag granulair materiaal met daarbinnen een laag fijnkorrelig materiaal. De fijnkorrelige laag is parallel aan het schuifvlak gepositioneerd, om de aanwezigheid van een Y- of B-type PSZ te simuleren, zoals gevonden in Hoofdstuk 2. De korrels in het model volgen het Hertz-Mindlin (HM) contactmodel en hebben slechts elastische en wrijvingsinteracties. De korrels kunnen niet breken en daarbij reduceren in grootte. Ik onderzocht de effecten van vier verschillende breedtes van de PSZ (1/8t, 1/4t, 3/8t en 1/2t waar t = 3,75 mm en is de totale dikte van het model) en vier verschillende korrelgroottes binnen de PSZ (0.9d, 0.75d, 0.6d en 0.5d waar d = 250 µm is de korrelgrootte van de omliggende laag granulair materiaal). Tijdens verplaatsing op een snelheid van 1 m/s vertoont het gesimuleerde monster geen verzwakking ('slip-weakening' gedrag), ondanks dat de verplaatsing lokaliseert in de fijnkorrelige laag. De mate van lokalisatie is sterk afhankelijk van de fijnere korrelgrootte, waarbij tot 90% van de verplaatsing gelokaliseerd is in de fijne zone wanneer de contrastverhouding in korrelgrootte 50% (0.5d) is. De breedte van de PSZ heeft slechts een gering effect op de mate van lokalisatie. De resultaten tonen aan dat slip lokaliseert bij het contact tussen lagen met verschillende korrelgroottes, waarschijnlijk omdat op deze grens een contrast in stijfheid van het korrelcontact en een contrast in krachten op korrelcontacten bestaan. Ik concludeer dat de aanwezigheid van een zwakkere, fijnkorrelige laag

binnen een breukzone resulteert in een positieve feedback waarbij de breuk zwakker wordt.

De bovenstaande twee hoofdstukken richten zich op lokalisatie en de bijbehorende distributie van breukverplaatsingen in experimentele en numerieke granulaire breuken, gedeformeerd bij lage en bij hoge verplaatsingssnelheden respectievelijk. Door deze resultaten te integreren, onthul ik dat i) de rol van lokalisatie van verplaatsing gedurende breukbeweging, waarbij het grootste deel van de verplaatsing wordt geaccommodeerd door B-shears, parallel aan het breukvlak, en slechts een klein deel door gedistribueerde (homogene) deformatie in het breukmeel, en ii) het belang van B-shears in het controleren van het mechanische gedrag van een breuk

In de volgende twee hoofdstukken onderzoek ik hoe lokalisatie van verplaatsing in combinatie met de ontwikkeling van warmte door wrijving het mechanische gedrag van breuken beïnvloedt. Dit doe ik met behulp van wrijvingsexperimenten in een zogenaamde rotary-shear setup, bij snelheden tussen 0.001 m/s tot 0.05 m/s (medium-velocity or MV). Het doel van deze experimenten is het bepalen van de effectiviteit en efficiëntie van 'flash heating' en 'thermal pressurization' (TP), de twee belangrijkste mechanismen die voor sterke verzwakking ('dynamic-weakening') kunnen zorgen in breuken met breukmeel en bij de aanwezigheid van vloeistoffen.

In **Hoofdstuk 4** rapporteer ik de resultaten van een experimentele studie over het karakteriseren van ´flash heating´, waarbij ik focus op de maximale temperatuur die gegenereerd kan worden als functie van normaalspanning, verplaatsingssnelheid en korrelgrootte. De experimenten zijn uitgevoerd op breukmeel, afgeleid van Ottowa zandsteen (breukmeel met ronde korrels), bij normaalspanningen van 1 tot 7.5 MPa, verplaatsingssnelheden van 0.001 tot 0.05 m/s, verschillende initiële korrelgroottedistributies (250–300 μm, 300–425 μm, 425–500 μm en 500–710 μm) en zowel met als zonder vloeistoffen. Ik gebruikte een high-speed (1200 Hz) infraroodcamera, met een specifieke IR-temperatuurbereik (60°C–200°C en 30°C–150°C voor droge en natte omstandigheden, respectievelijk), om lokale, korte-termijn temperatuursverhogingen te kwantificeren en dit te koppelen aan het wrijvingsgedrag. De thermische beelden laten zien dat temperatuursverhogingen

tot maximaal 220°C en 80°C kunnen worden gemeten en gekwantificeerd voor experimenten respectievelijk zonder en met water. Deze temperatuursveranderingen kunnen in ruimte en tijd worden gekwantificeerd en laten zien waar daadwerkelijk verplaatsing plaatsvindt. Ondanks dat er aanvullende experimenten nodig zijn (om te testen of temperatuursveranderingen plaatsvinden op korrelcontacten of op het contact met het IR-raam), laten de temperatuursveranderingen een afhankelijkheid van slipsnelheid en korrelgrootte zien. Dit komt overeen met de theoretische voorspellingen.

In **Hoofdstuk 5** onderzocht ik de effecten van (thermische en hydraulische) vloeistofeigenschappen op de efficiëntie van 'thermal pressurization' (TP) en de daarbij horende afname in sterkte van zandsteen breukmeel. Hiervoor gebruikte ik vier verschillende soorten vloeistoffen waaronder gedemineraliseerd water, water met opgeloste zouten met een samenstelling vergelijkbaar met die van het Groningen gasveld en Dow Corning 200 siliconenolie (met een viscositeit van 1 en 5 centistokes). De experimenten werden uitgevoerd bij een normaalspanning van 12 MPa, bij een verplaatsingssnelheid van 0.05 m/s, een initiële vloeistofdruk van 0.1, 1 en 2 MPa en in gesloten systeem (geen vloeistof stroming naar buiten toe). Alle experimenten hadden een totale verplaatsing van 0.75 m. Bij alle experimenten met vloeistof werd een maximum in wrijving bereikt, gevolgd door twee fases van verzwakking, namelijk een eerste korte, sterke afname in wrijving, gevolgd door een tweede, langdurige en langzame afname in wrijving, waarschijnlijk voornamelijk veroorzaakt door respectievelijk 'flash pressurization' en 'Thermal pressurization'. De waargenomen TP-geïnduceerde afname in wrijving neemt af met een toename in viscositeit. Deze experimentele observaties komen overeen met theoretische voorspellingen van TP-modellen wanneer wordt aangenomen dat de permeabiliteit met een orde van grootte toeneemt. Zo'n toename komt overeen met de microstructurele observaties die laten zien dat minder korrelgroottereductie plaatsvindt bij experimenten met vloeistoffen met een hogere viscositeit. Daarnaast laat ik zien dat experimenten met een hoge viscositeit voor een grotere temperatuurtoename zorgen, zonder dat de wrijving extra afneemt.

Samenvattend: de resultaten van de 'medium-velocity' (MV) wrijvingsexperimenten, gepresenteerd in Hoofdstuk 4 en 5, laten zien dat i) er sprake is van aanzienlijke breuk verzwakking, die afwezig is in droge breuken,

ondanks dat 'flash heating' hier juist meer efficiënt is, ii) verminderde verzwakking door TP en hogere dynamische wrijving wanneer breuken gesatureerd zijn met een vloeistof met hoge viscositeit, ondanks een hogere temperatuurstijging en vloeistofeigenschappen die TP zouden moeten bevorderen, en iii) het belang van de evolutie van breukzones en de daarbij horende veranderingen in permeabiliteit die de efficiëntie van verzwakking door TP controleren. De resultaten geven belangrijke inzichten in de mogelijke seismische (re)activatie van breuken in reservoirs waar verschillende vloeistoffen (met verschillende viscositeit, compressibiliteit, etc.) onttrokken of geïnjecteerd worden of aanwezig zijn.

In **Hoofdstuk 6** rapporteer ik de resultaten van een reeks hoge snelheid ('high-velocity', HV) 'rotary-shear' experimenten waarbij de hoeveelheid verplaatsing en de snelheden typisch zijn voor M3–4 aardbevingen. Het doel van deze experimenten is het bepalen van de mechanismen die verantwoordelijk zijn voor de dynamische sterkteafname van breuken in Groningen en het kwantificeren van de dynamische wrijving. De experimenten werden uitgevoerd op gesimuleerde zandsteen breukmeel. Dit granulaire materiaal werd tussen twee intacte zandsteenplaten geplaatst, die het omliggende intacte gesteente simuleren. De zandstenen platen werden ten opzichte van elkaar geroteerd met een sterke, kortstondige toename en afname in snelheid (driehoekig vs. gemodificeerde Yoffe snelheidsfunctie), bij een initiële effectieve normaalspanning van 4.9–16.6 MPa. De totale verplaatsing in deze experimenten betrof 7.5 – 15 cm, waarbij een maximale snelheid (Vpk) en maximale versnelling van respectievelijk 1,8 m/s en 42 m/s2 werden behaald. De experimenten vonden plaats bij kamertemperatuur en in de aanwezigheid van argon of water in de poriën (initiële vloeistofdruk Pi = 0.1 en 1.0 MPa). De resultaten van alle experimenten laten een sterke snelheidsafhankelijkheid zien van de wrijvingscoëfficiënt μapp met sterke afzwakking en versterking gedurende de acceleratie en deceleratie, respectievelijk. Het droge experiment laat slechts een kleine afname in wrijving zien (μpk van 0.75 naar μmin van 0.48 bij een normaalspanning van 12 MPa). De experimenten waarbij water aanwezig is, laten een afname van 30–70% zien (μpk van 0.6–0.8 naar μmin van 0.25–0.41), afhankelijk van de hoeveelheid verplaatsing, de normaalspanning en de hoeveelheid pre-compactie. Een controle-experiment waarbij poreuze stalen platen in plaats van zandstenen platen werden gebruikt, liet een veel kleinere dynamische sterkteafname zien. De

resultaten van het microstructureel onderzoek in combinatie met thermo-mechanische modellering suggereren dat TP met een faseovergang van vloeistof naar gas in de breuk verantwoordelijk is voor de dynamische sterkteafname bij de aanwezigheid van vloeistoffen. De resultaten van dit hoofdstukken bieden betere waardes voor belangrijke parameters zoals de dynamische wrijvingscoefficient, de afstand waarover verzwakking plaatsvindt en de snelheid waarmee dit gebeurt. Deze waardes kunnen geïmplementeerd worden in op fysica gebaseerde numerieke modellen voor aardbevingen. Met behulp van deze modellen kan de maximale momentmagnitude van geïnduceerde seismiciteit in bijvoorbeeld het Groningen gasreservoir beter ingeschat worden.

De resultaten in dit proefschrift bieden belangrijke inzichten in het (micro)mechanische gedrag van kleine aardbevingen in kwartsrijk breukgesteente in de bovenkorst. Met zowel experimenteel as numeriek onderzoek bied ik inzichten in de temperatuursverandering door wrijvingswarmte ('frictional heating'), de daarmee gepaard gaande verzwakking ('dynamic weakening') en lokalisatie van verplaatsing, gedurende de nucleatie, propagatie en het tot stilstand komen van breuken. In **Hoofdstuk 7** vat ik de belangrijkste conclusies van dit proefschrift samen. Daarnaast ga ik verder in op wat dit betekent voor geïnduceerde seismiciteit in het Groningen gasveld en voor andere toepassingen in de ondergrond waarbij kleine breukbewegingen kunnen plaatsvinden. Als laatste benoem ik onbeantwoorde vragen die de aandacht verdienen in toekomstig onderzoek.

(translated from the original by Job Arts and André Niemeijer)

Chapter 1

General introduction

1.1 Motivation and scope of this study

Earthquakes, one of the most catastrophic natural hazards worldwide, occur as a result of the release of elastic strain energy stored in the surrounding rocks nucleating at a depth of tens to hundreds of kilometers (Scholz, 2002). Destructive natural earthquakes mainly result from the propagation of ruptures, nucleating between 7 to 15 km depth, for tens or hundreds of kilometers along faults. During earthquake propagation, a large amount of coseismic displacement is localized on relatively thin faults and narrow slip zones (a few tens to hundreds of microns wide; Chester et al., 2013; Li et al., 2013; Ma et al., 2006), where stored energy is dissipated through, among others, frictional heating driven by rapid sliding along the bare-rock or gouge-filled fault surfaces. This process activates numerous weakening mechanisms, by raising the temperature of the fault-zone materials and substantially reducing the fault strength over a characteristic slip weakening distance. For example, pore fluids existing within fault zones can become thermally pressurized (thermal pressurization or TP; Rice, 2006), which reduces the effective normal stress and the bulk fault strength. TP becomes more efficient with higher temperature rise and if the fault zone is relatively impermeable allowing for fluid pressures to build up. Strain localization, which controls the development of the shear zone width, simultaneously plays a crucial role in governing heat generation and, thus, facilitates thermally activated weakening processes (Platt et al., 2014; Rice et al., 2014; Smith et al., 2015). A thorough understanding of the localization process of fault slip and fault temperature rise is needed to characterize and quantify the controlling dynamic weakening mechanism that occurs during earthquake rupture propagation. The associated stress drops and slip weakening distance resulting from the specific weakening mechanisms active can further determine the heat budget of a fault in a coupled manner. These factors are critical in assessing the potential maximum moment magnitude of an earthquake and associated seismic hazard in a physics-based dynamic rupture model.

In the past 30 years, a large body of laboratory studies on dynamic fault friction have been reported, made possible by the invention of high-velocity rotary-shear apparatuses (Tsutsumi and Shimamoto, 1997), which allows researchers to reproduce and simulate fault behavior with several meters of displacement at seismic slip rate (>1 m/s, e.g. Niemeijer et al., 2011). A consistent observation which has been reported for most simulated fault materials, is that a

significant amount of friction reduction occurs, from a static friction (~0.6–0.85; Byerlee, 1987) to a dynamic friction coefficient of order 0.1 over a slip weakening distance D_w, at slip rates above ~0.1 m/s, irrespective of the fault rock composition (Di Toro et al., 2011; Niemeijer et al., 2012; Tullis, 2015). A wide variety of dynamic weakening mechanisms depending on the fault rock composition have been proposed, based on microstructural characterization of the deformed samples, which was further used to infer physicochemical processes that occur during natural earthquakes. Bulk frictional melting is one of the most common physical phenomena reported in high-velocity friction experiments on cohesive quartz-rich rocks and has been demonstrated to be one of the dominant weakening mechanisms that occurs in natural pseudotachylyte-bearing fault zones (Di Toro et al., 2006; Hirose and Shimamoto, 2005; Niemeijer et al., 2011).

The vast majority of high-velocity friction experiments conducted to date have mainly focused on simulating natural large earthquakes (e.g. M > 6) with meter-scale displacement, while less attention has been paid to small earthquakes (e.g. M < 4) which show pulse-like slip behavior and a limited amount of displacement (e.g. few tens of centimeters; Wentinck, 2018). However, small events have received increasing attention in recent years, because of increased human-induced seismicity resulting from subsurface activities at shallow depths (less than 5 km), such as hydrocarbon production from or fluid injection into subsurface reservoir systems. When occurring in populated areas, such events can cause significant risks and often societal unrest – not least in the Netherlands where the vast Groningen gas field has been essentially shut down due to induced seismicity. So far, the mechanics and mechanisms of large earthquakes have been quite well studied, but such studies are still largely lacking for small-magnitude earthquakes – both natural and induced. Thus, it is important to improve our understanding of the extent to which strain localizes, temperature rises, and weakening occurs for fast and short displacement earthquakes.

In this thesis, I explore the role of strain localization and frictional heating in determining the mechanical behavior of quartz-rich, gouge-filled faults, under conditions relevant to induced earthquake nucleation and propagation related to hydrocarbon production in the Groningen gas reservoir, the Netherlands – Europe's largest gas field. First, I conducted direct shear experiments on simulated fault gouges from nucleation-relevant velocities up to three orders of

magnitude faster (10^{-6}–10^{-3} m/s) to investigate the development and evolution of the internally localized shear zone fabrics as a function of shear strain and slip velocity, and the relationship to the observed mechanical behavior. I quantified how much fault displacement was distributed over the developed localization features. The study of fabrics and associated displacement partitioning during rupture nucleation may provide insight into where and to what extent seismic slip localizes and self-heats during rupture. Second, I used 3-D numerical simulations with the discrete element method (DEM) to investigate the effect of PSZ thickness and grain size on slip localization in sheared granular fault gouges containing a pre-defined, shear-parallel, fine-grained layer at seismic velocities (≥ 0.1 m/s). Third, I conducted medium-velocity (MV) rotary-shear friction experiments equipped with a high-speed infrared camera on Ottawa sand gouges, with variable grain sizes, under different normal stresses and at a wide range of slip velocities (10^{-3}–5×10^{-2} m/s). The aim here was i) to characterize the effects of these parameters on flash temperature rise at grain contacts induced by flash heating and ii) to investigate the effectiveness and efficiency of the flash heating on the mechanical strength of dry and wet quartz-rich faults. Fourth, I conducted MV rotary-shear friction experiments on simulated, fluid-saturated fault gouges, at a constant intermediate slip velocity (5×10^{-2} m/s), using different types of pore fluids to explore the effect of their differing thermal and hydraulic properties on the effectiveness of TP and thus slip weakening. The results obtained from different types of fluid provide pointers for assessing the potential slip behavior of faults in gas reservoirs, such as Groningen, where the in-situ pore fluid consists of a mixture of brine and methane. Finally, I conducted slip-pulse friction experiments, at high slip velocities (1–1.8 m/s), to simulate induced events of magnitude 3 to 4 with the aim of quantifying the amount of weakening and identifying the controlling weakening mechanism during the seismic slip-pulse. The overall aim of these high-velocity experiments was to identify the conditions at which a particular dynamic weakening mechanism controls the breakdown in frictional strength during small-displacement earthquakes, and to better constrain the level of dynamic friction that ultimately controls the potential maximum moment magnitude – as input for geomechanical rupture models.

1.2 Long-displacement fault zone structure and its relations to fault mechanics

1.2.1 Fault damage and core zones and associated fluid flow

Field and borehole observations conducted on large-displacement brittle fault zones have shown that a fault zone typically consists of a fault core surrounded by a damage zone of fractured wall rocks (Chester and Logan, 1986; Chester et al., 1993; Faulkner et al., 2003, 2010; Mitchell and Faulkner, 2009; Sibson, 2003). Multiple core zones with many fractured lenses have also been inferred from some field and borehole observations (e.g. Faulkner et al., 2003; Zoback, 2010). These structures are the products of localization of strain along crustal faults where most of displacement, including seismic displacement, is accommodated within the core zone and an associated damage zone is formed by distributed fractures and subsidiary, small displacement faults, related to the growth of the fault zone (Chester and Logan, 1986; Chester et al., 1993; Sibson, 1977). Generally, the fault core consists of a layered, fine-grained wear product (mm-cm thickness), referred to as fault gouge, which is the result of grain comminution between two sliding wall-rock surfaces (Chester and Chester, 1998; Collettini et al., 2009; Sibson, 1986). Fault gouges further exhibit one or more narrow (a few tens of microns), highly comminuted shear-parallel structural fabrics, known as principal slip zone (PSZ), which are generally interpreted as indicators of extreme strain localization providing evidence for where the majority of the fault slip has been accommodated (De Paola et al., 2008; Heermance et al., 2003). A classic example of a crustal brittle fault zone consisting of a damage zone and a core with extreme strain localization has been documented for the well-known Punchbowl fault. This inactive fault, located in southern California and hosted in sandstone (Chester and Chester, 1998; Figure 1.1a), contains a 1 mm thick principal slip zone (PSZ) consisting of <100 nm gouge particles (Chester et al., 2005). Riedel shear fabrics (i.e. R_1 and R_2 shears; Riedel, 1929; Figure 1.1c-e) and other corresponding localization features (X and P shears), each oriented at a specific range of angles to the gouge/host-rock boundary (e.g. Logan et al., 1979, 1992; Rutter et al., 1986), are also often observed in the field and borehole cores (e.g. He et al., 2018; Moore and Byerlee, 1991).
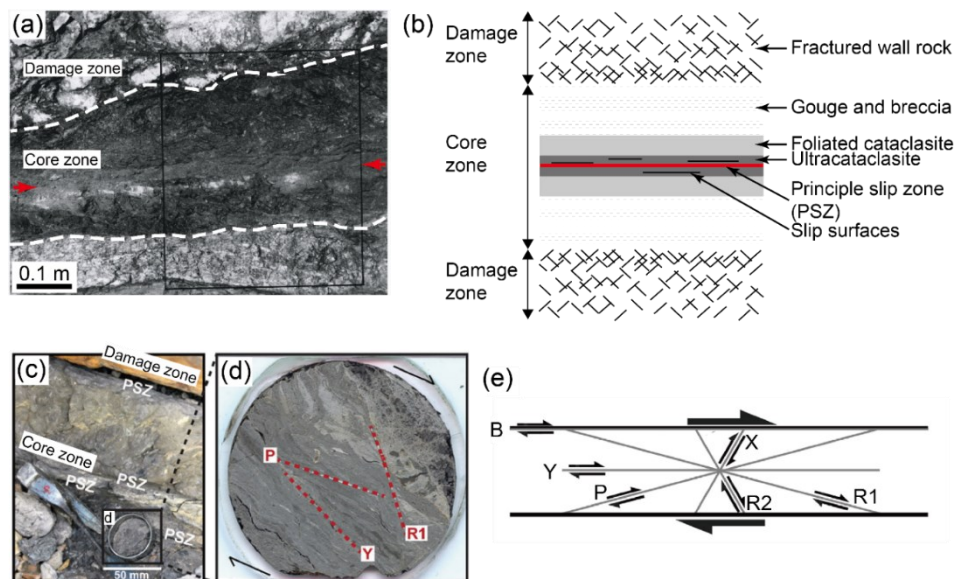
Figure 1.1: *(a) Fault zone structure of the Punchbowl fault, a mature large displacement strike-slip fault (> 100 km displacement), consisting of a damage and a core zone. Adapted from Chester and Chester (1998). A principle slip zone (PSZ) marked by red arrows is hosted within an ultracataclasite zone within the core zone. (b) Schematic diagram of the Punchbowl model fault zone structure. The core zone can be further subdivided into gouge and breccia, foliated cataclasite, and ultracatalastite zones. Note that the boundary between the core zone and damage zone might not be completely straight in nature. (c) Field exposure of the Ninety Fathom Fault (Northeast England) juxtaposing Rotliegend sandstone against grey Carboniferous shales (Whitley Bay, UK). (d) Internal R$_1$, P, and Y shears within the core zone of c). (e) Schematic drawing of the orientations of fractures formed in association with brittle fault zones. The overall sense of shear is shown by the bold arrows in the country rock bounding the shear zone. Adapted from Niemeijer et al. (2020).*

Since fluids are pervasive in the Earth's crust and saturate fractures and faults, the relative proportion of the fault core and damage zone structures, and their inherent variability in grain scale and fracture permeability, significantly control the permeability structure of the fault zone (Caine et al, 1996). The formation of shear-parallel localization features (i.e. one or more PSZ's), accompanied by the decrease in grain size, further reduces the porosity and permeability normal to the fault zone, while permeability may increase towards the fault rock boundaries due to the presence of boundary parallel fractures (Logan et al., 2007; Zhang and Tullis, 1998). As a result, whether the fault zone

will act as a fluid conduit, barrier, or combined conduit-barrier system is strongly governed by the processes controlling faulting and localization. The degree of localization and the resulting permeability structures further play a crucial role in affecting the dynamic slip of a fault, since TP, one of the effective dynamic weakening mechanisms proposed to be active in crustal faults (e.g. Brantut and Platt, 2017; Rice, 2006; Wibberley, 2002), is favored by extreme localization and low permeability environments.

1.2.2 Experimental shear localization features developed at nucleation velocities

Earthquakes nucleate on a fault when the shear stress resistance along the fault surface exceeds a threshold value τ which can be described by a sliding friction coefficient μ_s, following a Mohr-Coulomb type relation of the form:

$$\tau > S_0 + \mu_s(\sigma_n - P_f) \tag{1.1}$$

where S_0 is the intrinsic shear cohesion of the rock sliding surface or gouge-filled fault (typically assumed to be zero; Byerlee, 1978), σ_n is the normal stress, and P_f is the pore fluid pressure. Whether earthquake nucleation (i.e. accelerating, seismic slip) occurs or not, depends on the fault stability, which is in turn determined by the velocity-dependence of friction (see Marone, 1998 for a review) and a critical length scale tied to the elastic stiffness of the surroundings. Numerous laboratory friction experiments have been conducted on simulated fault gouges under variable loading (e.g. slip rate and normal stress) and environmental (e.g., dry or wet) conditions to investigate the role of shear localization on the mechanical behavior of gouge-filled faults at low sliding (nucleation-relevant) velocities (in the order of μm/s). In these experiments, thin (~1–2 mm) gouge layers were sandwiched between two forcing host blocks of intact rock material or steel and were sheared relative to each other in direct-shear (e.g. Bedford et al., 2022; Verberne et al., 2014a, b), double direct-shear (e.g. Collettini et al., 2009; Ikari et al, 2015; Linker and Dieterich, 1992; Marone et al., 1998; Scuderi et al., 2017a, b), saw-cut (e.g. Logan et al., 1979, 1992; Shimamoto and Logan, 1981) or ring-shear mode (e.g. Bos and Spiers, 2000; Mandl et al., 1977) to simulate fault motion. To study the evolution of gouge microstructure with displacement and link this to the frictional response, it is necessary to perform multiple experiments at different frictional stages of the evolution of friction with the same starting materials under identical conditions and analyze the resulting microstructures.

Figure 1.2 shows a general synopsis of the correlation between the mechanical strength and the shear features developed in an experimentally deformed gouge layer at low sliding velocities. Most studies have shown that these localization features and patterns develop in a repeatable and reproducible manner within the shear zone, regardless of gouge materials (non-clay or clay-rich), initial grain size distribution, and experimental configuration (Bedford and Faulkner et al., 2021; Beeler et al., 1996; Hains et al., 2013; Logan et al., 1992, 1979; Mercuri et al., 2018; Moore and Byerlee, 1991, 1992; Noël et al., 2023; Volpe et al., 2022; Wojatschke et al., 2016). The incipient localization along Riedel shears can already be observed when the peak stress is attained during a strain-hardening phase, accompanied by gouge dilatation. The subsequent strain softening is mainly associated with the rotation of R_1 shears to shear-parallel Y shears, enabling accommodation of the ongoing fault slip. P shears are also observed at this stage although they are less common than the R_1 and Y shears. When observed, the onset of unstable slip (stick-slip or oscillation events) occurs when the relative displacement along these fractures increases until most is along shear-parallel shears. The formation of a PSZ (a single Y or boundary shear) has been reported to be a precursor for slip instability associated with the observed velocity-weakening behavior (Ikari, 2015). However, unstable slip does not necessarily occur in all experiments, but depends on normal stress, grain size, ambient temperature, and other conditions (e.g. Bedford and Faulkner, 2021). Nonetheless, laboratory friction experiments have shown that the shear fabrics observed in natural fault-zone gouges can be reproduced and that they play a major role in the evolution of frictional strength and stability.
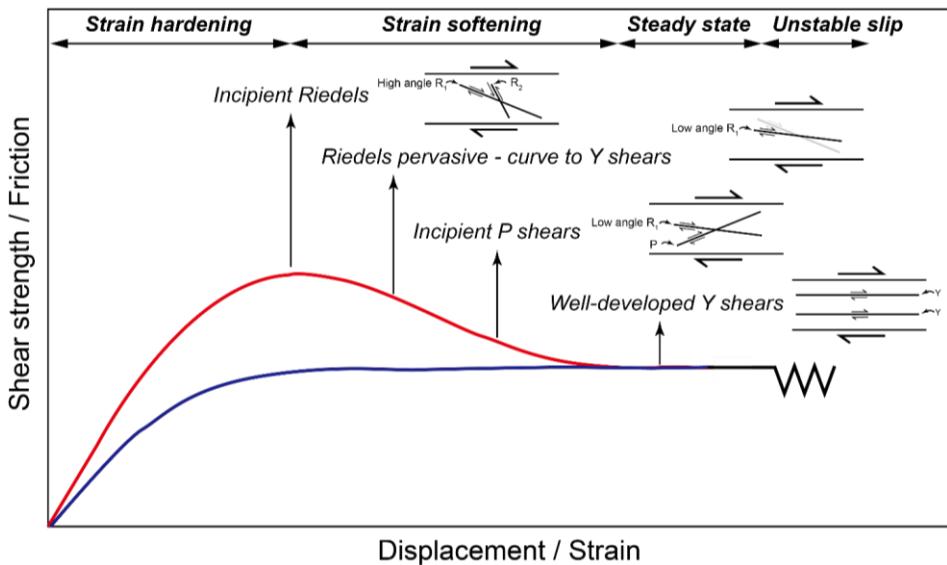
Figure 1.2: *Synoptic diagram summarizing typical mechanical strength evolution against shear displacement/strain data, alongside corresponding observations of localization features – as observed for (simulated) fault gouges deformed at a constant (nucleation-relevant) shearing velocity. Adapted from Niemeijer et al. (2020). Note that the scale of the displacement/strain is not shown because the strain at which Y or B-shears are well-developed is variable and depends on the mineralogy, initial grain size distribution, and experimental configuration. The red curve represents an over-compacted gouge sample, i.e. one which dilates as shear stress increases. The blue curve represents an under-compacted gouge sample without peak stress at the onset of shear deformation. The saw-cut curve indicates the occurrence of unstable slip ("stick-slips").*

1.2.3 Displacement partitioning between localization features

A crucial question is how much fault displacement is distributed between these localization features and whether these shear-parallel localization features accommodate the ongoing displacement. Logan et al. (1992) used a 1-mm thick layer of dry, black-coated calcite gouge segment, as a strain marker within regular white calcite gouges, to quantify the amount of displacement that is accommodated on these fabric elements. The rotation of the marker boundary indicates homogeneous shearing within the gouge layer, while the offset along the boundary indicates localization of displacement. Figure 1.3 shows the deformation of the marker boundary from one of the experiments reaching a quasi-steady state after 14.5 mm displacement. Quantitative measures of the angle of the boundary as well as the offsets give estimates for the percentage of

displacement that is accommodated on the different features. Logan et al. documented that before the peak stress, most of the displacement is homogeneously distributed within the gouge layer with only 10% of displacement accommodated along R_1 shears. After the peak stress but before the steady state, the relative amount of displacement along R_1 shears increases up to 50%. At the same time, Y shears begin to develop which accommodate approximately 10% of the total displacement. Finally, displacement is partitioned roughly equivalently (~30–35%) between homogeneous shearing, R_1 shears, and Y shears. The result indicates that the attainment of steady state or the onset of unstable slip does not necessarily require full localization of displacement along shear-parallel features where the partial bulk displacement is still accommodated along Riedel R_1 shears. Logan's work provided the first insight into fault slip distribution in a gouge fault and its correlation to fault strength during earthquake nucleation slip.
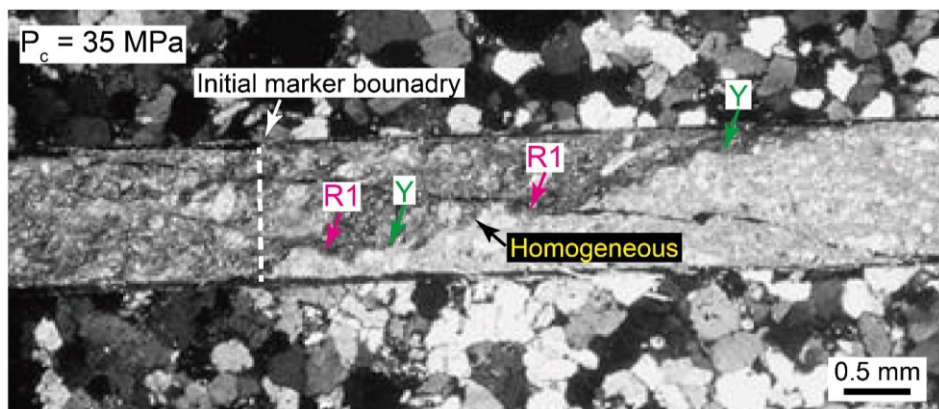
Figure 1.3: *Photomicrograph of one of the simulated fault zones investigated by Logan et al. (1992) deformed in right-lateral shear showing the boundary between white and black calcite. The gouge layer is about 1 mm thick. Localization features including Riedel R_1 and Y shears are indicated.*

1.2.4 Strain localization, frictional heating, and dynamic weakening at seismic slip velocities

When the slip velocity approaches seismic slip rates (0.1 to 10 m/s), frictional heating induced by rapid sliding and acceleration at solid contact points is expected to occur. High-velocity rotary-shear friction experiments conducted at seismic slip rates with long-displacement shearing (> few meters) have been used to investigate the role of localization and frictional heating on the dynamic slip behavior of simulated fault gouges, under both room-dry and wet conditions (e.g. Boulton et al., 2017; Chen et al., 2013; Ferri et al. 2010). Typically, most dry

and wet granular gouge materials (i.e. granular materials like quartz- or carbonate-rich gouges, as opposed to clay-rich gouges), deformed at seismic slip rates, exhibited a narrow (<100 μm) and fine-grained shear localization zone cut by a discrete, layer-parallel sliding surface or surfaces coated with extremely small ("nano"), often sintered grains (De Paola et al., 2011; Fondriest et al., 2013; Han et al., 2010; Kitajima et al., 2010; Kuo et al., 2022; Smith et al., 2013; Yao et al., 2013). By contrast, clay-rich gouges may show multiple narrow shear zones, which may be indistinguishable under wet conditions due to fluidization (e.g. Ferre et al., 2010; Ujiie et al., 2010, 2013). Regardless of gouge material, any narrow shear zone sliding at high velocity and undergoing sufficiently rapid heat production will show a significant temperature rise, which can cause softening of the gouge materials or pressurization of pore fluid, if is present within the fault zone.

Smith et al. (2015) performed systematic experimental and microstructural investigations on calcite gouges with a thin layer of dolomite gouge added as a strain marker (following the method of Logan et al., 1992). The samples were deformed at seismic rates in experiments stopped at the observed slip-strengthening, slip-weakening, and steady-state stages, i.e. stages 1, 2, and 3 as indicated in Figure 1.4. Smith et al. showed that most of the bulk shear strain is initially distributed across the full thickness of the gouge layer, with partial strain accommodated within a series of R_1 Riedel shears during the strengthening phase. The onset of dynamic weakening begins with the localization of displacement along micro-slip surfaces, each surrounded with nanoparticles formed by frictional heating (thermal decomposition of calcite) within a shear band of ~100 μm thick. With progressive displacement and ongoing weakening, subsequent strain is extremely localized to a single, ~2–3 μm thick PSZ accompanied by recrystallization within the narrow PSZ. It was thus demonstrated that slip localization, accompanied by the concentration of frictional heating, facilitated thermally activated mechanisms (i.e. carbonate decomposition) within the fault gouge materials and thus dynamic weakening. Similar occurrences of gouge microstructures with the formation of a single PSZ after dynamic weakening have also been documented in quartz-bearing (e.g. Chen et al., 2013; Kuo et al., 2022; Yao et al., 2013, 2016) and clay-rich (e.g. Boulton et al., 2017; Ferri et al., 2010; Ujiie et al., 2010, 2013) fault gouges, though the detailed mechanisms were different.
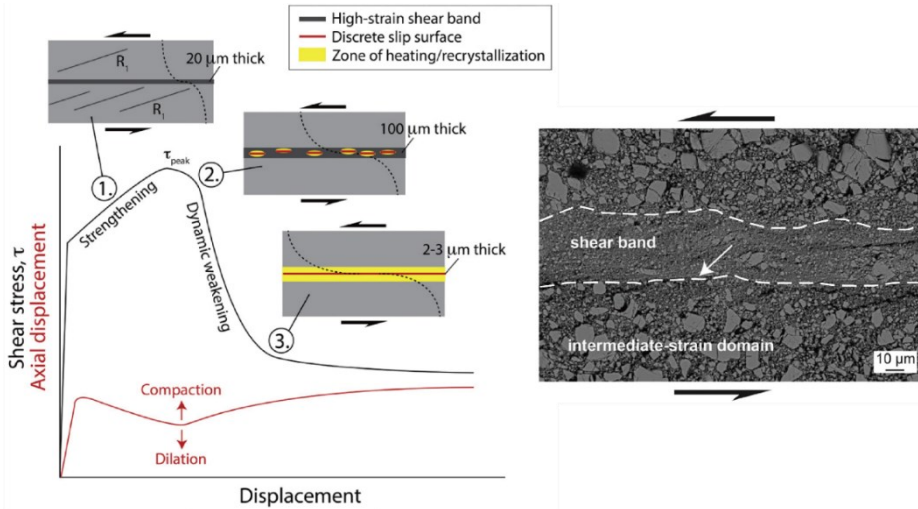
Figure 1.4: *Schematic plot of the evolution of shear stress and axial displacement as a function of displacement, with corresponding gouge microstructures retrieved at different frictional stages. Adapted from Smith et al. (2015). Right-hand side is an SEM-BSE image obtained at the onset of weakening (state 2), showing a well-developed shear band and micro-slip surfaces (indicated by the white arrow).*

In fact, several physical and chemical mechanisms have been proposed to explain the dynamic weakening behavior observed in high-velocity laboratory experiments with meter-scale displacement – and postulated to occur in natural gouge-filled faults (Di Toro et al., 2011; Niemeijer et al., 2012). The activation of these thermal processes is always accompanied by strong dynamic weakening in all types of fault-rock materials where the friction coefficient decays from a peak value μ_{pk} (e.g. 0.6–0.8 for granular gouges; 0.3–0.4 for clay-rich gouges) to a low steady-state (or dynamic) value μ_{dyn} (e.g. 0.01–0.3) over a given slip weakening distance D_w (Di Toro et al., 2011). They include flash heating and associated weakening at early stages of slip (Proctor et al., 2014; Yao et al., 2016a, b), frictional melting at grain contacts (Wang et al., 2023), thermal decomposition (De Paola et al., 2011), bulk thermo-mechanical pore fluid pressurization (TP mentioned above; Aretusini et al., 2021; Faulkner et al., 2011; Hunfeld et al., 2021; Togo et al., 2011), silica gel production and lubrication (Di Toro et al., 2004; Rowe et al., 2019), thermochemical pressurization (Brantut et al., 2010), thermally activated super-plasticity (Chen et al., 2021; De Paola et al., 2015), pore water phase transitions from the liquid to the gaseous or supercritical state

(Chen et al., 2017; Ferri et al., 2010: Oohashi at al., 2011), and flash pressurization (combined flash heating and TP at asperity contacts; Chen et al., 2023; Yao et al., 2018). The activation of any of the above-mentioned weakening mechanisms is typically dependent on the amount of frictional heat generated, which is controlled by experimental conditions (e.g. normal stress, ambient temperature, pore pressure, and background stress), material properties (e.g. mineralogy), as well as temperature increase, which is further controlled by environmental conditions (i.e. whether fluid is present, and boundary conditions (undrained or drained), and gouge microstructures (e.g. grain size and porosity). Although dramatic dynamic weakening is always observed at seismic slip rates, the slip weakening distance and the level of dynamic friction vary between different weakening mechanisms. Therefore, determining the amount of heat generation is crucial to identify weakening mechanisms during seismic slip events, as it provides crucial constraints on the energy budget and rupture dynamics.

Among all reported weakening mechanisms, flash heating and thermal pressurization are the two main dynamic weakening mechanisms expected to be active within fluid-infiltrated gouge-filled faults, based on theoretical analyses. Flash heating at asperity contacts is expected to be active as soon as dynamic slip starts (e.g. Beeler et al., 2008; Goldsby and Tullis, 2011; Rice, 1999, 2006), whereas thermal pressurization is expected to become significant for slip distances larger than few mm to centimeters, potentially leading to a total loss of strength (e.g. Noda and Shimamoto, 2005; Rice, 2006; Rempel and Rice, 2006; Wibberley and Shimamoto, 2005). Below we review the effectiveness and efficiency of these two mechanisms within a gouge-filled fault, based on analytical analyses from previous theoretical studies.

1.2.3.1 Flash heating in gouge-filled faults

Flash heating is based on the concept that the local temperature rise of a highly stressed frictional asperity far exceeds the average bulk temperature rise (Rice, 1999, 2006). It is widely reported to be a common dynamic weakening mechanism in high-velocity experiments on bare-rock surfaces from the onset of slip at (sub)seismic slip rates (typically above 0.1 m/s). The high velocity (hence local strain rate) combined with the high stress at the scale of grain contact asperities (<<1 mm) induces grain fragmentation, but also an instantaneous high

temperature rise driven by frictional heating within the contact lifetime (ms). This may result in thermal softening of the materials (e.g. microscopic melting in quartz-rich fault rock) and, thus, a lowering of the apparent macroscopic friction, typically from the onset of slip. However, the efficiency of flash heating in gouges remains unclear because of the possibility that the imposed velocity is distributed over multiple grain contacts.

For distributed deformation within a gouge layer, the total slip velocity V is shared between an array of grain contacts. Flash heating and associated weakening occur when the local slip rate at each contact exceeds the characteristic weakening slip rate V_w (Beeler et al., 2008; Brantut and Platt, 2017; Proctor et al., 2014; Platt et al., 2014; Rice, 1999, 2006; Rempel and Rice, 2006; Yao et al., 2018), described as:

$$V_w(T_{bulk}) = N_a \times V_w^a(T_{bulk}) = N_a \times \frac{\pi \alpha_{th}}{D_a} [\frac{\rho c(T_w - T_{bulk})}{\tau_c}]^2 \qquad (1.2)$$

Here, T_{bulk} is the background temperature, N_a is the number of asperity contacts mobilized across the gouge zone, V_w^a is the weakening velocity for the bare surface case, ρ is the gouge density, c is the heat capacity per unit reference volume, $\alpha_{th} = K/\rho c$ is the thermal diffusivity where K is the thermal conductivity, D_a is the diameter of the circular (grain) asperity, T_w is the characteristic weakening temperature, and τ_c is the grain/asperity contact shear strength. If flash heating is active, the evolution of macroscopic friction μ as a function of slip rate from an unweakened state (or at low slip rates) μ_s to a weakened state μ_w, can be predicted as:

$$\mu = (\mu_s - \mu_w)\frac{V_w}{V} + \mu_w \qquad (1.3)$$

From one-dimensional thermal modeling with a Green's function approach, flash temperature on an asperity contact (T_a) within a gouge layer can be expressed as (Proctor et al., 2014):

$$T_a = T_{bulk} + \frac{\tau_c}{\rho c} \sqrt{\frac{(V/N_a)D_a}{\pi \alpha_{th}}} \qquad (1.4)$$

Values for T_w, τ_c, D_a, and N_a are not well known but have been suggested in reasonable ranges in many studies (e.g. Goldsby and Tullis, 2011; Proctor et al., 2014; Rice, 2006). In particular, the values of D_a and N_a could be strongly influenced by localization of slip because of the reduction in grain size and the

generation of a thin localized shear zone, which could further influence the flash temperature rise. The parameter D_a is often obtained as a fitting parameter with typical values of a few to tens of microns (5–10 μm) at normal stresses of a few MPa at room temperature. The value of N_a is typically taken to be around 10 to 20 (Rice, 2006), or even smaller (i.e. down to 4) considering highly localized deformation (Proctor et al., 2014; Yao et al., 2018).

1.2.3.2 Thermal pressurization in fluid-infiltrated gouge-filled faults

Thermal pressurization (TP) is another dynamic weakening mechanism expected to occur in both experimental and natural fault zones during high-velocity slip. TP is driven by thermal expansion of in-situ pore fluid (e.g. Lachenbruch, 1980; Mase and Smith, 1984, 1987; Rice, 2006), which leads to an increase in pore pressure and a decrease in effective stress and thus fault strength (see equation 1.1). Many theoretical studies have looked at the role of thermal pressurization during seismic slip (Lachenbruch, 1980; Mase and Smith, 1984, 1987; Rice, 2006; Rempel and Rice, 2006). Two end-member models were derived to solve for shear strength and temperature evolution in a deforming gouge zone: i) coupled with the TP problems for short slip distances where the effects of heat and fluid mass transport can be neglected (adiabatic undrained model; Lachenbruch, 1980), and ii) for large slip distances where the finite shear zone thickness is expected to have a negligible effect on the system evolution (slip-on-plane model; Mase and Smith, 1984, 1987; Rice 2006; Rempel and Rice, 2006). In the case of the adiabatic/undrained model, the shear strength evolution is solved as:

$$\tau = \mu_s(\sigma_n - p_0)\exp\left(-\frac{\mu_s \Lambda}{\rho c}\frac{\delta}{W}\right) \tag{1.5}$$

where p_0 is the ambient pore fluid pressure before the onset of rapid slip, ρ is the gouge density, c is the heat capacity per unit reference volume, δ is the total slip distance, W is the gouge width, and Λ is the thermal pressurization factor defined by Rice (2006) as:

$$\Lambda = \frac{\lambda_f - \lambda_n}{\beta_f + \beta_n} \tag{1.6}$$

where λ_f and λ_n are the thermal expansivities of the fluid and pores, respectively, and β_f and β_n are the compressibilities of the fluid and pores, respectively. The temperature evolution is given by Rice (2006) as:

$$T = T_0 + \frac{\sigma_n - p_0}{\Lambda}(1 - \exp\left[-\frac{\mu_s\Lambda}{\rho c}\frac{\delta}{W}\right]) \tag{1.7}$$

where T_0 is the ambient temperature before the onset of rapid slip. The total strength drop associated with thermal pressurization leads to a finite maximum temperature rise:

$$\Delta T_{max} = \frac{\sigma_n - p_0}{\Lambda} \tag{1.8}$$

In the case of the slip-on-plane end-member model, shearing is assumed to act as a line heat source in 2-D. The solution for the shear strength evolution is then obtained as:

$$\tau = \mu(\sigma_n - p_0)\exp\left(\frac{\delta}{L^*}\right)erfc(\sqrt{\frac{\delta}{L^*}}) \tag{1.9}$$

In this equation, L^* is a decay distance, defined as:

$$L^* = \frac{4}{\mu^2}(\frac{\sigma c}{\Lambda})^2 \frac{(\sqrt{\alpha_{hy}} + \sqrt{\alpha_{th}})^2}{V} \tag{1.10}$$

where V is the slip velocity, $\alpha_{th} = K/\rho c$ and $\alpha_{hy} = k/\eta\beta$ are the hydraulic and thermal diffusivities of the slip zone, respectively, K is the thermal conductivity, k is the permeability, η is the fluid viscosity, and β can be expressed as $n(\beta_f + \beta_n)$, with n being the gouge porosity. Finally, in the slip-on-plane model, the fault plane temperature as a function of displacement can be expressed as:

$$T = T_0 + \left(1 + \sqrt{\frac{\alpha_{hy}}{\alpha_{th}}}\right)\frac{(\sigma_n - p_0)}{\Lambda}\left[1 - \exp\left(\frac{\delta}{L^*}\right)erfc(\sqrt{\frac{\delta}{L^*}})\right] \tag{1.11}$$

and the maximum temperature increase on the sliding surface can be written as:

$$\Delta T_{max} = \left(1 + \sqrt{\frac{\alpha_{hy}}{\alpha_{th}}}\right)\frac{(\sigma_n - p_0)}{\Lambda} \tag{1.12}$$

In comparison, the ultimate temperature rise predicted from the slip-on-plane model (equation 1.8) is higher by a factor of $\left(1 + \sqrt{\alpha_{hy}/\alpha_{th}}\right)$ than the prediction from the adiabatic/undrained model (equation 1.12). This becomes particularly significant when the hydraulic diffusivity exceeds thermal diffusivity. According to the representative parameter values assumed for α_{hy} and α_{th}

summarized by Rempel and Rice (2006), the ratio of α_{hy} to α_{th} can range from ~1.23 (the nominal value of 0.86 and 0.7 for α_{hy} and α_{th}, respectively) to ~12.42 (the average value on the damaged *P–T* path of 6.71 and 0.54 for α_{hy} and α_{th}, respectively), resulting in a factor of ~2.1 and ~4.5. This indicates that the maximum predicted temperature rises could be 110% up to 350% higher in the slip-on-plane solution than in the adiabatic/undrained solution, which demonstrates the importance of α_{hy} and α_{th} in determining the maximum temperature rise within the fault zone.

In addition, combining these two end-member solutions with thermal and hydraulic diffusion within the gouge layer, Rice et al. (2014) and Platt et al. (2014) used two types of localization limiting mechanisms, frictional rate strengthening and dilatant hardening, to determine the thickness of the localized shear zone during rapid shear (refer to the papers for more details of the analysis). They predicted localized zone thicknesses to be in between 4–44 *μ*m and 1–2 *μ*m for rate-strengthening and dilatant hardening alone, respectively, at a depth of 7 km, roughly consistent with field and experimental observations. The predicted thicknesses are independent of the initial gouge layer thickness. If localization occurs, the temperature rise and shear strength reduction together with TP could become much larger within such a narrow shear zone than a fault without localization.

1.2.5 Numerical investigations of strain localization and mechanical behavior of a sheared granular layer

Discrete element modeling (DEM) has been widely used to study the deformation of granular materials and fault mechanical behavior numerically (e.g. Casas et al., 2022; Mair and Hazzard, 2007; Nguyen et al., 2021; Papachristos et al., 2023). Using DEM, we can investigate dynamic microscale processes occurring within shear zones as they deform and evolve, as well as the corresponding mechanical response, for varying packing configurations, particle parameter values, contact laws, and deformation rates. Both 2-D and 3-D numerical simulations of gouges sheared at either subseismic or seismic slip rates, have shown that transient and/or persistent localization of strain can occur along Riedel (R_1 and R_2) and shear-parallel (Y and B) shears within a finite thickness granular gouge layer. Shear localization was identified using micro-strain mapping (e.g. Morgan and Boettcher, 1999) and a passive strain marker (Morgan,

2004; Nguyen et al., 2021), respectively. The occurrence of strain localization depends on whether time-dependent processes such as grain comminution or contact healing are considered during numerical shearing.

At subseismic slip rate (0.1 mm/s) and in the absence of time-dependent mechanisms, Morgan and Boettcher (1999) conducted 2-D numerical simulations of sheared granular gouge by varying both particle size distributions (PSD) and interparticle friction. They showed that both an increasing number of fine grains and a larger value of interparticle friction favor transient localization of strain. They interpreted this to be the result of an increased importance of interparticle rolling in accommodating granular deformation. They further showed that transient localization of strain results in a sudden drop in macroscopic friction due to a decrease in volumetric changes. When time-dependent contact healing is introduced, Morgan (2004) reported that shear strain tends to persistently localize within a boundary-parallel shear band (1 to ~10 grains thick depending on the imposed sliding velocity) due to particle interlocking. In addition, the observed stick-slip like friction variations (i.e. unstable slip) are more comparable to experimental observations. Van den Ende and Niemeijer (2018) also reported regular stick-slips when time-dependent compaction by pressure solution is considered, i.e. where the stress drop and recurrence time of stick-slips are controlled by the kinetics of pressure solution. With the introduction of grain fragmentation, Mair and Abe (2008) used a particle-based 3-D DEM model with breakable bonds to simulate grain fracturing processes during fault gouge evolution. Their simulations revealed that strain localization is strongly correlated to enhanced grain size reduction and reduction in friction.

At seismic slip rates (> 1 m/s), Casas et al. (2022) conducted a 2-D numerical study of cemented granular fault gouge to investigate the effect of interparticle bond strength (i.e. cohesion) on gouge deformation and slip weakening. Figure 1.5 shows the evolution of gouge deformation in the form of relative damage between particles at different frictional stages for a highly cohesive (cementation = 95%) and dense (porosity = 11%) gouge layer. The figure shows that a gouge layer with high cohesive strength between particles, and low porosity, is prone to large weakening effects and to the development of localized deformation features, such as R_1 and Y shears, as a result of the relatively small (< 1%) critical dilation value (i.e. dilation necessary for

macroscopic shear failure). The authors postulated that the slip weakening is associated with two different mechanisms, namely interparticle frictional sliding due to the breakage of an interparticle bond at initial slip (state B to C), and bulk gouge dilatancy (state C to H). The development of localization features is generally comparable to high-velocity experimental observations where long-term slip-weakening behavior is related to the generation of a continuous shear-parallel feature (B shear).
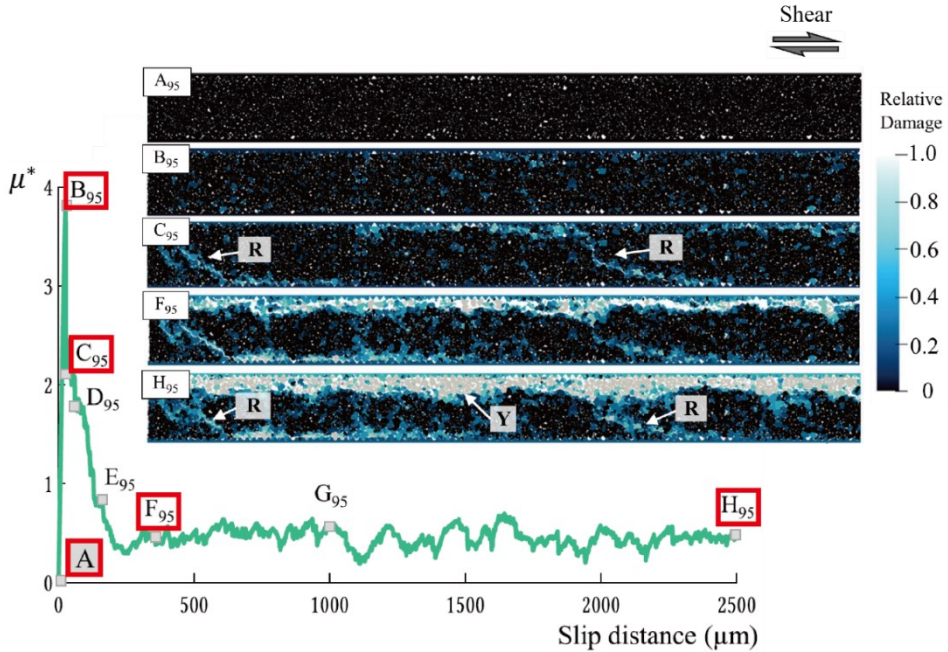
Figure 1.5: *2-D numerical results of the evolution of effective friction μ*, defined as the ratio of shear stress to normal stress, against slip distance, illustrated with corresponding relative damage snapshots of the gouge layer at different frictional states. Adapted from Casas et al. (2022). μ* is larger than 1 because of the introduction of variable cohesive bond strength (0–2500 MPa).*

In summary, previous numerical studies have shown that slip localization and the associated slip weakening, as observed in experimental observations, can be reproduced in numerical shearing of gouge zones at a wide range of slip velocities (from subseismic to seismic slip rates), to some extent. So far, these models do not include frictional heating by frictional sliding, nor thermally-induced mechanisms which might cause additional stress drop. Nonetheless,

DEM modeling remains a useful tool to investigate localization processes at the gouge scale.

1.3 Current knowledge of fault dynamics in small-magnitude earthquakes

Small-Magnitude earthquakes (M < 4), including both natural (tectonic-driven) and human-induced events, are widely considered to be self-similar with large earthquakes, assuming similar physical processes control the genesis of both (e.g. Ide and Beroza, 2001; Kwiatek et al., 2011). In both cases, fault (re)activation is controlled by the nearby state of stress, which in the natural case increases as a result of motion of tectonic plates, but in the induced case is influenced by the mechanical effect of pore fluid injection or extraction and associated poro-elastic effects, or by thermo-elastic effects (e.g. Buijze et al., 2017b; Hunfeld et al., 2020). The poro-elastic or thermal-elastic effects describe that the change in the stress state is caused by the change in pore pressure or temperature within the reservoir formation and in the surroundings when a porous rock formation is depleted (e.g. hydrocarbon production) or when cool water is injected (e.g. geothermal production). Based on the source-time function, large earthquakes (M > 6) typically show rapid fault acceleration to velocities of the order of several meters per second with meter-scale displacement (Kanamori and Brodsky, 2004). For small earthquakes (M 3–4), fault slip events are limited to a few centimeters or decimeters following a similar pulse-like slip behavior featuring rapid accelerations and immediate decelerations (Buijze et al., 2019; Dost and Kraaijpoel, 2013; Heaton, 1990; Tomic et al., 2009; Wentinck, 2018; Zoback and Gorelick, 2012).

Geological evidence like mirror-like slip surfaces (another form of localization feature) with tens to hundreds of micrometers thickness observed in exhumed fault zones (e.g. Fondriest et al., 2013; Kuo et al., 2016; McDermott et al., 2017) has been used to interpret the occurrence of earthquakes experiencing small but rapid slip. McDermott et al. (2017) applied (U+Th)/He thermochronometry to estimate the peak temperature recorded in hematite fault mirrors and showed that transient flash temperatures of 700–1200°C can be reached in a fault that was active at less than 2 km depth with estimated earthquake magnitudes of smaller than 3. Kuo et al. (2016) also suggested high transient temperatures for short seismic slip events, based on the observation of melt patches at asperity contacts on silicate-rich fault mirror surfaces. These

observations suggest that fault slip can also be localized within a narrow slip zone with the generation of high (local) temperatures for short but rapid earthquake slip, i.e. in small-magnitude earthquakes.

Previous high-velocity friction experiments on gouge materials have mostly involved a few meters of displacement imposed at a constant high velocity and were conducted with the aim of understanding fault physics in large-displacement, natural earthquakes. Experimental studies of imposed short, slip-pulse behavior have only been documented for rock-on-rock materials at a normal stress less than 10 MPa under room-dry conditions (Fukuyama and Mizoguchi, 2010; Liao et al., 2014; Spagnuolo et al., 2015). Previous triaxial experiments on dry saw-cut cohesive rocks (e.g. French et al., 2016; Hayward et al., 2021; Lockner et al., 2017; Passelègue et al., 2013) or gouge layers (e.g. Xing et al., 2019) have achieved peak slip rates ranging from mm/s to m/s and slip displacements of up to few mm under high confining pressures of up to 400 MPa, though the short "seismic" slip pulse in these experiments was controlled by stress loading rather than an imposed slip-pulse function. Before the last ten years, it was a challenge to conduct high-velocity experiments on "gouge" materials under extreme conditions because of the difficulty in confining materials during rapid sliding, not to mention the introduction of pore fluid. In recent years, thanks to the improvement of experimental setup and pressure vessel design, higher normal stresses (up to 25 MPa) and elevated pore fluid pressures can be applied to water-saturated gouges deformed at seismic slip rates, with limited loss of gouge materials while maintaining an (undrained) fluid pressure to simulate more realistic natural faulting conditions (e.g. Aretusini et al., 2021; Chen et al., 2023; Hunfeld et al., 2021; Kuo et al., 2021).

Recent seismic slip-pulse studies on both N_2-saturated (room-dry) and water-saturated fault gouges, at high effective normal stress (up to 25 MPa), have shown that wet faults significantly slip-weaken during the rapid acceleration phase within only few centimeters of displacement – independently of gouge composition (clay-rich or quartz-rich gouges; Chen et al., 2023; Hunfeld et al., 2021). By contrast, room-dry gouges showed only minor weakening, despite observed extreme slip localization and higher temperature rises (up to ~490°C). These authors proposed that flash heating might not be effective in dry gouge-filled faults and that TP is the most likely weakening mechanism in fluid-

infiltrated gouge-filled faults at upper crustal stress. However, remaining questions are i) at what scale TP occurs; in other words, whether TP occurs at grain contacts induced by flash heating (flash pressurization) or at bulk shear-band scale with bulk temperature rise, and ii) whether TP can explain the whole dynamic weakening process or whether other mechanisms might also be involved in different stages of weakening (as the effectiveness or efficiency of TP strongly depends on fluid transport properties like fluid diffusivity and permeability). Overall, the experimental observations of Hunfeld et al and Chen et al suggested that TP is likely to be effective during small-displacement earthquakes on gouge-filled faults under water-saturated conditions.

1.4 Induced seismicity in Groningen gas field, the Netherlands

The Groningen gas field is the largest onshore natural gas (gaseous hydrocarbons mainly comprised of methane) field in Western Europe, located in the northeastern part of the Netherlands (Figure 1.6a). The natural gas is trapped in the Rotliegend sandstone formation (the Slochteren Sandstone), distributed along the east–west trending in northwestern Europe. The field was initially discovered in 1959 with the drilling of the Slochteren-1 well (SDM-1; Figure 1.6b) and began to be produced in 1963. By July 2022, approximately 75% of natural gas (2250 billion cubic meters (bcm) out of a total volume close to 3000 bcm) had been produced. In 1991, small-magnitude earthquakes (M $\geq$ 1) were first detected in the northern part of the Netherlands, which is thought to be a tectonically inactive region. In the following decades, the number of small seismic events increased in frequency and magnitude, mainly in the central portion of the field, where the degree of surface subsidence is greatest, reaching ~35 cm in the central part of the field (Figure 1.6b; NAM, 2020). This reflects the compaction of the reservoir sandstone due to the increasing vertical effective stress (Hettema et al., 2002; Spiers et al., 2017), suggesting that seismicity has been induced by gas production (van Thienen-Visser and Breunese, 2015). The largest event recorded to date was an M 3.6 event on 16 August 2012, located near the village of Huizingen (Figure 1.6c). The depth of relocated hypocenters of these seismic events suggests that most, if not all, events occur on the pre-existing normal faults that cut the sandstone reservoir (~3 km, i.e. reservoir depth; Dost et al., 2020; Smith, 2019; Smith et al., 2020; Spetzler and Dost, 2017; Van Eijs et al., 2006). Thus, even though the magnitude of the events was, seismologically speaking, not high, intensities were observed as high as VI

(EMS-98 intensity scales), because of the shallow depth of the events and the soft surface soils in the area, causing damage to housing in the area.
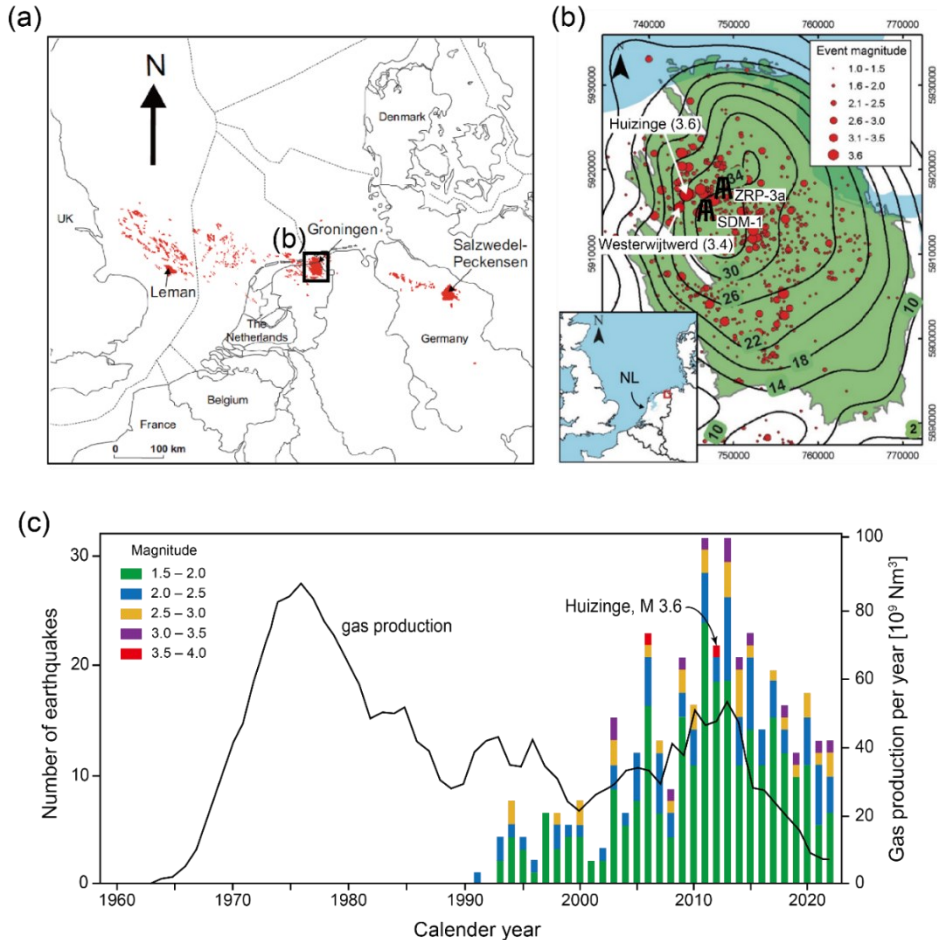
Figure 1.6: *(a) Rotliegend gas fields in northwestern Europe. Adapted from de Jager and Visser. (2017). (b) Map showing the location of the Groningen gas field, the subsidence in the field (black contour lines, numbers in cm's) as measured during a subsidence survey from 2018 (NAM, 2020), and the induced earthquakes with magnitudes greater than 1, including the locations of the 2012 Huizinge earthquake (M 3.6) and the 2019 Westerwijtwerd earthquake (M 3.4), plus the locations of the Stedum (SDM)-1 and Zeerijp (ZRP)-3a wells. (c) Annual gas production and the number of induced earthquakes with M 1.5 or greater recorded up to 2022. The unit Nm³ indicates "normal cubic meter", and is equivalent to the amount of gas occupying 1 m³ at zero °C and pressure of 1 atm. The data are derived from https://www.nam.nl/feiten-en-cijfers and https://www.knmi.nl.*

The orientation of the normal (extensional) faults cutting through the reservoir is mainly along NNW-SSE, but also in the trend of E-W and N-S (Figure 1.7a). The fault density is shown to be the highest in the southern part of the gas field, which does not correlate to the porosity distribution of the reservoir. Figure 1.7b shows a schematic plot of a NW-SE cross section cutting through the gas field. The sandstone reservoir (i.e. Slochteren Formation) is located at depths between approximately 2600 to 3200 m, with thicknesses varying from ~ 100 m in the south-southeast to ~ 300 m in the north-northwest of the field. From east to west, thickness is relatively uniform (Mijnlieff and Geluk, 2011; van Ojik et al., 2011). The top 50-150 m of the reservoir are gas-bearing while the lower portion (~1/3) is fully saturated with highly saline brine containing ~4.4 M NaCl (25.5 wt%) (Waldmann, 2012). The boundary between gas and water is denoted by a gas-water contact (GWC) at depths of ~2971 m true vertical depth, which has been observed to shift upward by ~12 m due to the decrease in reservoir pore pressure during depletion (Waldmann et al., 2017). The seal is formed by overlying Ten Boer Claystone (10–80 m thick) and anhydrite-carbonate rich Basal Zechstein formation (~50 m thick) and the underlying source rock is Carboniferous shale/siltstone substrate (> few km thick). Offsets on the majority of the faults cutting the reservoir system are in the range of 20-100 m but can be up to ~300 m (Buijze et al., 2017b). These faults were likely most active during Late Jurassic to Early Cretaceous rifting, with some being reactivated during the Late Cretaceous to Early Tertiary Alpine inversion phases involving north–south compression (de Jager and Visser., 2017). The overburden stress (σ_v) and temperature at the reservoir depth of ~3 km is expected to be ~65 MPa and ~100°C. The pore pressure (P_f) in the field has fallen from the initial 35 MPa to a near-uniform 8 MPa since production started in 1963. The minimum horizontal stress in the field, prior to depletion, was estimated to be approximately 43 MPa (Breckels and van Eekelen, 1982). The maximum horizontal stress is oriented NNW-SSE and has a magnitude of approximately 1.05-1.20 times the minimum horizontal stress (Van Eijs, 2015).
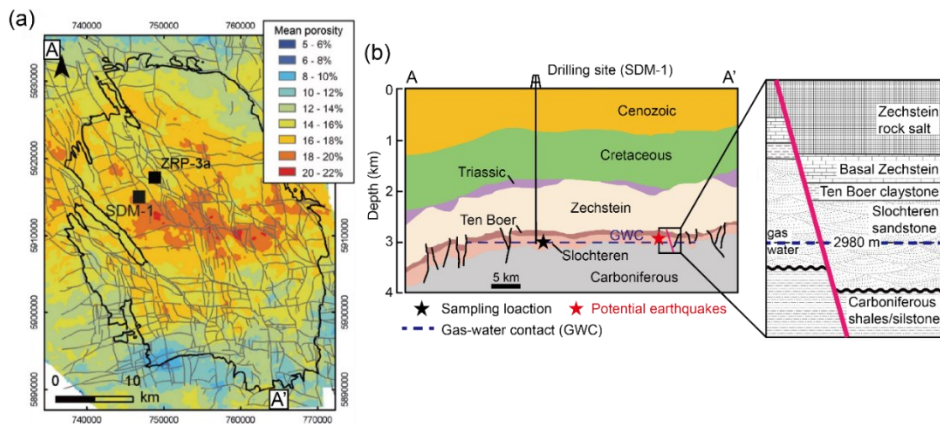
Figure 1.7: (a) Contour map of the mean (vertically averaged) porosity in the reservoir. (b) Schematic NW-SE cross section of the stratigraphy and fault systems in the Groningen gas field along (location marked A-A' in panel (a)). The depth of relocated hypocenters of induced seismic events suggests that most, if not all, events occur within the reservoir (red star; Dost et al., 2020). The black star indicates the sampling location of the starting materials (i.e. Slochteren sandstone) used in this thesis. Adapted after Hunfeld et al. (2020).

One of the most concerning questions in Groningen is what the highest possible earthquake magnitude, M_{max}, could be after production ceases (on 1 October 2023). A reliable estimate of the maximum possible magnitude relies on knowledge of the initial stress on the subsurface faults as well as physics-based constraints on the fault dynamics (e.g. dynamic weakening mechanisms, the level of dynamic friction, weakening rate) for dynamic rupture models (Buijze et al., 2017b; 2019). Since 2015, the Groningen field operator, the Nederlandse Aardolie Maatschappij (NAM), has involved laboratory-based studies to understand dynamic fault friction associated with induced seismicity in the context of Groningen (Chen et al., 2023; Hunfeld et al., 2017, 2019, 2020, 2021; Ji et al., 2022; Spiers et al., 2017). So far, the stress drops (peak value of ~0.6 to a dynamic friction value of 0.2–0.3) and the weakening rates of all key Groningen lithologies derived from slip-pulse experiments (Chen et al., 2023; Hunfeld et al., 2021) are in accordance with the values used to explain the slip-patch size and stress drop inferred from ground motions and seismic data for the largest induced events (up to M 3.6) that have occurred in the Groningen field to date (Wentinck, 2018). Also, the lab data support the finding of the location/depth distribution of the earthquake hypocenters (e.g. Dost et al., 2020; Spetzler and Dost, 2017),

showing that induced events occur over the full extent of the reservoir system and tend to propagate towards both the overlying caprock and underlying source rocks (Chen et al., 2023). However, other factors such as background stress, pore fluid properties, and host-block properties, which also play a crucial role in affecting heat generation (i.e. generation rate) and effectiveness and efficiency of TP, have not been considered, or documented in the previous studies. It is essential to include the effects of these factors in rupture models to better constrain dynamic friction and further the possible M_{max} that might occur in Groningen in the future, as well as for other ongoing or future subsurface applications that target the Slochteren sandstone as a reservoir.

1.5 Aims and structure of this thesis

From the above, it is clear that a full characterization of slip localization and partitioning from aseismic to seismic slip is essential to determine frictional heat production and to determine the principal dynamic weakening mechanism during seismic slip. This is crucial for constraining earthquake source parameters and estimating the propagation behavior of an earthquake rupture using physics-based dynamic rupture models (e.g. Buijze et al., 2017b, 2019; NAM, 2022; Van Wees et al., 2017) as well as linear elastic fracture mechanics (LEFM) models (Weng and Ampuero, 2019; Weng et al., 2021). In order to understand fault dynamics, combined analyses of laboratory friction experiments, fault microstructural development and numerical investigations that can be extrapolated to nature are required. We took the production-induced seismic events occurring in the Groningen gas field as a case study for small-magnitude earthquakes that occur within gouge-filled faults at upper crustal stress with in-situ pore fluid conditions. We focused on the quasi-static and dynamic friction behavior of simulated fault gouge prepared from Slochteren sandstone core material, (a quartz-rich rock with 72–90 vol%) as this unit is the main reservoir lithology hosting most induced events. The results of this thesis are not only relevant to Groningen earthquakes but can also be applied to other small earthquakes in the upper crust, induced and natural. They also provide input for feasibility studies of future projects in the subsurface (e.g. geothermal energy production, hydrogen storage, CO_2 storage). The aims of this thesis are defined as follows:

1. To comprehend the phenomenon of slip localization, evolution of shear fabrics, and how the total fault slip distributes over localization features of simulated fault gouges derived from Slochteren sandstone under the in-situ

pressure, temperature conditions during fault acceleration - in other words, at varying slip velocities relevant to earthquake nucleation conditions. (**Chapter 2**)

2. To quantify the slip distribution within a granular gouge assemblage containing an existing fine-grained layer oriented parallel to the shear plane, and to quantify how much localized grain size reduction (producing fine-grained layers with variable thicknesses) is required to induce localization at seismic slip rates. (**Chapter 3**)

3. To assess the role of flash heating in determining dynamic weakening behavior by experimentally characterizing flash temperatures at asperity grain contacts, within both room-dry and wet simulated quartz-rich gouge materials (Ottawa sand) with variable grain sizes, under different normal stresses and at slip velocities ranging from sub-seismic to seismic. (**Chapter 4**)

4. To evaluate the effect of the thermal and hydraulic properties of pore fluid on the effectiveness and efficiency of TP as a dynamic weakening mechanism, through medium-velocity gouge friction experiments employing a selection of pore fluids with different viscosities and compressibilities, including in-situ reservoir brine. (**Chapter 5**)

5. To determine the dominant dynamic weakening mechanism during seismic slip-pulse experiments on Slochteren-derived "gouges" under simulated reservoir conditions, using sandstone rock plates as host-block materials plus a controlled pre-stress at higher slip acceleration and shorter displacement than employed in previous work. (**Chapter 6**)

These topics are tackled sequentially in Chapters 2-6, as indicated above. Finally, in Chapter 7, I list the general conclusions and implications of this work and offer suggestions for future research.

Chapter 2

Strain localization in sandstone-derived fault gouges under conditions relevant to earthquake nucleation

Chien-Cheng Hung, André R. Niemeijer, Ivan Vasconcelos
To be re-submitted to Journal of Geophysical Research: Solid Earth.

Abstract

Constraining strain localization and the growth of shear fabrics within brittle fault zones at sub-seismic slip rates is important for understanding fault strength and frictional stability. We conducted direct shear experiments on simulated sandstone-derived fault gouges at an effective normal stress of 40 MPa, a pore fluid pressure of 15 MPa, and a temperature of 100°C. Using a passive strain marker and X-ray Computed Tomography (XCT), we analyzed the spatial distribution of deformation in gouge samples deformed in the strain-hardening, subsequent strain-softening, and then steady state regimes at displacement rates of 1, 30, and 1000 μm/s. We developed a machine-learning-based automatic boundary detection method to recognize the shear zone fabrics and quantify displacement partitioning between each fabric element. Our results show shear fabrics orientated along R_1 Riedel shear and Y shear (including boundary shear) are the two major localization features. At rates of 1 and 30 μm/s, the amount of displacement on R_1 shears is displacement dependent, increasing to ~20% of the imposed displacement up to the strain-softening state, then decreasing to ~10–18% at the steady state. This trend is absent at the high rate where ~18% of the displacement occurs on R_1 shears throughout all investigated stages. At all rates, the relative amount of displacement on Y shears increases linearly with displacement to a total of larger than 50% at the steady-state stage. Our study provides constraints on the development of the active (principal) slip zone, which is an important factor controlling heating and weakening associated with small-magnitude earthquakes with limited displacement (mm-dm), such as induced seismic events.

2.1 Introduction

Field and borehole observations conducted on brittle fault zones have provided evidence indicating that fault cores frequently consist of fine-grained wear products, referred to as fault gouge (Chester and Chester, 1998; Collettini et al., 2009; Sibson, 1986). Fault gouges often exhibit structural fabrics characterized by distinct distributions of grain size and shape, which can be attributed to the processes of grain fragmentation and wear occurring during fault slip. These fabrics are generally interpreted as indicators of strain localization in near planar zones where fault slip has been accommodated. Gouge fabrics can also be used to infer faulting mechanisms (Boullier et al., 2009) and estimate stress states after earthquakes (Kuo et al., 2022). Comprehending the phenomenon of strain localization and the evolution of shear fabrics within brittle fault zones holds paramount importance, as these shear fabrics bear direct implications for the mechanical strength and overall stability of faults (e.g. Ikari et al., 2015 Moore and Byerlee, 1992; Scuderi et al., 2017a, b) as well as for their hydrological behavior (e.g. Caine et al., 1996; Wibberley, 2005).

Laboratory friction experiments have shown that natural shear fabrics can be reproduced in experimental fault zones from subseismic ($V < 100$ μm/s; e.g. Beeler et al., 1996; Bedford and Faulkner et al., 2021; Haines et al., 2013; Logan et al., 1979; Mercuri et al., 2018; Moore and Byerlee, 1991, 1992; Noël et al., 2023; Volpe et al., 2022; Wojatschke et al., 2016) to seismic rates ($V > 1$ m/s; e.g. Kuo et al., 2014; Smith et al., 2013). At earthquake nucleation velocity (i.e. of order 1 μm/s), Logan et al. (1992) systematically reported on the evolution of experimental shear fabrics within simulated calcite gouges with variable gouge thicknesses, shear strains, and confining pressures. To identify the development of gouge fabrics and to quantify the amount of displacement that is accommodated on these fabric elements, as well as to elucidate any correlations to the mechanical behavior, they used a 1-mm thick layer of hydrocarbon-coated calcite gouge with a black color as a strain marker within regular white calcite gouges. They found that the simulated fault gouges developed four major localization features, i.e. R_1, R_2, P, and Y (or boundary shear, referred to as B) shears (e.g. Riedel, 1929), in a repeatable and predictable manner, which evolved with increasing shear strain. Note that the B shear was not defined separately by Logan. A general observation is that the onset of localization (i.e. R_1 and R_2 shear) occurs during an initial strain-hardening phase and is accompanied by gouge

dilation. As a result, the dilatancy of the sample and the development of R_1, R_2 shear planes accommodate most of the deformation. Strain softening or occasionally unstable sliding follows, during which the strain shifts to be accommodated within shear-parallel shears (i.e. Y or B shears), developed due to the presence of rigid boundary walls and rotation of the stress field (Bedford and Faulkner, 2021; Hains et al., 2013; Logan, 1992; Niemeijer et al., 2020; Scuderi et al., 2017a, b). Haines et al. (2013) studied the evolution and development of gouge fabrics within clay-rich fault gouges at a similar range of shear strains but a larger range of normal stresses. They demonstrated that the fabric elements evolved in a systematic manner, from Riedel shear along R_1 orientations at low strain to shear-parallel Y (and B) shears at high strain, where clay particles could accommodate strain within multiple narrow Y or B surfaces without much grain size reduction. However, studies of gouge microstructure evolution with displacement remain relatively limited, not to mention the quantification of displacement partitioning between these localization features and the bulk gouge. This is primarily due to the time-consuming nature of conducting multiple experiments achieving different displacements, using identical starting materials and consistent conditions, followed by the analysis of resulting microstructures. Therefore, it remains poorly understood how the total fault slip is distributed over these localization features, particularly in quartz-rich gouges, during fault acceleration, i.e. at varying slip velocities such as during earthquake nucleation.

In this study, we systematically investigate how strain localization evolves at different frictional stages (i.e. during an initial strain-hardening stage, subsequent strain-softening stage, and then steady-state stage) and at varying imposed displacement rates, using Slochteren sandstone gouges (i.e. simulated, quartz-rich gouges) retrieved from the Groningen gas field, located in the Northeast of the Netherlands. All friction experiments were performed at an effective normal stress of 40 MPa, a pore fluid pressure of 15 MPa, and a temperature of 100°C, which is comparable to the in-situ reservoir conditions in Groningen. Three different shearing velocities of 1, 30, and 1000 μm/s were employed to simulate different stages during fault slip acceleration leading to instability (i.e. an earthquake). The key aim is to understand how displacement partitioning between different localization features depends on shear displacement and displacement rate, as well as how this affects the associated mechanical response.

2.2 Methods

2.2.1 Starting materials

We used crushed Slochteren sandstone obtained from the Groningen gas field, as the starting material (courtesy of the field operator, the Nederlandse Aardolie Maatschappij BV – NAM). The Slochteren sandstone, sourced from the core of the Stedum 1 (SDM-1) borehole, served as the material of interest. Sandstone cores, extracted both above and below the gas-water contact (GWC, at a depth of ~2980 m below the surface during drilling), were crushed into a powdered form using a jaw crusher. The resulting powder was employed as the starting material to simulate the fine-grained gouge product typically found within the principal slip zones of natural fault zones (Chester and Chester, 1998; Sibson, 1986), such as those hosting induced seismicity in the Groningen gas reservoir. Note that the resulting powder, derived from the core below the GWC, may contain some salts because the high-salinity brine present in the core upon recovery resulted in salt precipitation in the pore space during core storage. The grain size distribution of the crushed materials is characterized by a mean grain size of ~25 μm with a maximum grain size up to ~ 200 μm where approximately 80 wt% of grains are smaller than 50 μm (see Figure S2.1). The mineral composition of the Slochteren sandstone gouge (SSG) consists of ~75 wt% quartz, ~12 wt% feldspar, minor amounts of clay minerals (~5 wt%, kaolinite, and phengite), carbonates (~5 wt%), and other minerals (~3%). The composition given here is the average value of the mineral composition of the SSG below and above the GWC as reported by Hunfeld et al. (2017). Around 2.86g of the SSG materials were used to produce a roughly 1 mm thick gouge layer for direct shear testing (Figure 2.1a-c).

To visualize strain distribution within simulated gouge layers after deformation, we added a ~5 mm wide (~0.34 g), 1 mm thick gouge strip of pure albite, with a grain size < 106 μm, as a passive strain marker to the middle of the SSG layer (~2.86 g) (Figure 2.1a-c). The use of the albite can provide significant gray-scale intensity contrast versus quartz, in X-ray Computed Tomography (XCT) scans, to allow the identification of a visible boundary before and after the shearing experiment (Figure 2.1d). In addition, the use of a minor amount of albite has a negligible impact on the mechanical behavior of the material (see Figure S2.2).
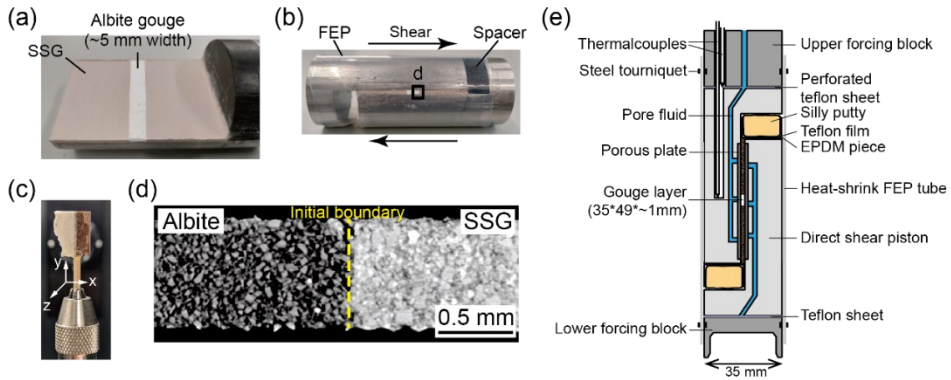
Figure 2.1: *Direct shear set-up with a starting Slochteren sandstone gouge (SSG) layer with a 5 mm wide albite marker layer. (a) Photograph of the starting layer. (b) The assembled set-up with the shear sample sandwiched by the set-up, jacketed by FEP heat shrink tube. (c) A section of the sample containing albite-SSG boundary prepared for analysis with the Zeiss Versa 510 X-ray microscope. (d) Example of X-ray CT reconstruction showing the initial sample with the albite marker layer after compaction. The boundary between the albite and the SSG is indicated by the yellow dashed line and can clearly be identified on the basis of contrast in the gray-scales. (e) Schematic plot of the direct shear setup.*

2.2.2 Direct shear experiments

To conduct the experiments, we utilized a direct shear assembly (Figure 2.1e) incorporated within a conventional triaxial apparatus known as the Shuttle apparatus, located in an Instron 1362 loading frame (as described by Verberne et al., 2014b). The simulated fault gouge layers of approximately 1 mm thickness were sandwiched between two L-shaped pistons with individual dimensions of 35 mm in diameter by 70 mm total length, containing a 35 mm × 49 mm, grooved piston face (in contact with the sample), a 35 mm × 9 mm smooth surface, plus a cylindrical 35 mm × 12 mm end-piece. To minimize the rebound effect of the pistons during the unloading process, we use a heat-shrink FEP tube and a silicone polymer ("silly putty") as the outer confining jacket and the spacer material, respectively.

A total of 15 experiments were performed, including 14 constant-velocity experiments and one velocity-stepping experiment, conducted at a confining pressure of 55 MPa, a pore fluid (DI water) pressure of 15 MPa (drained conditions), and a temperature of 100°C, to simulate the in-situ reservoir conditions in Groningen (Hunfeld et al., 2017; 2020). Due to the presence of salts in the SSG, any salts present in the SSG presumably would dissolve in the DI water in the experiments, which would lead to slightly salty water for all experiments. The piston set, including the simulated fault, was subjected to

loading at a constant displacement rate, using the Instron 1362 electro-servo-controlled loading frame. Silicone oil was employed as the confining medium during the experiments, and the application of confining pressure was initially achieved using a compressed-air-driven diaphragm pump. The confining pressure and pore fluid pressure were controlled by an ISCO pump. Heating was facilitated through the utilization of a Thermocoax internal furnace. The temperature control was implemented using a three-term CAL2300 industrial controller, which allowed precise regulation within 0.1°C of the designated set-point temperature. The temperature of the sample was monitored using a thermocouple that penetrated the upper direct shear piston and reached a position within 24 mm of the sample layer. In our experimental setup, the application of shear stress to the gouge layer was accomplished by advancing the loading piston within the Shuttle vessel. Before shearing, all tested samples remained pressurized at the targeted conditions for at least 12 hours to ensure thermal and pressure equilibration as well as chemical equilibrium between soluble phases in the sample and the pore fluid.

Throughout each experiment, data on axial load, piston displacement in the axial direction, confining pressure, temperature, pore fluid pressure, and pore fluid volume were collected at a logging rate ranging from 10–100 Hz. Shear stress (τ) was calculated by dividing the internal axial load by the contact area of the shear surface, which was assumed to be equal to the initial contact area. The apparent coefficient of sliding friction (μ_{app}) was determined as the ratio of τ to the effective normal stress (σ_n^{eff}), under the assumptions of zero cohesion as described by Byerlee (1978) and uniform pressure in the pore-fluid/sample system. The maximum error in the effective normal stress (σ_n^{eff}) was within ± 0.004 MPa. Since P_c is always equal to σ_n in the current testing assembly, the effective normal stress, defined as $\sigma_n^{eff} = P_c - P_f$, was equal to 40 MPa in all experiments. Measured displacement was corrected for machine stiffness yielding data with an error within 20 μm.

With the aim of investigating the partitioning of displacement at different stages of the τ vs displacement curve, and at different slip velocities, we analyzed deformed samples produced in experiments stopped after (1) 1.3 mm of displacement corresponding to the attainment of the peak stress, termed as the "strain-hardening stage", (2) 2.1 mm of displacement after the peak stress (i.e.

3.4 mm total displacement), termed as "strain-softening stage", and (3) 5.5 mm of displacement corresponding to the steady-state stage, under slip velocities of 1, 30, and 1000 μm/s. The experiments performed are listed in Table 2.1, along with the conditions and key information. We additionally conducted a velocity-stepping experiment with velocity steps to 1-30-1000-30 μm/s, each over a displacement interval of 1–2 mm (see Figure S2.2b), for control purposes of the mechanical strength on the pure SSG.

Table 2.1: *List of experiments and corresponding key information. All the experiments were conducted at a confining pressure of 55 MPa, a pore fluid (DI water) pressure of 15 MPa (drained conditions), and a temperature of 100°C.*

ID	V (μm/s)	Disp. (mm)	$\mu_{hardening}$ (μ_{pk})	$\mu_{softening}$	μ_{ss}	Strain marker
s015	1000	5.5	0.53	0.55	0.51	albite
s018	1	1.5	0.64	-	-	albite
s029	1	5.5	0.64	0.63	0.60	Pure SSG
s032	1-30-1000-30	5.5	-	-	-	Pure SSG
s043	1	3.5	0.63	0.61	-	albite
s046	30	1.5	0.61	-	-	albite
s050	1000	5.5	0.64	W0.63	0.60	Pure SSG
s052	1000	1.5	0.60	-	-	albite
s053	1000	3.5	0.50	0.52	-	albite
s055	1000	5.5	0.59	0.62	0.59	albite
s056	30	5.5	0.64	0.62	0.60	albite
s057	1000	3.5	0.58	0.60	-	albite
s058	30	3.5	0.56	0.57	-	albite
s059	1	5.5	0.64	0.62	0.59	albite
s060	30	1.5	0.60	-	-	albite

Note. We took the friction coefficient reached at the strain-hardening stage $\mu_{hardening}$ as "peak" friction μpk. V = the slip velocity. Disp. = the total imposed displacement. $\mu_{hardening}$ = the apparent friction coefficient measured at the strain-hardening stage. $\mu_{softening}$ = the apparent friction coefficient measured at the strain-softening stage. μ_{ss} = the apparent friction coefficient measured at the steady-state stage.

After each experiment, the length of the sample assembly was measured, and the entire assembly was oven-dried for at least 7 hours. The length change of the sample assembly before and after each experiment is defined as the external shear δ for the gouge sample. Subsequently, the direct shear setup was disassembled, and intact fragments of the sheared gouge layers were retrieved for

further microstructural analysis. We carefully collected the fragments of the deformed gouge sample containing the albite-SSG boundary. To make the sample more cohesive, we added a few drops of Paraloid B72 binder in 10% Acetone to the sample and let it air-dry for at least 10–15 minutes. The dried samples were then glued on the tip of pencil leads or toothpicks for X-ray computed tomography (XCT) analysis (Figure 2.1c). For clarity, we define the width, length, and thickness of the gouge sample as the x, y, and z directions, respectively (Figure 2.1c).

2.2.3 X-**r**ay **c**omputed **t**omography (XCT) **s**can

A Zeiss Versa 610 XCT Versa high-resolution microscope system was used to investigate the microstructures of the samples. This provides mm-scale observations of the orientation of the shear band and fracture arrays within the deformed gouge sample. In addition, the scan provides 2-D projections and 3-D imaging of the sample without damaging the sample. For each XCT run, the sample with pencil lead (or toothpick) was mounted vertically on a sample holder and installed in the XCT machine between the X-ray source and detector.

We used a detector with an objective of 4x magnification and applied an X-ray beam with a voltage of 60 kV and a power of 6.5 W to the sample with an exposure time of 20 seconds. These conditions, together with the distance between the sample and detector, provide a square field of view of dimension 5 mm and an image resolution of ~2.5 μm per pixel. Based on the field of view and pixel resolution, we exported an average number of ~2000 2-D slice images for each sample.

2.2.4 Automatic **b**oundary **d**etection and **q**uantification of **s**lip **l**ocalization

We employed a custom-designed machine-learning (ML) trainable segmentation tool from "scikit-image", an open-source image processing library (available at https://scikit-image.org/; Van der Walt et al., 2014), to develop our automatic boundary detection method. This was used to identify the albite-quartz boundary for more than hundreds of XCT images for each sample. Trainable segmentation is a pixel-based segmentation method computed using local features and a "random forest" approach (Ho, 1995). We first pre-defined the albite and the SSG regions to train a random-forest classifier. Based on local intensity and textures at different scales, the pixels of the mask were trained to

obtain a classifier (e.g. Kreshuk and Chang, 2019; Pedregosa et al., 2011). The trained classifier can then automatically identify and predict the unlabeled pixel content in the remaining SSG region. This allows segmentation boundaries, inferred by the classifier between the albite gouge and the SSG, to be subsequently and automatically retrieved. With this ML-based segmentation approach, we can significantly reduce the time required to analyze hundreds to thousands of images. Detailed information on the ML training (e.g. training parameterization) and validation (e.g. training data) are summarized in the supplementary material (see text S2.1).

Figure 2.2 shows the workflow of the automatic boundary detection and localization quantification method. The entire procedure is divided into six main steps:

1. For each analyzed sample, we first picked five images out of the total images that have equal intervals of image number in the space domain of the entire analyzed width of the sample, as the standard images for training the segmentation. For each of the five images, we labeled the albite gouge and the SSG regions by drawing masks (blue and green rectangles for albite gouge and SSG, respectively) to automatically find the main color boundary (yellow curve) (Figure 2.2b). One thing to note is that some samples show extremely thin B shears which are too thin to be identified with the current resolution. To circumvent this problem, we did not consider these B shears during the automatic detection procedure. The amount of displacement along B shears for each experiment was determined as the difference between the external shear δ and internal shear L, determined by the projected length of the albite-SSG boundary (without B shear) on the gouge-forcing block boundary. This relation is schematically illustrated in Figure S2.3 and will be further discussed in section 4.3.1. The displacement along the B shear is added to the internal shear L and Y shear afterward when quantifying displacement partitioning between deformation features.

2. To remove spurious boundaries, we used the Density-Based Spatial Clustering of Applications with Noise (DBSCAN; Ester et al., 1996) clustering method to retrieve the albite-SSG boundary with the highest density of clusters (Figure 2.2c)

3. We applied a moving average with a moving window of 4 (pixel) and a window step size of 1 (pixel) to the high-density cluster to perform the first step of smoothing (Figure 2.2d).

4. We applied the Ramer-Douglas-Peucker (RDP) algorithm (Douglas and Peucker, 1973; Ramer 1972), a non-parametric line fitting and turning point (i.e. point of max curvature) detection method, to reduce the number of points in the boundary curve and performed a second smoothing and to subsequently identify the turning points (Figure 2.2e). The degree of simplification of the fitted curve is controlled by the "tolerance" parameter, which defines the maximum allowable deviation between the simplified path and the original path (i.e. the smoothed curve from step iii). As the tolerance value increases, the resulting simplified path becomes coarser or less refined in its representation. The determination of the turning points of the boundary curve is controlled by a minimum angle (between 0 to π in radians). If the angle between the direction vectors on the simplified curve is larger than the defined minimum angle, we consider the point where the direction vector changes as the turning point. We selected a tolerance level of 5 (maximum distance with five pixels) and a minimum angle coefficient of 0.05 (minimum angle = $0.05 \times \pi$) for the line fitting and the turning point detection. These selected values provide good consistency of the turning points between the manual identification and the automatic detection (Figure 2.2a, e).

5. After the boundary and turning points were identified, we adopted the same methods used by Logan et al. (1992) to assess strain partitioning between different deformation features (e.g. homogeneous deformation vs. R_1, and Y shears) and to quantify the amount of displacement on each feature. We define R_1 shears as bands oriented in a range from -45 to -3 degrees relative to the gouge-host block boundary (clockwise rotation from the shear direction to be positive), as previous experimental studies have shown that R_1 shears can be nearly parallel to the shear direction at the shear-zone boundary but become larger further away from the boundary (e.g. Verberne et al., 2014b). For the definition of a Y shear, we selected the angle ranging from -3 to +3 degrees relative to the shear direction. Figure 2.2f shows that the displacement accommodated by homogeneous/distributed deformation, slip on R_1, and slip on Y shears, obtained from both the automatic and manual methods have a good consistency. Manual identification of the

marker boundary and localization quantification is a crucial process we applied to validate the training data. Here, we defined good consistency such that the displacement tolerance misfit for a specific deformation feature between the automatic and manual results is within a pre-defined value of 10%. Once the results of the first five images of the manual and automatic methods are consistent, we further applied identical trainable segmentation conditions to another five images as the validation data to examine whether the segmentation boundary produced by the segment classifier is acceptable and does not produce much overfitting. This is another validation process, which is not shown here in the main workflow (see Figure S2.4 for more details).

6. Finally, we fit the rest of the images with the segment classifier and run the same procedure (indicated by the pink arrows). Figure 2.2g shows the total displacement and the displacement partitioning between homogeneous, Y, R_1, and R_2 shears as a function of slice number. The interval between slices is equivalent to 1 pixel resolution which is 2.54 μm in this case. Despite identical segmentation conditions, we still obtain a few discontinuous segmentation boundaries which can be easily identified in both the total displacement and the output images. For example, in some slices, the segmentation boundary was not detected to be a continuous cluster as compared to the good example. We used the Z-score to remove these outliers to obtain the final result, as shown in Figure 2.2h.
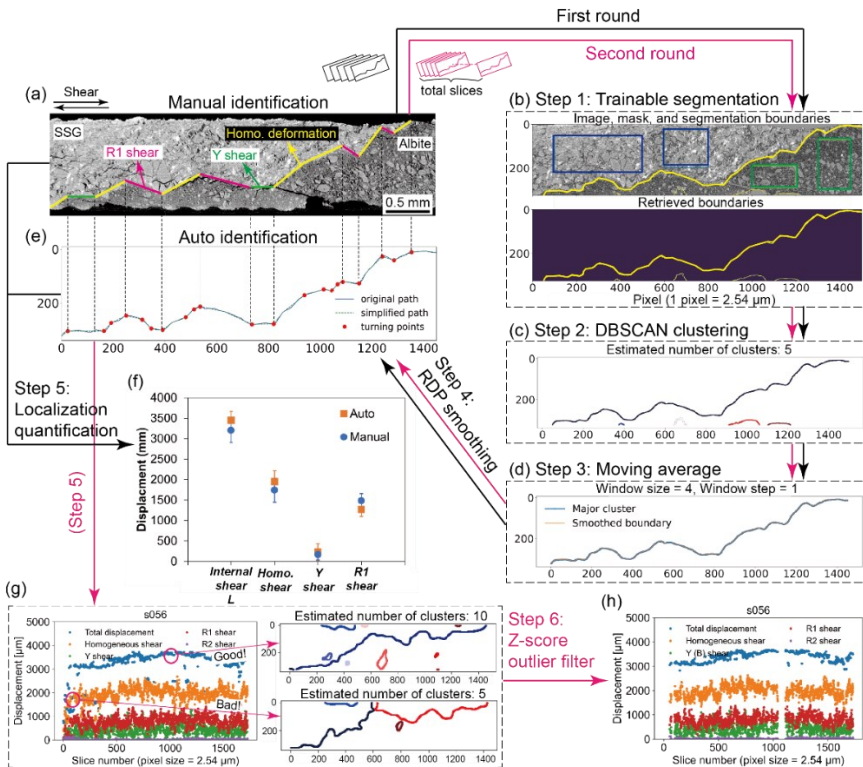
Figure 2.2: *The workflow of image processing and quantification applied to our stacks of XCT slice images (a) An example of the XCT image slice of the gouge layer deformed at 30 μm/s at steady-state stage, which shows different localization features along the SSG-albite boundary. (b) Step 1: Trainable segmentation by masking the SSG and albite gouge regions based on the different features such as local intensity, textures, and edges at different scales to train a random-forest classifier. (c) Step 2: Density-Based Spatial Clustering of Applications with Noise (DBSCAN) clustering to retrieve the boundary with the highest density of clusters. (d) Step 3: Moving average with a moving window of 4 (pixel) and a window step of 1 (pixel) to perform first smoothing. (e) Step 4: Ramer-Douglas-Peucker (RDP) algorithm to perform a second smoothing and to subsequently identify the turning points along the boundary. (f) Absolute amount of localized displacement against homogeneous, R_1, and Y shears obtained from the automatic and manual methods. (g) Displacement partitioning between homogeneous, Y, R_1, and R_2 shears as a function of slice number. Two examples of good and bad segmentation boundaries are shown where good represents a continuous cluster along the boundary while bad represents discontinuous clusters of the boundary. (h) Final result of the displacement partitioning between different deformation features after applying Z-score to remove the outliers. See main text for more detailed descriptions. Black and pink arrows indicate the first and second rounds of segmentation, respectively.*

2.3 Results

2.3.1 Frictional behavior

All the experiments exhibit a similar evolution of apparent friction coefficient μ_{app} with displacement, but for small variations with displacement rate, as exemplified in Figure 2.3. Note that the displacement shown here has been corrected for the elastic deformation of the apparatus. After initial loading (sample settling), μ_{app} shows a rapid and near-linear increase, reaching an apparent yield point (departure from linearity) within the first ~0.5 mm of displacement. This is followed by hardening towards a broad peak friction μ_{pk} and subsequent softening towards a roughly linear softening stage then to a "steady-state" friction μ_{ss}. At the displacement rate of 1000 μm/s, we notice that the μ_{app} at the strain-hardening stage (~0.59) is lower than at the strain-softening stage (~0.62). For the purpose of comparison, we take μ_{pk} as the μ_{app} reached at the strain-hardening stage for all the experiments. In addition, since "steady-state" sliding was not attained in all the experiments, we take μ_{ss} as the minimum μ_{app} reached during or after the strain-softening stage (i.e. at around 5.5 mm displacement). Overall, μ_{pk} at 1 and 30 μm/s lies at ~0.63, which is slightly larger than that at 1000 μm/s (~0.59). Values of μ_{ss} of ~0.59–0.6 are achieved at all velocities. Our results show good reproducibility of the μ vs. displacement curves obtained at 1 and 30 μm/s, while curves obtained at 1000 μm/s generally show lower strength at any given displacement, especially at 0.5 to 3 mm displacement (Figures 2.3 and S2.2). On the other hand, in this displacement range at 1000 μm/s, we observed a sharp pore pressure increase by up to ~0.5 MPa, peaking at a displacement of 0.8 mm followed by a steady decrease and ultimate approach to sub-background levels (i.e. ≤15 MPa).
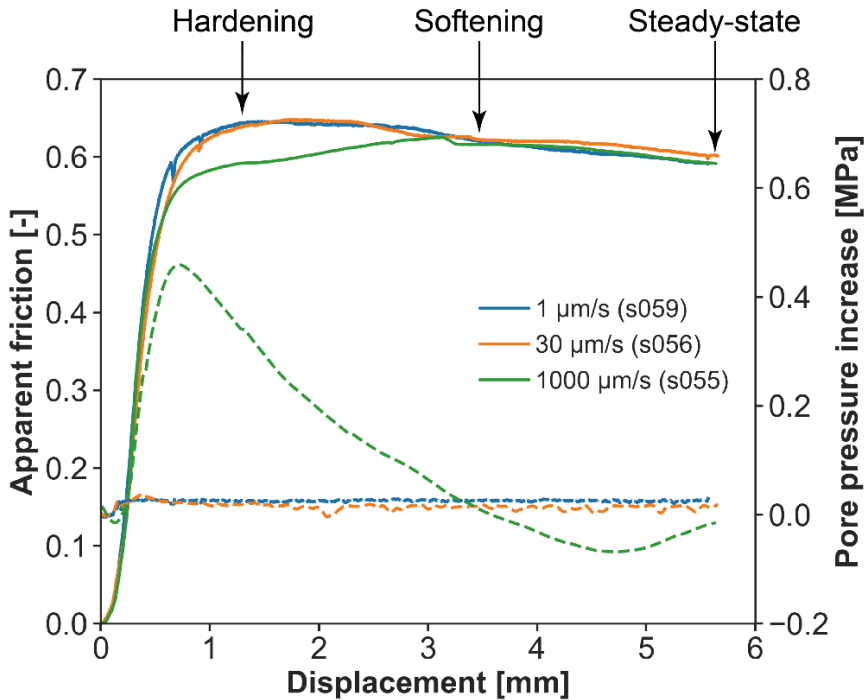
Figure 2.3: *Representative frictional behavior of the Slochteren sandstone gouges for ~5.5 mm displacement at three different displacement rates of 1, 30, and 1000 µm/s. Experiments were stopped at the strain-hardening, strain-softening, and steady-state stages, which are equivalent to ~1.3, ~3.4, and ~5.5 mm displacement, respectively, as indicated. The solid curve indicates apparent friction while the dashed curve indicates pore fluid pressure measured at the ISCO pump.*

2.3.2 Deformed gouge observations

2.3.2.1 Macroscopic observations

After dismantling the L-shaped pistons, most of the gouge samples remained attached to one of the two forcing blocks (left pictures in Figures 2.4 to 2.6). In general, we found that the completeness (i.e. physical integrity) of the recovered sample depends on the imposed amount of shear strain. Most samples deformed into the strain-hardening and strain-softening stages only show a high degree of completeness (i.e. splitting occurred along one of the sample-forcing block boundaries). However, the gouge samples sheared to large displacement disintegrated into cohesive fragments within the central portion of the albite gouge layer, splitting along shear-induced fabrics aligned with the shear planes in R_1 type Riedel shears, and attaching to both forcing blocks (Figure 2.5c and 2.6). In addition, most of the samples show an extremely thin layer of the albite gouge smeared on top of the SSG layer at the gouge-forcing block boundary,

which indicates the development of a boundary shear (Figure 2.4h, 2.5e, 2.6b, d, and g). The sampling location at the boundary of the gouge layer is nearly identical for each experiment, as indicated by the red rectangles in Figures 2.4 to 2.6.

2.3.2.2 X-ray CT microstructural observations

The pictures on the right in Figures 2.4 to 2.6 show representative XCT images of the gouge microstructures. All samples show a clear gray-scale intensity boundary between the albite gouge (dark gray area) and the SSG (light gray area). The presence of groove imprints observed at the boundaries of the cross sections is attributed to the porous plates of the forcing blocks. This observation suggests complete (local) sample recovery at the gouge-forcing block boundary, as shown in Figure 2.4a. In the shear zone, we observed that R_1 shear and Y shear (including B shear) are the two major shear fabrics at all frictional stages, while none of the samples exhibited a shear band in the P orientation. The criteria used to define these two shear localization features were based on the following observations: i) if a developed band (or fracture) is orientated as defined in the automatic localization quantification, and/or ii) if the albite-SSG boundary is offset by the corresponding shear sense. Note that most of the identified R_1 shears do not cause visible offset to the marker boundary (Criterion 2) because they often develop without accommodating much displacement. For a Y shear, both criteria must be satisfied because a shear-parallel fracture present in either the albite or SSG layers might result from opening during sample recovery. We did not consider grain size reduction as an essential criterion to determine the localization feature because in some cases we do not observe significant grain size reduction on R_1 or Y shear planes while they do offset the marker boundary; for example, the Y shear observed in Figure 2.5a (the towards center one).

In the strain-hardening stage, we see that the samples at all displacement rates do not show evident offsets of the marker boundary, but rather a fracture array orientated along R_1 shear with an angle of about -30 to -40 degrees to the shear direction (Figure 2.4). Though virtually no displacement was visible along these R_1 shears, some grain size reduction can be observed (Figure 2.4f). Despite the absence of an offset of the albite-SSG boundary, we note that the angle of the marker boundary to the shear direction does not completely follow the expected

simple shear angle (i.e. ~45° boundary rotation in this sample with shear strain around 1). At 1000 μm/s only, we observed one B shear also occurred, accompanied by visible grain size reduction and smearing of an extremely narrow SSG layer (less than 50 μm thick) (Figure 2.4h and i).

In the strain-softening stage, samples deformed at all displacement rates exhibited offsets developed along the marker boundary with an angle of about -15° to -20° relative to the shear direction (Figure 2.5). R_1 and Y shears are easier to distinguish in this stage at all velocities. Displacement along the shear-zone boundaries is also visible together with zones of grain size reduction, which is particularly significant at velocities of 1 and 30 μm/s (Figure 2.5b, c, and e). The nearly vertical opening cracks observed at 1 μm/s result from sample recovery/handling (Figure 2.5b and c).

At the large-displacement or steady-state stage, more abundant Y and B shears developed at all velocities. In the B shears, the marker boundary was further smeared out, and an extremely thin (~few microns) localized layer can be clearly identified (Figure 2.6e). The R_1 shears remain observable, especially at the displacement rates of 1 and 30 μm/s (Figure 2.6b and d), while the angle of some R_1 shears becomes lower with an angle of less than -10° (Figure 2.6d).
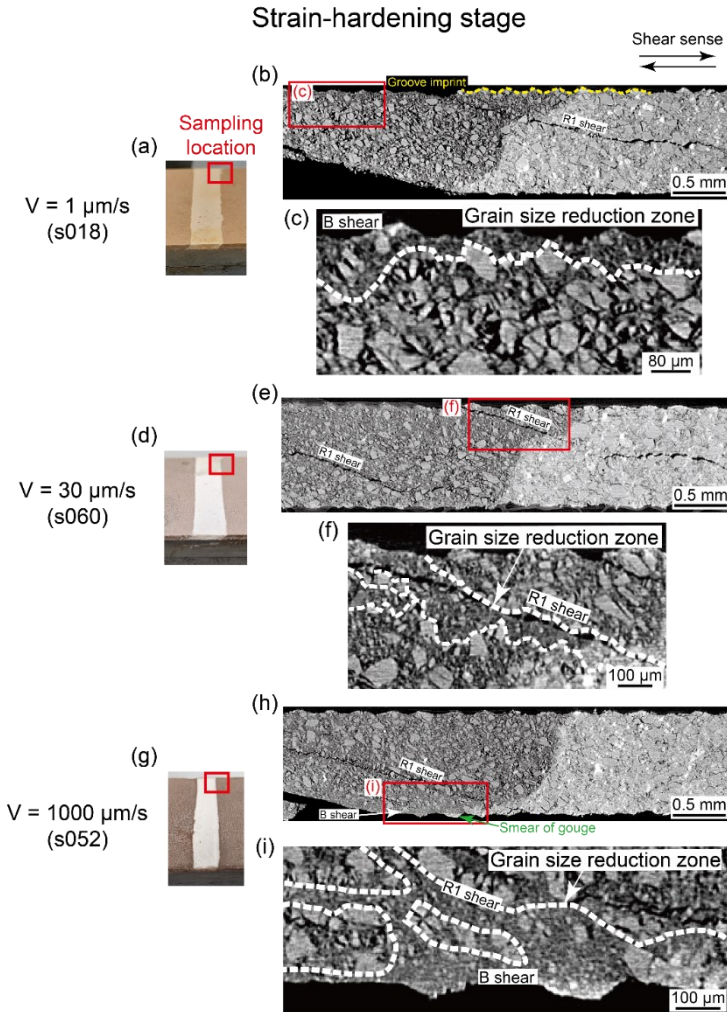
Figure 2.4: *Macroscopic (left) and microstructural (right) observations of gouge samples deformed at displacement rates of (a-c) 1 μm/s, (d-f) 30 μm/s, and (g-i) 1000 μm/s in the strain-hardening stage. The pictures on the left show the appearance of the deformed gouge after dismantling the L-shaped pistons. The sampling location for the XCT analysis is indicated by the red rectangle. The images on the right show representative XCT images of the deformed gray-scale color boundary between the albite gouge (dark grey) and Slochteren sandstone gouge (light grey). The groove imprint is indicated by the yellow dashed line in a). In general, R_1 shear bands are the dominant localization feature without accommodating much displacement. Some Y (or B) shear also developed, as indicated, particularly at higher slip velocities (b, c).*
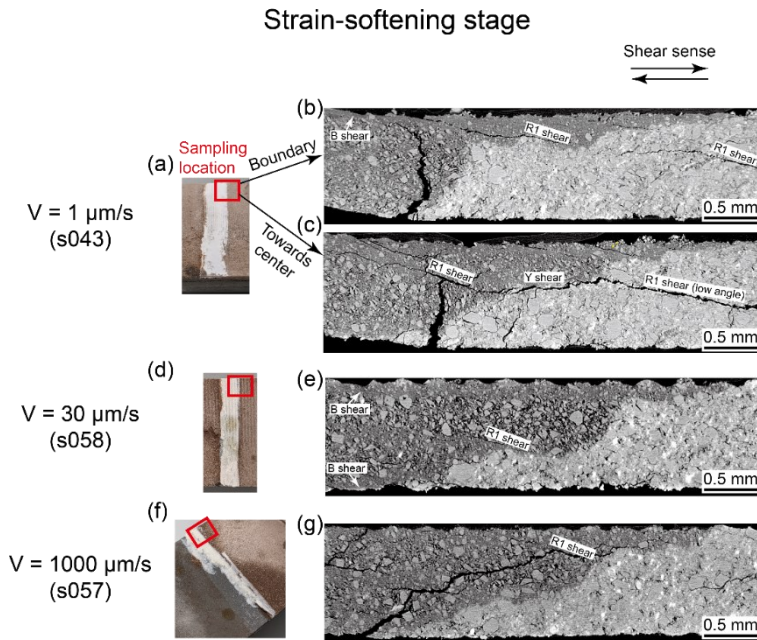
Figure 2.5: *At strain-softening stage. Macroscopic observations show that all recovered samples split along the gouge-forcing block boundary (a and d) except the sample at 1000 μm/s, which split along the R_1 fractures (f). The XCT images show that displacement starts to localize along the fracture arrays, mostly on the R_1 shears, indicated by the offset of the marker boundary. In addition, a significant contrast in grain size between the localized zone and the remainder of the gouge layer is visible. The sample deformed at 1 μm/s shows a clear spatial variation in terms of the pattern of deformation where the cross section at the sample boundary developed more boundary shears than the one closer to the center.*
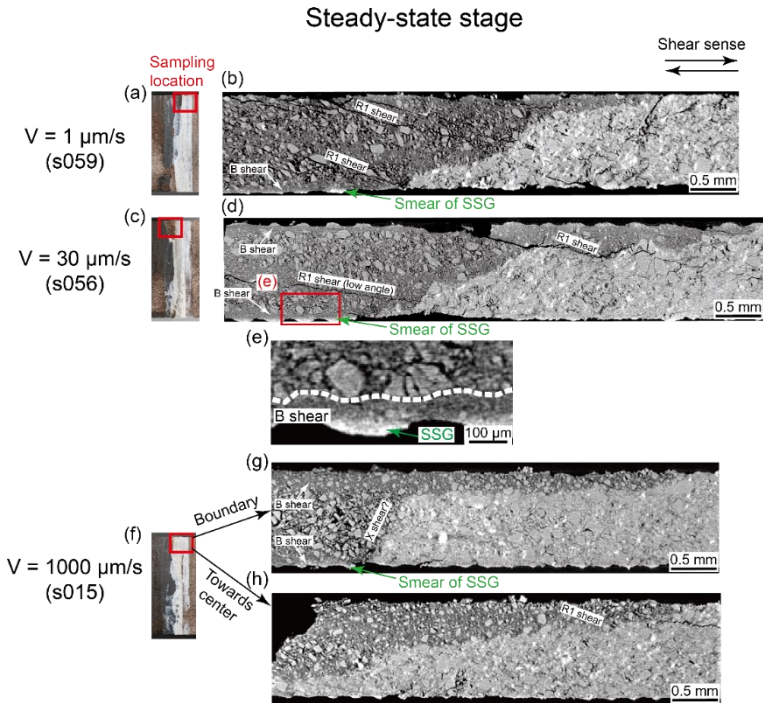
Figure 2.6: *At steady-state stage. Macroscopic observations show that all recovered samples split along R₁ fractures, and a small portion of the albite gouge is attached to the gouge-forcing block boundary. The microstructures are similar to the ones in the strain-softening stage (Figure 2.5) while gouge smearing with only few microns thick at the gouge-forcing block boundary and grain size reduction becomes significant at all velocities. One thing to note is that only the sample deformed at 1000 μm/s shows spatial variation with respect to the deformation where the cross section at the sample boundary (g) shows a better developed boundary shear than the one close to the center (h).*

2.3.3 Quantification of displacement partitioning

Figure 2.7 shows the image-inferred partitioning of displacement between different shear features across the analyzed sample length after removal of the outliers. Overall, the proportion of the outliers is less than 10% of the total number of images. The slice number from small to large indicates the analysis from the gouge boundary towards the center. The total displacement (blue dots) and Y (B) shear (green dots) shown here include the B shears (the difference between L and δ) which were not considered during the automatic boundary detection procedure. Here, we should note that there is a clear increase in variability of displacement, particularly for the shear features, from the strain-hardening stage to the steady-state stage; in other words, the determined displacement becomes less horizontally stable (across slices, i.e. a larger variation in the amount of displacement). The reason for this will be further discussed in

74

section 2.4.2. In general, the amount of displacement, for all shear features, and the microstructurally resolved total displacement increase with increasing displacement at all velocities. An exception is the experiment at 1 μm/s at the steady-state stage, which shows a decrease in the total displacement from the softening to steady-state stages. This mainly results from the missing boundary shear which is difficult to identify with the automatic boundary detection method, as mentioned in section 2.2.4.

Along the entire analyzed width of the sample, we do not observe significant variation in the displacement partitioning between the shear features, though the results seem in contrast with few observations of the XCT microstructures (e.g. Figure 2.5a; Figure 2.6c) which show more B shears developed at the sample boundary. In other words, the results do not reveal an observable increasing trend in the amount of displacement for Y shear with increasing slice number. Thus, we determined the spatial average and standard error of displacement for each deformation feature.
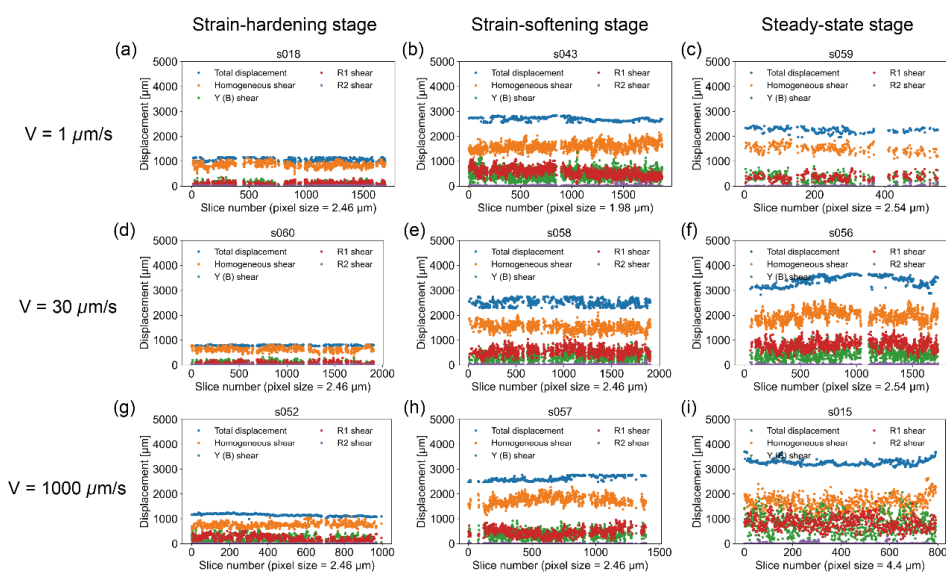
Figure 2.7: *Displacement against individual XCT slicve number for different deformation features after removing the outliers for each experiment. The slice number from small to large indicates the analysis from the gouge boundary towards the center. Note that the amount of the slip along R_2 shear is almost zero and no P shear was identified. Some experiments have less than a thousand slices due to the removal of substandard-quality images.*

The compiled data of the characteristics of the albite-SSG boundary and the displacement partitioning for the different deformation features for the nine experiments, are summarized in Table 2.2. We note that the external shear δ, in all experiments, is shorter than the elastically corrected imposed shear D. The amount of variation $(D - \delta)$ increases with D from 0.26–0.35 at the strain-hardening stage to 0.55–0.78 at the steady-state stage. In addition, some experiments show L/δ larger than 1. These observed variations will be discussed in section 2.4.3

Table 2.2: *Data compiled from the albite-SSG boundary and the strain partitioning between different shear features.*

ID	Frictional stage	W (mm)	D (mm)	L (mm)	W/L	δ (mm)	D − δ (mm)	L/δ	Homo. shear (%)	Y (and B) shear (%)	R₁ shear (%)
					Experiments at V = 1 μm/s						
s018	SH	0.89 ± 0.01	1.3	1.06 ± 0.033	0.84 ± 0.025	0.95	0.35	1.12 ± 0.035	84% ± 9%	8% ± 7%	8% ± 6%
s043	SW	0.90 ± 0.01	3.4	3.15 ± 0.026	0.29 ± 0.002	2.85	0.55	1.11 ± 0.009	53% ± 5%	30% ± 6%	17% ± 5%
s059	Steady-state	0.85 ± 0.01	5.5	3.87 ± 0.096	0.22 ± 0.005	4.95	0.55	0.78 ± 0.019	39% ± 4%	52% ± 4%	9% ± 3%
					Experiments at V = 30 μm/s						
s060	SH	0.93 ± 0.01	1.3	0.79 ± 0.013	1.18 ± 0.019	1.04	0.26	0.76 ± 0.013	83% ± 10%	8% ± 9%	9% ± 8%
s058	SW	0.81 ± 0.01	3.4	2.79 ± 0.067	0.29 ± 0.007	2.90	0.50	0.96 ± 0.023	60% ± 5%	21% ± 6%	19% ± 6%
s056	Steady-state	0.84 ± 0.01	5.5	4.88 ± 0.156	0.17 ± 0.006	4.95	0.55	0.99 ± 0.032	43% ± 5%	41% ± 5%	16% ± 4%
					Experiments at V = 1000 μm/s						
s052	SH	0.90 ± 0.01	1.3	1.17 ± 0.033	0.77 ± 0.022	1.00	0.30	1.17 ± 0.033	66% ± 8%	18% ± 11%	16% ± 9%
s057	SW	0.91 ± 0.01	3.4	2.82 ± 0.041	0.32 ± 0.005	3.00	0.40	0.94 ± 0.014	64% ± 6%	20% ± 6%	16% ± 6%
s015	Steady-state	0.90 ± 0.01	5.5	4.00 ± 0.084	0.23 ± 0.005	4.73	0.78	0.85 ± 0.018	42% ± 7%	38% ± 10%	20% ± 6%

Note. SH = Strain hardening, SS = Strain softening. W = the gouge thickness after shearing, D = the imposed displacement, L = the internal shear, δ = the external shear. The uncertainties for the thickness W and the external shear δ are the resolution of the caliper we used (0.01 mm). The uncertainties for the internal shear L represent the spatial standard error of the total displacement data obtained from Figure 2.7 with a 95% confidence interval.

In Figure 2.8, we show the amount of slip attributable to homogeneous deformation, R_1 shear, and Y shear at slip velocities of 1, 30, and 1000 μm/s. Each deformation feature exhibits a similar evolution with increasing displacement regardless of the slip velocities. During the period of strain hardening, over 80% of the total displacement is homogeneously distributed within the bulk gouge layer without much slip on localized features (< 10%), with the exception of the 1000 μm/s experiment, which shows a slightly larger amount of localized slip (~16–18%), occurring along both R_1 and Y (or B) shears. From the strain hardening to the strain softening stages, slip attributable to homogeneous deformation continuously increases, while R_1 and Y shear bands start to accommodate a larger proportion of displacement (20-30% and 16-19%, respectively). From the strain-softening stage to the steady-state stage, the amount of displacement due to homogeneous deformation remains nearly constant without much variation. Instead, a large proportion of the displacement, up to 50% of the total slip, is localized along the Y shears.
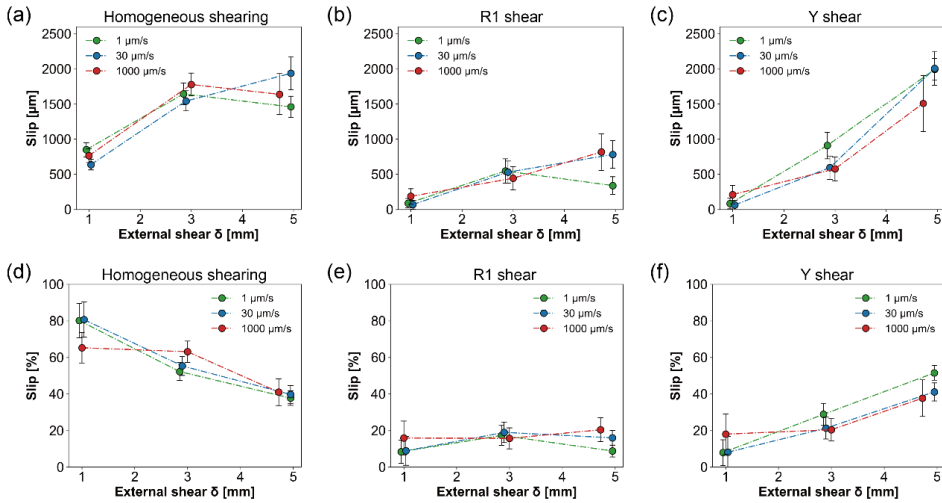
Figure 2.8: *Absolute and relative amounts of slip as a function of external shear δ (mm) at slip velocities of 1, 30, and 1000 μm/s for different shear features. (a)(d) Homogeneous shearing; (b)(e) R₁ shear; (c)(f) Y shear. The error bars represent the standard errors, indicating the variability in the measurements, with a 95% confidence interval.*

2.4 Discussion

2.4.1 Comparison with previous mechanical data

We compare our mechanical results with those reported by Hunfeld et al. (2017) who conducted experiments with nearly identical starting materials and experimental conditions. Few differences in terms of the experimental methods are that i) we added a ~10 weight % of albite gouge layer to the SSG layer obtained from cores from both above and below the GWC interface while they tested both separately; ii) we used SSG with 20 wt% of grains larger than 50 μm while they used a grain size overall less than 50 μm; iii) we performed experiments at a single velocity in contrast to velocity-stepping experiments. Both our and their mechanical data display comparable frictional characteristics with a strain-hardening stage, a strain-softening stage, and a steady-state stage (linear softening stage).

At displacement rates of 1 and 30 μm/s, our powdered Slochteren sandstone with an albite gouge layer shows similar μ_{pk} of 0.63 and μ_{ss} of 0.59–0.6. This is in accordance with previous results for simulated sandstone gouges (Bakker et al., 2016; Benford et al., 2021; Hunfeld et al., 2017; Leeman et al., 2016; Samuelson and Spiers, 2012; Scuderi et al., 2017a, b; Tembe et al., 2010; Verberne et al., 2010), demonstrating that the added albite gouge had a minor influence on the bulk frictional properties at these two velocities, if at all.

At a displacement rate of 1000 μm/s, our samples show a slight decrease in both μ_{pk} and μ_{ss} down to 0.59, suggesting a velocity weakening/neutral behavior between 30 μm/s and 1000 μm/s, as also observed in a velocity-stepping experiment that we performed for control purposes on the pure SSG (Figure S2.2). We observed that the μ_{app} in the strain-hardening stage (~0.58–0.60) is lower than in the strain-softening stage (~0.60–0.61), indicating a delay in the generation of peak friction. The development of peak friction is associated with gouge dilatation at the onset of shearing (Bos and Spiers, 2001; Marone, 1991; Niemeijer et al., 2020). In all the experiments at $V = 1000$ μm/s, the amount of final gouge compaction is similar (approximately 200 μm, see Table S2.1), with a minor dependence on the imposed shear strain and displacement rate. This suggests that the bulk of the gouge compaction occurred already during the initial slip (i.e. during strain hardening), regardless of the final imposed displacement. However, we observed an instantaneous pore fluid pressure increase up to 0.4

MPa, measured externally, at initial slip at a displacement rate of 1000 μm/s (Figure 2.3). The minor observed fluid pressure increase is suggested to result from shear-induced compaction because the gouge layer was insufficiently drained under these relatively high-velocity conditions. Thus, the delay in the generation of peak friction might be explained by the observation of an increased pore pressure, which suggests compaction during initial sliding as opposed to dilatation. On the other hand, we note that the delay in the generation of peak friction and fluid pressure increase are not observed in the pure SSG experiment (Figure S2.2). This suggests that the presence of the albite marker only seems to affect the initial slip behavior at the highest displacement rate investigated. The reason for the above observations could be that the albite marker allows for a higher initial porosity after the pre-compaction so that shear-enhanced compaction with fluid pressurization can occur. However, we find that this compaction behavior only influences the initial frictional behavior and occurred only at 1000 μm/s. Also, the strain-hardening-stage gouge microstructure at this velocity is comparable to those at lower velocities (Figure 2.4). Thus, we argue that the added albite gouge had a minor influence on the gouge microstructure, if at all, despite the difference in the value of μ_{pk}. Similar frictional behavior close to this velocity range (i.e. 1–1000 μm/s) was also observed in previous room temperature studies on different materials (e.g. Mair et al., 2007). Overall, our mechanical results show good reproducibility and consistency compared to the published data (Hunfeld et al., 2017).

2.4.2 Reliability of the automatic boundary detection method

As far as we are aware, our study is the first to investigate the evolution of shear fabrics within quartz-rich fault gouges utilizing the X-ray CT technique. Unlike optical and SEM analysis, XCT scanning avoids artifacts resulting from epoxy-impregnation, cutting, and polishing of the sample, as well as providing the spatial strain distribution across the gouge layer (quasi-3D) (though a few papers have produced SEM without using epoxy resin – Haines et al., 2013; Wojatschke et al., 2016). To automatically identify the boundary between the albite gouge and the SSG for thousands of XCT images, we developed an automatic boundary detection method based on machine learning. This segmentation approach is shown to be effective and efficient in retrieving the boundary from most of the images, which is needed for the quantification of slip partitioning, i.e. to identify localization (Section 2.2.4; Figure 2.2; S2.4). The

relatively few proportions of the outliers with less than 10% (Figure 2.7) indicate that more than 90% of the boundary detections are reliable. The main reason for the outliers is due to the development of fractures, either during shearing, unloading, or sample recovery, that crosscut the interface which is then incorrectly registered as a discontinuous boundary by the trainable segmentation (see Figure S2.4f for example). In addition, sample recovery becomes more difficult when the sample has experienced more shear strain, as more fractures develop either during shear or upon unloading. Some parts of the gouge layers would stick to the piston, which likely results from the thinning of the gouge layer due to the shearing. This increases the likelihood of internal splitting, rather than splitting on the gouge-forcing block boundary, which may explain why we observe more outliers in experiments stopped in the steady-state stage (Figure 2.7c, f, i).

Another possible factor that could affect the automated analysis is related to the variation in the intensity of grayscales across the analyzed regions. Local intensity has much higher importance than local textures and edges in the trainable segmentation method (van der Walt et al., 2014). For most of our recovered samples, their width (x-direction) is not uniform across the sample length (y-direction). Thus, even in an identical cross section, the average gray-scale intensity of the same material (i.e. quartz) within the cross section might be slightly different due to variations in the recovered gouge width or thickness. This variation is likely to be more significant when sample recovery is poor. Because we only applied one classifier trained from a few images to fit the rest of the images for each experiment, undesired segmentation outcomes can also result from variations in average intensity between cross sections.

In summary, the present method offers a reliable method of boundary detection, with less than 10% of detections being rejected by the outlier filter. To further improve segmentation quality, future improvements in image pre-processing could be made within the framework of automatic boundary method; for example, by employing fracture suturing or intensity adjustment. This, in principle, can be done relatively easily, if only processing a few images, but becomes more challenging when dealing with more than hundreds or thousands of images – thus demanding further application of efficient machine learning tools for these purposes.

2.4.3 Localization quantification

2.4.3.1 Determination of shear-parallel B shear

We first discuss the relationship between different terminologies that we reported in Table 2.2 because these parameters influence how we quantify the shear-parallel B shear and the result of the displacement partitioning. Here, we ignore the effect of gouge compaction because the amount of compaction for each experiment does not show much variation, even for experiments with different amounts of displacement, and, in addition, it is difficult to determine when the compaction occurred exactly. Mainly, we present three different length parameters D, L, and δ, which are defined as elastically corrected imposed shear, internal shear, and external shear. Considering pure homogeneous gouge deformation, if we imposed a load-point displacement of 1 mm to a 1 mm thick gouge layer, the D, δ, and L would be 1, 1, and 1, respectively. If shear displacement begins to localize along R_1 shear planes, D and δ would remain at 1 while L becomes less than 1 due to the offset of the marker boundary. The more R_1 shears develop (or other non-shear-parallel localization features), the shorter the L-value, while the development of shear-parallel fabrics such as Y or B shears does not reduce L. The above description can be visualized in the schematic plots summarized in Figure S2.3.

As mentioned previously, we quantify the amount of displacement along the B shears as the difference between L and δ (instead of D). This choice is based on the following assumptions and observations: i) the localization of slip on non-shear-parallel planes (or zones) does not cause much shortening in the L, otherwise, the amount of displacement on B shears would be overestimated; ii) we inferred that back shear of the pistons might occur and might cause reverse shear to the sample. Assumption (i) should be reasonable, as we barely observe any high-angle offset along the marker boundary in all gouge microstructures (e.g. R_2 shear). Thus, if no B shear develops, the difference between L and δ should be negligible. In the case of assumption (ii), the inference of the back shear is based on the observation that the δ is always shorter than the D in all experiments and this difference (D - δ) increases with D (Table 2.2). This discrepancy in displacement might be due to i) compaction of the gouge sample and ii) the back shear of the pistons caused by elastic relaxation of the jacket during the unloading process as the confining pressure and/or fluid pressure are removed. Since the gouge compaction does not show much variation between the experiments, we

infer that the back shear of the pistons is the main factor causing such differences. We argue that the back shear influences the microstructure to some extent because the gouge layer remains under shear stress when we depressurize the vessel and the sample. However, it is difficult to quantitatively examine how significantly the back shear affects the gouge microstructure. Here, we consider the effect of back shear and adopt δ rather than D to determine the amount of displacement on B shears where Y shears were quantified by the automatic detection method.

2.4.3.2 Displacement partitioning between deformation features

To obtain the displacement partitioning between the deformation features for each experiment, we averaged the displacement of identical deformation features (i.e. homogeneous vs. R_1, Y (including B) shears) across all profiles. This is based on the observation of an absence of any clear spatial trend in the strain distribution within the analyzed regions after removing the outliers. It is noted that the error bars (absolute value) become larger with increasing shear displacement for all deformation features (Figure 2.8a, b, c). The largest error bars suggest that the localization of slip varies largely perpendicular to the shear plane within only a few microns (equivalent to the pixel resolution). We argue that the increasing trend is likely attributable to an artifact of our automatic detection method due to the combined effect of poor sample recovery as well as the transformation of R_1 to Y shear in high-strain experiments. With increasing shear strain, gouge samples become thinner and more difficult to recover due to the increased development of slip localization and shear fractures within the gouge layer. This would result in an increasing number of turning points identified on the intensity boundary and, thus, likely increase the errors of the amount of localized slip quantified between slices.

On the other hand, a general observation for the evolution of shear zone fabrics, which almost all previous studies agree on, is that R_1 shears initially form at high angles (~30–40°) to the shear plane, in response to Mohr-Coulomb failure, and adopt lower angles during the rotation of the stress field. Figure 2.9 schematically illustrates the progression of gouge deformation from distributed shear to localization of slip on the principal R_1, R_2, and Y shear bands. During the initial slip, homogeneous shearing plays a significant role in accommodating the initial displacement within the zone (Figure 2.9a). However, once the major localization features such as R_1 and Y shears are formed, homogeneous shearing

becomes comparatively passive and less influential in accommodating further displacement (Figure 2.9b, c). With increasing shear strain, low-angle R_1 shears rotate to become parallel to the gouge-forcing block boundary due to the rigid boundaries of the shear zone (Figure 2.9c; Logan et al., 1992; Logan, 2007). Thus, at low shear strain (i.e. strain-hardening stage), fewer turning points would be identified as only high-angle R_1 shears and homogeneous deformation were observed within the gouge layer (Figure 2.4). In contrast, at high shear strain (after the strain-softening stage), more turning points would be detected due to the ongoing development and transformation of the R_1 shears. Once more turning points are identified, the variability in the proportion of localization attributed to each shear feature, from one slice to another, is prone to become significant due to the spatial distribution of shears and the variation in grey-scale intensity within images. For example, for a pure Y shear (defined as $-3° < \theta < +3°$) identified in successive slices, we might obtain different amounts of slip due to differences in the position of the turning points defining the Y shear.
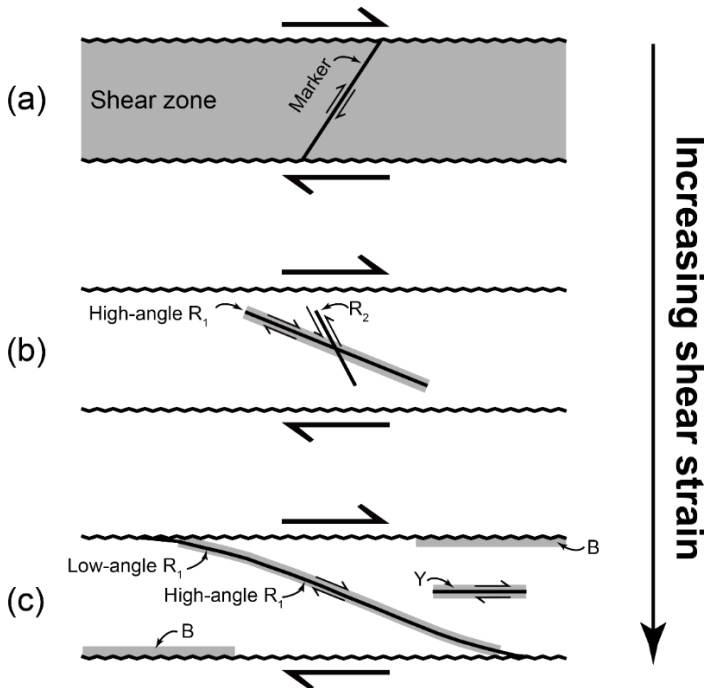
Figure 2.9: *Schematic plot of the evolution of localization features with progressive shear strain, modified from Logan et al. (1992). The grey color indicates the zones in which displacement is mostly accommodated. (a) Homogeneous shearing distributed across the entire shear zone. (b) Formation of R_1 and R_2, shears. (c) Transformation of the R_1 shears to shear-parallel Y (and B) shears.*

2.4.4 Spatial variation in gouge deformation

In general, the pattern of gouge deformation is consistent (i.e. uniform) throughout the analyzed gouge width, for most experiments. However, the deformation of the marker boundaries in two experiments, one at 1 μm/s in the strain-softening stage and the other at 1000 μm/s in the steady-state stage (experiment s043 and s015 in Table 2.1, respectively), show a clear variation from one end (i.e. top) towards the center of the gouge layer segment analyzed (Figure 2.5b, c; Figure 2.6g, h). In both cases, more deformation appears to be accommodated by a B shear, and less by R_1 shears, at one end of the analyzed gouge segment width, whereas the deformation looks more "distributed" for sections closer to the center. However, we do not see a clear trend in the amount of slip computed on either the R_1 shears or Y shears (Figure 2.7b and 2.7i). Despite the insignificant difference in displacement partitioning obtained from our automated analyses, we argue that this change in deformation pattern is real and could be related to the difference in the initial stress field at the sample end versus center likely due to i) the radial effect of the cylindrical shape of the direct shear setup and/or ii) the proximity to the free surface of the gouge sample in the shear direction. It is impossible to link the change of the gouge deformation to the effect of the normal stress or rotation of the principal stress axes without detailed FEM modeling (e.g. Logan et al, 1992), including realistic boundary conditions, which is beyond the scope of this study.

2.4.5 Shear fabric evolution, displacement partitioning, and mechanical response

Overall, we observe that the evolution of the shear fabrics, displacement partitioning between these fabrics, and the mechanical response are highly consistent at all tested velocities. Slip localization in our samples has a minor dependency on displacement rate within the observed velocity range. One of the important findings is that the shear fabrics evolve with increasing shear strain in a repeatable and hence predictable manner. R_1 shears were first initiated during the attainment of the peak stress followed by the development of Y shears from the strain-softening stage to the steady-state stage. This geometric evolution is fully consistent with the results of Logan et al. (1992) for calcite gouges, using Tennessee Sandstone as forcing blocks, a similar normal stress of 30–35 MPa and an initial gouge thickness of ~1 mm, - despite the pore fluid pressure of 15 MPa and the temperature of 100 °C applied in this study. While the presence of similar fabric elements has been observed across a diverse range of lithologies, including

pure quartz and calcite (Bedford and Faulkner, 2021; Friedman and Higgs, 1981; Noël et al., 2023; Scuderi et al., 2017a, b, 2020; Wang, 1989), as well as mixtures containing clays (Hains et al., 2013; Logan and Rauenzahn, 1987; Moore et al., 1989; Wojatschke et al., 2016), the extent of strain required for the development of these fabric elements varies depending on the composition of the simulated gouge. Softer materials like halite (e.g. Chester and Logan, 1990; Buijze et al., 2017a) and calcite (e.g. Verberne et al., 2014a, b) generally have lower mechanical strength and tend to exhibit steady-state fabrics at lower shear strains compared to harder minerals (e.g. quartz or feldspar; Masuda et al., 2019), because the fracturing and compaction processes are easier.

To conclude, our quartz-rich samples show similar evolution of shear fabrics, displacement partitioning, and mechanical response to previous work on calcite gouges, despite differences in experimental conditions. This suggests that the mechanics of localization should also be comparable to that previously suggested, based on ring-shear experiments on granular materials (Mandl et al. 1977) and finite-element studies of gouge zones (Logan et al. 1992). These studies demonstrated that the initial high-angle R_1 shears form in response to Mohr–Coulomb failure as the stress level increases to a critical level. Due to the rotation of the stress field, the angle of the R_1 shears becomes progressively lower and ultimately (sub)parallel to the gouge-forcing block boundary. Our microstructural observations also support this observation. In previous work, Y and B shears are then suggested to occur, owing to kinematic constraints, whereby the most displacement becomes localized along these shear-parallel features due to the limited displacement that can be accommodated within R and P shears. Although P shears are not identified in our sample, we also showed that multiple Y and B shears develop, crosscut by a few R_1 shears within the simulated gouge zone at the steady-state stage. While this geometric change is consistent with previous studies on gouges that are clay free or clay poor (e.g. Higgs, 1981; Logan 1992), we note that the importance/presence of P shears and the stage (imposed displacement) at which Y and B shears develop do show some dependency on gouge composition, i.e. on whether the fault zone is clay-rich (e.g. Hains et al., 2013), quartz-rich (e.g. Noël et al., 2023; Benford et al., 2021) or polymineralic (e.g. Logan and Rauenzahn, 1987; Moore et al. 1989).

2.4.6 Implications for small-displacement earthquakes

Localization of strain has broad influences on the aseismic and seismic nature of tectonic faulting. For instance, the development of shears along Y orientations may increase the permeability parallel as opposed to normal to the fault zone, due to an increase in porosity or anisotropy. This could enhance the fluid flow within the fault zone during aseismic creep, as observed in some natural fault zones (e.g. Caine et al., 1996). For seismic events with large displacement (> few meters), localization of slip is reported to play a critical role in facilitating dynamic weakening as generated frictional heat would be localized within a narrow shear band facilitating thermal softening of the fault materials (e.g. Smith et al., 2015). However, whether the same mechanism operates in small-displacement earthquakes (i.e. cm- or mm-scale, equivalent to M 2.0–4.0) remains uncertain.

Our results show that about 60% of displacement is localized along the developed localization features in the quasi-steady state simulated gouge zone, of which up to 50% (i.e. 5/6 of 60%) is localized on the shear-parallel Y (including B) shears, in a fault with only ~5.5 mm displacement. We further show that the localization process has only minor dependence on displacement rates in the range from 1 μm/s to 1000 μm/s, similar to the velocity range expected during fault acceleration during the nucleation stage of rupture development. If the dependence of strain partitioning on velocity remains small, and the fault slip is localized along one Y shear (i.e. principle slip zone, PSZ), when a fault subsequently accelerates to seismic slip rates (i.e. > 0.1 m/s), our study provides constraints on the development (thickness) of the active slip zone. This is a crucial input parameter for the heat budget of mm-scale seismic slip events, and hence for constraining effects such as thermal pressurization or flash heating effects that may control dynamic slip weakening during seismic slip (*cf.* Hunfeld et al 2021; Chen et al 2023; Chapters 5 and 6).

Based on numerical simulations, Platt et al. (2015) showed that the thickness of the PSZ has a major influence on various earthquake parameters. For a fault-zone gouge in which thermal decomposition and thermal pressurization are active, these authors showed that a decrease in PSZ thickness leads to faster rupture velocity and shorter total slip of an earthquake. Our microstructural observations show that the B shears were the most well-developed localization

features at the steady-state stage, typically dominating at one side of the gouge layer, with an overall thickness less than 150 μm (Figure 2.6e). In addition, the results of the localization quantification indicate that over half of the displacement was accommodated in these shear-parallel features (Figure 2.8). If ongoing fault slip is accumulated within such a thin deforming zone, the rupture velocity of the fault could therefore increase at least 3–4 times faster than a 1 mm thick layer of a homogeneously deforming fault gouge. However, the PSZ thickness within a natural fault gouge becomes difficult to estimate when considering the evolution of slip localization and natural earthquake conditions. For example, our gouges spend a short time at PT conditions before slip starts, whereas natural faults will have a long slip history, including previous earthquakes which will affect the initial microstructural state. The above implications can be better constrained if the characteristics of the PSZ (i.e. thickness and grain size) for a small-displacement earthquake are understood from borehole core observations or other exhumed analog faults with a similar lithology.

2.5 Conclusions

In this study, we presented a quantitative 3-D analysis of the evolution of gouge microstructures and displacement partitioning in sandstone-derived quartz-rich gouges, using X-ray CT (XCT) scanning. Albite gouge segments are shown to be a useful strain marker owing to the significant intensity contrast vs. quartz gouges in XCT scanning. The automatic boundary detection method based on machine learning developed in this study is shown to be an efficient and reliable tool to identify the albite marker gouge boundary, to detect shear bands, and to quantify the displacement partitioning along R_1, Y, and B shears versus homogeneous shear of the gouge body. We find that our quartz-rich gouges show similar evolution of the shear fabrics, partitioning of displacement, and mechanical response with increasing shear strain at all tested velocities. The results also agree with previous studies but for the first time provide quantitative data on the displacement partitioning on the evolving shear band structures. At all velocities, a total of up to 60% displacement has accumulated on boundary-parallel shears (Y and B shear) within a shear strain of 5.5 measured with respect to initial gouge thickness. With the total imposed displacement of 5.5 mm, our results suggest that about 2 mm of fault slip will be accommodated through homogeneous shearing during rupture nucleation, at least up to slip velocities of

1 mm/s. Our study provides constraints on the development of the active (principal) slip zone, which is an important factor controlling heating and weakening associated with small-magnitude earthquakes with limited displacement (mm-dm), such as induced seismic events.

Supplementary information

Text S2.1: Trainable segmentation using local features and random forests

To retrieve the albite-SSG grey-scale color boundary for hundreds to thousands of X-ray CT images, we used a segmentation algorithm called trainable segmentation combined with local features of the image and random forest classification. Below, we present how the segmentation is done in general.

Figure S2.4 shows the workflow from training data to data validation with both automated and manual identification and quantification. First, we selected five XCT images out of the stack of images for each experiment as the training data (Figure S2.4a). For example, if there are 2000 images in total, we picked image numbers 1, 500, 1000, 1500, and 2000 which have an equal interval in the space domain on the sample. The reasoning behind this is to reduce the selection bias of the image quality and intensity due to the spatial variation in fracture development and the variation in the gouge sample width (x-directions in Figure 2.1c) which would affect image intensity. We suggest that five images would be sufficient to train the data for the following reasons: i) The sample from each experiment was analyzed under the same XCT experimental conditions. This means that the variation in the grey-scale intensity between each slice should be consistent. ii) We selected the training images with equal intervals in the space domain of the entire analyzed width of the sample. This should further limit the effect of intensity difference on training. iii) We used at least four to five pre-defined masks to train five images at the same time. This means that there are more than 25 masks used to train both albite and SSG domains. In addition, based on the number of pre-defined masks, we find that what dominantly controls the performance of the data is the training parameters, as shown in Figure S2.5. To differentiate the albite and the SSG layer, we manually labeled these two materials with a few pre-defined masks (Figure S2.4b, as also described in Figure 2.2b in the main text). The pixels of the defined mask are then used to train a random-forest classifier based on local intensity and textures at different scales. A random forest is a meta-estimator that fits a number of decision tree classifiers on various sub-samples of the dataset and uses averaging to improve the predictive accuracy and control overfitting. To minimize overfitting of the data, we tested different values of the parameters such as the number of trees, the maximum depth, the maximum sample number, and the minimum number of samples that are required to split a node. Figure S2.5 shows an example of how

the combination of these parameter values controls the fitting of the segmentation boundary. In general, we find that the prediction gives the best performance on the test data with the combinations of number of trees of 100, the maximum depth of 5, the maximum sample of 5 (to draw from X to train each base estimator), and the minimum number of samples of 10 (required to split an internal node).

We used two different ways to subsequently validate whether the segmented boundary is acceptable and does not produce (much) overfitting. The first one is to also conduct manual identification and quantification on these five images and compare the result to those obtained from the automatic analysis (Figure S2.4c, d; as documented in figure 2.2f in the main text). If the data is not comparable, i.e. if the displacement tolerance misfit for a specific deformation feature between the automatic and manual results is over a pre-defined value of about 10%, we return to the segmentation procedure and adjust the pre-defined mask until the displacement tolerance misfit is within about 10%. Once we find the data is comparable, we use the trained classifier to segment another five images as the validation data (Figure S2.4e, f). These five images were picked in between the original five images with equal distance on the space domain on the sample. We follow the same manual validation procedure to examine whether the segmentation boundary in the validation data is acceptable without much overfitting (Figure S2.4g, h). Once we make sure the comparison of the localization quantification results from these two validation methods are comparable, we use the trained random forest classifier to segment the rest of the thousands of images.
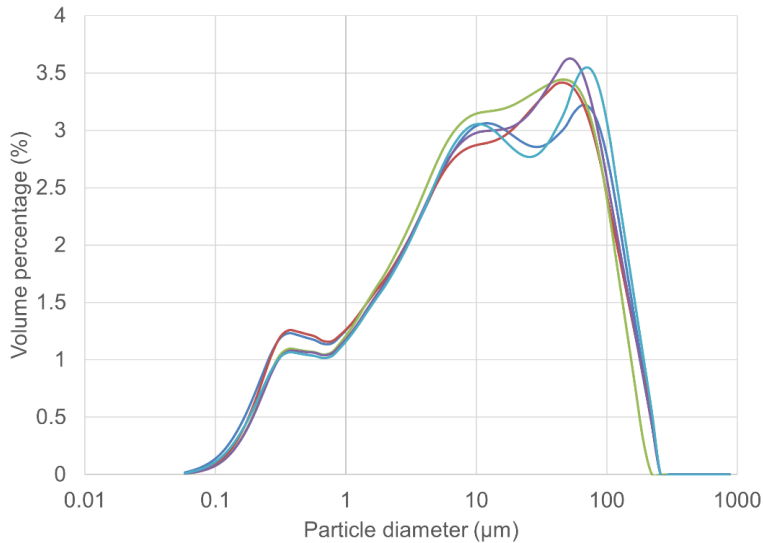
Figure S2.1: *Particle size distribution of the powdered Slochteren sandstone gouge without sieving, i.e. as used in the experiments, plotted as volume percentage against particle diameter from five analyses.*
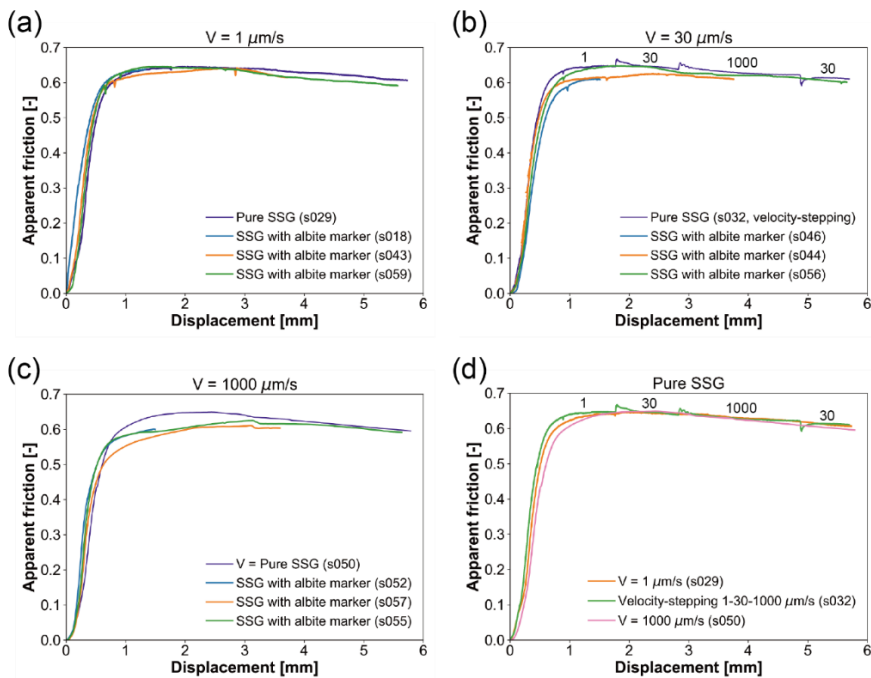
Figure S2.2: *Experiments terminated at variable displacement representing the strain-hardening stage, strain-softening stage, and steady-state stage at a slip velocity of (a) 1, (b) 30, and (c) 1000 μm/s. (d) Comparison of the frictional behavior of the pure SSG at a constant displacement rate of 1 and 1000 μm/s and velocity stepping (1-30-1000-30 μm/s).*

(a) Pure homogeneous gouge deformation

Shear sense

$\delta = 0$

1 mm

color interface

gouge-forcing block boundary

$\delta = 1$ mm

$L = 1$ mm

$\delta = 4$ mm

$L = 4$ mm
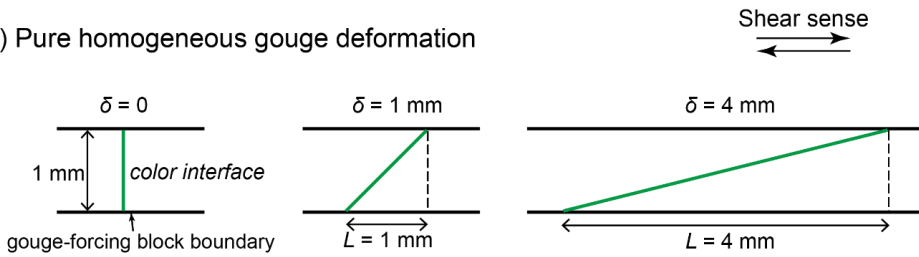
(b) Gogue deformation with R1 and Y shears

$\delta = 4$ mm

R_1

Y

R_1

a   b   'c'   d   'e'   f   'g'

$L = a + b + c + d + e + f + g < 4$ mm

$R_1 = b + f$

$Y = d$
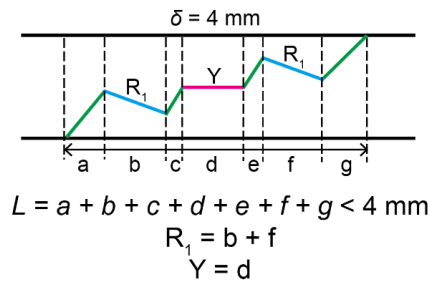
(c) Gouge deformation with R1, Y, and B shears

$\delta = 4$ mm

R_1 B

Y

R_1

B

a   'b'   c   'd'   e   'f'   g   'h'   i

$L = b + c + d + e + f + g + h < 4$ mm

$R_1 = c + g$

$Y = e$

$B = a + i$
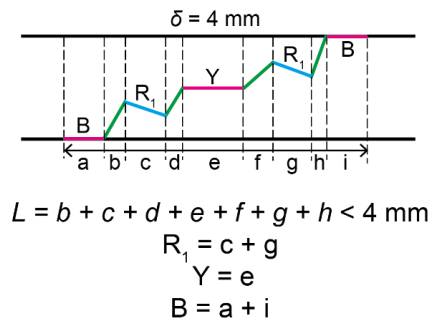
Figure S2.3: Schematic plot of the gouge deformation with a strain marker with (a) pure homogeneous deformation, (b) with the development of R_1 and Y shears, and (c) with the development of R_1, Y, and boundary shears.
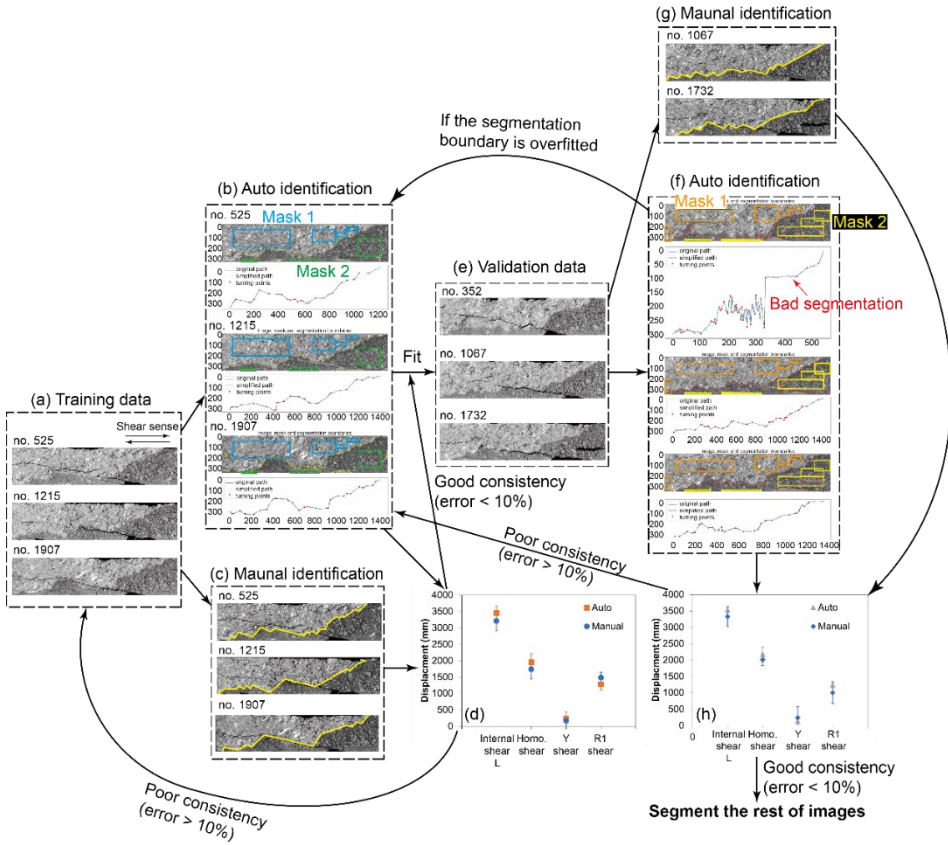
Figure S2.4: *The workflow of trainable segmentation for training and validation data. Here we only show examples of three XCT images instead of five.*
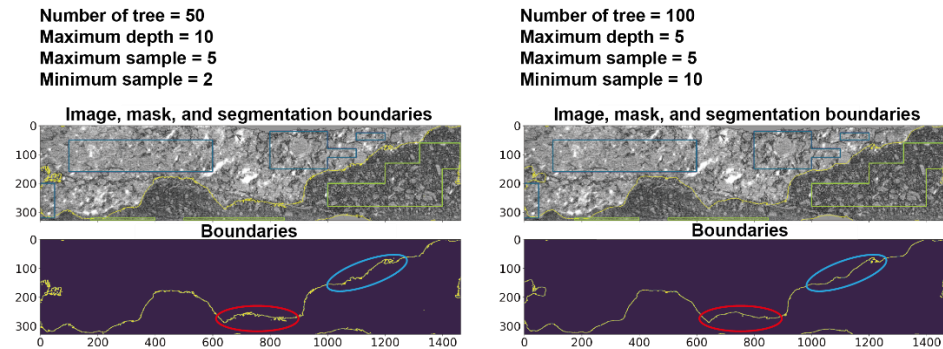
Figure S2.5: *Segmentation boundaries with different values of random forest parameters. The maximum sample refers to the number of samples to draw from X to train each base estimator. The minimum sample refers to the minimum number of samples required to split an internal node. In general, overfitting becomes less significant when increasing the number of samples, reducing the maximum depth, and increasing the minimum number of samples required to split a node, as highlighted in the red and blue circles.*

Table S2.1: *Sample compaction determined from the water volume change externally measured from the ISCO pump and the microstructural observations. The symbol of "*" indicates the data observed from microstructural observation.*

ID	Frictional stage	Water volume decrease (m^3) after density correction	Thickness change (mm)	*Initial thickness after compaction (mm)	*Final thickness (mm)	*Compaction (mm)
			Experiments at V = 1 µm/s			
s018	SH	0.00029	0.17	1.10	0.89	0.21
s043	SS	0.00055	0.32	1.10	0.90	0.20
s059	Steady-state	0.00124	0.72	1.10	0.85	0.25
			Experiments at V = 30 µm/s			
s060	SH	0.00017	0.10	1.10	0.93	0.17
s058	SS	0.00023	0.13	1.10	0.81	0.29
s056	Steady-state	0.00027	0.16	1.10	0.84	0.26
			Experiments at V = 1000 µm/s			
s052	SH	0.00016	0.09	1.10	0.90	0.20
s057	SS	0.00026	0.15	1.10	0.91	0.19
s015	Steady-state	0.00024	0.14	1.10	0.90	0.20

Note. SH = Strain hardening, SS = Strain softening.

Chapter 3

Investigation of strain localization in sheared granular layers using 3-D discrete element modeling

Chien-Cheng Hung: Conceptualization, Data curation, Formal analysis, Investigation, Methodology, Validation, Visualization, Writing – original draft

André R. Niemeijer: Conceptualization, Funding acquisition, Project administration, Resources, Supervision, Writing – review & editing.

Amir Raoof: Methodology, Software, Supervision, Writing – review & editing.

Thomas Sweijen: Conceptualization, Methodology, Software, Validation, Visualization, Writing – review & editing.

Abstract

In this work, we investigate slip localization in sheared granular faults at seismic velocities using 3-D numerical simulations with the discrete element method (DEM). An aggregate of non-destructive spherical particles is subjected to direct shear by using two moving boundaries in a sandwich configuration to identify the impact of particle-scale parameters on slip localization. We impose a thin layer of fine-grained particles with variable contrast in thickness and grain size adjacent to the boundary as well as in the middle of the granular layer to simulate boundary and Y shears observed in both natural and laboratory fault gouges. The results show that larger amounts of strain are accommodated within the pre-described finer-grained layer even with a small (< 10%) contrast in grain size. Up to 90% of the displacement is localized in a finer-grained layer when the contrast ratio of the grain size is 50%. Based on the concept of the average spreading velocity of particles and squeeze expulsion theory in granular flow, we suggest that the phenomenon of localization is likely to result from the contribution of larger grains collisions with smaller grains. Since the amount of frictional heat generated depends on the degree of localization, the results provide crucial information on the heat generation and associated slip accommodation in sheared gouge zones. We conclude that the occurrence of a weaker, fine-grained layer within a dense fault zone is likely to result in self-enhanced weakening of the fault planes.

3.1 Introduction

Field and borehole observations of active seismogenic fault zones show that earthquake slip is often focused within a gouge-bearing slip zone of a few centimeters thick surrounded by damage zones of cataclasite with or without foliation and fractured country rock (Boullier et al., 2009; 2011; Chester, 1993; Chester and Chester, 1998; Heermance et al., 2008). Microstructural studies further demonstrate that most of the slip occurs within a fine-grained principal slip zone (PSZ) cut with a discrete sliding surface or multiple surfaces with a thickness less than a few hundreds of microns (Boullier et al., 2009; Chester and Chester, 1998; De Paola et al., 2008; Fondriest et al., 2012; Heesakkers et al., 2011; Smith et al., 2011). Laboratory friction experiments performed on granular fault materials at seismic slip velocity, like 1 m/s, have demonstrated the reproducibility of such an extreme localization of shear zones (with a thickness < ~100 μm) commonly characterized by grain size reduction, which are defined as boundary (B) or Y shears (De Paola et al., 2011; Fondriest et al., 2013; Han et al., 2010; Kitajima et al., 2010; Kuo et al., 2014; Smith et al., 2013, 2015; Yao et al., 2013).

Smith et al. (2015) experimentally investigated the dependency of the mechanical behavior on strain localization by shearing calcite gouges at seismic slip velocity for meters displacement and found that the formation of a localized high-strain shear band (i.e. PSZ) may play a critical role in the dynamic weakening of a fault. Once the PSZ has formed, it accommodated subsequent deformation and more shear heating and thus faster weakening would occur. Based on numerical simulations Platt et al. (2015) showed that the thickness of the PSZ has a great influence on various earthquake parameters. For a fault-zone gouge in which thermal decomposition and thermal pressurization are active, they showed that a decrease in PSZ thickness leads to faster rupture velocity and shorter total slip of an earthquake. Thus, understanding of strain localization and the distribution of earthquake slip within a gouge-filled fault zone is critical to constrain local heat production, temperature rise, and weakening; hence, the fault behavior and associated earthquake physics. Localization of strain at nucleation velocities and small displacement as well as at seismic velocities and large displacements has been studied in laboratory experiments (e.g. Logan et al., 1992; Smith et al., 2015) and numerical simulation (e.g. Casas et al., 2022; Mair and Hazzard, 2007). However, slip localization has not been investigated so far for

seismic velocity and small displacements (i.e. few centimeters) which is important for induced seismicity.

Numerical discrete element modeling (DEM) has been widely used to study the deformation of granular materials. Using DEM, we can investigate dynamic microscale processes of shear zones as they deform and evolve. Morgan and Boettcher (1999) conducted 2-D numerical simulations of homogeneous sheared granular gouge by varying both particle size distributions (PSD) and interparticle friction at subseismic slip rates of 0.1 mm/s). They showed that both an increasing number of fine grains and a larger value of interparticle friction favor transient localization of strain. They interpreted this to be the result of an increased importance of interparticle rolling in accommodating granular deformation. Mair and Hazzard (2007) used DEM to investigate homogeneous sheared granular materials in 3-D in which out-of-plane deformation is considered and found that contact force networks are sensitive to PSD. Despite observing changes in the network of grains that support the bulk of the force with changes in PSD, they do not report discernible persistent localized deformation in the granular layer.

In natural fault zones, grain fragmentation and time-dependent processes such as contact healing are important mechanisms operating during both aseismic and coseismic slip. On the basis of 2-D DEM simulations at subseismic velocities, Morgan (2004) reported that shear strain tends to localize within a boundary-parallel shear band (1 to ~10 grains thick depending on the imposed sliding velocity) when time-dependent contact healing is introduced. Mair and Abe (2008) used a particle-based 3-D DEM model with breakable bonds to simulate grain fracturing process during fault gouge evolution and revealed that in their simulations strain localization is strongly correlated to enhanced grain size reduction. A recent 2-D numerical study of cemented granular fault gouge by Casas et al. (2022) reported that interparticle bond (i.e. cohesion) plays a key role in influencing slip weakening and gouge deformation at seismic velocity. A gouge layer with high cohesion (> 95%) is prone to generate large weakening and develop localized deformation such as R and Y shears owing to its relatively small (< 1%) critical dilation (i.e. necessary dilation for macroscopic shear failure).

In the absence of the above-mentioned time-dependent processes at grain contacts, Zhu et al. (2018) performed 2-D interface shear simulations at medium

slip velocity (few mm/s) and showed evident features of slip localization similar to boundary shear. They reported that a localized shear band would occur at an early stage of sliding (i.e. strain hardening phase) in both loose and dense granular layers and the degree of localization has a strong correlation with shear stress. Ferdowsi and Rubin (2020) studied sliding from subseismic (10^{-5} m/s) to coseismic (1 m/s) velocity using 3-D simulations of velocity-steps where momentum transfer was suggested to be the only time- dependent process; however, no sign of persistent localized deformation was observed shortly after an increase in velocity. They suggested that the formation of localized deformation may be characterized using different values of dimensionless parameters such as inertial number, I, or dimensionless pressure, P. (Ma et al., 2020).

Based on the previous numerical studies, it is clear that slip localization would occur within a numerical homogeneous sheared gouge zone at a wide range of slip velocity (subseismic to seismic) if a time-dependent process is considered. Without considering time-dependent processes, whether persistent localization deformation would occur may depend on various input parameters, such as sample dimension, slip velocity, and grain size distribution. In this study, we focus on 3-D gouge deformation sheared at seismic slip rate (1 m/s) for short displacement (up to 20 mm) within a non-breakable gouge assemblage. We systematically investigated slip distribution within a granular assemblage with an existing fine-grained layer parallel to the shear direction as shear strain is often reported to localize within a thin shear band with finer grain size. We then quantified how much slip occurs within the localized shear band if localization occurs to see how much localized grain size reduction (producing fine-grained layers with variable thicknesses) is required to induce localization. Finally, we provide insight into the physical mechanism of strain localization, the link between natural and experimental observations on mechanical behavior, as well as the role of fine-grained particles in fault dynamics.

3.2 Methods
3.2.1 Discrete element method
The discrete element method (DEM) is widely used to investigate the mechanics of granular materials. In this technique, individual particles are considered as discrete elements, or grains, which interact with each other at their

contact points. An explicit numerical scheme is applied to solve the translational and rotational equations of motion for every particle, given as, respectively:

$$\vec{F_i} = m_i \vec{\ddot{x_i}} \tag{3.1}$$

$$\vec{M_i} = I_i \vec{\dot{\omega_i}} \tag{3.2}$$

where $\vec{F_i}$ and $\vec{M_i}$ are the net force and moment of particle i, m_i and I_i the mass and moment of inertia, and $\vec{\ddot{x_i}}$ and $\vec{\dot{\omega_i}}$ the linear and angular acceleration, respectively. Vectors $\vec{F_i}$ and $\vec{M_i}$ are updated each time step and are obtained from the sum of the corresponding network of contact forces $\vec{F_{ij}}$ applied on each particle i with its neighboring particles j. Contact forces $\vec{F_{ij}}$ are computed from a given force-displacement relationship (see equations 3.5 and 3.6).

The time step used in this study is constrained by the amount of time that an elastic wave takes to propagate within a given particle of a specific size. Assuming Young's modulus and density of particles have continuum-like quantities, the critical time step can be written as:

$$\Delta t_{cr} = \min_i \left[R_i \sqrt{\frac{\rho_i}{E_i}} \right] \tag{3.3}$$

where R_i is the particle radius, ρ_i the particle density, and E_i the Young's modulus. A safety factor of 0.3 is used in equation (3.3) which satisfies the critical time step calculated from the minimum eigenvalue of a system of interacting particles, given as:

$$\Delta t_{cr} = \sqrt{\frac{m_i}{K_{stiff}}} \tag{3.4}$$

where K_{stiff} is an estimated equivalent contact stiffness (Itasca, 1999). The resulting time step in the range $\sim 10^{-8}$ to $\sim 10^{-9}$ s, depending on the grain size, produces both stable and accurate numerical simulation. For more details on the implementation of the methods, see the documentation of the DEM open-source code in Yade (Šmilauer et al., 2010).

Here we use the DEM to simulate direct shear of a granular layer with an assembly of spherical particles in 3-D. All the spherical particles are indestructible and prescribed by specific micro-properties (Table 3.1). Particle-particle interactions follow the Hertz-Mindlin (HM) contact model with no

micro-slip solution (Mindlin, 1949) which is appropriate for elastic contact bodies (Thornton, 2011). In the HM model, the normal force-displacement and shear force-displacement relationships are expressed as:

$$F_n = \frac{4}{3} E^* R^{*1/2} u_n^{3/2} \tag{3.5}$$

$$F_s = 8aG^* u_s \tag{3.6}$$

where u_n and u_s are the normal and shear displacement between particles, a is the contact radius, E^*, R^*, and G^* are the equivalent elastic modulus, equivalent radius, and equivalent shear modulus, respectively, which are given by:

$$\frac{1}{E^*} = \frac{1 - v_1^2}{E_1} + \frac{1 - v_2^2}{E_2} \tag{3.7}$$

$$\frac{1}{R^*} = \frac{1}{R_1} + \frac{1}{R_2} \tag{3.8}$$

$$\frac{1}{G^*} = \frac{2 - v_1^2}{G_1} + \frac{2 - v_2^2}{G_2} \tag{3.9}$$

where v_1 and v_2 are the Poisson's ratios of the two conforming bodies. The normal and shear stiffness, k_n and k_s can then be written as

$$k_n = 2E^* \sqrt{R^* u_n} \tag{3.10}$$

$$k_s = 8G^* \sqrt{R^* u_n} \tag{3.11}$$

The shear force F_s at each grain contact is limited according to the Mohr-Coulomb failure criterion which follows from the coefficient of interparticle friction assuming zero cohesion. Once the shear force is overcome, two particles will slide relative to each other at their contact point.

Aside from interparticle sliding, interparticle rolling is also introduced in the model, particularly owing to the use of spherical particles. To investigate the relative importance of rolling and sliding in our simulations, we add rolling resistance to the particle interactions. The rolling resistance model adopted in this study was implemented in Yade by Modenese (2013). In the model, we first define the torsional rotation $\vec{\theta}_t$, and the rolling rotation $\vec{\theta}_r$ from the total relative rotation $\vec{\theta}$ of two contacting particles as:

$$\vec{\theta}_t = (\vec{\theta}_t \cdot \vec{n})\vec{n} \tag{3.12}$$

$$\vec{\theta}_r = (\vec{\theta} \cdot \vec{n})\vec{n} \tag{3.13}$$

where $\vec{n}$ is the unit vector defining the normal to the contact. The torsional moment is disregarded while the bending moment is finally computed as:

$$\vec{M}_r = k_r\vec{\theta}_r = \beta k_s R^{*2}\vec{\theta}_r \qquad (3.14)$$

where β is a dimensionless parameter which is set to be 1, k_r and k_s the rolling stiffness and shear stiffness, respectively, and R^* the equivalent particle radius. The maximum rolling moment that can be exchanged between two particles is then limited by the normal contact force, F_n, in a form equivalent to the MC criterion, according to:

$$M_r \leq M_{max} = |F_n|R^*C_{rr} \qquad (3.15)$$

where C_{rr} is the coefficient of rolling friction. Therefore, we can set the interparticle rolling resistance by defining k_r and C_{rr}. In the present study, we determine k_r as 1.75×10^{-3} by following equation 3.14 for all the simulations where k_s and R^* are 4.5×10^5 N/m and 6.25×10^{-5} m, respectively (e.g. Iwashita and Oda, 1998).

Table 3.1: *DEM simulation parameters and coefficient values.*

Numerical setup parameter	Value	Particle parameter	Value
Sample dimension (length × width × height)	10 × 3.75 × 3.75 (mm)	Density, ρ	2500 (kg/m²)
Normal stress, σ_n	**5**, 20, 40 (MPa)	Young's modulus, E	55 (GPa)
Slip velocity, V	**1**, 0.1 (m/s)	Poisson ratio, λ	0.25
Mean particle diameter, d	250 (μm)	Viscous damping	0.3
		Interparticle friction, μ (compaction / shearing)	0.017 / 0.5
		Rolling friction coefficient, C_{rr}	**0**, 0.5

Note. The values with bold font refer to the reference model value.

3.2.2 Design of numerical experiments

3.2.2.1 Gouge sample configurations

The numerical simulation represents a direct shear experiment of a particle packing having a layered, sandwiched structure. The simulation consists of top and bottom frictionless walls, top and bottom boundary granular layers, and a main granular layer (Figure 3.1). Top and bottom frictionless walls are used to confine particles in the vertical direction (i.e. *y*-coordinate) and top and bottom controlled granular boundary layers are used to provide roughness to the interface with the gouge layer. Such top and bottom boundary layers were randomly

generated without a perfect ordering of grains to simulate a random surface roughness. We apply periodic boundary conditions in the horizontal direction (i.e. x and z-coordinate) so that particles exiting from one side reappear from the opposite face. No walls are applied to confine the front, back, left, and right sides of the assemblage. The size of the main granular layer is $40d$ (length) $\times$ $15d$ (height) $\times$ $15d$ (width) in the x, y, and z directions, respectively, where d is the mean particle diameter of 250 μm.

In this study, we use a principal slip zone (PSZ) model, referring to a granular packing with a single-size PSD with an additional layer of particles with a single-size PSD with a finer grain size (Figure 3.1). The fine-grained layer is parallel to the shear direction within the main granular layer to mimic the presence of a Y or boundary shear due to localized grain size reduction. With this model, we explore how much contrast in grain size and thickness of the PSZ is required for slip to be fully accommodated within the PSZ by changing its grain size and thickness while maintaining the same total thickness of the layer. This results in a change in the total number of particles within the granular assemblage. We choose four different particle sizes of the finer grain layer ($0.9d$, $0.75d$, $0.6d$, and $0.5d$) and four different thicknesses of the PSZ ($1/8t$, $1/4t$, $3/8t$, and $1/2t$ where t is the thickness of the gouge layer with a value of 3.75 mm without controlled boundary layers). For comparison, we additionally use a homogeneous model which is a randomly distributed granular assemblage with a uniform grain size distribution without any additional layers of particles. With this model, we generate a particle packing with a narrow to a wide particle size distribution (PSD) and create random spatial variations in grain size (see Figure S3.1 for more details).

The chosen particle population and sizes with the top and bottom controlled boundary layers provide a total sample thickness h of ~4 mm, normal stress σ of 5 MPa, slip velocity V of 1 m/s, interparticle friction μ of 0.5, with viscous damping of 0.3, and no interparticle rolling resistance (free rolling) as the reference settings. We select $0.5d$ and $1/8t$ as the reference contrast in grain size and layer thickness, respectively. The values of these parameters are chosen to be comparable to previous DEM numerical simulations while applying a slip velocity appropriate for granular shearing at seismic velocity (Morgan, 1999; Hazzard and Mair, 2003; Mair and Hazzard, 2007). The shear velocity is high and

yields a shear strain rate $\dot{\gamma}$ of 266, defined as the ratio of shear velocity (1 m/s) to the undeformed sample height (3.75 mm). Such a high strain rate yields an inertial number $I = \dot{\gamma}\bar{d}/\sqrt{\sigma/\rho} \approx 1.5\times10^{-3}$, which put our simulations just in the dense flow regime ($10^{-3} < I < 10^{-1}$) (Ferdowsi and Rubin, 2019; Ma et al., 2020). In fact, the I value remains similar in all simulations for our applied input parameters.

3.2.2.2 Numerical setup for direct shear simulations

The sample is sheared to a maximum of 500% shear strain, defined as $\gamma =$ dx/h, where x and h are the instantaneous displacement in the shear direction and the instantaneous sample thickness, respectively. Note that the actual shear strain of the gouge layer is ~10% larger than the imposed value as the thickness of the actual gouge layer t accounts for ~90% of the total sample thickness h, In the following, we use the imposed value (500%) for the results.

We apply the following procedure to perform simulations for direct shear:
1. Generate a loose granular assemblage in a cell in which particles with the assigned micro-properties are randomly distributed.
2. Apply isotropic compression to the cell until a cell pressure of 10 kPa is reached to achieve a dense granular packing with a controlled porosity (as a function of the interparticle friction μ).
3. Apply normal stress vertically to the top frictionless wall until the equilibrium is reached. To maintain the desired normal stress, a servo-control mechanism which adjusts vertical (z direction) wall velocity throughout the experiment is applied.
4. Impose a velocity with a progressive acceleration ramp to the top boundary layer in the positive x direction to apply shear to the granular layer. During shearing, top boundary particles are made to move only in the vertical motion (xy-plane) while at the bottom boundary particles are fixed.

(a) Fine-grained layer
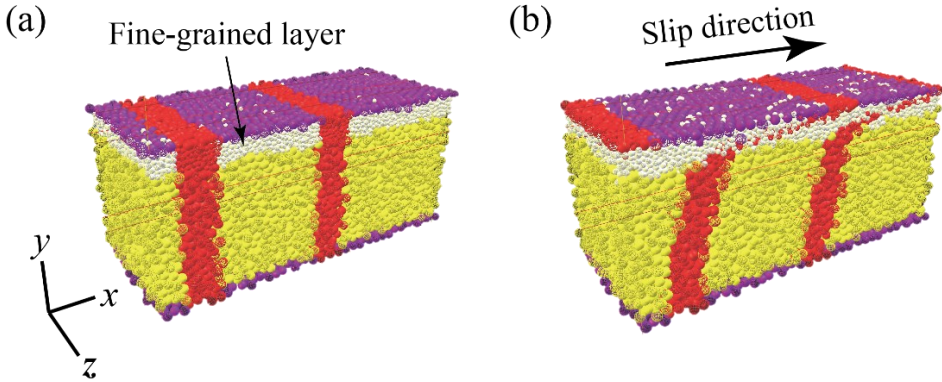
(b) Slip direction

Figure 3.1: *The principal slip zone (PSZ) model with a 0.5d and 1/8t fine-grained layer (shown in white) parallel to the slip direction. (a) Conditions before shearing, and (b) after shearing with a total shear strain of 100%. The boundary layer particles are shown in purple. Two vertical layers of grains are colored red to serve as strain markers. Fully homogeneous deformation would result in a rotation of the vertical boundaries of these layers to an angle of 45° at a final shear strain of 100%. The top and bottom frictionless walls are not shown.*

During the shearing, we continuously monitor the particle-scale properties, such as particle motion, as well as macroscopic properties, such as friction and gouge volume (dilation). Particle motion parameters like particle displacement, linear velocities, and rotations are measured to observe the dynamics of particle interactions. For example, using a Gaussian weight function, we can define the particle displacement at a specific height y as the weighted averages of the displacement in the x direction associated with the particles present at (or near) this height. The Gaussian weight function has a form of: $\Omega(x) = e^{(-\frac{(x-\mu)^2}{2\sigma^2})}$, where x is the specific sample height, μ is the location of the center, and σ determines the width of the bell curve. This information provides profiles of particle displacement as a function of sample height to visualize the deformation of the 3-D sheared granular layer. The macroscopic friction coefficient of the granular system is obtained by calculating the ratio of the sum of the shear force acting on the top (which drives boundary particles) to the applied normal load (i.e. shear stress divided by normal stress). The volumetric behavior of the gouge layer is a macroscopic reflection of dynamic particle motions associated with interparticle sliding and rolling.

3.3 Results

3.3.1 Macroscopic behavior

Figure 3.2 shows the macroscopic behavior of the granular assemblages, including macroscopic friction, dilatancy rate, and volumetric strain for the PSZ reference model with different seed conditions (i.e. different realizations). For the dilatancy rate and volumetric strain, we monitor the change of the vertical displacement of the top wall to measure the volume of the system throughout shearing, expressed as a dilatancy rate, dh/dx, as well as volumetric strain, $(h-h_0)/h$, respectively. Note that positive values indicate dilation and negative values indicate compaction. In general, our PSZ model has good reproducibility in macroscopic behavior as a function of shear strain. For the macroscopic friction, a peak friction of about 0.4 was first achieved followed by a sharp friction drop to approximately 0.32 within 10% of shear strain. With increasing shear strain, quasi-steady-state friction (~0.37) was attained. A positive correlation between friction and dilatancy rate can be observed. For the volumetric strain data, during initial shearing, all granular systems show instantaneous compaction followed by dilation. With increasing shear strain, the gouge layer begins to compact once more until 50-70% of the shear strain depending on the seed conditions, followed by continuous dilatation. The non-constant level of the volumetric strain at 200% shear strain may suggest the mixing of the fine- and coarse-grained layer.

(a)

(b)

(c)
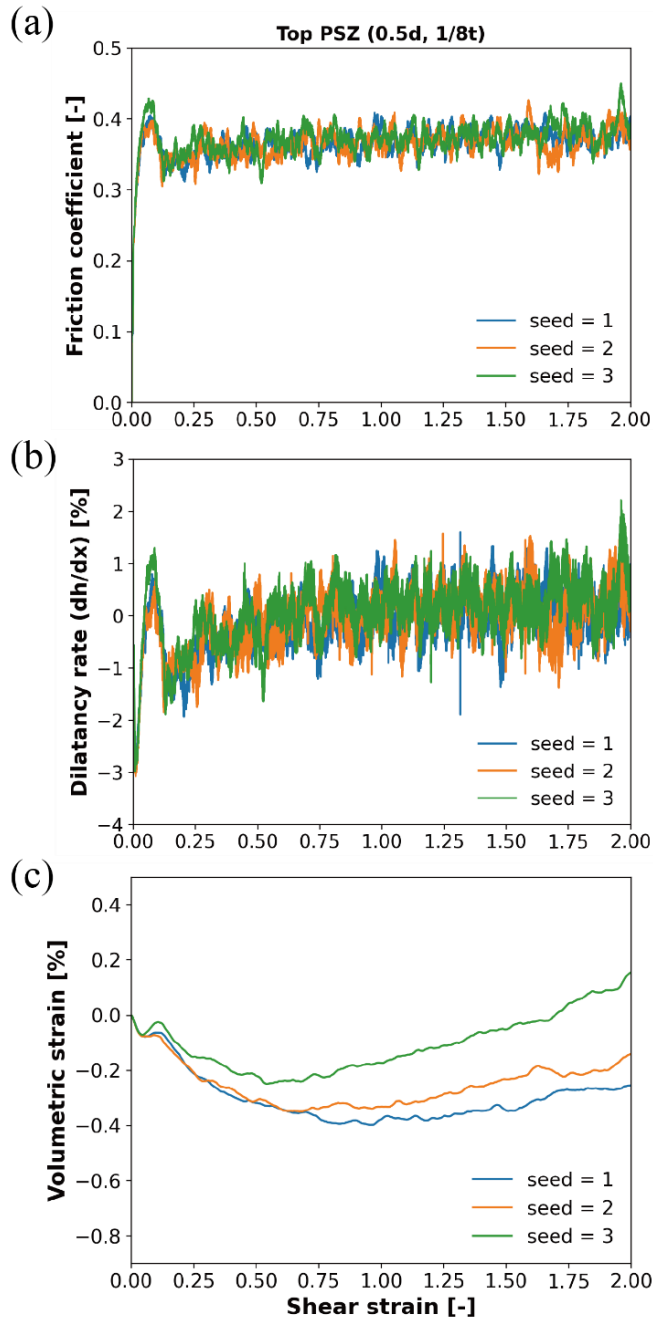
Figure 3.2: *Evolution of the macroscopic friction, dilatancy rate (dh/dx), and volumetric strain ((h-h$_0$)/h$_0$) as a function of shear strain up to 200% shear strain for the simulations of the top PSZ model with 0.5d and 1/8t. A positive change in dilatancy rate and volumetric strain indicates dilation and a negative change shows compaction. The gray dashed lines indicate a positive correlation between the friction and the dilatancy rate.*

3.3.2 Particle displacement

We divide the shear zone (thickness of ~4 mm including controlled boundary layers) into 100 sub-layers and obtain the weight averaged particle displacement for each region (in the y direction) of the sub-layer. In averaging, the relatively fine (e.g. 100 division) or relatively coarse (e.g. 64 division) resolution of the division did not influence the particle displacement curve. Figure 3.3 shows the particle displacement plot of the PSZ model with 0.5d and 1/8t with different seed conditions. The gray dashed line indicates the interface between the fine- and coarse-grained layers (FCG). The results not only show good reproducibility but also illustrate qualitative consistency with the visual deformation of the boundaries of the marker band in the 3-D model (Figure 3.1). For most of the PSZ models, the displacement curve displays a critical point roughly at the interface between the fine- and coarse-grained layers, defined as FCG interface afterward. Such a pattern demonstrates that most of the slip is accommodated within the fine-grained layer and little strain is accommodated in the coarse-grained layer (less than 10% of the total strain).
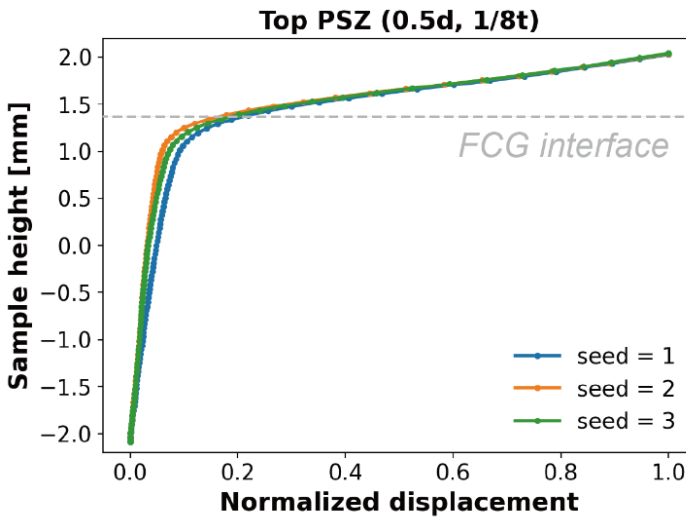
Figure 3.3: *Normalized particle displacement (Δx/max(x)) along the height of the sample for the top PSZ model with 0.5d and 1/8t using different seed conditions. The gray dash line indicates the initial fine- and coarse-grained interface (FCG interface).*

3.3.2.1 Influence of PSZ parameters: Grain size and layer thickness effects

In Figure 3.4, we compare the results of the PSZ model with different contrasts in grain sizes and thicknesses of the fine-grained layer. The FCG interface is kept at the same height in all shearing simulations. For most simulations, the results show that the particle displacement significantly increases from the bottom to the top when passing through the FCG interface and a clear change of slope in displacement can be observed. This demonstrates that most of the slip is accommodated within the fine-grained layer and not much strain occurs outside of it. In addition, the amount of slip that occurs outside of the PSZ decreases with increasing contrast in grain size and PSZ thickness. Note that there is no clear critical point in all simulations with a grain size contrast of $0.9d$ and the displacement curve is similar to the one with the single-size PSD (Figure 3.4a). We observe that the localization pattern within the fine-grained layer can be varied between different thickness contrast ratios, specifically for $0.5d$ grain size contrast. The pattern evolves from a straight line to an upward curved line with increasing thickness contrast which indicates that more slip is localized near the FCG interface.
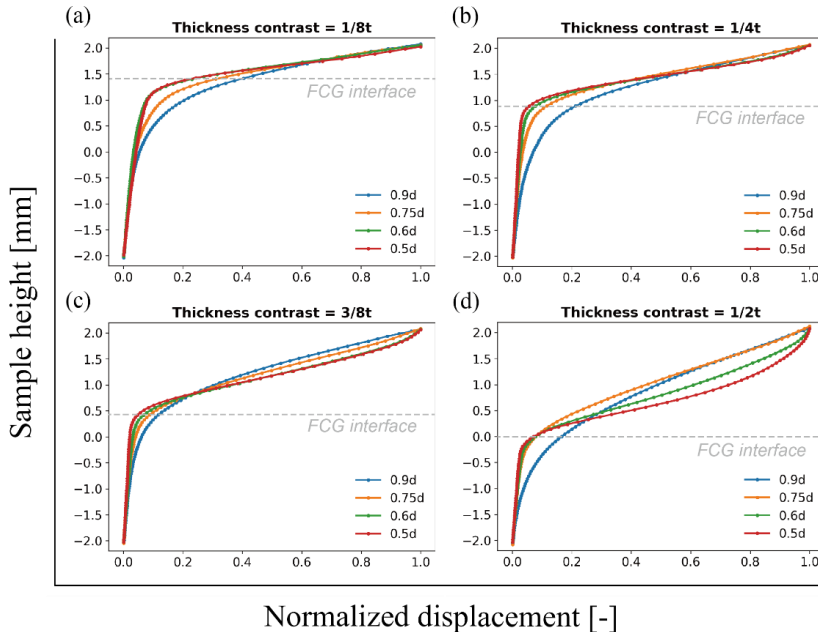
Figure 3.4: *Normalized particle displacement along the height of the sample for all grain size variation for a given thickness of the fine-grained layer. All the numerical samples are sheared to 200% shear strain. (a) 1/8t PSZ thickness (b) 1/4t PSZ thickness (c) 3/8t PSZ thickness (d) 1/2t PSZ thickness.*

3.3.2.2 Influence of location of PSZ on deformation pattern

To see the influence of the location of the PSZ on the shear deformation and further analyze to what extent slip localization operates in the model configuration of $0.9d$ and $1/8t$, we run additional simulations where a fine-grained layer is imposed at the middle and bottom of the granular layer. In Figure 3.5, we compare the displacement curves for the top, middle, and bottom boundary PSZ models with $0.9d$ and $1/8t$ as well as 0.5d and 1/8t at about 500% shear strain. For the simulation with $0.9d$ (Figure 3.5a), the results show that the displacement curves of the top and bottom PSZ have opposite patterns where for the bottom PSZ boundary simulation, most of the deformation is accumulated at the bottom region. On the other hand, the simulation with a middle PSZ shows nearly linear deformation. By comparison with the simulation using a single-size, localized deformation is hardly affected by the presence of a PSZ at the top boundary. When the contrast in grain size is larger ($0.5d$ in Figure 3.5b), we can clearly identify the critical point of the displacement curves, regardless of the location of the PSZ, suggesting that a larger amount of slip is localized within the PSZ.
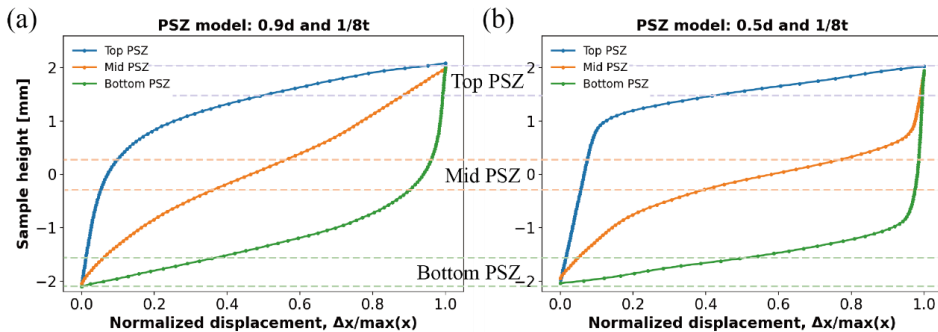
Figure 3.5: *The comparison between the single-size model, top, middle, and bottom PSZ models with (a) 0.9d and 1/8t and (b) 0.5d and 1/8t. The dashed line with the respective color indicates the location of the PSZ.*

3.3.2.3 Influence of shear strain on deformation pattern

Figure 3.6a shows the normalized particle displacement for the top PSZ model with $0.5d$ and $1/8t$ with shear strain from 10%, roughly the state of peak friction for all models, up to 500%, the maximum shear strain imposed in laboratory direct shear experiments (e.g. Hunfeld et al., 2017). For the 1/8 thickness ratio, we show an increasing localization of slip until 100% shear strain is reached. The degree of localization does not change further from 100% to 500% shear strain. We find that slip is already localized at the peak friction. To

further investigate the location and the instance of the localization, we look at the top PSZ model with 0.5d and 1/2t with shear strain starting from 1%, at strain-hardening state, to up to a value of 50%. We find that the gouge deformation begins to exhibit visible localization between the shear strain of 1% and 5%. The deformation pattern changes from a nearly linear curve at 1% to a non-linear curve at 5%, indicating that the initial slip is localized at the FCG interface as well as the boundary between the top boundary layer and the fine-grained layer. With increasing shear strain, slip is more localized within the fine-grained layer and specifically accumulates near the boundary with significant contrast in grain size (red rectangle region).
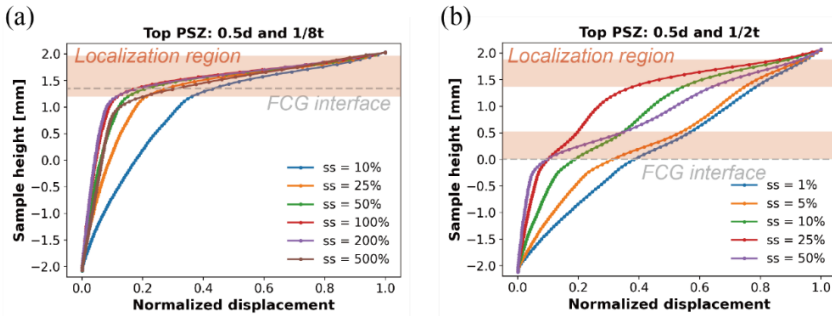
Figure 3.6: *Normalized particle displacement along the height of sample from 1% to 500% shear strain for (a) the top PSZ model with 0.5d and 1/8t and (b) top PSZ model with 0.5d and 1/2t.*

3.3.2.4 Influence of interparticle friction and rolling resistance on deformation pattern

Figure 3.7a-c shows the results of the deformation patterns with varied interparticle friction μ and rolling friction C_{rr} for PSZ models with different contrasts in grain size and PSZ thickness. We find that an increase in μ leads to a more localized deformation whereas the simulation with lower μ has a broader deformation zone. In addition, the simulation with C_{rr} of 0.5 becomes indistinguishable in the simulations with the power-law PSD (Figure 3.7c).

To explore whether the low interparticle friction of the fine-grained layer itself could induce further slip localization, we performed simulations using the PSZ model with 0.9d and varied layer thicknesses (1/8t and 1/2t), but only decreasing the μ of the fine-grained layer. Figures 3.7b and 3.7c show that slip becomes more localized within the fine-grained layer with decreasing μ_{PSZ}, regardless of PSZ thickness.
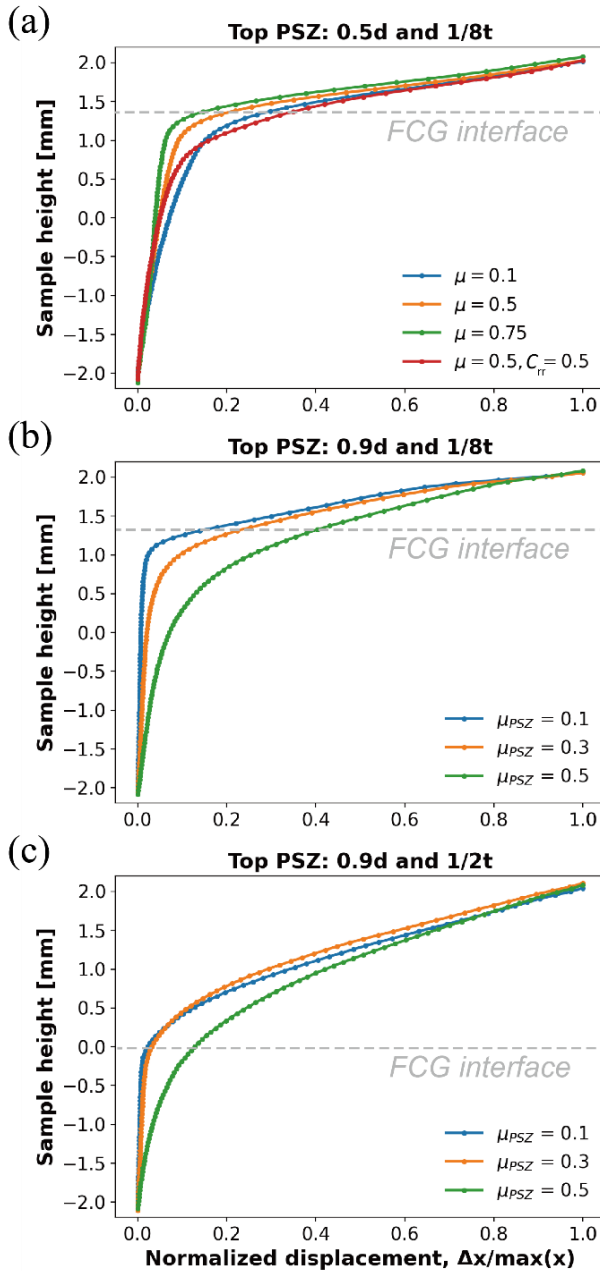
Figure 3.7: *Sample height as a function of normalized particle displacement for numerical models using different values for µ (0.1, 0.5, and 0.75) and C_{rr} (0, 0.5). (a) Top PSZ model with 0.5d and 1/8t; (b, c) Top PSZ models (0.9d and 1/8t as well as 0.9d and 1/2t) with varied $µ_{PSZ}$ of 0.1, 0.3, and 0.5.*

3.3.3 Porosity profile

Figure 3.8 shows assemblage porosity along the sample height for numerical models with different contrasts in PSZ thicknesses and grain sizes as well as the location of the PSZ. Calculation of the porosity is based on the triangulation of the spheres, in which the particle-centered volume V_σ of a particle can be obtained. Thus, the porosity of each particle can be calculated as $(V_\sigma - V_{particle})/V_\sigma$ (see Catalano et al., 2014 for more detail). In Figures 3.8a and 3.8b, we show that the deformed fine-grained layer has relatively higher porosity than the deformed coarse-grained layer. For the PSZ thickness contrast of $1/2t$, the porosity of the fine-grained layer lies within a range of 0.431 to 0.438. For the PSZ thickness contrast of $1/8t$, the porosity of the fine-grained layer is slightly higher (~0.46 to ~0.47) than that using a thickness contrast of $1/2t$. The porosity contrast between the fine- and coarse-grained layers is the smallest for the model of 0.9d, and slightly increases with increasing contrast in PSZ grain size. We note that there is a significant porosity drop below the FCG interface, suggesting a mixing of the fine- and coarse-grained layers. Figures 3.8c-d show that the porosity is relatively constant (around 0.43) across the gouge layer for the model with 0.9d whereas porosity increases up to 0.48 only in the fine-grained layers when the contrast in PSZ grain size is down to 0.5. Such observation of the relatively high porosity region is consistent with the slip localization zone (Figures 3.4 and 3.5). This indicates that the fine-grained layer exhibits much more dilatation than the coarse-grained layer during slip and suggests localization of slip within this layer.
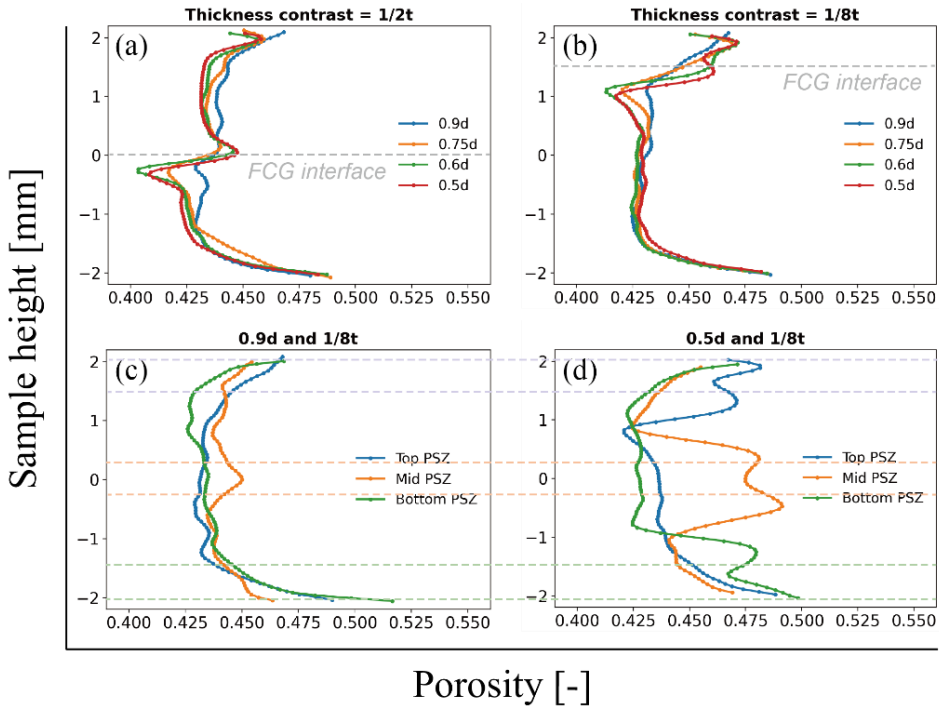
Figure 3.8: *Assemblage porosity along the sample height for numerical models with different PSZ thicknesses and grain sizes as well as the location of the PSZ. (a) 1/2t PSZ thickness (b) 1/8t PSZ thickness (c) 0.9d PSZ grain size and 1/8t PSZ thickness (d) 0.5d PSZ grain size and 1/8t PSZ thickness.*

3.3.4 Quantification of slip localization

To quantify the amount of slip localization, we first define the boundary between the spectator and localized regions by determining a critical point (CP) in the displacement curve. Then, the amount of localization can be calculated by the ratio of the projected length of the localized region on the shear boundary and the total displacement. In most of the PSZ models, we can clearly identify a CP in the displacement curve. However, some simulations show a sign of persistent localization of slip without a distinguishable critical point, such as the PSZ model with $0.9d$ and $1/8t$ (Figure 3.3 and Figure 3.5a). To define a CP in those simulations, we apply three different methods: the slope method, the ratio method, and the thickness method. We compare the amount of localization obtained from these methods with each other to infer whether localization exists in those simulations.

In the slope method, we calculate the slope between each adjacent sub-layer of the shear zone and compare the bulk slope pattern with the homogeneous one,

as shown in Figure 3.9a-b. If the slope between two adjacent sub-layers is larger than that of the homogeneous one, we deduce that this sub-region is potentially a localized region. Based on this information, an intersection point could be found to obtain the critical point. In the ratio method, we calculate the ratio of particle displacement deviation between homogeneous deformation and gouge deformation ($\Delta X = X_{homo} - X_{gouge}$) to homogeneous deformation at each height of the sub-layer. The ratio reflects the degree of slip localization of the entire gouge layer. If the gouge layer is homogeneously deformed, the ratio value is zero across the entire gouge layer, and, in contrast, if there is some localization of slip in the gouge layer, the ratio would be larger than zero. Here, we assume that localization occurs within the gouge layer when the ratio at any sample height is larger than 0.75 or 75%. We chose three different ratios of 0.75, 0.8, and 0.85 as varied PSZ criteria to compare the results with those obtained from the slope method. A critical point is defined as the intersection point between the PSZ criterion and the ratio pattern (Figure 3.9c-d). For the middle PSZ model, two intersection points are required to determine the spectator and the localized regions. Note that the region with a ratio larger than 0.75 or 75% determined by the intersection point does not correspond to the location of slip localization. However, the rest of the region with a ratio smaller than 0.75 or 75% matches the localization area. The thickness method is only applied to PSZ models where a pre-defined fine-grained layer is used. Instead of determining a critical point, we take the intersection point between the pre-defined FCG interface and the displacement curve as the boundary between the spectator and localized regions. In this method we only quantify the slip within the pre-defined PSZ, and, therefore, we neglect the localization that occurs outside of the PSZ.

In Figure 3.9e-f, we show the amount of localization for different locations of PSZ with $0.9d$ and $1/8t$ sheared to 200% and 500% strain. These models all show a poorly defined CP. The amount of localization of other simulations is summarized in Table S3.1. We find that over 80% of localization can be obtained from the slope and ratio methods, irrespective of shear strain, with the exception of the middle PSZ model which shows particularly low values of 50-60% for localization. For the result obtained from the thickness method, the amount of localization is, in general, 5% to 40% less than that obtained from the slope and ratio method, depending on the location of the PSZ, and its value slightly decreases with the shear strain. This means that (localized) slip is not fully

accommodated within the pre-defined PSZ and partial slip occurs within the spectator region, and its contribution increases with accumulating strain.
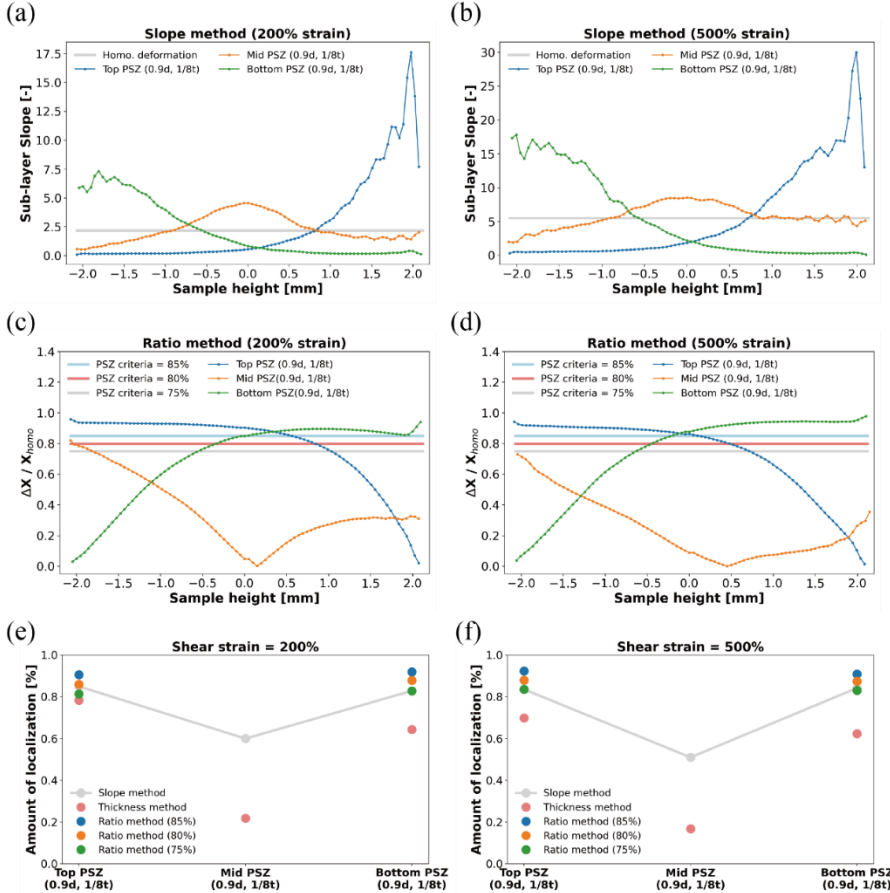
Figure 3.9: *The slope and ratio methods together with the quantification of slip localization for the top PSZ, middle PSZ, and bottom PSZ models at shear strain of 200% and 500%. (a, b) The slope method; (c, d) The ratio method; (e, f) The obtained amount of localization from the three methods for different simulations.*

3.4 Discussion

3.4.1 Comparison with previous homogeneous data

We first compare our homogeneous results with Mair and Hazzard (2007) to which our model geometry and the applied particle parameters are comparable. The evolution of the macroscopic friction and the mean friction level of the μ_{qss} for all homogeneous simulations (Figure S3.2) is consistent with previous laboratory experimental and 3-D numerical data (Hazzard and Mair, 2003; Mair et al., 2002; Mair and Hazzard, 2007). A notable difference is that, in all the

homogeneous models, a peak in friction appears at initial shearing stages, accompanied by an increase in gouge dilation, and variable amounts of displacement-dependent weakening can be observed for the models with different PSDs. The deformation patterns of the gouge layer are also comparable. Figure 3.10 shows the comparison of the gouge deformation pattern between ours and Mair and Hazzard (2007). In Mair and Hazzard (2007), the gouge deformation in both the Gaussian PSD (green curve) and D of 2.6 (purple curve) also reveals a degree curvature non-linearity, which suggests that the shear rate across the interface is non-linear. Although their results do not show deviation from a narrow to wide PSD as much as ours (orange and red curves), which might be owing to lower shear strain rate (lower inertial number) or other factors like the applied timestep, the comparison of the results demonstrates that the numerical results obtained in our study are accurate and reliable. In fact, the evolution of the pattern of gouge deformation from localized deformation to homogeneous deformation with increasing PSD is more systematic in our study. Such a transition may be associated with the number of fine grains in the granular packing that facilitates homogeneous shearing. However, the underlying mechanisms remain unclear and is out of the scope of the current study.
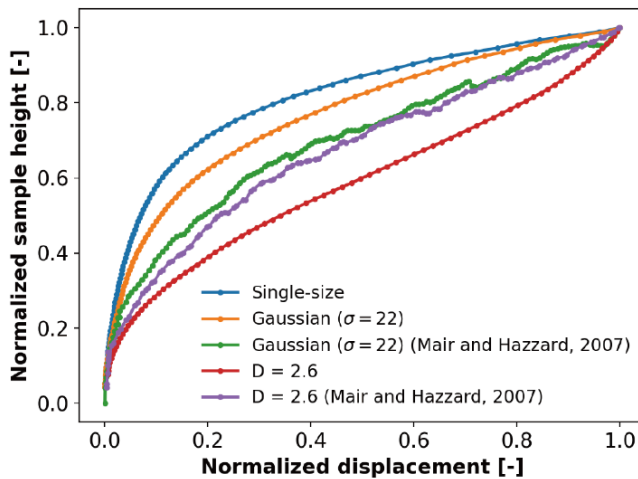
Figure 3.10: *Comparison of the gouge deformation pattern between our homogeneous shear model and Mair and Hazzard (2007). Note that the imposed shear strain is 200% and 100% in our and Mair and Hazzard (2007), respectively.*

3.4.2 The PSZ model

3.4.2.1 Evolution of macroscopic friction and volumetric behavior

The evolution of the macroscopic friction and the mean friction level of the μ_{qss} for all PSZ simulations is comparable to the homogeneous simulations. An imposed fined-grained layer, independent of its thickness and grain size, does not show an influence on the mechanical response. This is different from previous laboratory experimental observations where a weakening behavior (i.e. stress drop from a peak to steady-state friction) is usually observed to be accompanied by the generation of a principal slip zone (e.g. Smith et al., 2015). Such a difference can be explained by the absence of grain comminution processes and frictional heating at grain contacts in the current numerical simulation.

3.4.2.2 Granular deformation

The previous 2-D and 3-D numerical studies have shown that persistent localized deformation is hardly observed in a homogeneous granular layer under low single shearing velocities (i.e. $V < 1$ μm/s, for example in Mair and Hazzard, 2007; Morgan and Boettcher, 1999) or seismic velocity-stepping simulations (i.e. $10^{-3} < V < 10^0$ m/s; Ferdowsi and Rubin, 2020) when processes like grain breakage (e.g. Mair and Abe, 2008; Abe and Mair, 2009), time-dependent healing (e.g. Morgan, 2004), cohesion of grain contacts (e.g. Casas et al., 2022), or fluid overpressurization (e.g. Nguyen et al., 2021) are not included in models. In our homogeneous model, we also do not observe persistent localization in the granular packing in the Gaussian PSD and power-law PSD models, except for the single-size and narrow Gaussian PSD models where we find that the slip is accommodated preferentially in the top about 1.2 mm of the gouge layer after 200% shear strain (Figure S3.3). These non-linear displacement curves were also observed in Mair and Hazzard (2007). Note that we used nearly the same model configuration and particle parameters as their model. However, our results show a more systematic evolution of deformation from a "localized" pattern to a homogeneous pattern with increasing particle size distribution. Such a transition may be associated with the number of fine grains in the granular packing that facilitates homogeneous shearing.

In the PSZ models, we observe persistent localized deformation in the gouge layer where, regardless of which quantification methods we use, most models show more than 75% of slip is localized, with the exception of the middle PSZ

model with a grain size contrast of 0.9 and a thickness of 1/8 that shows a particularly low amount (~20 %; Figure 3.9e, f). Although the amount of localization varies slightly using different methods of quantification, all values progressively increase with increasing contrast in grain size and PSZ thickness, indicating that the amount of localization is highly sensitive to the grain size and the thickness of the fine-grained layer.

3.4.2.3 FCG interface

A major question is how and why shear displacement localizes in the layer of smaller grains in the absence of any time-dependent grain-contact mechanism. In Figure 3.4d, we show that the amount of localization increases with increasing grain size contrast for a PSZ model with a thickness contrast of $0.5t$. With this thickness contrast, we can observe that over 90% of slip is localized within the fine-grained layer when the contrast in grain size is more than 25%. However, the localized patterns in the fine-grained layer vary between different grain size contrasts, which transforms from a nearly straight line with $0.75d$ to a curve-shaped line with $0.5d$. This observation indicates that more slip is accommodated close to the FCG interface even though the strain is nearly fully localized within the fine-grained layer. In addition, the phenomenon suggests that the initial slip occurs at the boundary, i.e. at the FCG interface. This is consistent with the model configuration we applied for the initial packing conditions of the fine-grained and coarse-grained layers. Both layers should possess identical porosity, average coordination number of each particle, and contact force network (i.e. pipe-like network) due to the use of single-size PSD within each layer. The main difference might be that the total contact force at grain contacts of the fine-grained layer is lower compared to the coarse-grained layer (Figure 3.11) due to the decrease in the contact radius and thus the contact stiffness. However, the total grain contact area for both layers should remain identical as the number of grain contacts in the fine-grained layer also significantly increases. Therefore, it is complicated to explain why localization occurs within a layer of smaller grain sizes. However, properties at the FCG interface are significantly different. At the FCG interface before shearing, the mixture of fine and coarse grains provides a lower porosity and an increase in the average coordination number of large grains. The interface region also becomes a contrasting boundary in terms of grain size, contact stiffness, and contact force. The above factors likely trigger the initial slip at the

grain contacts at the interface; however, the controlling role of each variable remains unclear.
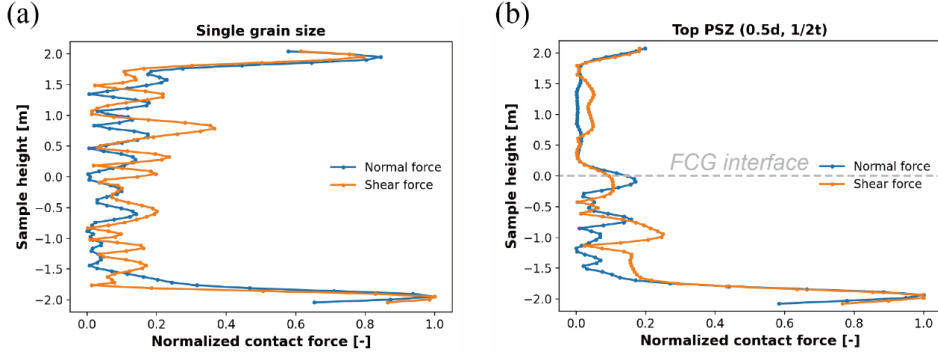
Figure 3.11: *The normalized contact forces (both normal and shear forces) along the sample height for (a) the single-size model, and (b) the top PSZ model (0.5d, 1/2t) at 200% shear strain.*

To explore the localization of strain within the fine-grained layer after the slip initiates at the boundary, we apply the concept of the average spreading velocity parameter V_k^v and the squeeze expulsion theory parameter T_k^v (e.g. Jing et al., 2017; Lai et al., 2017) to investigate the kinematic differences in a layer with different-sized particles and the developed force imbalances when particles are squeezed between each other. The V_k^v and T_k^v are defined as:

$$V_k^v = \frac{1}{N_k} \sum_{i=1}^{N_k} V_i^v \tag{3.16}$$

$$T_k^v = \frac{1}{N_k} \sum_{i=1}^{N_k} \frac{F_i^v}{\rho \pi r^3} \tag{3.17}$$

where V_i^v is the vertical velocity of particle i, N_k is the number of the d-size particles for the fine- and coarse-grained layer, F_i^v is the vertical resultant force of particle i via particle interactions, ρ is the grain density, and r is the grain radius. The V_i^v and F_i^v of particles only considers the direction away from the FCG interface to evaluate the contribution of particle interactions to the fine and coarse grains. For example, if the fine-grained layer is on top of the coarse-grained layer (i.e. most of the scenarios in this study), we adopt the positive and negative values for both V_i^v and F_i^v for the fine- and coarse-grained layers, respectively. The larger values of V_k^v indicate more enhanced granular flow mobility and the collision dominant flow pattern, and the larger values of T_k^v

indicates more contributions of particle interactions to accelerate the spread of particles.

Figure 3.12 shows the evolution of V_k^v and T_k^v as a function of shear strain of 1% to 50% for the fine- and coarse-grained layers. We find that the coarse-grained layer initially possesses relatively large V_k^v of ~0.026 m/s and T_k^v of ~220.5 m/s² at the shear strain of 1% without visible persistent slip localization. As shear strain increases up to 5%, we observe a significant drop for both V_k^v and T_k^v for the coarse-grained layer accompanied by a sharp increase in the fine-grained layer. The differences in the values of V_k^v and T_k^v between the fine- and coarse-grained layers do not vary with further shear strain and the localization process carries on. The combined results suggest that the phenomenon of slip localization is associated with the kinematic difference and the force imbalance between the fine- and coarse-grained layers. Initially, larger contributions of particle interactions happen within the coarse-grained layer than the fine-grained layer which is likely due to the particle mass variation. Shortly, with progressive slip, the fine grains become more vigorous and can slip more than the coarse grains because smaller grains acquire more spreading velocity when in contact with a large grain. This concept is similar to momentum transfer where most of the momentum of the coarse-grained layer is transferred to the fine-grained layer. We suggest that the contrast in the stiffness and contact force causes an initial slip on the boundary, and the fine-grained layer is prone to slip and dilate owing to the transition of the contributions of the particle interactions from the coarse-grained layer.
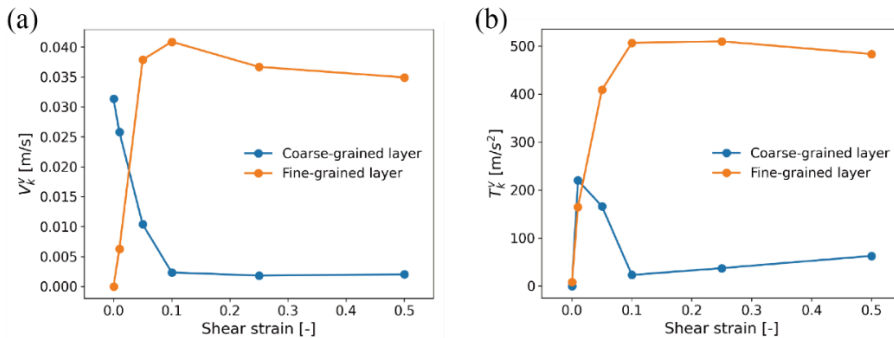
Figure 3.12: *(a) average spreading velocity parameter V_k^v and (b) mechanical parameter T_k^v as a function of shear strain (1%, 5%, 10%, 25%, and 50%) for the fine- and coarse-grained layers. An example of the top PSZ model with 0.5d and 0.5t.*

3.4.2.4 Effect of interparticle friction on slip localization

According to Morgan (1999), for the same contact force, sliding between particles will be activated more easily in a low μ system than in a high μ system because of the low assigned critical force. On the other hand, interparticle rolling will become more active if μ is sufficiently high to inhibit sliding to occur. Based on the results of the different μ systems, we show that the slip becomes more localized within the fine-grained layer with increasing μ for the entire system (Figure 3.7). This suggests that interparticle rolling is the main mechanism that accommodates slip as we have shown that particles are easier to dilate within the fine-grained layer during shearing. In addition, we show the profile of the angular velocity distribution for each particle for the single-size and PSZ model with $0.5d$ and $1/8t$ fine-grained layer at the top, middle, and bottom of the granular layer at 200% shear strain (Figure 3.13). Large angular velocity of particles is observed specifically in the fine-grained layer, indicating that slip is accommodated largely by interparticle rolling, which is consistent with the result of the PSZ model with different μ (Figure 3.7a), showing that the high μ assemblage (system favored to interparticle rolling) provides the largest degree of localization. The volumetric strain data also supports the observation where the granular layer with high μ exhibits the largest amount of dilation whereas the one with low μ exhibits mostly compaction (see Figure S3.4). Since high μ inhibits interparticle sliding and promotes interparticle rolling (also the dilation angle between particles), the granular layer would dilate more than the one dominated by the interparticle sliding.

However, if we only reduce the μ of the fine-grained layer to a lower value (0.1 and 0.3) instead of the entire granular assemblage (Figure 3.7b, c), the degree of localization still increases. Such difference is likely to be due to the variation of contact normal and shear forces between the fine- and coarse-grained layers. Even in a high μ granular assemblage, interparticle sliding might still be very likely to occur within the fine-grained layer due to the low contact force. On the other hand, the decrease in μ for the entire system does not necessarily facilitate localization. Altogether, our results also suggest that the increasing percentage of interparticle sliding can facilitate slip localization.
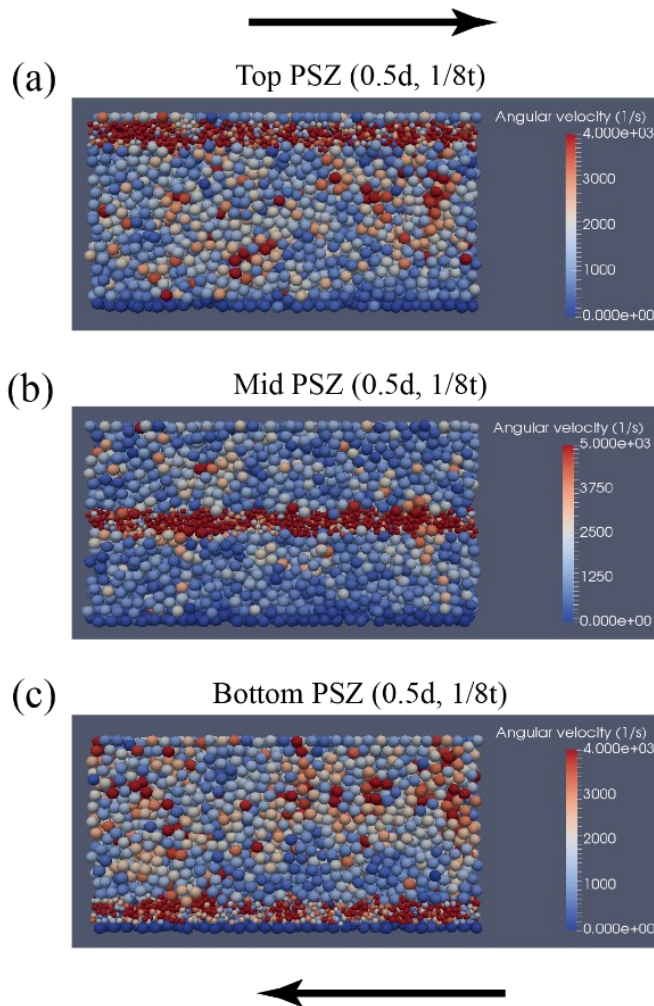
Figure 3.13: Distribution of angular velocity in the shear direction (x-direction) of each particle after 200% shear strain for the models with (a) a top PSZ; (c) a middle PSZ; (d) a bottom PSZ all with 0.5d and 1/8t of the granular assemblage. The warm color indicates high angular velocity while the cool color indicates low angular velocity.

3.4.3 Comparison with laboratory results and implications

Numerous laboratory experiments performed on room-dry and wet gouges at high slip velocity (i.e. > 0.1 m/s) have reported that slip tends to be localized at the boundary of the gouge layer, forming a so-called PSZ (Boulton et al., 2017; Hunfeld et al., 2021; Kuo et al., 2014; Smith et al., 2015; Yao et al., 2018). Smith et al (2015) reported that the formation of a PSZ through grain fragmentation is a critical precursor to dynamic weakening in calcite gouges which is associated

with thermal-induced mechanisms like flash heating and weakening. In addition, he reported different types of shear localized features that developed at different frictional stages, in which R-shear is initially developed at around peak stress followed by Y- or boundary shears at steady-state. However, our results do not show a clear link between the development of the localization and different frictional stages which might be due to the method of analyzing the localization.

On the other hand, without thermal-induced mechanisms, Reches and Lockner (2010) inferred that dynamic gouge formation is an effective lubrication mechanism to reduce fault strength. Han et al. (2010) also reported that the presence of nanoparticles in a fault zone can be an important lubrication process due to nanoparticle rolling. However, according to our PSZ models, the presence of the fine-grained layer does not necessarily reduce the shear strength and the bulk macroscopic friction only decreases when the fine-grained layer has lower interparticle friction (which also promotes particle sliding rather than rolling). Thus, frictional-induced heating mechanisms such as flash heating or thermal pressurization at grain contacts are required for dynamic weakening (see also Yao et al., 2016a, b).

Previous low- and high-velocity friction experiments reported that slip tends to be accommodated within the PSZ once a fine-grained layer has formed due to grain size reduction (Ikari, 2015; Smith et al., 2015). As grain size reduction may induce rounding of particles, according to our numerical results (Figure 3.7e), less slip may be accommodated within the PSZ instead due to the increasing importance of interparticle rolling within the fine-grained layer. Such contradictory observation may suggest that only the rounding effect on particles due to grain-to-grain comminution is not sufficient for further localization of slip within a PSZ. This suggests that in the absence of thermal weakening mechanisms within the PSZ, the layer with fine-grained particles (PSZ) will continue to grow during shear due to grain size reduction, resulting from slip occurring outside of the PSZ.

3.5 Conclusions
We use 3-D DEM simulations to investigate strain localization in a non-destructive granular layer under seismic slip velocities. We build a direct shear model with a distinct configuration, a principal slip zone (PSZ) model with

variation in grain size and thickness between the single-size fine- and coarse-grained layer. In addition, a series of particle parameters and values are used to investigate their effect on slip localization. The conclusions are summarized below:

1. For an assemblage with a pre-defined fine-grained layer, we show that slip is prone to be localized within the fine-grained layer and the amount of localization is sensitive to the relative grain size and layer thickness of the PSZ.

2. We reveal that slip is prone to be largely accumulated near the grain-size contrast boundary. This is likely due to the fact that the boundary represents a significant contrast in the contact stiffness and contact force between the fine- and coarse-grained layers. The applied concept of spreading velocity and squeeze expulsion theory provides a plausible explanation for slip localization as smaller grains acquire more kinematic energy when large grains bump into them.

3. By comparison with natural and laboratory observations, we conclude that the presence of a weaker, fine-grained layer within a dense fault zone is likely to result in self-enhanced weakening of the fault zone. In addition, thermal mechanisms at grain-to-grain contacts (i.e. flash heating and weakening) are needed to induce dynamic weakening of a fault.

Supplementary information

Text S3.1: Particle size distribution

The particle size distribution (PSD) used in this study includes a single-size, a Gaussian distribution, and power-law distribution. We select d of 250 μm for the single-size model. For the Gaussian distribution, the PSD is determined by the standard deviation ρ of 22 μm about d. This means that the entire particle size ranges from 228 μm to 272 μm. This selected value is identical to those applied in Mair and Hazzard (2007) and an approximation of the narrow PSD used in previous laboratory experiments (Mair, 2002). To model a wider range of grain sizes, we additionally use ρ of 44 and 66. Power-law distributions have frequently been used to describe a wide PSD of a shear band in both natural and experimental gouges (An and Sammis, 1994; Hadizadeh et al., 2010; Marone and Scholz, 1989; Sammis et al., 1987). The PSD of the power-law distribution is defined by the fractal dimension D which is inferred to be an indicator of fault maturity. We choose D values ranging from 0.8 to 2.6 with four different grain diameters (62.5 μm, 125 μm, 250 μm, and 500 μm) as a representative of a coarse-grained matrix support (e.g. $D = 0.8$, an immature fault) to a fine-grained matrix supported fault (e.g. $D = 2.6$, a mature fault). The distribution is defined as

$$N_i = N_{max} * (R_{max}/R_i)^D \qquad (S3.1)$$

where N_i and R_i are the incremental number (i.e. abundance) and particle radius respectively. N_{max} and R_{max} are the abundance and radius of the maximum size fraction (i.e. 250 μm).
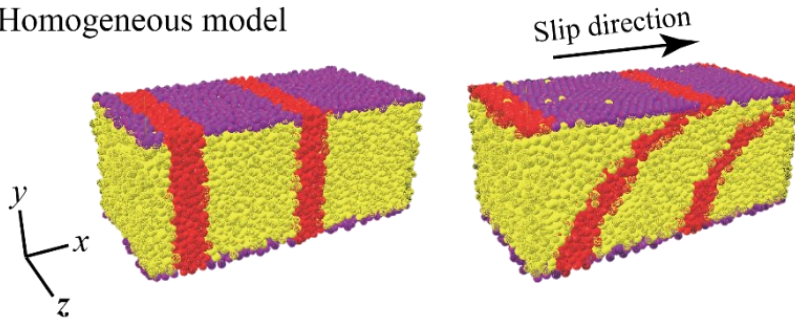
Figure S3.1: *(a) Homogeneous model before and after shearing (100% of shear strain); (b) Particle size distribution plotted as cumulative particle density as a function of grain diameter for the selected Gaussian PSD with mean particle size of 250 and the standard deviation of 22, 44, and 66 as well as the power-law PSD with D of 0.8, 1.6, and 2.6.*
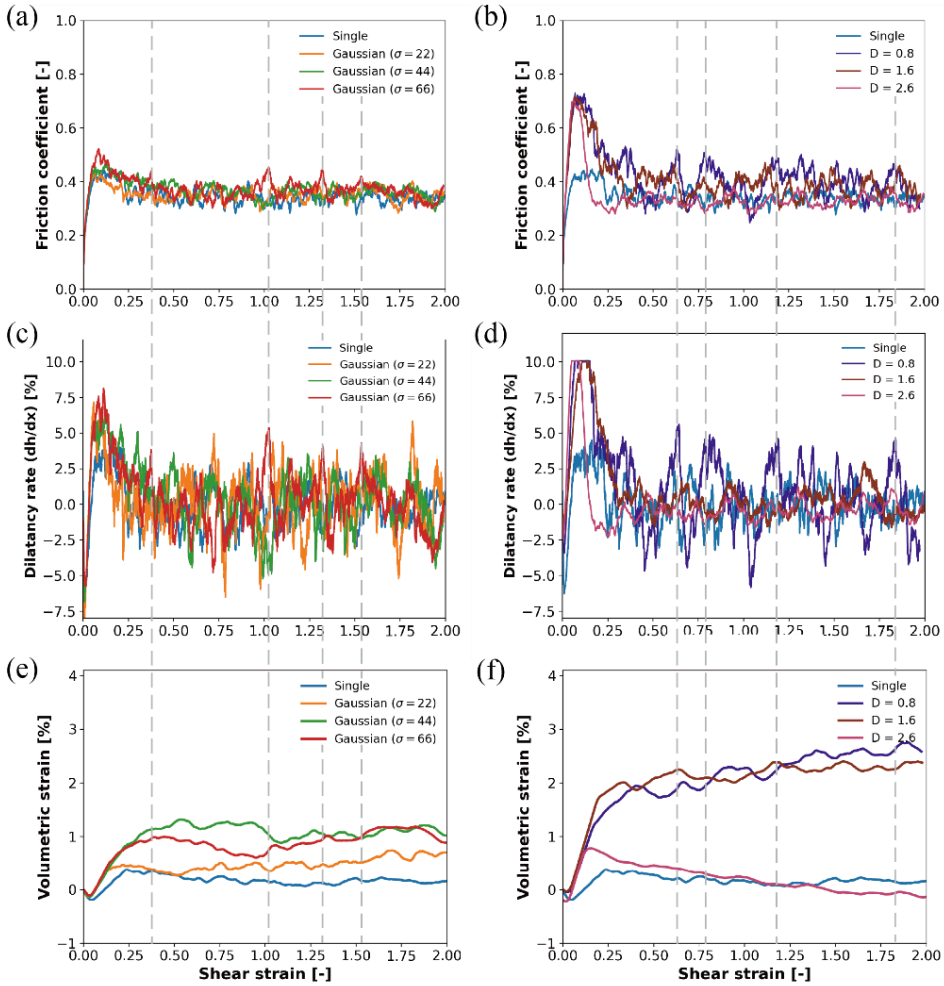
Figure S3.2: Evolution of the macroscopic friction, dilatancy rate (dh/dx), and volumetric strain ((h-h_0)/h_0) as a function of shear strain up to 200% shear strain for the simulations using homogeneous models. We compare the results between (a, c, e) the single-size model and the Gaussian PSD model with a standard deviation of σ = 22, 44, and 66 as well as (b, d, f) the single-size model and the power-law distribution with D = 0.8, 1.6, and 2.6. (a, b) Friction coefficient as a function of shear strain; (c, d) Dilatancy rate as a function of shear strain; (c, d) Volumetric strain as a function of shear strain. A positive change in dilatancy rate and volumetric strain indicates dilation and a negative change shows compaction. The gray dashed lines indicate a positive correlation between friction and dilatancy rate.
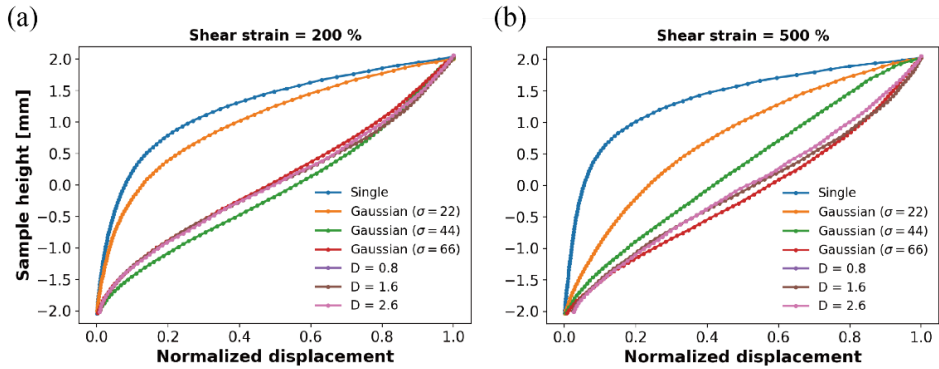
Figure S3.3: *Normalized particle displacement along the height of sample between single-size, Gaussian, and power-law PSD under quasi-steady state conditions for 200% and 500% shear strain. The deformation patterns can be categorized into two types: (i) Type I showing a curve in which the slope is particularly gentle at the top and sharp at the bottom, indicating that more slip is accommodated within the top shearing region of the granular assemblage; (ii) Type II showing either a slight, but limited, S-bend shapes or a nearly straight line indicating relatively homogeneous deformation.*
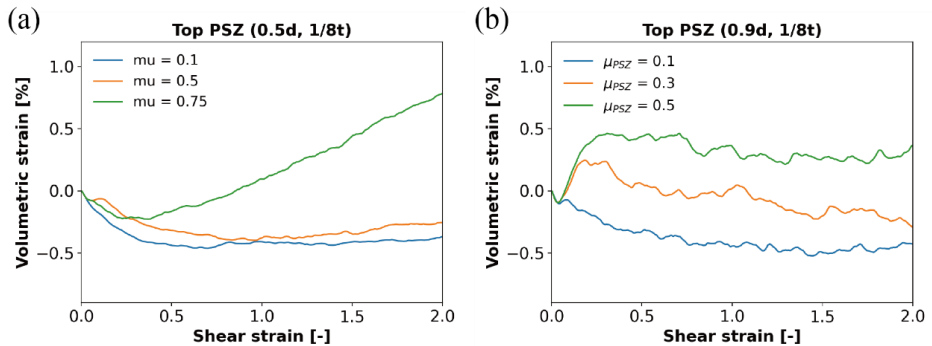
Figure S3.4: *Evolution of the (a) macroscopic friction, (b) dilatancy rate (dh/dx), and (c) volumetric strain (h-h_0/h_0) data as a function of shear strain up to 200% shear strain for the single-size model and the PSZ model.*

(a)

(b)

(c)
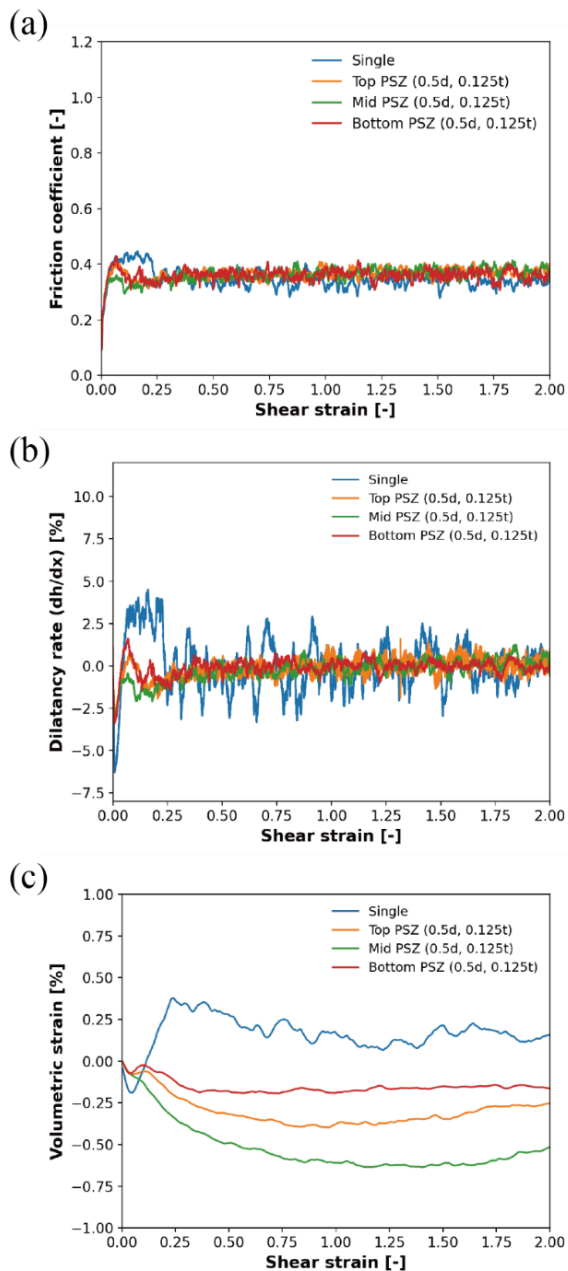
Figure S3.5: *Evolution of the volumetric strain (h-h₀/h₀) data as a function of shear strain up to 200% shear strain for the top PSZ model with (a) 0.5d and 1/8t and (b) 0.9d and 1/8t.*
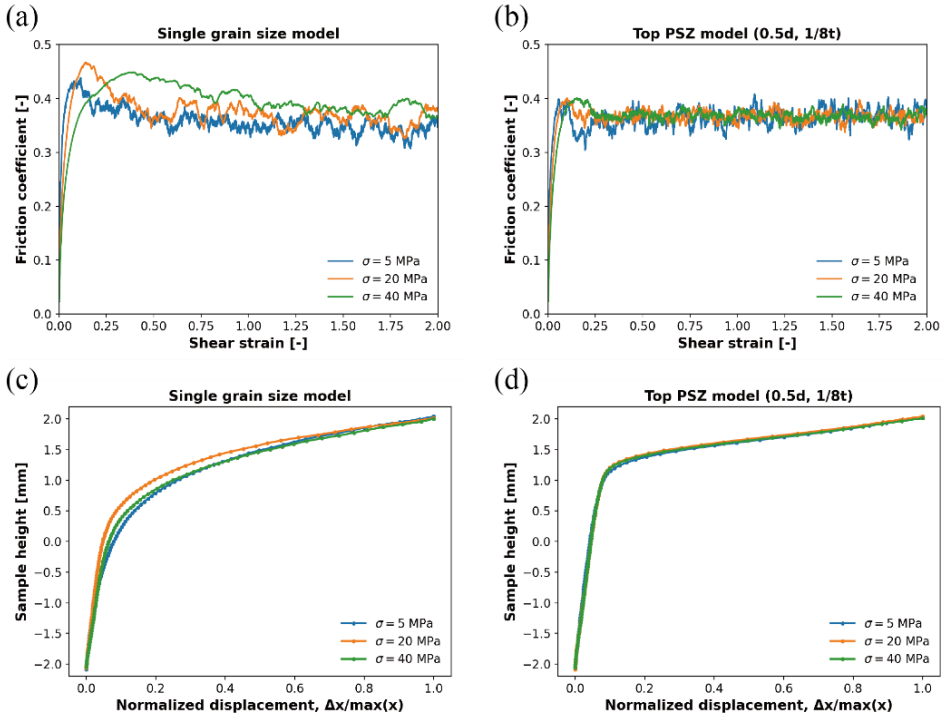
Figure S3.6: *Evolution of macroscopic friction against shear strain and normalized particle displacement along the height of sample for different normal stresses of 5, 20, and 40 MPa. (a, b) macroscopic friction for the single-size and the top PSZ models (0.5d, 1/8t). (a, b) Deformation pattern for the single-size and the top PSZ models (0.5d, 1/8t). We find that an increase in normal stress influences the generation of the peak friction, but not on the deformation of the granular layer for both the homogeneous model and PSZ. The selected normal stresses of 20 and 40 MPa would result in a smaller inertial number, which is ~7.4 $\times$ 10^{-4} and ~5.3 $\times$ 10^{-4}, respectively, falling in the quasi-static regime.*
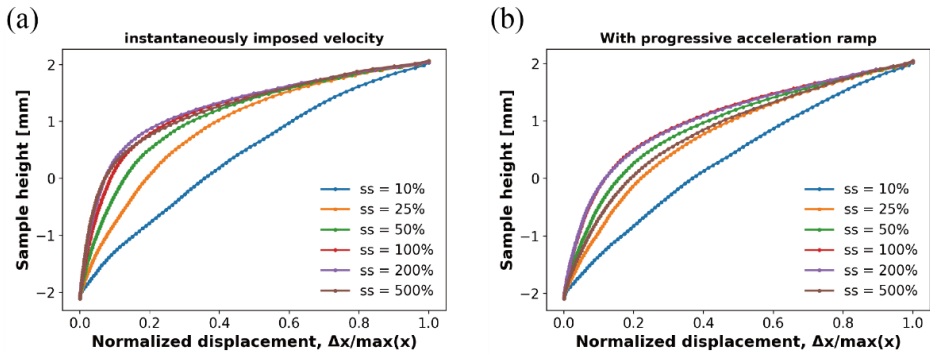
Figure S3.7: *Normalized particle displacement along the height of the sample for different shear strains. (a) Instantaneously imposed velocity; (b) With a progressive acceleration ramp of 0.01 m/s.*
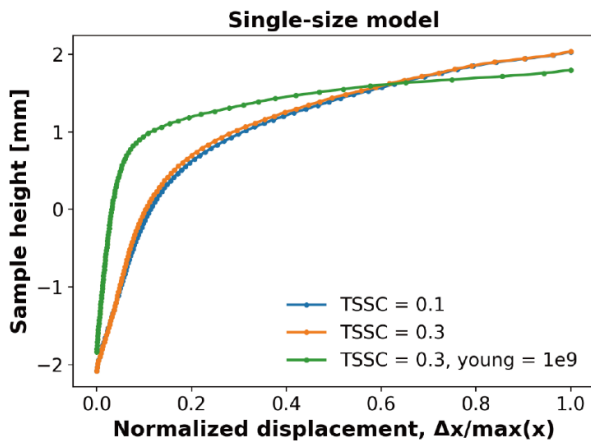
Figure S3.8: *Normalized particle displacement along the height of the sample for the single-size model with different timestep safety coefficients (0.1 and **0.3**) and Young's modulus (1 × 10⁹ and **5.5 × 10¹⁰**). Bold font indicates the reference settings in this study.*
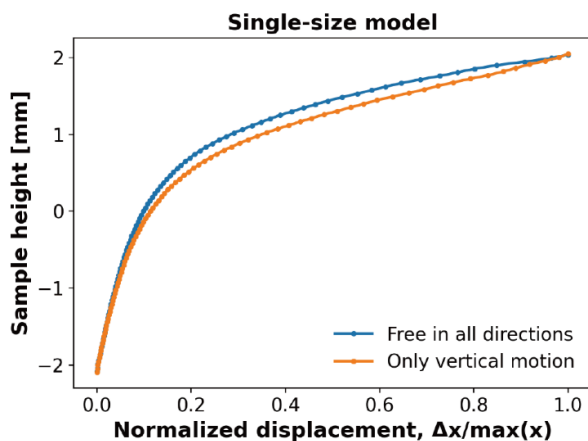
Figure S3.9: *Normalized particle displacement along the height of the sample for the single-size model with different settings for the particles in the top boundary layer.*
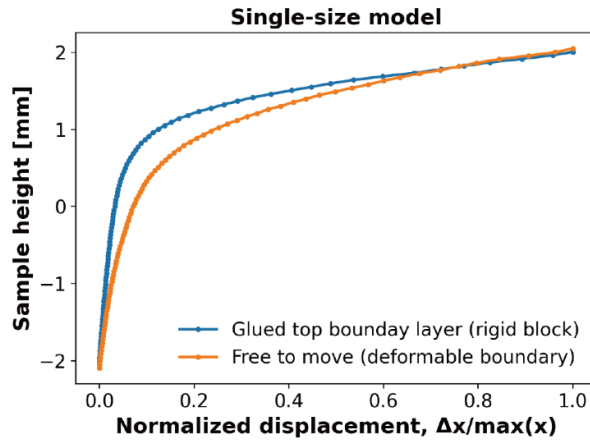
Figure S3.10: *Normalized particle displacement along the height of the sample for the single-size model with different settings for the top boundary layer and the frictionless wall. The rigid block indicates that the top boundary layer is glued to the top frictionless wall whereas the deformable boundary indicates the current setting in this work.*

Table S3.1: *Summary of the amount of localization for all PSZ models at 200% shear strain.*

PSZ grain size	PSZ thickness	Slope method	Ratio method (85%)	Ratio method (80%)	Ratio method (75%)	Thickness method
0.9*d*	1/8*t*	84.0%	91.2%	87.0%	81.6%	75.4%
0.9*d*	1/4*t*	84.4%	92.1%	87.9%	83.3%	85.4%
0.9*d*	3/8*t*	87.5%	91.7%	87.5%	83.9%	92.3%
0.9*d*	1/2*t*	83.7%	96.0%	93.4%	89.9%	89.2%
0.75*d*	1/8*t*	88.5%	89.8%	85.5%	80.7%	84.1%
0.75*d*	1/4*t*	90.7%	89.9%	85.7%	81.7%	93.1%
0.75*d*	3/8*t*	95.4%	91.3%	87.6%	84.4%	94.8%
0.75*d*	1/2*t*	90.3%	93.8%	89.2%	86.6%	95.5%
0.6*d*	1/8*t*	91.0%	88.4%	84.2%	78.2%	91.0%
0.6*d*	1/4*t*	93.4%	89.5%	85.3%	79.5%	95.6%
0.6*d*	3/8*t*	93.3%	90.9%	87.6%	83.1%	96.2%
0.6*d*	1/2*t*	93.4%	93.4%	89.6%	85.9%	96.5%
0.5*d*	1/8*t*	90.4%	87.8%	83.5%	80.4%	91.2%
0.5*d*	1/4*t*	94.5%	87.8%	85.0%	81.8%	97.0%
0.5*d*	3/8*t*	94.4%	90.0%	87.8%	82.6%	97.6%
0.5*d*	1/2*t*	95.2%	94.2%	89.4%	87.2%	97.3%

Note. d = the mean particle diameter of 250 μm. t = the thickness of the gouge layer with a value of 3.75 mm without controlled boundary layers.

Chapter 4

Characterization of flash temperatures in experimentally sheared fault gouge analogues

Chien-Cheng Hung, André R. Niemeijer

Abstract

Flash temperatures induced by flash heating can lead to thermal softening or decomposition of fault-zone materials at microscopic grain contacts and, consequently, cause a reduction in fault strength during seismic slip. To systematically quantify the efficiency of short-term frictional heating at the contact scales and its impact on the mechanical fault strength, we conducted rotary-shear friction experiments on Ottawa quartz sand "gouges" with variable grain sizes of 250–710 μm at a range of normal stresses of 1–7.5 MPa and slip velocities of 1–50 mm/s under room-dry and wet conditions. We employed a high-speed infrared camera to monitor temperature fluctuations along the outer circumference of the ring-shaped gouge layer during sliding, utilizing a high-frequency frame rate of up to 1200 Hz with a spatial resolution of 25 μm to capture flash temperature occurring at asperity contacts. We show that flash temperature can be captured within the gouge layer in both room-dry and wet conditions with a peak value up to ~220°C and ~80°C, respectively. In addition, the flash temperature increases with increasing slip velocity and grain size, while decreasing at higher normal stress, which is likely associated with enhanced grain size reduction. More systematic experiments are required to fully quantify the flash temperatures and weakening, including measurement of local pore fluid pressure and property fluctuations from the background, as well as calibration of the camera, used to quantify the thermal emissivity of different materials.

4.1 Introduction

Characterizing temperature rise from frictional sliding is crucial to understanding the thermally activated mechanisms that cause faults to weaken during coseismic slip and associated earthquake rupture propagation (Rice, 2006). Several theoretical and experimental studies have proposed various dynamic weakening mechanisms, depending on fault rock composition and experimental conditions, to account for the reduction in friction coefficient seen when sliding velocities approach seismic slip rates ($V > 0.01$ m/s; see Di Toro et al., 2010, Niemeijer et al., 2012, and Tullis, 2015 for summary). Among these weakening mechanisms, flash heating at highly stressed asperity contacts is believed to be one of the major mechanisms causing dramatic weakening at the onset of rock-on-rock slip (e.g. Goldsby and Tullis, 2011; Kohli et al., 2011; Spagnuolo et al., 2015) and shearing of gouge materials (e.g. Yao et al., 2016a, b). So far, the inferred role of flash heating and weakening is generally based on predictions using a flash-heating model (Beeler et al., 2008; Brantut and Platt, 2017; Proctor et al., 2014; Rice, 2006; Yao et al., 2018) and/or the microstructural evidence of thermal softening (e.g. local melting) at asperity contact scales (e.g. Acosta et al., 2018). Recent studies using laboratory friction experiments by Saber (2017) and Barbery et al. (2021) have shown that surface temperature increases at contact points on sliding surfaces between Westerly granite blocks, under room-dry conditions, can be successfully captured by employing a high-speed infrared camera (a frame rate of 300 Hz). These authors documented that flash temperatures and stress distribution are highly heterogeneous at the rock-on-rock interface during seismic slip. In addition, no visible dynamic weakening was observed, even at flash temperatures up to 300°C, perhaps due to wear reducing local normal stress and increasing true contact area with slip. Currently, experimental constraints on flash temperatures in a sheared granular gouge layer are lacking. In particular, direct detection of thermal signals, from flash heating occurring within a shearing gouge layer, remains challenging due to difficulties with gouge confinement, the small scale of grain contact asperities (<<1 mm), and short contact lifetimes (ms).

In an attempt to make new progress, we developed an experimental setup, with a high-speed infrared camera, that allows us to acquire in-situ thermal images across the entire thickness of the gouge layer during rapid shearing under room-dry and wet conditions. In the present chapter, we aim to experimentally

characterize the dependence of peak flash temperature on normal stress, slip velocity, and grain size to understand better how flash heating is influenced by these variables, and to assess whether the results are consistent with the predictions of previous theoretical analyses (Rice, 2006; Proctor et al., 2014; Brantut and Platt, 2017).

4.2 Materials and methods

4.2.1 Starting materials

We used ASTM standard C778 Ottawa quartz sand obtained from the U.S. Silica Company (Ottawa, IL, USA) as starting materials. The materials contain a SiO_2 content of 99.7 wt%, minor quantities of Al_2O_3 (0.06 wt%), Fe_2O_3 (0.02 wt%), and TiO_2 (0.01 wt%). Scanning electron microscopy showed that most sand grains are well-rounded, with smooth surfaces characterized by pressure solution indentations and quartz overgrowths (Hangx and Brantut, 2019). We prepared four fractions of the sand with grain sizes of 250–300 μm, 300–425 μm, 425–500 μm, and 500–710 μm by double-sieving the material as received. We adopted the grain size of 425–500 μm as the reference grain size for most of the experiments. For each experiment, we used 35 grams of the Ottawa sand gouge, which results in an initial gouge thickness of ~4.5 mm after normal loading at 2.5 MPa (effective) normal stress and before shearing.

4.2.2 Rotary-shear friction experiments

We performed medium-velocity friction experiments, at Utrecht University, the Netherlands (Figure 4.1a; Korkolis, 2019), using a newly developed rotary shear apparatus (abbreviated as RAP) plus a high-speed infrared camera. We developed a gouge setup that allows us to confine gouge samples and pressurize the pore fluid within the simulated fault zone during rapid sliding (Figure 4.1b). The gouge layer is confined between two ring-shaped, steel pistons (100-mm external, 70-mm internal diameters), allowing loading in the axial direction. The piston faces are toothed, with the teeth spaced at 1 mm intervals (groove depth 1 mm) and oriented perpendicular to the direction of sliding. A brass outer ring and an inner ring were used to confine the gouge layer laterally to avoid gouge extrusion during shearing. Local pore fluid pressure changes during sliding were measured using two pressure transducers (10 MPa full range, with 0.01 MPa resolution and less than 10 ms response time) installed at opposite sides, and at identical radial position (centered at d=85 mm), in the bottom rotary piston

(Figure 4.1b). To detect thermal signals across the full gouge layer thickness, we installed a circular, transparent sapphire window (10 mm in diameter) in the outer confining ring (Figure 4.1c, d). The screw-in design of the window allows its position to be adjusted to be as close as possible to (in contact with) the gouge layer.
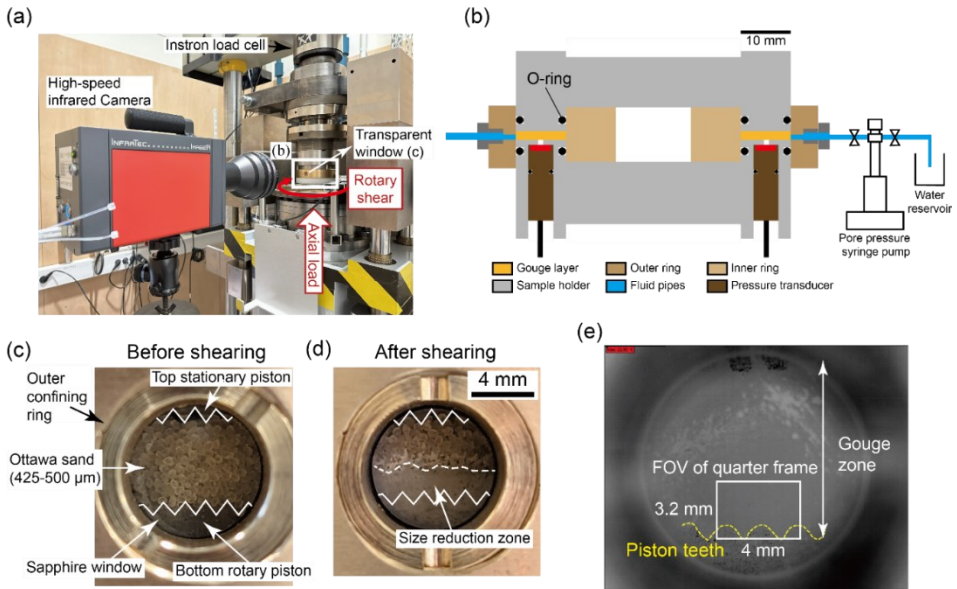
Figure 4.1: Experimental setup. (a) Photograph of the pressurized gouge setup installed in the Rotary-shear apparatuses (RAP) with the high-speed infrared camera. (b) Cross-section of the pressurized gouge setup. Pressure transducers are installed in the bottom rotary piston at ~2 mm distance from the gouge layer. (c) Photograph of the profile of the undeformed, room-dry Ottawa sand gouge layer, sandwiched between the pistons, and laterally confined by an outer brass ring with a transparent sapphire window. (d) Photograph of a deformed room-dry gouge layer showing a zone/layer of reduced grains. (e) Thermography of the gouge layer before sliding under a full-frame field of view (FOV) (16 mm × 12.8 mm). The white rectangle indicates the field of view (FOV: 4 mm × 3.2 mm) under quarter-frame analyses applied in all our tests.

Friction experiments were conducted on both room-dry and wet gouges at an applied normal stress σ_n of 1.0–7.5 MPa and a constant slip velocity V in the range 1–50 mm/s, reaching a total displacement of up to 750 mm (equivalent to ~2.8 of full rotations of the piston assembly). Grain size comminution was least in our experiments at the lower normal stresses and sliding velocities applied, so we chose a normal stress of 2.5 MPa and a slip velocity of 10 mm/s as ideal reference conditions at which flash heating could be resolved spatially. Before applying the normal load to the target value, wet gouges were prepared by saturating the sample with DI water using a syringe pump (ISCO pump; Figure

4.1b) through the pore fluid inlet port until water came out of the outlet drainage ports, without bubbles. All wet experiments were conducted under undrained conditions at initially atmospheric pore pressure conditions (i.e. 0.1 MPa) by closing the outlet ports. After the target normal stress was applied, we initiated shearing of the gouge sample, recording the thermal imaging at synchronized time. During the entire experiment, data on shear stress τ, normal stress σ_n, axial displacement, and velocity V, were obtained at a logging rate of 5 kHz. All the tests performed are listed in Table 4.1.

Table 4.1: *List of experiments and conditions with the average temperature increase ΔT_avg as well as the measured and predicted (using equation 4.1, section 4.3.4) flash temperatures T_max. The IR temperature range chosen for the room-dry and wet experiments is 60–200°C and 30–150°C, respectively. The number of flashes represents the number of flashes within the actual gouge zone. Predictions of flash temperature for wet conditions are not included.*

ID	σ_n (MPa)	Pore fluid	V (mm/s)	D (mm)	Grain size (mm)	Number of flashes	ΔT_{avg} (°C)	Measured T_{max} (°C)	Predicted T_{max} (°C)
Room-dry conditions									
r228	2.5	-	50	500	0.425-0.5	30	61.84	183.54	568.95
r229	2.5	-	25	750	0.425-0.5	31	55.87	222.60	408.17
r230*	2.5	-	10	750	0.425-0.5	23	48.42	137.72	265.50
r231	2.5	-	1	75	0.425-0.5	N/A	12.42	N/A	97.63
r232	2.5	-	5	600	0.425-0.5	23	38.82	124.25	193.59
r234	5	-	10	750	0.425-0.5	28	50.92	-	291.41
r235	1	-	10	400	0.425-0.5	27	36.44	123.96	228.63
r236	7.5	-	10	200	0.425-0.5	1	52.37	90.26	309.32
r237	2	-	10	750	0.425-0.5	15	49.68	221.98	251.46
r238	3	-	10	750	0.425-0.5	22	45	169.36	272.23
r239	7.5	-	50	450	0.425-0.5	1	73.24	101.34	666.94
r240	2.5	-	10	750	0.3-0.425	23	53.62	125.88	228.63
r241	2.5	-	10	750	0.25-0.3	2	52.69	119.03	202.98
r242	2.5	-	50	750	0.25-0.3	4	60.83	150.07	429.16
r245	2.5	-	10	750	0.5-0.71	30	53.33	222.60	297.51
Wet conditions									
r249	2.5	DI water	50	750	0.425-0.5	3	8.74	81.74	-
r251*	2.5	DI water	10	750	0.425-0.5	13	5.28	43.74	-
r254	5	DI water	10	750	0.425-0.5	27	4.69	158.40	-
r255	5	DI water	50	750	0.425-0.5	43	7.32	61.67	-
r256	7.5	DI water	10	750	0.425-0.5	15	5.22	85.42	-
r257	4	DI water	10	750	0.425-0.5	6	3.77	44.17	-
r258	6	DI water	10	750	0.425-0.5	4	3.18	38.40	-
r259	2.5	DI water	10	750	0.5-0.71	5	3.85	40.09	-
r260	2.5	DI water	10	750	0.25-0.3	N/A	3.49	N/A	-

Note. N/A denotes no visible flash temperature. The symbol "" indicates reference experiments for the room-dry and wet conditions. σ_n = the applied normal stress. V = the imposed slip velocity. D = the imposed total displacement.*

4.2.3 High-speed infrared thermal imaging of gouge profiles

We used an Infratec ImageIR 8300 hp infrared camera with a precision microscope lens M=1.0x and a working distance of 20 cm (Figure 4.1a) to provide the requirements for high-speed thermography. The combined setup has a detector format of 640×512 pixels and a wide range of IR frame capture rates from up to 355 Hz (a full frame window size) to up to 5000 Hz (a line measurement) with a spatial resolution down to 25 μm per pixel. All the infrared radiation (IR) signals acquired from the infrared camera were processed using IRBIS® 3.1 Infrared Thermographic Software (https://www.infratec.eu/thermography/thermographic-software/) to convert the digital IR signal data to thermographs (i.e. temperature distributions) with the user choice calibration (e.g. emission, absorption, and transmission). Currently, we took an emissivity of 1 (full reflection of IR from the object), an absorption coefficient of 0 (no attenuation of IR), and a transmission of 1 (full penetration of incident IR) as the inputs for the calibration of the IR signal to arrive at the target object temperature in the software. We have not yet taken the effect of the sapphire window and the presence of water on the IR signal into account in the present work. Due to the presence of the 1-mm thick sapphire window between the gouge layer and the microscope lens, the focus on the gouge layer was adjusted until the piston teeth were visible on the real-time thermograph (Figure 4.1e). During shearing of each experiment, we adopted a quarter-frame analysis of up to 1200 Hz (~0.83 ms) with a field of view (FOV) of 4 mm × 3.2 mm and a spatial resolution of 25 μm per pixel to capture thermographs that emerged from the FOV of the gouge shear zone. These mostly covered the bottom third of the gouge layer (i.e. rotating side) plus a small portion of the piston teeth (Figure 4.1c, e). For experiments conducted at the chosen reference conditions (ID r230, r251), a sequence of at least 90000 thermographs (75 seconds × 1200 Hz) was acquired from the FOV throughout the experiment. The IR camera is equipped with a neutral density filter and is capable of measurements over several pre-set, calibrated temperature ranges with multiple integration times. We took the factory-calibrated settings for two different IR temperature ranges of 60–200°C and 30–150°C, for room-dry and wet test conditions, respectively. After each experiment, we exported the maximum temperatures and the corresponding location (X and Y coordinates), as well as the average temperatures over the FOV of every acquired thermograph, to investigate the temporal and spatial evolution of peak temperatures with displacement.

4.3 Preliminary results

4.3.1 Mechanical behavior

Figure 4.2 shows the evolution of apparent friction μ_{app} (= shear stress τ / normal stress σ_n) against displacement obtained for the room-dry and wet gouges at the variable slip velocities, normal stresses, and initial grain sizes shown. For the room-dry gouges (Figure 4.2a, c, e), the frictional evolution is generally similar, regardless of slip velocity, normal stress, and grain size. Specifically, μ_{app} firstly overcomes a "static" peak friction μ_s of ~0.9, soon after slip initiation, subsequently rapidly drops to a constant (dynamic) level of ~0.65 within ~0.3 m displacement. This is followed by minor displacement weakening beyond the first full rotation (~267 mm displacement) reaching a near-constant value of ~ 0.6 during the late stage of slip. The overall level of friction systematically decreases with increasing normal stress (Figure 4.2c), with the exception of the experiment conducted at 5 MPa normal stress (ID r234), which shows anomalous behavior in the form of marked displacement strengthening after one rotation, probably due to jamming of material between the piston and the confining ring.

For the wet gouges (Figure 4.2b, d, f, and 4.3), the initial frictional behavior is similar to the room-dry gouges, featuring a peak μ_{app} value μ_s of ~0.9 followed by a sharp friction drop. Different levels of slip weakening occur depending on the slip velocity, normal stress, and grain size. At a normal stress of 2.5 MPa, the wet gouge subjected to a slip velocity of 50 mm/s showed increased slip-weakening towards a lower dynamic friction of ~0.45, compared with the behavior seen at the lower slip velocity of 10 mm/s (Figure 4.2b) or in dry samples. At a slip velocity of 10 mm/s, the wet gouges significantly slip-weaken only when the normal stress is equal to or greater than 4 MPa. Under these conditions, the onset of weakening starts earlier and the dynamic friction level decreases with increasing normal stress (Figure 4.2d). Increased slip weakening is also observed, compared with the reference test, when the grain size is either greater or smaller than the reference value, without any systematic correlation between grain size and the level of dynamic friction (Figure 4.2f).
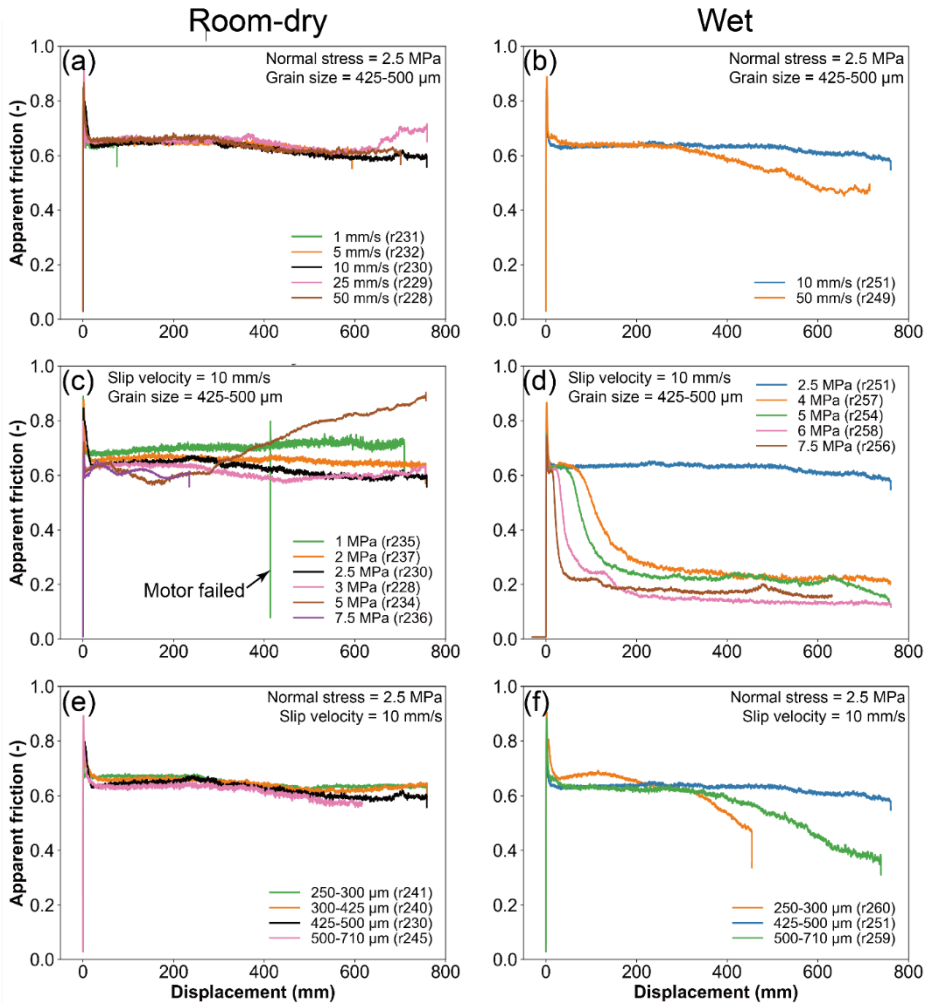
Figure 4.2: *Evolution of apparent friction μ$_{app}$ as a function of displacement for room-dry (a, c, e) and wet gouges (b, d, f) under variable slip velocities, normal stresses, and initial grain sizes. The sudden friction drop observed in (c), the blue curve, is the result of re-shear due to a motor failure.*

Fluid pressure increases were always observed in the wet experiments at the displacement at which weakening starts, i.e. beyond the peak static friction – see Figure 4.3. This shows that the fluid pressure increase has a positive correlation with applied normal stress, since the maximum fluid pressure increased from ~3.5 MPa, at a normal stress of 4 MPa, to ~7 MPa at a normal stress of 7.5 MPa. In addition, each experiment shows a sudden gouge dilatation during the attainment of peak friction, followed by ongoing gouge compaction (Figure 4.3). The

amount of compaction shows the same trend with normal stress as fluid pressure, i.e. more compaction occurs in experiments with higher normal stress.
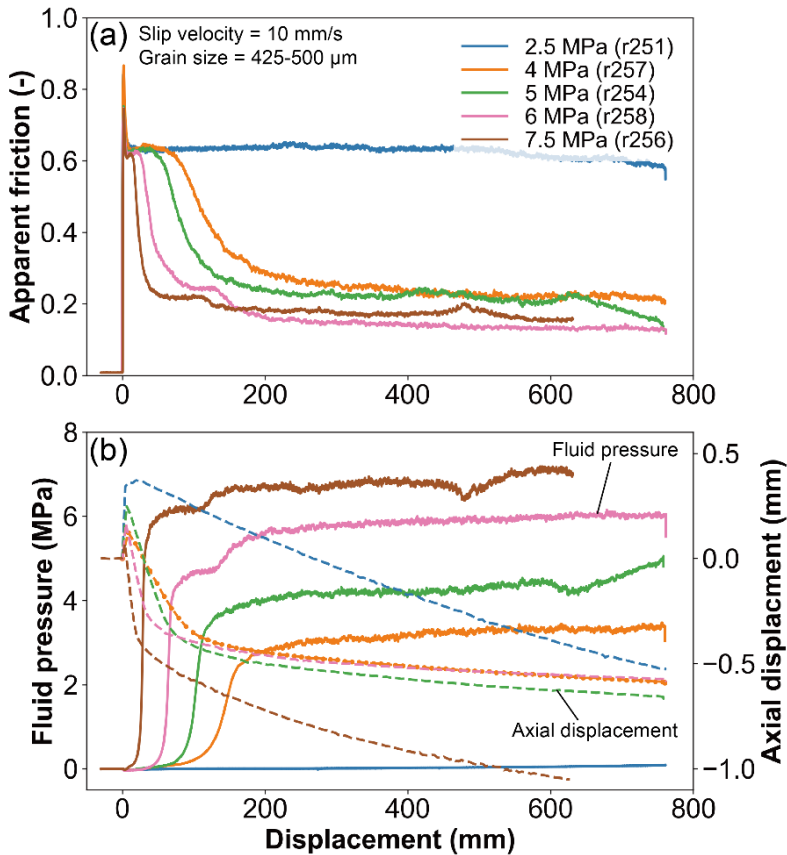
Figure 4.3: *Evolution of a) apparent friction and b) pore fluid pressure and axial displacement, as a function of shear displacement for the wet experiments at a slip velocity of 10 mm/s, using an initial grain size of 425–500 μm. Dashed curves in (b) represent axial displacement data whereby positive values indicate dilatation and negative values indicate compaction. Solid curves in (b) represent pore fluid pressure in these undrained tests.*

4.3.2 Evolution of maximum temperature rise with displacement

The maximum temperature obtained from each thermal image is plotted as a function of displacement in Figures 4.4, 4.5, and 4.6. Generally, multiple temperature peaks (i.e. spikes) with a duration of one frame (~0.83 ms) can be observed, representing flashes in most experiments with the largest peak temperatures being ~220°C and ~100°C in the room-dry and wet gouges, respectively. For most of the experiments, the maximum temperatures in the FOV showed a rapid increase after the slip initiation, with a faster rise with increasing

velocity, but then soon reached a plateau (at a base level of ~25–40°C), which becomes higher at higher velocity (Figure 4.4). The presence of a temperature plateau is due to the settings of the IR temperature measurement range (60–200°C and 30–150°C for room-dry and wet experiments, respectively); below the lower bound of the range, temperature cannot be accurately determined or displayed. Another thing that should be noted is that Figures 4.4, 4.5, and 4.6 include all thermal flashes that occurred within the full FOV throughout the entire slip period of each experiment. Thus, the observed flashes might not only result from the sliding between grain-grain contacts but also from sliding between the grains and the window as well as between the grains and the piston, due to gouge extrusion with or grain fragments jamming between the sapphire window and the piston.

Nonetheless, these preliminary results still provide insight into systematic differences in the evolution of temperature and the magnitude of the peak temperatures. Overall, we observed that peak temperature rises are significantly reduced in the presence of water, and the peak temperature systematically increases with increasing slip velocity (Figure 4.4). In both the room-dry and wet gouges, the number of flashes becomes much less and their magnitudes become much lower at the lowest applied slip velocity of 1 mm/s, compared with higher values. In the dry experiments, the magnitude of the flashes appears to be the greatest (up to 200°C) at 2.5 MPa, while becoming less significant with both decreasing and increasing normal stress (Figure 4.5a). The dependence of peak temperature on normal stress is not visible in the wet experiments (Figure 4.5b). Note that the dry experiment (ID r236) at 7.5 MPa normal stress was terminated soon (~3 seconds) after slip initiation (Figure 4.5a) because of sounds indicating unwanted abrasion of the outer ring. For the range of grain sizes explored, the variations in the magnitudes of flashes are similar in both the dry and wet tests, and are difficult to quantify based on this preliminary data (Figure 4.6).
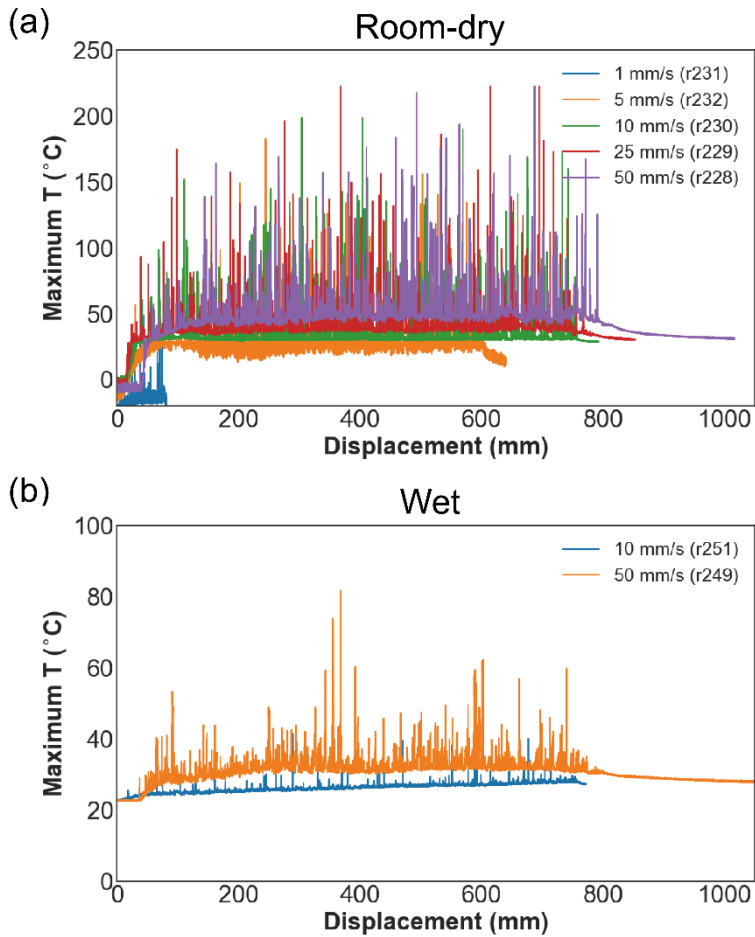
Figure 4.4: *Evolution of maximum temperature within the FOV (4 mm × 3.2 mm) as a function of displacement for the room-dry gouges (a) and the wet gouges (b) tested at a normal stress of 2.5 MPa and different slip velocities.*
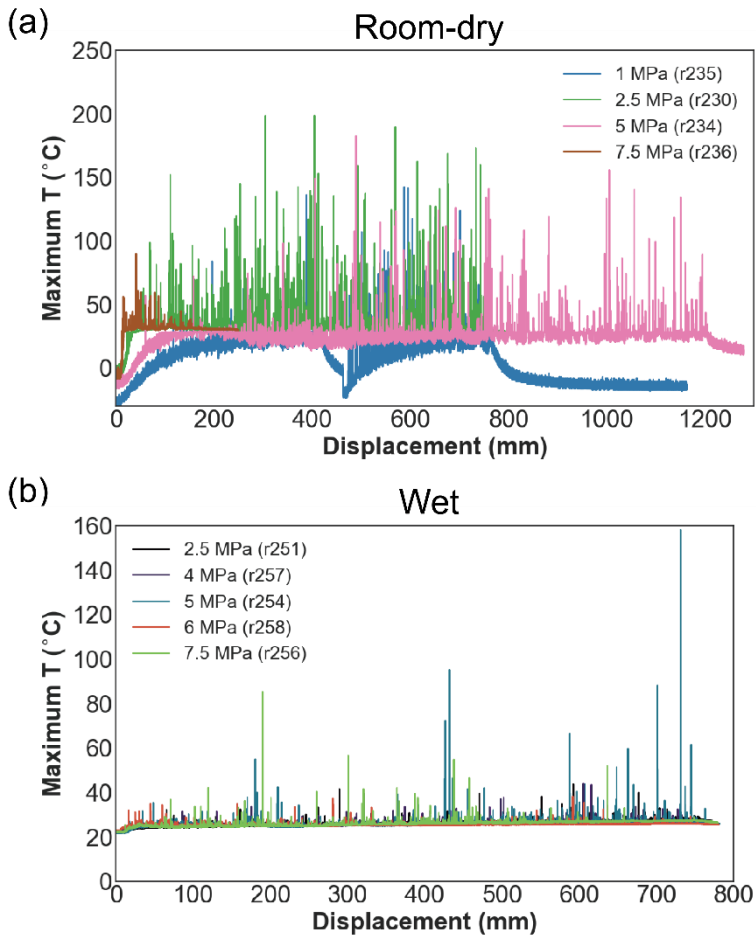
Figure 4.5: *Evolution of maximum temperature within the FOV (4 mm × 3.2 mm) as a function of displacement for the room-dry gouges (a) and the wet gouges (b) tested at a slip velocity of 10 mm/s and different normal stresses.*
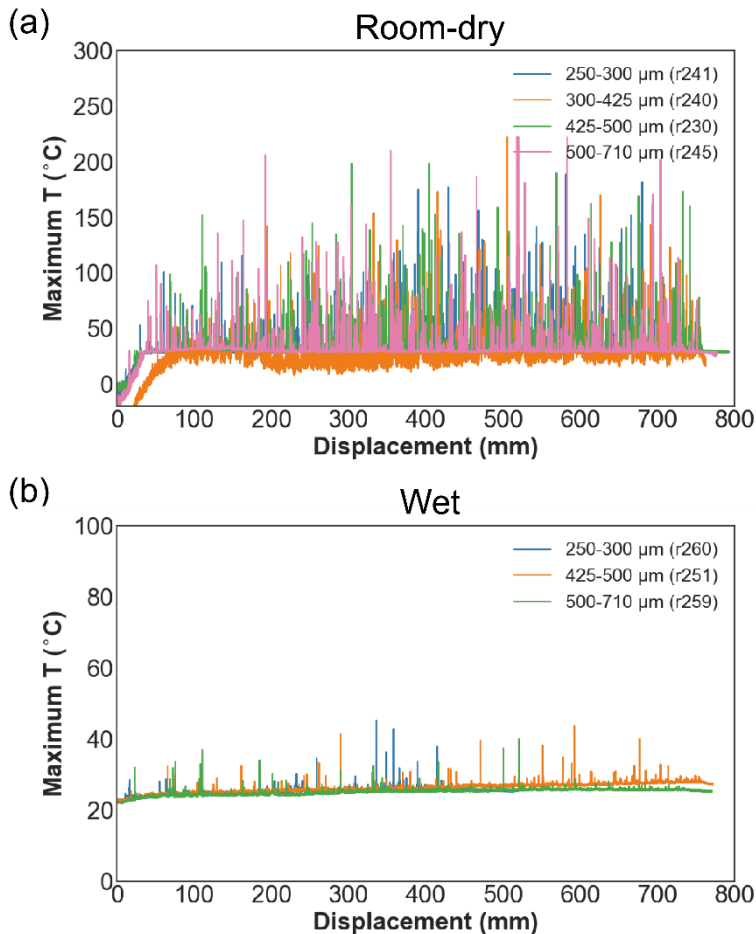
Figure 4.6: *Evolution of maximum temperature within the FOV (4 mm × 3.2 mm) as a function of displacement for the room-dry gouges (a) and the wet gouges (b) tested at a normal stress of 2.5 MPa and a slip velocity of 10 mm/s, with different initial grain sizes.*

4.3.3 Spatial and temporal distributions of flashes

We located the position of the thermal flashes to see if they occurred within the actual gouge zone, as opposed to the portion of the FOV below the teeth tops. Figure 4.7 presents the spatial and temporal distributions of the flashes, here taken as those frames (duration ~0.83 ms) with temperature rise ΔT larger than 50°C and 4°C, for the reference room-dry and wet gouges, respectively. These results exclude the flashes with a position at and below the horizontal level (i.e. Y position) of the teeth tops on the bottom rotary piston (dashed lines), which shifted upwards with progressive slip as indicated by the axial displacement data (i.e. compaction) and by initial through-window observations (Figure 4.1c, d).

This is to rule out the flashes that potentially resulted from sliding between the grains and the piston. After filtering out data from below the chosen moving datum, we still observed many flashes, which we infer occurred within the main gouge zone. The peak temperature and the number of these flashes in each experiment are summarized in Table 4.1. Generally, in terms of spatial distribution, flashes tend to be concentrated within a narrow zone (~500 μm thick) under room-dry conditions (Figure 4.7a, b) whereas flashes are more separated under wet conditions.
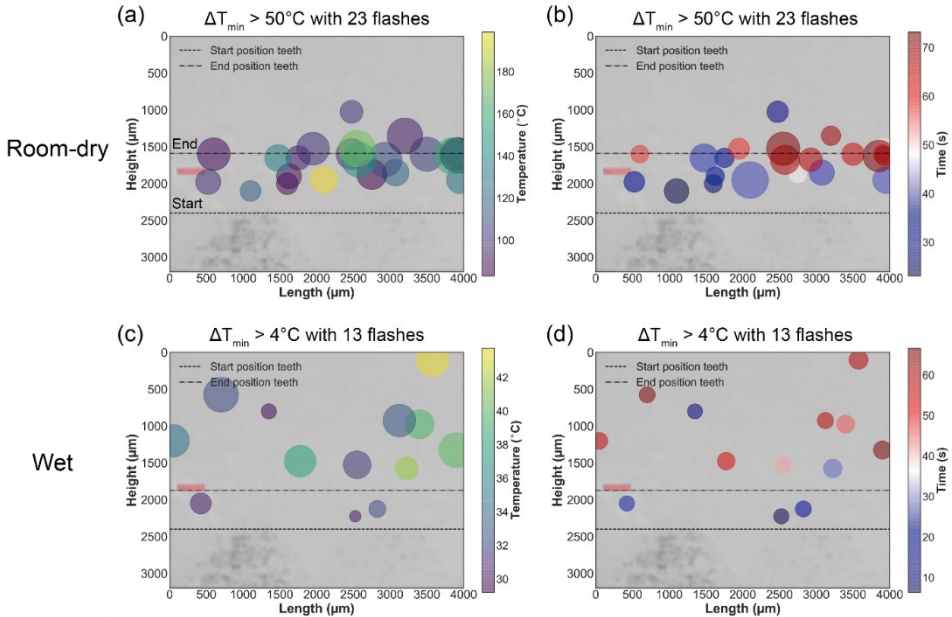
Figure 4.7: *Spatial and temporal distribution of flashes within the main gouge zone with a minimum temperature rise ΔT (relative to the bulk maximum temperature) larger than 50°C and 4°C for the reference experiments of the room-dry (a and b; ID r230 with 23 flashes) and wet gouges (c and d; ID r251 with 13 flashes), respectively. Tests performed at 2.5 MPa normal stress and 10 mm/s sliding velocity. Larger dots indicate later occurrence (a,c) or higher temperature rise (b,d). The Start and End positions delineate the initial and final positions of the teeth tops in the lower piston, which moved upwards during each experiment due to sample compaction.*

4.3.4 Estimation of flash temperature

Based on the flash-weakening model (e.g. Rice, 2006; Beeler et al., 2008; Proctor et al., 2014; Yao et al., 2018), the flash temperature on an asperity (grain) contact (T_a) within a gouge layer can be expressed as:

$$T_a = T_{bulk} + \frac{\tau_c}{\rho c}\sqrt{\frac{(V/N_a)D_a}{\pi \alpha_{th}}} \tag{4.113}$$

Here, T_{bulk} is the initial bulk temperature of the fault zone, τ_c is the contact shear strength, ρ is the gouge density, and c is the specific heat capacity of the gouge, N_a is the number of asperity contacts sharing the total slip velocity V, D_a is the diameter of asperity contact, and $\alpha_{th} = K/\rho c$ is the thermal diffusivity of the gouge, where K is the thermal conductivity. For a first-order estimate, the latent heat of possible reaction (e.g. fluid evaporation) is not considered in the equation. Here we only applied the model to the dry samples. For the dry Ottawa quartz sand with a grain size of 425–500 μm, we took τ_c as ~9–12 GPa (Goldsby and Tullis, 2011), ρ as 2650 kg/m³, c as 730 J/kgK and α_{th} as ~1.5 × 10^{-6} m²/s. Considering the thickness of the shear zone in dry gouges (~4 mm or ~16–20 grains), where ~50% of the gouge layer was involved in shearing (Figure 4.1d), this results in N_a values ranging from ~8 to 10, which is within a reasonable range, comparable to previous studies (4–10 Yao et al., 2018; 10–20 Rice, 2006; 4–13 Proctor et al., 2014; 10 Chen et al., 2023). For D_a, we assumed two different particle packings (hexagonal packing vs. centered cubic packing) to estimate the range of D_a between two spherical grains, assuming Hertzian contact mechanics. Based on the elastic moduli of Ottawa sand (e.g. Erdoğan et al., 2017), for the grain size of 450–500 μm, we adopt average values of D_a as 13, 18, 22, and 25 μm at normal stresses of 1, 2.5, 5, 7.5 MPa, respectively. At a normal stress of 2.5 MPa, we take D_a to be 10, 13, 17, and 23 μm for grain sizes of 250–300 μm, 300–425 μm, 450–500 μm, and 500–710 μm, respectively.

Figure 4.8 shows the comparison of the maximum flash temperature obtained from the model prediction and from the measurements for the dry experiments. Overall, the measured values are lower than the predicted ones. Predicted flash temperature increases with increasing slip velocity, normal stress, and grain size, following equation 4.1, but this increasing trend is less (or not) visible in the measurement. The discrepancy between the predicted and measured flash temperature tends to increase with slip velocity and normal stress (Figure 4.8a, b) but remains relatively consistent with variable grain sizes (Figure 4.8c).
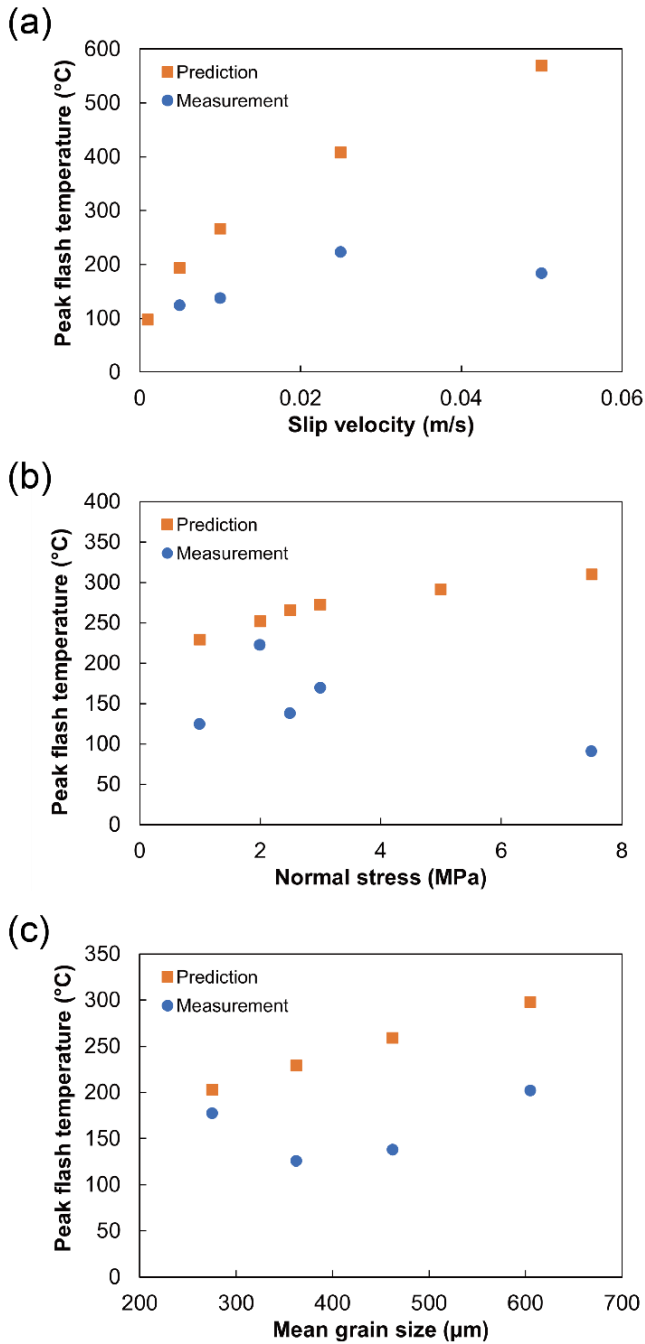
Figure 4.8: *Comparison of the peak flash temperatures between the prediction based on the flash weakening model (Rice, 2006) and the infrared measurement with different slip velocities (a), normal stresses (b), and grain sizes (c). The measured peak flash temperature at a slip velocity of 1 mm/s is not shown in (a) because the overall measured temperatures are lower than the selected temperature range (60–200°C).*

4.4 Discussion

4.4.1 Robustness of the flash temperature measurement

In the literature, flash heating is suggested to occur within a short contact lifetime (ms), depending on the scale of asperity contact (typically μm) as well as the sliding velocity at the contact (Rice, 2006). The current setting of the infrared camera can accurately measure thermal information with spatial and temporal resolutions of 25 μm and ~0.83 ms, respectively. This means that any short-term IR signal cannot be detected if its occurrence time is shorter than ~0.83 ms and that the measured temperature might be underestimated compared to the actual value if the contact size is smaller than 25 μm (e.g. Madding et al., 2007). Based on our measurement of the maximum temperature within the FOV, it is shown that multiple peak temperatures (i.e. flashes) with extremely short duration were recorded from the observed region of both the room-dry and wet gouges when the imposed slip velocity is higher than 1 mm/s (Figure 4.4). This suggests that the duration of these flashes is at least (or around) 0.83 ms.

Figure 4.9 shows the contact lifetime against the contact size D_a, assuming a specific grain size and slip velocity. The contact size D_a is estimated following the method described in section 4.3.4. The contact lifetime is then obtained from the ratio of D_a to the contact sliding velocity (= imposed slip velocity V / number of asperity contacts N_a). Based on the calculated contact size of the asperity D_a (10–25 μm) and the assumed number of asperity contacts N_a (10), the contact lifetime of the asperity for our samples and experimental conditions should approximately range from 10–25 ms to 0.2–0.5 ms at the imposed sliding velocity of 1 mm/s to 50 mm/s, respectively. These ranges lie around the limit of the temporal resolution of the camera, though the contact lifetime for V larger than 5 mm/s appears to be shorter than the duration of one frame, being strongly controlled by the estimated values of the D_a and N_a. This implies that the measured flashes likely resulted from flash heating between grains. Here, we should note that most of the calculated asperity sizes are smaller than the spatial resolution of the camera, suggesting that the actual temperature might be higher than the measurement. Moreover, if the flashes have a shorter duration than the frame duration, their actual temperature was also likely higher than the measured values.
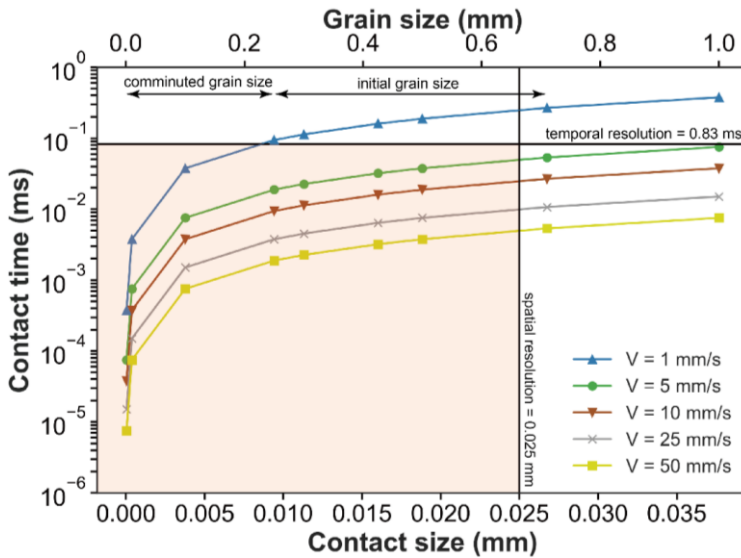
Figure 4.9: *Contact lifetime against contact size D_a for flashes for a specific grain size and slip velocity. The D_a is estimated following the method described in section 4.3.4. N_a is assumed to be 10. The black horizontal line gives a temporal resolution of 0.83 ms, and the vertical line has a spatial resolution of 0.025 mm. The light red rectangle region represents the region for which the IR camera with the current settings does not have sufficient spatial and/or temporal resolution.*

After filtering out the flashes occurring within the region of the rotating piston, we could still observe a few tens of flashes within the actual gouge zones under both room-dry and wet conditions (Figure 4.7; Table 4.1). Among these flashes, we cannot exclude the possibility that some flashes result from the sliding of a grain against the window due to the lateral force and the dragging shear force acting on the grains that are attached to the window. Thus, these flashes might exhibit different characteristics in terms of shape in the thermographs due to the potential of scraping of the grain along the sapphire window. Figure 4.10 shows three different characteristics of flashes that can be observed from the thermographs. Generally, most of the flashes have a circular shape with the highest temperature at the center which gradually decreases towards the boundary (Figure 4.10a, b). Some of these flashes are located within the interior of grains (Figure 4.9a), where the individual grain outline can be identified, suggesting the flashes might result from the grain-to-window sliding. For other flashes, it is difficult to identify their position relative to the solid grains (Figure 4.10b). Yet another type of flash displays a tail shape (Figure 4.10c) which may indicate the existence of grain-to-window flash. With the current data, it is difficult to distinguish whether the flashes were actually generated at grain-to-grain contacts
156

or whether they were mainly related to grain-to-window sliding. To avoid the grain-to-window flashes, improvements in the experimental set-up are required, such as using a curved window to help ensure that the grains can pass along the window without creating temperature flashes. Another possibility might be to include a low-friction coating on the window.
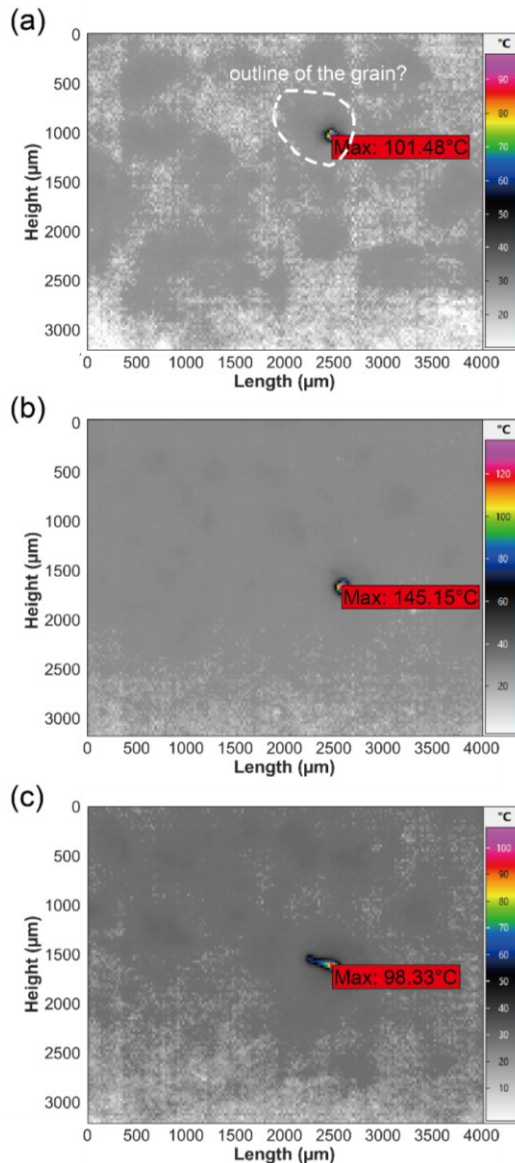
Figure 4.10: *Thermographs with a flash identified in the actual gouge zone, as obtained from the reference room-dry experiment (r230) at displacements of 293 mm (a), 676 mm (b), and 526 mm (c).*

157

Comparing our measurements to the predictions, we have shown that the measured flash temperatures are overall lower than predicted and the discrepancies between them become larger with increasing normal stress and slip velocity (Figure 4.8). As discussed above, both the limited spatial and temporal resolution of the IR camera may explain the observed low values of the measured flash temperatures as compared to the predictions. We argue that the increasing discrepancies could be related to the process of grain size reduction during frictional sliding, and/or possibly the setting of the IR temperature ranges. As can be seen in the measured particle size distribution of the deformed sample (see Figure S4.1), abundant fine grains were generated during the experiment. The initial grain size (425–500 μm) is reduced to a minimum value of ~50 nm, with the largest proportion of grains smaller than the starting material having a size of 10 μm. In addition, the proportions of fine grains are systematically larger at a higher normal stress and slip velocity. This indicates that high normal stress and slip velocity increase the degree of grain size reduction, which leads to a decrease in asperity size D_a and a possible increase in N_a (at a constant thickness of the localized zone). This would further affect our ability to spatially and temporally (the contact exists for a shorter time because it is smaller, see Figure 4.9) resolve the flash temperatures. However, if grain size reduction is one of the reasons causing the increasing variations, this implies that the measured flash temperatures should decrease due to the limitation of the spatial resolution but this is not observed. To characterize the flash temperature distribution in the gouge layer robustly, multiple temperature ranges or a combined temperature range should be utilized in multiple repeat experiments (Barbery et al., 2021). Despite all this, our preliminary results still show some dependence of flash temperature on slip velocity and grain size.

4.4.2 Mechanical behaviors under room-dry and wet conditions

We observed that the measured average temperature and flash temperatures can reach up to ~73°C and ~220°C, respectively, under room-dry conditions (Table 4.1). Despite high flash temperatures, suggesting the high effectiveness of flash heating, the room-dry gouges do not show any significant weakening which remains at a constant friction level of 0.6 (typical quasi-steady friction for quartz; as also shown in the result of Chapter 2; Byerlee, 1978). This might be explained by the relatively low measured and predicted flash temperatures as compared to the softening (i.e. melting) temperature of quartz (~1720°C, Spray, 1992).

By contrast, the water-saturated gouges reveal slip weakening accompanied by fluid pressure increase at relatively high normal stresses (>2.5 MPa) and slip velocities (>10 mm/s), while the average and flash temperature rises are only up to ~9°C and ~80°C, respectively (Figure 4.4, 4.5, and 4.6; Table 4.1). In addition, we show that the rapid fluid pressure increases are always accompanied by rapid gouge compaction (Figure 4.3). Firstly, this suggests that temperature increase can be strongly limited by the presence of water, though the effect of sorption by water on the IR signal has not been considered in the data processing. Secondly, the above temperature increases of 9°C and 80° C are insufficient to account for the observed fluid pressure increase (3.5–7 MPa). We expect the bulk fluid pressure increase to be less than 1 MPa, taking a reasonable range for the thermal pressurization factor Λ (e.g. 0.075–0.11 MPa/°C for quartz-rich gouges, Hunfeld et al., 2021 – see also Chapters 5 and 6 of this thesis). Third, the correlation between the fluid pressure increases and the sample compaction suggests that the compaction-driven pore fluid pressurization (Faulkner et al., 2018; Oohashi et al., 2015) is active in our sample during shearing. This is likely because we did not impose a low-velocity pre-slip conditioning stage on the gouge layer before initiating fast shearing. Therefore, the gouge layer would experience significant grain size reduction and compaction during initial sliding, which leads to a rapid fluid pressure increase. On this basis, we suggest that the mechanism causing slip weakening in the wet samples is most likely associated with compaction-induced pore fluid pressurization (compaction softening; Faulkner et al., 2018; Oohashi et al., 2015), which is supported by the data shown in Figure 4.3. Compaction softening is negligible in dry experiments due to the absence of water in the gouge layer.

At the same time, however, noting that we did not correct for IR sorption by water, other candidate mechanisms related to the presence of water, such as thermomechanical pore fluid pressurization (Rice, 2006; Badt et al., 2020), flash pressurization resulting from local thermal pressurization at grain contacts induced by flash heating (e.g. Chen et al., 2023; Yao et al., 2018), and/or the water/vapor phase transition (e.g. Chen et al., 2017) cannot be completely excluded. Silica-gel lubrication due to amorphization of silica and gel formation via shearing and comminution in the presence of moisture (Di Toro et al., 2004; Goldsby and Tullis, 2002) might be another possible candidate for the dynamic weakening seen in fast shearing of wet quartz materials. To test these hypotheses,

we need to ensure the gouge sample is well-compacted before the initiation of a high slip velocity to prevent significant compaction during the experiment. This is typically achieved by applying a conditioning stage (i.e. shear at low slip velocity) to the gouge layer. However, this was intentionally not included in the current study because the initial grain size reduction and associated comminution products would limit thermal radiation from grain contacts. In addition, thermal flashes would become difficult to measure due to the shorter asperity contact lifetime. For silica-gel lubrication, microstructural investigations on the deformed quartz samples are needed. Identifying the controlling weakening mechanisms in a fluid-saturated gouge layer at seismic slip rates is further investigated in Chapters 5 and 6.

4.5 Conclusions

To conclude, the important findings in the present work are as follows:

1. We can successfully monitor and quantify flash heating with instantaneous temperature rises occurring in an experimental fault gouge under room-dry and wet conditions.

2. The presence of pore water likely limits flash temperature rise, though the extent of the effect is unclear due to uncertainties in the extent of IR absorption of flash thermal signatures by the water phase.

3. Flash heating can be effective in dry gouge at a medium velocity (5 cm/s) but is insufficient to cause dynamic slip weakening in a dry gouge-filled fault when the flash temperature is insufficiently high to reach the softening temperature of the gouge grains.

4. The slip weakening effects that we observed in our wet experiments but not in dry tests are best explained by compaction softening, though a contribution from thermal pressurization at some scale cannot be eliminated.

5. We have experimentally demonstrated that the flash temperature depends on slip velocity and grain size, to some extent, in broadly agreement with theoretical predictions.

4.6 Suggestions for future work

Here, we list some suggestions for future work to further improve our understanding of flash heating in a sheared granular (gouge) layer on the basis of the current results:

We suggest:

1. Calibration of infrared camera (thermal emissivity) for different materials (quartz and feldspar) and pore fluid (water or brine).
2. Testing multiple IR temperature ranges.
3. Using a normal high-speed camera to measure sliding velocity at grain-to-grain contacts and observe grain size reduction.
4. Testing the window with a curved shape to avoid particle dragging along the window surface due to strong lateral force.
5. Investigate the dependence of peak flash temperature on particle parameters such as grain shape (round vs. angular), grain roughness, as well as different background fluid pressures and pore fluids.

Supplementary information
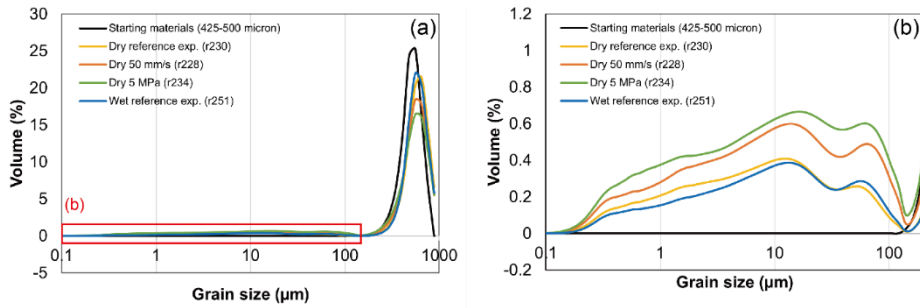
Figure S4.1: *Particle size distribution of the starting materials (425-500 μm Ottawa sand gouge) and the deformed samples with the same initial grain size under different conditions, plotted as volume percentage against grain size.*

Chapter 5

**Effect of pore fluid properties
on dynamic slip in fault gouges derived
from the Groningen gas reservoir**

Chien-Cheng Hung, André R. Niemeijer
To be submitted

Abstract

The slip behavior of faults is significantly influenced by the thermal and hydraulic properties of pore fluids within the fault core, as thermal pressurization resulting from frictional heating is controlled by these parameters. Previous seismic slip-pulse experiments have demonstrated significant weakening of water-saturated faults, containing gouges prepared from the Groningen gas reservoir sandstone (Chen et al., 2023; Hunfeld et al., 2021). However, it is important to note that the in-situ pore fluid within the gas reservoir is more complex, consisting of brine or a mixture of brine and gas (mostly methane + nitrogen), each with different viscosity η and thermal pressurization factor Λ. To investigate the potential slip behavior of faults in the gas reservoir, we conducted medium-velocity (5 cm/s) rotary-shear friction experiments on simulated reservoir (Slochteren sandstone) gouges, using four different pore fluids (DI water, in-situ brine, 1 cSt, and 5 cSt silicone oil), under various drained and undrained fluid pressure conditions. We compare our experimental observations with the slip-on-plane model derived by Rice (2006). Our results highlight that thermal pressurization (TP) is the primary weakening mechanism for all investigated fluid types, with brine-saturated gouges showing the least effective TP. Additionally, experiments with relatively high fluid viscosity reveal a smaller degree of grain size reduction while generating higher temperatures. We find that the levels of the predicted stress drop and temperature rise become comparable to the experimental observations when we consider potential changes in the permeability of the gouge layer for different pore fluids. Our findings contribute valuable insights for refinement of slip-weakening parameters within rupture models, leading to better constraints on modeling maximum moment magnitude of future induced earthquakes.

5.1 Introduction

Fluids within tectonically active fault zones, and within faults subject to induced loading, play a crucial role in regulating fault slip behavior, from earthquake nucleation to propagation to arrest (Lachenbruch, 1980; Rice, 1992, 2006; Sibson, 1973). During natural seismic slip events, the dominant dynamic weakening mechanism is expected to be thermal pressurization (hereafter TP) of pore fluids, driven by frictional heating. This concept has been supported by theoretical models (e.g. Brantut and Platt, 2017; Lachenbruch, 1980) and experimental studies (e.g. Badt et al., 2020). However, previous research primarily focused on water as the pore fluid, whereas fluids within fault zones are more diverse, featuring variable compositions (e.g. gas, brine), rheological properties, and physical states. Notably, fluids with distinct thermal characteristics (e.g. expansivity) and hydraulic properties (e.g. viscosity, compressibility) may further influence TP effectiveness (Rice 2006). Understanding how pore fluid properties impact TP and, consequently, the evolution of dynamic friction, is essential for gaining deeper insights into fault zone mechanical behavior and for improving geomechanical rupture models (e.g. Buijze et al., 2019). This knowledge aids in assessing the potential for both natural and induced seismicity and associated seismic hazard.

Numerous authors have conducted high-velocity friction experiments on low-permeability experimental fault zones under pressurized pore fluid conditions. These experiments involved either sliding of bare-rock surfaces (e.g. Feng et al., 2023; Gomila et al., 2021; Violay et al., 2013, 2014, 2015, 2019; Yao et al., 2023) or shearing of mm-thick simulated fault gouge layers (e.g. Boulton et al., 2017; Chen et al., 2023; Hunfeld et al., 2021; Kuo et al., 2021, 2022; Wang et al., 2023; Yao et al., 2018). Across different lithologies, these studies have consistently reported the effectiveness of TP at scales ranging from the bulk shear zone to grain-to-grain asperity contacts. TP was attributed to temperature rises caused by frictional heating (or flash heating) and was put forward to explain the observed dynamic friction drop with displacement. However, most such investigations have been limited to pure water as pore fluid. In contrast, Cornelio et al. (2019) conducted friction experiments on bare rock surfaces of granite and marble, employing different viscosity pore fluids, and illustrated that fluid viscosity can have a significant impact on the mechanical behavior of a cohesive fault zone. They demonstrated that both static and dynamic friction decrease with

increasing fluid viscosity, proposing elastohydrodynamic lubrication (EHDL; Brodsky and Kanamori, 2001) as the controlling weakening mechanism. EHDL describes a phenomenon of fluid overpressure induced by the shearing of a thin viscous fluid film between two subparallel and rough surfaces, and has been invoked to explain dramatic weakening of fluid-infiltrated bare-rock faults during earthquake slip. Whether EHDL can occur, depends on the Sommerfeld number $S = \frac{6\eta V L}{(H_0)^2 \sigma_{eff}}$, where η is the fluid's dynamic viscosity at the estimated mean temperature of the slipping zone, V is the slip rate, L is the characteristic length over which the fluid pressure changes (related to the wavelength of the asperities), H_0 is the initial average gap between the asperities (related to the height of the asperities), and σ_{eff} is the effective normal stress. S values > 1 (Cornelio et al., 2019) suggest that normal stress starts to be supported by interstitial fluid or, in other words, EHDL is effective in fault weakening. However, this phenomenon might become more complicated (or less significant) in a gouge-filled fault because the gouge and pore fluid mixture would contribute different dynamic viscosity during shearing, and the contact sliding velocity V would decrease, considering the increased number of asperity contacts contributing to the total velocity. In addition, bulk TP could become effective in gouges, due to their low permeability (e.g. Aretusini et al., 2021), or even in a relatively permeable fault following ongoing wear-induced sealing (e.g. Yao et al., 2023). So far, EHDL has not been reported in friction experiments on fault gouges and might not be active in a saturated gouge-filled fault during fast sliding. Thus, the influence of fluid viscosity and related fluid transport properties on the mechanical behavior of fluid-saturated, gouge-filled faults remains poorly understood – despite the variation in fluid properties that may occur during natural seismic cycles (i.e. through fluid-rock interactions, e.g. Miller, 2013) and in the context of injection-induced seismicity (e.g. during wastewater injection, or geothermal energy operations).

Here, we investigate how the slip behavior of wet fault gouge, prepared from the Groningen gas reservoir sandstone (Netherlands), changes with variable thermal (i.e. expansivity) and hydraulic (i.e. viscosity, compressibility) properties of the pore fluid. This was achieved utilizing DI water (viscosity 1 cSt), in-situ brine (viscosity ~1.4 cSt), and silicone oil (with viscosities of 1 and 5 cSt) as pore fluids, under undrained boundary conditions suitable for activating TP. Previous

friction experiments on simulated Groningen gas field gouges showed that water-saturated faults weaken significantly in a short seismic slip pulse (Chen et al., 2023; Hunfeld et al., 2021). The results of the present work are intended to provide better constraints on the level of dynamic friction associated with the induced earthquakes occurring in the Groningen gas field, accounting for the more realistic pore fluids used.

5.2 Methods

5.2.1 Starting materials

We used crushed Slochteren sandstone obtained from the Groningen gas field, as the starting material (courtesy of the field operator, the Nederlandse Aardolie Maatschappij BV: NAM). Sandstone cores from the Stedum 1 (SDM-1) borehole, extracted from both above and below the gas-water contact (GWC, at a depth of ~2980 m below the surface during drilling), were crushed into a powdered form using a jaw crusher. As noted in Chapter 2, the resulting powder, derived from the core below the GWC, may contain some salts because the high-salinity brine present in the core upon recovery resulted in salt precipitation in the pore space during core storage. This resulting mixed powder was employed as the starting material to simulate the fine-grained gouge product typically found within the principal slip zones of natural fault zones (Chester and Chester, 1998; Sibson, 1986). The crushed materials have a particle size distribution with a mean grain size of ~25 μm, and a maximum grain size of up to ~ 200 μm with approximately 80 vol% of grains being smaller than 50 μm. The mineral composition of the Slochteren sandstone gouge (SSG) consists of ~75 wt% quartz, ~12 wt% feldspar, minor amounts of clay minerals (~5 wt%, kaolinite, and phengite), carbonates (~5 wt%), and other minerals (~3%). The composition represents the average value of the mineral composition of the SSG from below and above the GWC as determined by Hunfeld et al. (2017).

5.2.2 Friction experiments

We performed medium-velocity (i.e. 5 cm/s) friction experiments using a newly developed rotary shear apparatus (abbreviated as RAP) at Utrecht University, the Netherlands (Figure 5.1a-c, e.g. Korkolis, 2019). We developed a confined gouge setup which allows us to control and measure pore fluid pressure in the gouge layer during the experiment. The gouge samples (~4.4 mm thick before pre-shear) were confined between two ring-shaped steel pistons (100-mm

external, 70-mm internal diameters), loaded in the axial load direction (Figure 5.1b, c). The piston faces contain teeth that are closely spaced (~1 mm), have a groove depth of 0.7 mm and are oriented perpendicular to the direction of sliding. A brass outer ring and an inner ring were used to confine the gouge layer laterally to avoid gouge extrusion during shearing. These were sealed against the pistons using Viton O-rings (Figure 5.1c), enabling pore pressure to be applied to the sample. To directly measure local temperature and pore fluid pressure changes during sliding, two Pt100 sensors and two pressure transducers (10 MPa full range, with 0.01 MPa resolution and less than 10 ms response time) were installed alternately at 90-degree intervals, and identical radial position (centered at d=85 mm), in the bottom rotating piston. Each position of the sensor has a corresponding fluid port on the outer ring to allow fluid drainage. All sensors were mounted within 2 mm of the toothed surface of the lower piston. The initial pore fluid pressure is controlled with an ISCO pump connected to the inlet port. The driving platen is equipped with two angular potentiometers (0.001 degrees, or about 0.74 μm resolution) that measure its rotation.
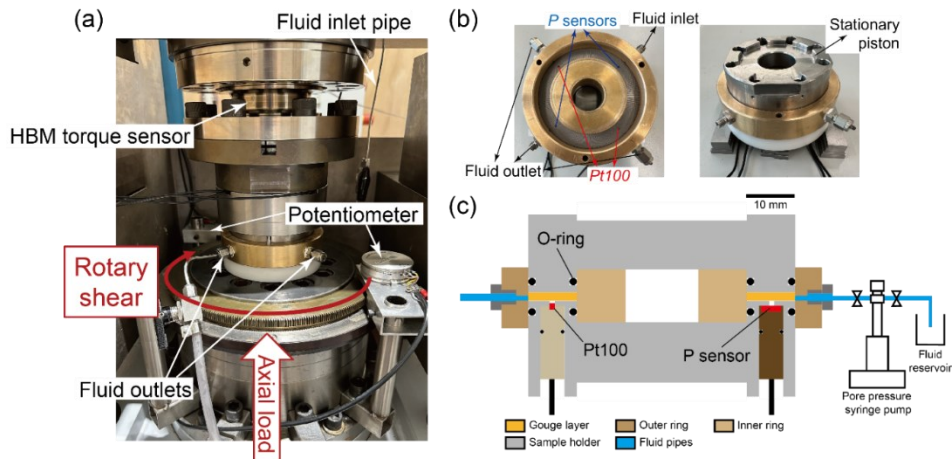
Figure 5.1: *The rotary-shear apparatus (RAP) with gouge setup and pore fluid pressurization system. (a) Photo of the internally pressurized gouge setup installed in the RAP. (b) Top view of the bottom sample holder (rotary piston) and the assembled sample piston. Pressure sensors and the Pt100 are always installed alternately every 90 degrees, corresponding to the locations of the fluid inlet and outlets in the outer confining brass ring. (c) Schematic diagram of the cross-section of the pressurized gouge setup. Pressure transducers and Pt100 (only one of each is shown here) are installed at the bottom rotating piston at ~2 mm distance away from the gouge layer.*

Friction experiments were conducted at an applied normal stress σ_n of 12 MPa, and a slip velocity V of 0.05 m/s, applying a displacement of 0.75 m under undrained conditions with an initial pore fluid pressure P_i of 1 or 2 MPa. A total of 10 experiments performed are listed in Table 5.1, along with the corresponding conditions and key observations. We first weighed 35 g of SSG and distributed it evenly in the ring-shaped sample holder (rotary side) and then confined the gouge sample with the other (stationary) piston (Figure 5.1b). The entire gouge setup was then emplaced in the RAP and pre-loaded at 1 kN (equivalent to ~0.35 MPa of normal stress) before starting saturation. We then saturated the dry gouge sample with the pore fluid through the single inlet until no bubbles came out from the three outlets (Figure 5.1b). We chose four different types of fluid as pore fluid, including deionized (DI) water, Dow Corning 200 silicone oils (1 and 5 centistokes), and synthetic brine, with fluid viscosity of approximately 0.001, 0.001, 0.005, and 0.0014 Pa S, respectively at 20°C and 1 atm. Additional fluid properties are summarized in Table 5.2. The synthetic brine was prepared with a composition similar to the in-situ brine as determined from the Zeerijp (ZRP) 3A core material (Figure 1.6b, Hol et al., 2018). After saturation, we incrementally applied normal load and pore fluid pressure (in pressure control) to achieve the target conditions. Before initiating the main slip stage, the saturated gouge sample was pre-sheared at 1 mm/s for 1 m displacement (equivalent to ~3.75 rotations of the piston assembly) under drained conditions to achieve a consolidated condition, in a stage termed the "conditioning stage". We then closed all three fluid outlet ports (inlet port remained connected to ISCO pump - in pressure control) and waited for a "holding time" of 1 to 2 hours (i.e. the amount of time between the end of the conditioning stage and the start of the main slip stage) until the temperature and pore fluid pressure monitored from the PT sensors became stable. We additionally conducted a water-saturated experiment at a P_i of 2 MPa with a holding time longer than 15 hours to see the effect of the holding period on the mechanical behavior.

Before the initiation of the main slip stage, we closed the fluid inlet port, to create undrained conditions, and initiated the slip at a velocity of 0.05 m/s for 15 seconds (~0.75 m displacement; equivalent to ~2.6 of full rotations of the piston assembly). During the main slip stage, the slip velocity profile follows a ramp-like function with slip acceleration and deceleration of ~0.05 m/s^2 without specific control. During the entire experiment (conditioning + main slip stages),

data on shear stress τ, normal stress σ_n, axial displacement, shear displacement, near-sample temperature T, and near-sample pore fluid pressure P_f were obtained at a logging rate of 5 kHz. The pump fluid pressure $P_{f\text{-pump}}$ and the pore fluid volume were recorded at a logging rate of 20 Hz.

Table 5.1: *List of experimental conditions and key data for all tests. The ID with the symbol "*" represents the overnight experiment (with a holding time longer than 15 hours, as opposed to 1-2 hours). The missing data indicated as "-" in the test r392 is due to the malfunction of the fluid pressure transducer during the experiment.*

ID	Pore fluid	σ_{eff} (MPa)	P_i (MPa)	μ_s (-)	μ_{pk} (-)	μ_{min} (-)	μ_{min_true} (-)	$\Delta\tau_{initial}$ (MPa)	D_w (m)	W (MPa/m)	ΔT_{max} (°C)	ΔP_{max} (MPa)
r369	water	11	1	0.60	0.55	0.39	0.40	0.69	0.68	2.65	36.03	0.29
r349	water	10	2	0.75	0.68	0.45	0.58	1.36	0.48	5.12	34.96	3.85
r389*	water	10	2	0.77	0.54	0.33	0.60	2.34	0.66	3.27	32.09	3.63
r380	brine	11	1	0.68	0.58	0.42	0.44	0.69	0.65	2.66	37.43	0.53
r364	brine	10	2	0.67	0.62	0.49	0.53	0.88	0.51	2.86	54.78	1.26
r392	brine	10	2	0.62	0.64	0.48	-	0.25	0.46	3.61	56.37	-
r377	1 cSt oil	11	1	0.65	0.52	0.31	0.59	1.74	0.61	4.04	42.77	7.33
r379	1 cSt oil	10	2	0.56	0.50	0.26	0.62	0.56	0.64	3.79	30.09	6.26
r373	5 cSt oil	11	1	0.59	0.47	0.32	0.60	2.12	0.53	3.33	34.35	5.00
r362	5 cSt oil	10	2	0.73	0.55	0.35	0.60	2.10	0.65	3.42	52.54	6.20

Note. Pore fluid with DI water likely became saline when injected into the sample due to some residual salt content from the original formation fluid. σ_{eff} = the initial effecitve normal stress. P_i = the initially applied pore fluid pressure. μ_s = the apparent static friction. μ_{pk} = the apparent peak friction. μ_{min} = the apparent minimum friction, calculated using the measured average P_i obtained from the two pressure transducers before the main slip stage. μ_{min_true} = the true minimum friction, calculated using the instantaneous average P_f obtained from the two pressure transducers during the main slip stage. $\Delta\tau_{initial}$ = the stress drop for the first slip-weakening stage. D_w = the slip weakening distance. W = the weakening rate.

Table 5.2: *Fluid properties and associated parameters used in applying Rice's (2006) analytical solution for thermal pressurization during slip-on-plane.*

Experimental conditions and Common parameters assumed in all models	
Slip rate V, m/s	0.05
Normal stress σ_n, MPa	12
Initial pore fluid pressure range P_i, MPa	1, 2
Effective normal stress range σ_{eff}, MPa	11, 10
Initial temperature T, °C	20
Starting porosity n	0.15
Static friction coefficient μ_s	0.6
Pore space thermal expansivity λ_n, 10^{-3}/°C	-0.19
Pore space pressure expansivity β_n, 10^{-9}/Pa	0.65
Permeability k	1E-17

Solid grain properties	
Density ρ_s, kg/m^3	2657
Specific heat capacity C_s, J/kg°C	800
Thermal conductivity K_s, W/mK	3.78

Fluid properties				
	DI water[a]	Synthetic brine[b, c, d, e]	1 cSt silicone oil[f, g]	5 cSt silicone oil[f, g]
Density ρ_f, kg/m^3	1000	1140	820	913
Specific heat capacity C_f, J/kg°C	4180	3380	1393	1393
Thermal conductivity K_f, W/mK	0.6	0.58	0.15	0.15
Fluid thermal expansivity λ_f, 10^{-3}/°C	0.21	0.41	1.34	1.05
Fluid compressibility β_f, 10^{-9}/Pa	0.46	0.3	2	1.3
Fluid viscosity η, 10^{-3} Pa S	1.0–0.546	1.424–0.561	1–0.5	5–2.5

Resulting solid-fluid mixture (fault gouge) properties				
Density $(1\text{-}n) \cdot \rho_s + n \cdot \rho_f$, kg/m^3	2408.45	2429.45	2381.45	2395.4
Specific heat capacity $((1-n) \cdot \rho_s \cdot C_s + (n \cdot \rho_f \cdot C_f))/\rho_{gouge}$, J/kg°C	1010.51	981.60	830.65	833.92
Thermal conductivity $K_s^{(1\text{-}n)} \cdot K_f^n$, W/mK	2.87	2.85	2.33	2.33
Thermal diffusivity α_{th}, mm^2/s	1.18	1.20	1.18	1.17
Hydraulic diffusivity α_{hy}, mm^2/s	22.56	13.19	15.96	3.19
Undrained pressurization factor Λ, MPa/°C	0.36	0.63	0.58	0.63

Codes are a, National Institute of Standards and Technology (NIST); b, The Engineering Tool Box; c, Qasem et al. [2021]; d, Numbere et al. [1977]; e, Pitzer [1984]; f, Dow Corning; g, Sandberg and Sundqvist [1982].

5.3 Results

5.3.1 Experimental data

Figure 5.2 shows the evolution of apparent friction μ_{app} ($= \tau / (\sigma_n - P_i)$), fluid pressure P_f, axial displacement, and temperature T with displacement, under initial pore fluid pressure conditions P_i of 1 (Figure 5.2a) and 2 MPa (Figure 5.2b), during the late part of the conditioning stage and the entire main slip stage. Generally, during the conditioning stage the evolution of the μ_{app} with displacement is similar for all pore fluids, except for the water- and brine-saturated gouges which show a relatively low "static" or "yield" friction μ_s (~0.35–0.45) compared to the silicone oil gouges (~0.45–0.5, see Figure S5.1). After 1-m displacement at 1 mm/s in the conditioning stage, the final steady-state friction μ_{ss} also shows high consistency for all experiments, lying within a range of 0.55–0.65. Therefore, here we present only the late stage of conditioning for the purpose of comparison with the main slip stage. Full experimental data of the conditioning stage of each experiment is shown in Figure S5.1.

During the main slip stage, all the gouges exhibit a similar evolution of μ_{app}. At slip initiation, μ_{app} firstly overcomes a "static" friction μ_s, followed by a rapid friction drop over a displacement of ~2 mm (termed the first slip weakening stage). Subsequently, μ_{app} increases to a peak value μ_{pk} occurring at a displacement of ~5–50 mm and then decreases in a crude oscillatory manner to a minimum friction μ_{min}, defining a second slip weakening stage. Overall, the values of μ_s are greater than those of μ_{pk}. Finally, the μ_{app} slightly increases during the deceleration phase. Note that many oscillations in friction occurred, particularly significant at a P_i of 2 MPa, the frequency of which does not correspond to the number of full rotations imposed (~2.6 rotations). In some cases, oscillations caused μ_{min} to appear before the start of deceleration (Figure 5.2b).

During the second weakening stage (i.e. μ_{pk} to μ_{min}), μ_{app} for the water-saturated gouges with a similar holding time (1-2 hours, Samples r369 and r349) decreases from a μ_{pk} of ~0.55–0.68 to a μ_{min} of ~0.39–0.45. With a longer holding period (15 hours, Sample r389), μ_{pk} and μ_{min} decrease, down to ~0.54 and ~0.33, respectively (the brown curve in Figure 5.2b). For the 1 cSt and 5 cSt oil gouges, μ_{app} decreases from μ_{pk} of ~0.47–0.55 to μ_{min} of ~0.26–0.35. At the same time, the overall friction levels obtained using different fluids become more widely separated at the higher P_i of 2 MPa, showing a systematically decreasing trend in

the level of μ_{min} in the order of brine, DI water, 5 cSt silicone oil, and 1 cSt silicone oil for experiments with the same holding period. This trend cannot be distinguished in the experiments performed at a P_i of 1 MPa.
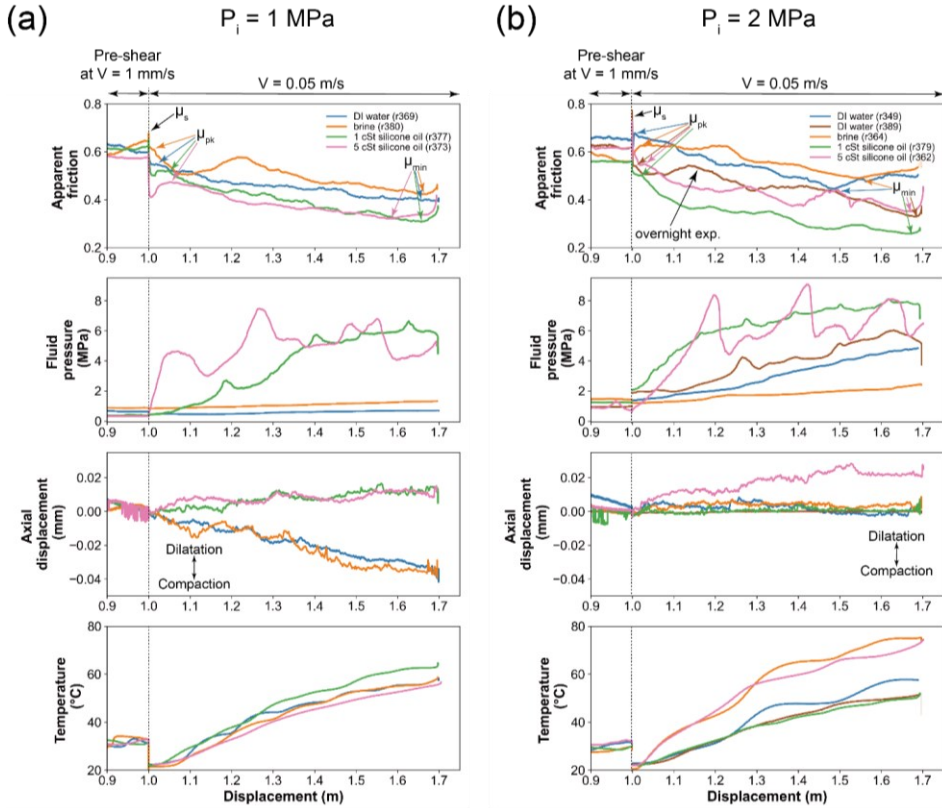
Figure 5.2: *Experimental results showing apparent friction, pore fluid pressure, axial displacement, and temperature as a function of displacement at an applied normal stress of 12 MPa under initial pore fluid pressure P_i of (a) 1 MPa and (b) 2 MPa. The apparent friction coefficient, $\mu_{app} = \tau / (\sigma_n - P_i)$, was calculated using the average P_i obtained from the two pressure transducers before the main slip stage. The gray dashed line in each plot indicates the displacement at which the conditioning stage at V = 1 mm/s was ended and the slip velocity was reset to the target value of 0.05 m/s, which was started when the PT system within the gouge layer became stable.*

Throughout the entire main slip stage, we observed continued fluid pressure increase, gouge dilatation (except for the DI water and brine gouges at a P_i of 1 MPa), and temperature rise (see Table 5.1). Figure 5.3 plots the maximum changes in temperature ΔT_{max} and fluid pressure ΔP_{max} versus μ_{min}, for the pore fluid viscosity corresponding to each experiment at a P_i of 1 and 2 MPa. Generally, at a P_i of 1 and 2 MPa, μ_{min} was achieved at roughly the same time (0.65–0.68m

174

displacement) as the maximum temperature and pore fluid pressure were reached, except for the water- and brine-saturated gouges (0.48m and 0.55m, respectively) tested at a P_i of 2 MPa. In these cases, the μ_{min} was achieved while temperature and fluid pressure were still increasing (Figure 5.2). Overall, ΔT_{max} does not show a systematic correlation with μ_{min}, e.g. higher temperature rise does not necessarily produce lower μ_{min} (Figure 5.3a). The observed separation in the level of μ_{min} for different fluids can also be observed in the ΔT_{max} data; at a P_i of 1 MPa all values of ΔT_{max} lie within a range of ~34–43°C, whereas at a P_i of 2 MPa the gouges with a relatively high viscosity pore fluid (brine and 5 cSt silicone oil) show higher ΔT_{max} up to ~55°C (Figure 5.3b). On the other hand, we observe that μ_{min} decreases with increasing ΔP_{max}, with the lowest μ_{min} value of ~0.25 being accompanied by the largest ΔP_{max} of up to ~6 MPa, observed in both oil-saturated gouges with a P_i of 2 MPa (Figure 5.3c, d).
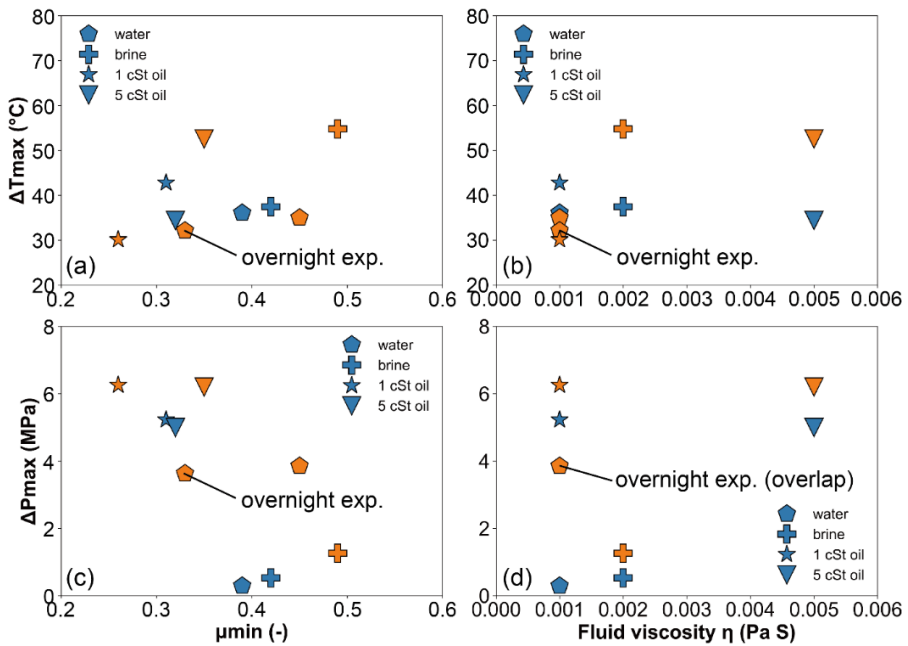
Figure 5.3: *Maximum temperature change ΔT_{max} and fluid pressure change ΔP_{max} plotted against the apparent minimum friction μ_{min} and fluid viscosity η. Blue symbols indicate a P_i of 1 MPa and orange symbols indicate a P_i of 2 MPa.*

Based on the dynamic fluid pressure change measured at the *P*-sensors mounted in the rotary piston, we corrected the apparent minimum friction μ_{min} into a true minimum friction μ_{min_true}, calculated as $\tau / (\sigma_n - P_f)$, using the

instantaneous average P_f obtained from the two pressure transducers before the main slip stage. Figure 5.4 shows the apparent peak friction μ_{pk}, apparent minimum friction μ_{min}, and true minimum friction μ_{min_true} for all four pore fluids at a P_i of 1 and 2 MPa. In general, the μ_{min_true} after correction is higher than the apparent value, due to the fluid pressure increase. At a P_i of 2 MPa, the μ_{min_true} for all pore fluids lies within a range of 0.5–0.6 close to the initial friction (steady-state friction after the conditioning stage) while at a P_i of 1 MPa, the negligible pore pressure increase measured for the water and brine gouges, leads to values similar to the apparent values (μ_{min}=0.4).
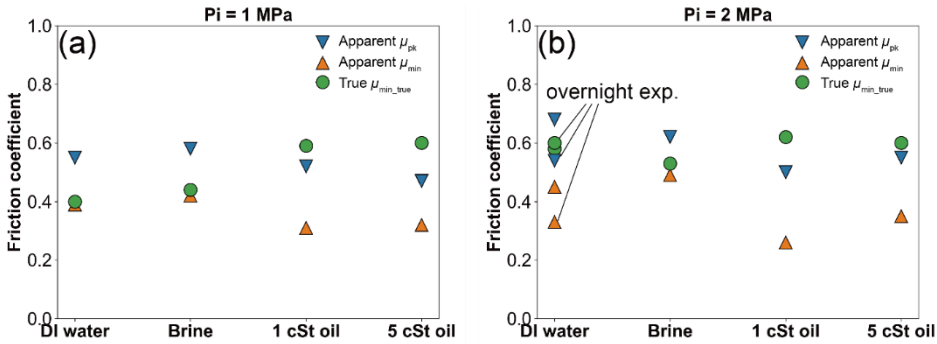
Figure 5.4: *Apparent peak friction μ_{pk}, apparent minimum friction μ_{min}, and true minimum friction μ_{min_true} (corrected after instantaneous fluid pressure change P_f) for the experiments performed using all four pore fluids.*

To characterize the second slip weakening and associated weakening parameters for each experiment, we determined the stress drop $\Delta\tau$ from the peak shear stress τ_{pk} to the minimum shear stress τ_{min} over a distance, defined as slip-weakening distance D_w, obtained from the shear stress versus displacement data. We then further determined the slip weakening rate W as $(\tau_{pk} - \tau_{min}) / D_w$. Figure 5.5 shows how these parameters vary with the thermal pressurization factor Λ and the fluid viscosity η for the different pore fluids under P_i of 1 (blue symbols) and 2 MPa (orange symbols). The thermal pressurization factor, as defined by Rice (2006), is given by:

$$\Lambda = \frac{\lambda_f - \lambda_n}{\beta_f + \beta_n} \tag{5.1}$$

where λ_f and λ_n are the thermal expansivities of the fluid and pores, respectively, and β_f and β_n are the compressibilities of the fluid and pores, respectively. In the calculation of Λ, we ignored any changes in compressibility or thermal expansivity with temperature or porosity. The associated parameters used are

176

summarized in Table 5.2. Overall, $\Delta\tau$ and W show no systematic correlations with Λ and η, though they are larger at a P_i of 2 MPa than at a P_i of 1 MPa for all types of pore fluid. At a P_i of 2 MPa, the brine-saturated gouge shows the smallest stress drop. By comparison, the oil-saturated gouges (star and inverted triangle symbols) show the highest weakening rates of all the pore fluids.
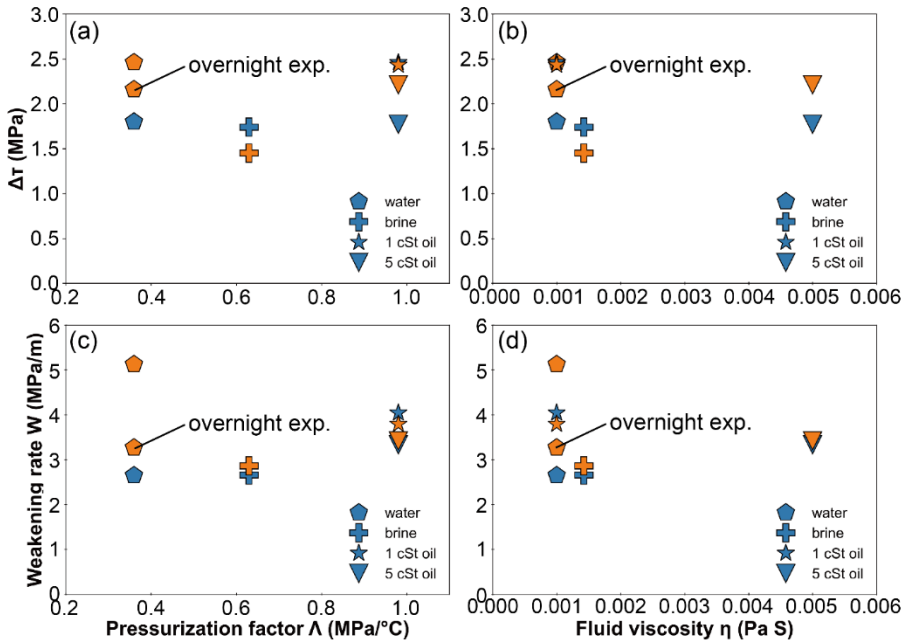
Figure 5.5: *Stress drop Δτ and weakening rate W for different pore fluids with P_i of 1 and 2 MPa as a function of thermal pressurization factor Λ (left) and fluid viscosity η (right). Blue symbols indicate P_i of 1 MPa and orange symbols indicate P_i of 2 MPa.*

5.3.2 Macroscopic and optical observations of deformed gouges

We collected the deformed gouge samples after each experiment and let them air-dry, at room temperature, before impregnating them with epoxy resin. Figure 5.6 shows the plane-polarized optical micrographs of the deformed gouge for the four different pore fluids at a P_i of 2MPa, along with photographs of the air-dried, deformed gouge sample. The optical images of the gouge microstructure at a P_i of 1 MPa are shown in Figure S5.3, which are generally consistent with the 2 MPa gouges. Note that the thin section of the brine-saturated sample is multiply fragmented. This is mainly because salt grains began to crystallize within the recovered gouge layer during drying, which caused expansion of the bulk gouge sample, particularly along shear bands/fractures and

unloading/opening cracks. Based on the macroscopic observations of the slip surface (top left corner-images, Figure 5.6a, c, e, g), the water-saturated and 1 cSt oil-saturated gouges generally display light and a few dark grey striations parallel to the rotary slip direction (Figure 5.6a, c). By contrast, the brine- and 5 cSt oil-saturated gouges show much darker slip surfaces (Figure 5.6b, d).

In shear-parallel cross section, all of the gouges generally exhibited three distinct regions with variations in grain size and porosity. Here, we characterized them as the damage zone (DZ), slip zone (SZ), and principal slip zone (PSZ). In all samples, the DZ shows abundant large (size > 50 μm) angular quartz grains whereas the SZ contains a few randomly oriented angular to sub-rounded clasts of quartz and minor feldspar with smaller grain size. In addition, the matrix of the SZ is darker than the DZ in all cases. The PSZ is identified based on a sharp boundary against the SZ (or between the DZ and SZ; Figure 5.6a) and a darker color and smaller clast grain size. Compared to the brine-saturated and 5 cSt oil-saturated gouges, the PSZ's in the water- and 1 cSt oil-saturated gouges (Figure 5.6a, b, e, f) show fewer large quartz grains (size > 50 μm) and a clearer contrast in grain size versus the SZ as (Figure 5.6c, d, g, h). Similar features and trends can also be observed in the gouge samples deformed at a P_i of 1 MPa (Figure S5.2). The thickness of the PSZ, from the thickest to the thinnest, is ~206–327 μm in the water-saturated samples, ~130–230 μm for 5 cSt oil, ~120–200 μm for 1 cSt oil, and ~80–120 μm for brine. We did not observe any clear correlation between the color of the slip surface and the thickness or other characteristics of the PSZ.
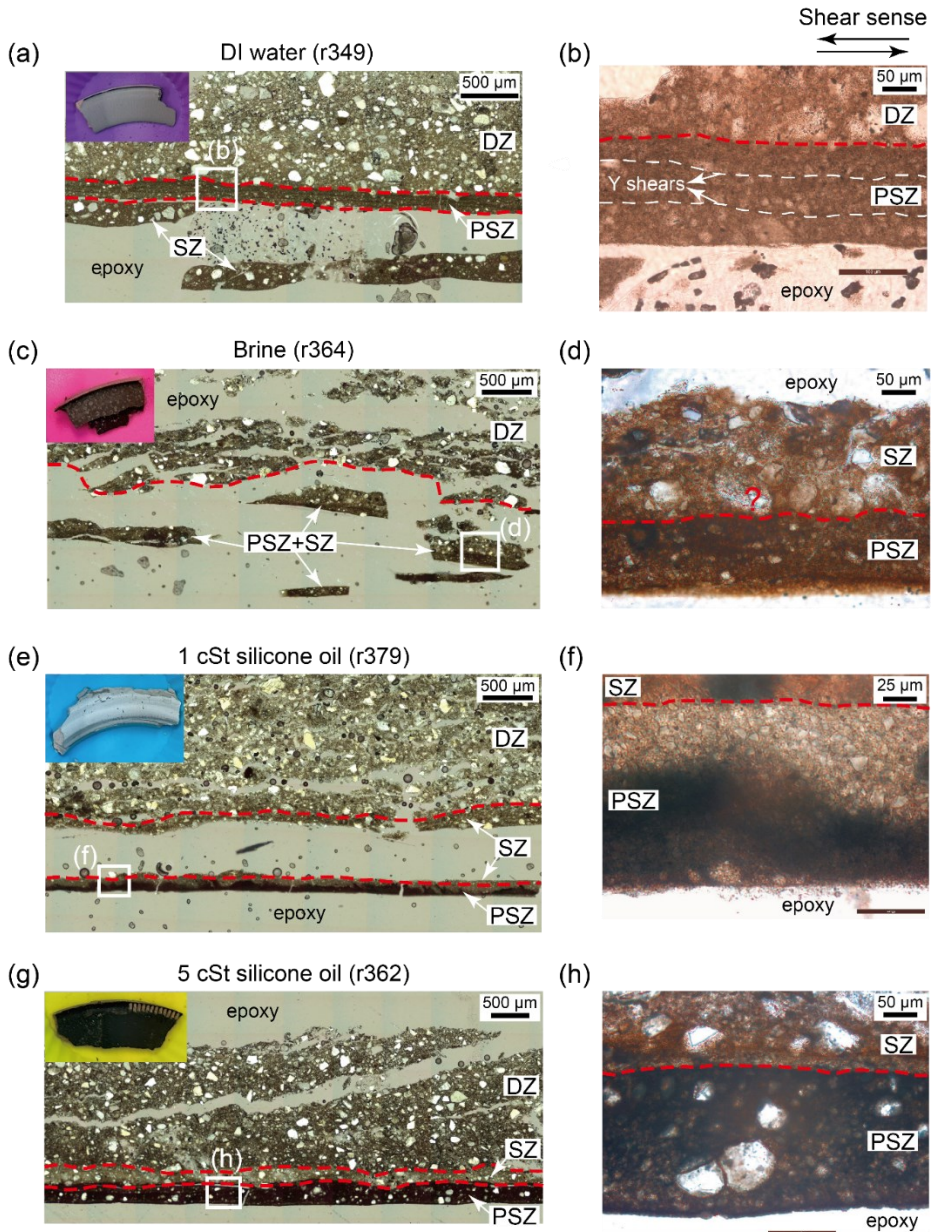
Figure 5.6: *Plane-polarized optical micrographs of the deformed gouges for four different pore fluids at a P_i of 2 MPa, together with photographs of the air-dried deformed gouge sample with the slip surface (rotating side) facing up (corner inserts in left column of images). The upward side of the optical micrographs shows the outer boundary while the downward side is the inner boundary. The full width of the gouge is 1.5 cm. (a, b) Water-saturated gouge sample; (c, d) Brine-saturated gouge sample; (e, f) 1 cSt oil-saturated gouge sample; (g, h) 5 cSt oil-saturated gouge sample. Red dashed lines indicate the boundaries of the damage zone (DZ), slip zone (SZ), and principle slip zone (PSZ). White dashed line indicates the boundary between opaque (black) material and the rest of the fine-grained layer within the PSZ.*

5.4 Discussion

5.4.1 Comparison with previous data

We focus on the comparison of our results with previous data (Yao et al., 2018 and Kuo et al., 2022) on water-saturated, quartz-rich gouges sheared at intermediate velocities ($0.01 < V < 0.4$ m/s), as shown in Figure 5.7. In our water-saturated gouge experiments, we observed slip-weakening behavior whereby the apparent friction coefficient dropped from a peak value of ~0.54–0.68 to a minimum value of ~0.33–0.45, accompanied by ongoing fluid pressure increase without significant volume change (Figure 5.2). Both the apparent μ_{pk} and μ_{min} values are lower (0.54 and 0.33, respectively) for a longer holding time between the conditioning and main slip stages (Figure 5.4). At the same time, the stress drops seen in the short (i.e. 1–2 hours) versus long (i.e. 15 hours) holding time experiments are similar, becoming larger at higher initial pore fluid pressure (Figure 5.5a, b) and accompanied by a larger fluid pressure increase (Figure 5.3).

Yao et al. (2018) conducted single-velocity friction experiments on wet granular gouges (quartz + plagioclase = 38% and clay = 21%) at effective normal stress of 1.3–1.5 MPa, using an initial pore pressure P_i of 2 MPa, at sub-seismic to seismic rates (10^{-6} m/s $< V < 1$ m/s). They showed that the gouge exhibited sharp slip-weakening behavior (i.e. the apparent friction dropped from μ_{pk} to μ_{min} within 5 cm slip) accompanied by instantaneous gouge dilatation when V reached 0.04 m/s with a μ_{min} down to ~0.25 (Figure 5.7) with further weakening with increasing V (μ_{min} of ~0.1 at $V = 1$ m/s). They attributed the sudden initial weakening to water vaporization and local pore fluid pressurization of a water film layer at grain contacts induced by flash heating (Rice, 2006), which they termed "flash pressurization" (*cf.* Chen et al., 2023). In general, we find that the level of the apparent μ_{pk} and μ_{min} reported in their study is lower than our observations (Figure 5.7). In addition, we do not observe the same degrees of sudden friction drop and gouge dilatation within the same weakening distance (0.1–0.25 m in their experiments, 0.48–0.66 m in ours). This could be related to the much lower quartz content (18 wt.%) and higher clay contents (21 wt.%) in their granular gouges as compared to our sandstone-derived gouges (75 wt.% and 5 wt.% for quartz and clay minerals, respectively). The presence of clay minerals can intrinsically reduce friction during sliding (Byerlee, 1978; Moore and Lockner, 2004) and potentially promote the effectiveness or efficiency of TP due to the interconnectivity of clays (i.e. low permeability of the fault zone, e.g.

Aretusini et al., 2021). Additionally, Yao et al. (2018) used a higher slip rate of 5 mm/s for the pre-shear (conditioning) stage, followed directly by the main slip stage with little or no holding time (not specified in the paper). Thus, the gouge was preheated but without enough time to equilibrate within the gouge layer before the main slip stage, which might also enhance the initial weakening. Here, we propose that normal stress might play an additional role in accounting for the absence of substantial initial weakening in our case. We argue that because the normal stresses applied for both our conditioning and main slip stages are much higher than those used by Yao et al. (2018), the grain size of the localized slip zone is expected to be smaller, which decreases the efficiency of flash heating and associated temperature rise. Thus, the initial sharp weakening induced by flash pressurization is likely to become less effective.
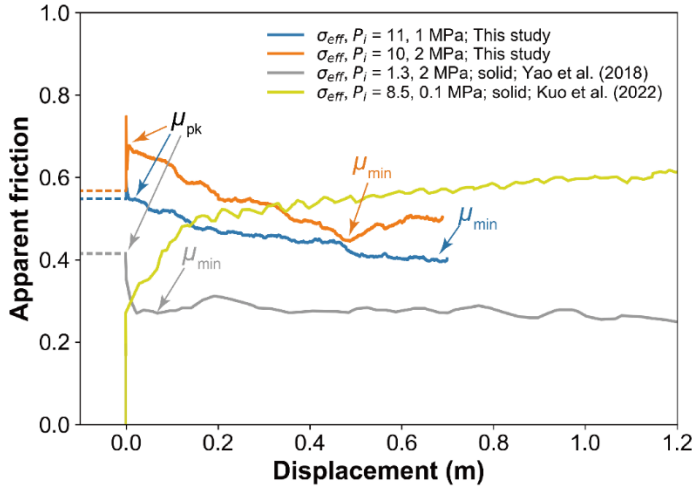
Figure 5.7: Comparison of the mechanical data plotted in terms of apparent friction as a function of displacement for the experiments with different levels of initial fluid pressures. The dashed lines indicate the level of the apparent steady-state friction after the conditioning stage in both our study and Yao et al. (2018). No pre-stress was maintained in the Kuo's et al. (2022) experiment.

Kuo et al. (2022) also conducted velocity-step and single-velocity experiments on wet granular quartz-bearing (~55 wt.%) gouges in the same velocity range employed by Yao et al. (10^{-6} to 1 m/s). In their experiments, much less conditioning displacement (only ~10 mm at 1 mm/s) was imposed and the initial pore fluid pressure was atmospheric. They showed that the wet gouge deformed at an applied normal stress of 8.5 MPa exhibited slip-strengthening behavior from a low apparent static friction μ_s of ~0.3 to a μ_{ss} of ~0.6 at $V = 0.05$

m/s, while the μ_{ss} dropped to ~0.14 when V was increased to 0.5 m/s. The slip-strengthening behavior and high apparent μ_{ss} were suggested to result from cataclastic deformation based on the microstructural observation of abundant R and Y shears and a thick PSZ (~ 2 mm) within the gouge layer. Dynamic weakening at $V = 0.5$ m/s was suggested to be controlled by thermal pore fluid pressurization. We suggest that the absence of weakening at $V = 0.05$ m/s in the Kuo et al study might (in part) be related to their short conditioning displacement. Our larger displacement could facilitate more extreme grain size reduction in the localized slip zone, and potentially result in a more impermeable shear zone, which should increase the effectiveness of TP. Another possible factor might be related to the low initial fluid pressure ($\leq$ 0.1 MPa). In our case, we also showed that the apparent μ_{ss} is relatively high (~0.6) at a low P_i of 0.1 MPa (see Figure S5.3), suggesting that TP was not effective at low-P_i conditions. Low-P_i could result in a smaller mass of water in the gouge layer which, in turn, may reduce the effectiveness of TP. However, the difference in the water mass is limited (~8%, estimated from NIST database), due to the small changes in density of water with a change in pressure from 1 MPa to atmospheric pressure (0.1 MPa), and might not play a major role in the effectiveness of TP and weakening. We suggest that the degree of saturation of the gouge layer may play a more important role in our low P_i test, since gouge saturation was done by flow-through instead of evacuation. It is thus possible that the gouge layer contained some air within pore spaces. Saturation of the gouge layer could be more difficult at a low-P_i, due to capillary entry effects and low efficiency of the drainage during initial saturation and conditioning. Thus, thermal pore fluid pressurization would be inhibited because intergranular porosity is not 100% filled with water. These concepts may explain the insignificant weakening observed by Kuo et al. (2022) and in our experiment at low-P_i conditions (i.e. 0.1 and 1 MPa).

Overall, the levels of the dynamic friction obtained at $V = 0.001$ mm/s (conditioning velocity) and 50 mm/s in our study are comparable to the previous data of Yao et al. (2018) for their most quartz-rich gouge (20% quartz, 18% plagioclase, 17% calcite, 15% illite, 12% smectite, 5% microcline, 5% hornblende, 4% chlorite, and 4% pyrite). The slightly lower dynamic friction values (at $V =0.05$ m/s) in their study are likely associated with the different mineral composition and/or the low applied normal stress in their study. On the other hand, the comparison with the experiments of Kuo et al. (2022) suggests

that the amount of conditioning displacement and the initial fluid pressure might also influence the effectiveness of TP at $V = 0.05$ m/s.

5.4.2 Evolution of apparent friction coefficient
5.4.2.1 First slip-weakening stage

The first weakening stage (within a displacement of ~2 mm) observed in all our experiments occurred without measurable (Dh < 5 μm) volumetric changes of the gouge samples. The cause of such a sharp first weakening is commonly associated with the activation of flash heating at asperity contacts, above a threshold slip velocity (e.g. > 0.01 m/s, Rice, 2006). The generation of flash temperatures softens or decomposes the material and causes instantaneous weakening (e.g. Goldsby and Tullis, 2011; Kohli et al., 2011). In water-saturated fault gouges, previous studies utilizing high-velocity friction experiments have suggested that local thermal pressurization/vaporization at grain contacts could be induced by flash heating (i.e. flash pressurization/vaporization, Chen et al., 2023; Oohashi et al., 2015; Yao et al., 2018). Speculation on the activity of this mechanism generally relies on the estimation of a flash temperature that could be attained at asperity contacts during rapid slip, based on the Rice flash heating model (Goldsby and Tullis, 2011; Proctor et al., 2014; Rice, 2006). Vaporization is inferred to occur if the flash temperature is higher than the boiling point of the pore fluid at the imposed pore fluid pressure, which may result in additional weakening (Chen et al., 2017).

The flash temperature at an asperity (grain) contact (T_a) within a gouge layer can be expressed as (Proctor et al., 2014; Yao et al., 2018):

$$T_a = T_{bulk} + \frac{\tau_c}{\rho c} \sqrt{\frac{(V/N_a)D_a}{\pi \alpha_{th}}} \tag{5.2}$$

Here, T_{bulk} is the fault bulk temperature, τ_c is the contact shear strength, ρ is the gouge density, c is the specific heat capacity of the gouge, V is the imposed slip velocity, N_a is the number of slip-parallel asperity contact layers accommodating slip, D_a is the diameter of the asperity, and α_{th} is the thermal diffusivity. Among these parameters, N_a and D_a are not well constrained but play a crucial role in controlling the efficiency of flash heating. According to Yao et al. (2018), the estimated flash temperature at a slip velocity of 0.04 m/s can reach between 250–400°C for their granular materials with 69% in total of

relatively hard minerals (assuming an asperity size D_a of 5 μm), depending on the number of asperity contact layers N_a (4–10) in the localized shear zone. In our case, the value of the D_a might be smaller because we applied a higher normal stress during the conditioning stage, which results in a smaller grain size and, thus, a lower estimated flash temperature. For N_a, the value could be similar because the grain size is smaller and the PSZ is thinner in our simulated fault gouges (Figure 5.6). Here, to provide a crude, first estimate of flash temperature, we assumed an identical value of the contact shear strength τ_c of 8 GPa used in Yao et al. (2018) because our sandstone-derived gouges have a similar "hard" mineral composition even with a larger amount of quartz (75 wt%) compared to their materials. Considering the density (2408 kg/m^3), heat capacity (1010 J/kg°C), and thermal diffusivity (1.18 mm^2/s) of the solid-fluid mixture properties of the bulk gouge layer (Table 5.1), D_a of 5 μm, and N_a of 4–10, we obtained an estimated range of flash temperature from 290–450°C for the water-saturated gouge. This range could be higher if the decrease in D_a is considered. Therefore, the flash temperatures in our experiments are probably towards the upper end of, or slightly higher than, the estimation (250–400°C) of Yao et al. (2018). Thus, flash pressurization/vaporization might still be an active mechanism accounting for the sharp first weakening stage. In addition, we note that the efficiency of the flash pressurization/vaporization could be spatially quite variable, because the grain sizes in the conditioned gouges are also variable. Whether the liquid/vapor phase transition of the pore fluid could occur is also controlled by the initial fluid pressure based on the phase diagram (Chen et al., 2017). These factors might explain why the magnitude of the initial slip weakening varies with the amount of holding time as well as with different pore fluids, in particular in the case of silicone oil (Figure 5.2 and Table 5.1), as discussed in the following.

Our results show that the magnitude of the first sharp weakening stage is higher in the water-saturated experiment at a P_i of 2 MPa with a longer holding time (experiment r389, Figure 5.2 and Table 5.1), than the water-filled sample with standard holding time. This suggests that the first weakening could be influenced by the spatial distribution of the fluid pressure in the gouge layer. We base this on the following: after the initiation of the conditioning stage, we observed a sudden increase in the fluid pressure of up to 4.5 to 6.5 MPa followed by a gradual decrease with displacement due to the drained boundary conditions (see Figure S5.1). The amount of fluid pressure increases and the diffusion rates

at different locations of the gouge layer appear to be variable based on the measurements at the different pressure sensors. This suggests that the development and the evolution of the localized slip zone in the gouge layer during the conditioning stage may also be quite spatially variable because a fine-grained layer is generated which presumably has low(er) permeability and could cause less efficient fluid drainage across the bulk gouge zone. Although the main slip stage was not initiated until we ensured that the measured fluid pressure was stable, the fluid pressure distributed within the bulk gouge zone might still not be equilibrated, in part perhaps due to the clogging of the porous filters after the conditioning stage. The filter clogging would form another relatively impermeable layer which inhibits a correct measurement of the fluid pressure. A longer holding time would ensure that the fluid pressure is much more uniformly distributed in the gouge layer. In a uniform case, because the background fluid pressure is more consistent (~2 MPa), the chance for water to get vaporized ($\geq$ 212°C for P_f = 2 MPa, *cf.* Chen et al., 2017) might increase within the estimated range of flash temperatures. This could cause additional weakening with additional volumetric expansion of 100 times larger (0.001 $\rightarrow$ 0.100 m^3/kg at 212°C at 2 MPa). By contrast, for a heterogeneous case, the local fluid pressure might remain high ($\geq$ ~212–276°C for P_f = 2–6 MPa), which inhibits pore water from getting vaporized. This could explain why the initial weakening is less significant in the short holding time experiment with water (experiment r349).

In addition, we observed that the oil gouges generally show a larger amount of first stage slip weakening than the water- and brine-filled gouges, for the same amount of holding time (Table 5.1). This seems to contradict expectations, because the boiling temperature of silicone oil (>315°C at 0.1 MPa) is higher than for water or brine, so that flash vaporization is expected to be less efficient. We argue that aside from the distribution of fluid pressure, another possible explanation for the different amounts of first-stage weakening, seen using different pore fluids, could be the effect of the pore fluid on grain size reduction. Previous studies on intact silicate rocks with double torsion tests have shown that the presence of (liquid) water facilitates subcritical crack growth, which can be one up to three times faster than in air-dry rocks, depending on silica content (e.g. Atkinson, 1984; Ma et al., 2023; Waza et al., 1980). If subcritical crack growth rates are faster in the water-saturated gouges, grain size reduction might also be more effective during the conditioning stage, which would produce smaller grain

sizes. The smaller grain sizes (potentially smaller D_a) would lead to a lower estimated flash temperature and, thus, to less weakening.

To more systematically investigate the effects of fluid pressure heterogeneity and the type of fluid on the weakening associated with flash pressurization, tests including different holding times and conditioning conditions (e.g. normal stress and displacement) are needed. In addition, microstructural investigations of the starting materials after the conditioning stage are required to constrain the (grain) asperity size (which affects the flash temperature) and the thickness and porosity of the PSZ (which affects flash temperature via the number of actively sliding contacts, N_a, and affects the fluid pressure distribution via the permeability).

5.4.2.2 Restrengthening and second slip-weakening stage

After the first slip weakening stage, a minor ($\Delta\tau = 0.03–0.73$ MPa) restrengthening occurred before the second slip weakening. We do not observe any systematic correlations between the amount of restrengthening, pore fluids, initial pore fluid pressure, or volumetric behavior. Assuming grain comminution continued, this would lead to a decrease in asperity size due to grain size reduction and to an increase in the number of sliding contacts per unity shear band thickness, which decreases the efficiency of flash weakening. On this basis, we suggest that the restrengthening behavior is likely associated with i) decreasing efficiency of flash heating caused by the process of grain fragmentation, and ii) ongoing grain size reduction.

For the second-slip weakening stage, we first exclude compaction-related pressurization (i.e. compaction softening; see also Chapter 4) as the dynamic weakening mechanism (e.g. Faulkner et al., 2018). This is because the gouge layer in most of the experiments exhibit dilatation accompanied by fluid pressure increase when first subjected to the main slip stage after the pre-slip conditioning stage, with the exception of water- and brine-saturated gouges at P_i of 1 MPa, showing compaction (Figure 5.2). Second, we suggest that the second slip-weakening cannot be fully explained by flash pressurization/vaporization because the magnitude of the second weakening and the associated weakening distance in our study are significantly different from the previous observations by Yao et al. (2018), as mentioned in section 5.4.1. The increase in temperature and pore fluid

pressure measured in most of our experiments, and notably the ΔP_{max} of ~6 MPa recorded in the 1 cSt silicone oil experiment (which accounts for nearly the full reduction in apparent friction - Figure 5.3 and Table 5.1) indicate that TP dominated the second stage weakening. As shown in Figure 5.4, in some cases (water- and brine-saturated gouges at a P_i of 1 MPa), the instantaneous measured fluid pressure increase fails to fully explain the observed weakening where the true minimum friction remains as low as the apparent minimum friction due to a minimal measured pore pressure increase (< 0.2 MPa). A possible explanation for this is a high degree of gouge clogging of the porous filters after the conditioning stage which caused some sensors to measure relatively low fluid pressure increases. The clogging would form a poorly drained layer which inhibits a correct measurement of the fluid pressure. However, we cannot rule out the possibility that the weakening was not caused by TP but by some other mechanism such as flash pressurization, in which the local fluid pressure increases would not be measured by the pressure sensor. However, considering the similarity in slip weakening distance in all experiments, we infer that TP is the dominant mechanism controlling the second slip weakening.

We showed that the minimum apparent friction μ_{min} systematically decreases with increasing ΔP_{max} (Figure 5.3), suggesting that TP was more efficient in the oil-filled gouges. This can be explained by a high thermal expansivity of silicone oil (~50 times higher than water), which results in a larger thermal pressurization factor. However, the stress drop $\Delta\tau$ and weakening rate W do not show systematic variations between different pore fluids (Figure 5.5). The reason for this could be related to either the different amount of initial slip weakening or the presence of friction oscillations (Figure 5.2; Table 5.1). The larger amount of first weakening observed for the oil-filled samples causes a lower μ_{pk}, resulting in a second stress drop $\Delta\tau$ that is similar to that in the water and brine gouges. In addition, the high amplitude of the friction oscillations, particularly notable in the brine-saturated samples, could influence the determination of the apparent μ_{pk} and μ_{min}, which further affect the weakening distance D_w and resulting W.

Currently, it remains difficult to directly compare which pore fluid generates more significant weakening or weakens faster based on the results of the $\Delta\tau$ and W. However, by comparing the second weakening curves (post-peak weakening),

plotted as the normalized shear stress (τ/τ_{pk}) as a function of displacement (Figure 5.8), we observe that the second weakening for all types of pore fluids is similar at a P_i of 1 MPa while showing greater variation at a P_i of 2 MPa. At higher initial fluid pressure, all gouges with different pore fluids generally reveal a larger (or similar) amount of weakening than with P_i of 1 MPa, except for the brine-filled gouge, which shows less weakening. This phenomenon may also be explained by the difference in gouge saturation at different initial pore fluid pressures, as discussed in the previous section 5.4.1, where the gouge layer is likely to be more fully saturated at elevated fluid pressure, enhancing the efficiency of TP.
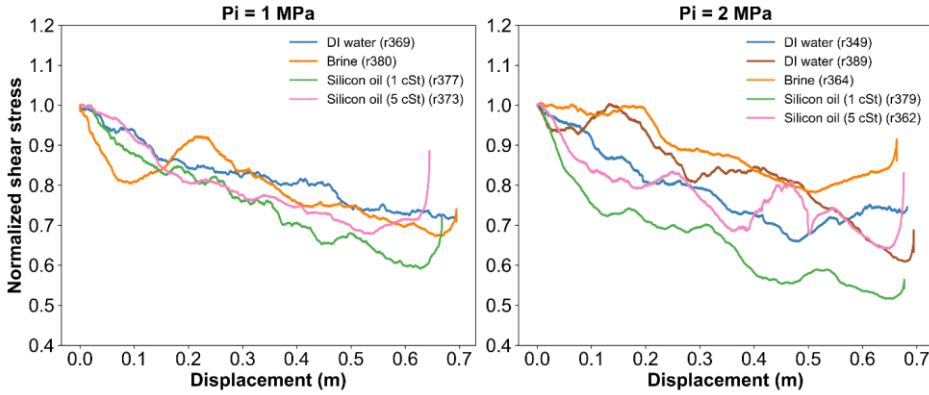
Figure 5.8: *Normalized shear stress (τ/τ_{pk}) as a function of displacement for the post-peak weakening of each experiment at a P_i of 1 and 2 MPa.*

In order to more systematically explore whether the variation in weakening with pore fluid type can be explained by TP, we use Rice's (2006) 2-D analytical solution of the slip-on-plane model, which assumes shear acts as a line heat source with negligible thickness and compare with our data. With this model, we can further investigate systematic differences in the maximum temperature rise ΔT_{max} between the observations and predictions. We use temperature rather than fluid pressure because the measured temperature is presumed to be more reliable since heat diffuses faster and is not affected by clogging of the filters. The analytical solution is written as:

$$\tau = \mu(\sigma_n - p) \exp\left(\frac{\delta}{L^*}\right) erfc(\sqrt{\frac{\delta}{L^*}})\tag{5.3}$$

Here, τ is shear stress, μ is the coefficient of friction, σ_n is normal stress, p is pore pressure, δ is displacement, and L^* is decay distance, defined as:

$$L^* = \frac{4}{\mu^2}(\frac{\sigma c}{\Lambda})^2 \frac{(\sqrt{\alpha_{hy}} + \sqrt{\alpha_{th}})^2}{V} \tag{5.4}$$

where ρc is the density times the heat capacity, V is the slip velocity, $\alpha_{th} = K/(\rho c)$ and $\alpha_{hy} = k/(\eta\beta)$ are the hydraulic and thermal diffusivities of the slip zone, respectively, where K is the thermal conductivity, k is the permeability, η is the fluid viscosity, and β can be expressed as $n(\beta_f + \beta_n)$, where n is the gouge porosity, β_f is the isothermal compressibility of the pore fluid and β_n is the isothermal pressure expansivity of the pore space. The fault plane temperature as a function of displacement can be expressed as:

$$T - T_{amb} = \left(1 + \sqrt{\frac{\alpha_{hy}}{\alpha_{th}}}\right)\frac{(\sigma_n - p_0)}{\Lambda}\left[1 - \exp{(\frac{\delta}{L^*})}erfc(\sqrt{\frac{\delta}{L^*}})\right] \tag{5.5}$$

where T_{amb} is the ambient temperature. We excluded the first slip weakening stage in the model comparison because the model only predicts weakening associated with the coupled TP problem (Rice, 2006). For the poroelastic parameter values, we took the conditions after pre-shear conditioning as the reference state. We assume constant poroelastic parameter values for each experiment, i.e. porosity n, permeability k, pore space expansivity λ_n, and pore space compressibility β_n were taken as 0.15, 1×10^{-17} m^2, -0.19×10^{-3} 1/°C, and 0.65×10^{-9} 1/Pa, respectively, for each model (Rice, 2006). For porosity n and permeability k, we also assumed lower values of 0.07 and 1×10^{-18} m^2 (adopted from Zhang and Tullis, 1998), respectively, for both the water- and 1 cSt oil-filled gouges, because we observed that their PSZ generally exhibit smaller grain sizes with a sharper boundary against the SZ than the brine- and 5 cSt oil-filled gouges (Figure 5.6; Figure S5.2). We varied temperature-dependent fluid viscosity within a reasonable range based on the measured temperature rise (>30–50°C). The viscosity of each pore fluid decreases overall to half of its initial value. All the associated parameters and their values are summarized in Table 5.2.

Figure 5.9 presents the model predictions (dashed and dash-dot lines) for normalized shear stress, pore fluid pressure, and temperature as a function of displacement for samples sheared with water, synthetic brine, 1 cSt, and 5 cSt silicone oil at a P_i of 2 MPa, together with the experimental observations (solid lines). The model predicts larger stress drops than observed experimentally, together with higher fluid pressure increases and temperature rises, for all types of pore fluids. In addition, assuming identical permeability for all types of pore

fluids, we find that the model fails to predict the systematic differences observed in the level of weakening using different pore fluids. As seen in Figure 5.9, the amount of predicted weakening is strongly influenced by the thermal pressurization factor Λ and the hydraulic diffusivity α_{hy}, with TP becoming more effective with an increase in Λ and a decrease in α_{hy}. Comparing the water- and brine-filled gouges, which have otherwise similar pore fluid properties, the latter with the higher Λ and the smaller α_{hy}, results in a larger amount of weakening. The same effect can also be observed by comparing the 1 cSt and 5 cSt silicone oil-filled gouges. However, our experimental data show the opposite trend for the water- and 1 cSt oil-filled gouges, which tend to exhibit more weakening than the brine- and 5 cSt oil-filled gouges, respectively. The predictions resemble the experimental observations more closely if we account for the differences in the permeability and porosity of the PSZ inferred from our microstructural observations. Since the model is purely based on the coupled TP problem, the above observations suggest that the evolution and the development of the PSZ also plays an important role in controlling the effectiveness of TP.
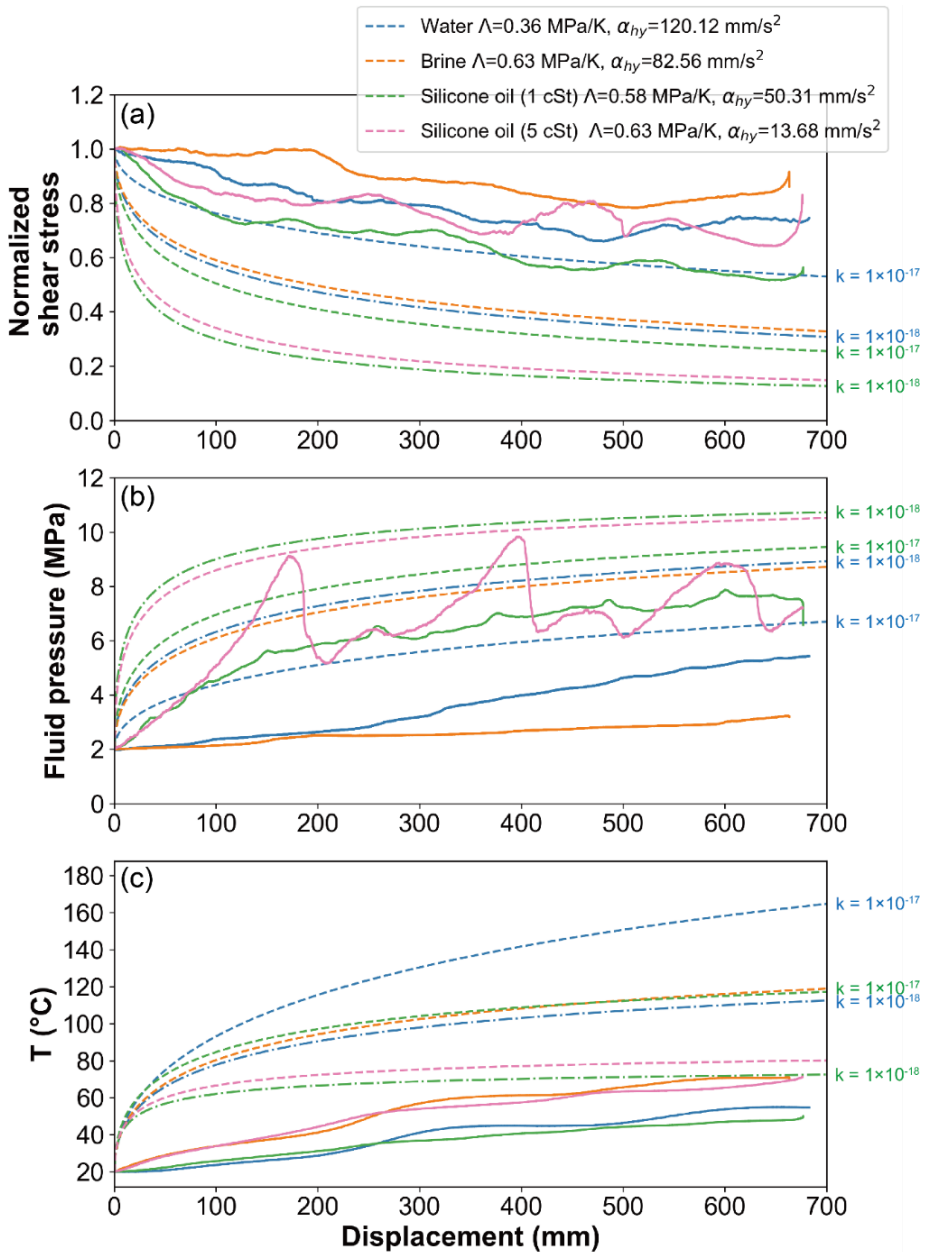
Figure 5.9: Evolution of (a) normalized predicted shear stress, (b) fluid pressure, and (c) temperature (dashed and dashed-dotted lines) as a function displacement, based on Rice's (2006) slip-on-plane model, and comparison with the experimental data (solid lines) obtained at a P_i of 2 MPa. Dashed lines indicate the predictions for a permeability k of $1 \times 10^{-17} m^2$ and dashed-dotted lines indicate the predictions for a k value of $1 \times 10^{-18} m^2$ (1 cSt oil and water tests only).

In addition, if we take permeability differences into account, the variations in the predicted temperature rise between different pore fluids become similar to the measurements (Figure 5.9c). However, the predicted temperature increases in the water and brine cases are much higher than the measured values (Table 5.3). Two things that should be further noted are that i) the temperature can be buffered by TP due to the thermal expansion of the pore fluid (e.g. Badt et al., 2020), which is not incorporated in the model, and ii) the actual temperature within the PSZ is expected to be higher than the measured value because the Pt100 elements are not directly attached to the active slip surface (2 mm distance). The first factor fails to explain the large temperature variations between the predictions and the measurements, because we do not observe significant volumetric changes for using any of the pore fluids. The second one is also unlikely because the predicted and measured temperature rises in the silicone oil experiments values are similar ($T = 60–70°C$), suggesting that the measured temperature is still representative of the slip-zone temperature to some extent. We suggest that the high predicted temperature in the water- and brine-filled gouges, compared with the experimental data, might be associated with the development, in those samples, of multiple Y shears within the PSZ which averaged out the total distributed slip velocity. Thus, the slip was distributed along more than one single slip plane which caused a smaller temperature rise. An additional effect of this is that the heat source and thus maximum temperature would be further away from the sensor than when the PSZ is right on the boundary.

Table 5.3: *Maximum measured and predicted temperatures for the four pore fluids employed in our experiments at a P_i of 1 and 2 MPa.*

Pore fluid	P_i (MPa)	Measured ΔT_{max} (°C)	Predicted ΔT (°C) at 700 mm	Predicted ΔT_{max} (°C)
DI water	1	36.03	137.99	248.30
Synthetic brine	1	37.43	88.74	119.57
Silicone oil (1 cSt)	1	42.77	85.85	107.02
Silicone oil (5 cSt)	1	34.35	53.11	60.09
DI water	2	34.96 / 32.09	125.44	225.73
Synthetic brine	2	54.78 / 56.37	80.67	108.70
Silicone oil (1 cSt)	2	30.09	78.05	97.29
Silicone oil (5 cSt)	2	52.54	48.28	54.62

To conclude, we suggest that TP is the dominant weakening mechanism during the second frictional weakening for all types of pore fluids. Using the slip-on-plane model coupled with the TP problem from Rice (2006), we have shown that thermal pressurization factor and hydraulic diffusivity are not enough to explain the experimental observations. It is necessary to consider the characteristics of the PSZ (e.g. grain size, PSZ thickness) and fault-zone permeability to obtain better agreement. To further investigate how the fluid properties influence grain size reduction and how the initial fluid pressure affects the effectiveness of TP, systematic microstructural analysis and numerical modeling are needed to address the complexities of TP at the scales from the bulk gouge zone to the shear band, to the asperity contact and/or grain/pore scale.

5.4.2.3 Oscillations in frictional strength

In all experiments, we observe oscillations in friction with a relatively large wavelength (at least > 0.5 m) during the main slip stage, these being particularly significant at a P_i of 2 MPa (Figure 5.2). Generally, the frequency of the oscillations does not correspond to the number of full rotations of the piston. In other words, the peaks and troughs do not occur systematically at equal displacement intervals, with the exception of the overnight results for the water-saturated gouge at a P_i of 2 MPa (Figure 5.2b). Oscillations do not only appear in the frictional curves but are also present in the evolution of the fluid pressure and temperature, though the frequencies are not systematically correlated with the friction. The oscillations in the fluid pressure and temperature, measured from the sensors in the rotary piston, suggest that the distribution of pressure and temperature within the gouge zone was quite heterogeneous during the rapid shearing. This is unsurprising because the fluid pressure increase has already been shown to be quite variable at different locations in the gouge layer during the conditioning stage, suggesting that the permeability of the shear zone (controlled by slip localization) could also be variable, as discussed in section 5.4.2.1. Low permeability shear bands likely generate high temperatures and thus high fluid pressures during the main slip stage, because slip tends to be accommodated within these localized shear zones (e.g. Ikari, 2015). This might be one of the reasons for the oscillations in friction. Though TP is effective in the bulk gouge layer, the efficiency of TP would be affected by the local amount of heating and the associated fluid pressure increase, thus becoming spatially variable in the gouge layer. The almost complete absence of irregular oscillations in the long

holding time experiment may further suggest that initial fluid pressure heterogeneity plays a role in controlling frictional behavior.

An alternative explanation can be found in a recent numerical study (finite element model) addressing the coupled Thermo-Hydro-Mechanical processes (THM) controlling fault friction and strain localization during seismic slip - see Stathas and Stefanou (2023). These authors showed numerical results with a traveling PSZ within the finite thickness of a gouge zone, leading to oscillations in the fault's frictional response. They suggested that the underlying mechanism for a traveling PSZ and the resulting friction oscillations are due to high pressure and temperature diffusion gradients near the boundaries of the fault gouge, where the width and period of the oscillations depend on the thickness of the gouge layer. This phenomenon is particularly visible in their isothermal drained and adiabatic undrained analyses. This concept may be applied to our experimental observations to explain the observed friction oscillations. To further investigate whether the friction oscillations are related to a traveling PSZ, tests including different gouge thicknesses, environmental conditions (i.e. drained conditions), and different shear displacements are needed.

5.4.3 Implications for induced earthquakes

The aim of this study has been to understand fault slip behavior and dynamic friction in small-displacement, induced earthquakes under reservoir conditions, focusing on the Groningen gas field, making use of pore fluids with varying properties. Our key finding is that brine- and water-saturated faults can experience weakening through TP at an intermediate seismic slip rate of 0.05 m/s. Among all pore fluids studied, faults saturated with in-situ brine exhibit the least amount of weakening and higher dynamic friction values (0.42–0.49) compared to water-saturated faults (0.33–0.45). Until now, slip-weakening parameters, including dynamic friction and weakening distance, used in dynamic rupture models (e.g. Buijze et al., 2019) have been based on high-velocity friction experiments with DI water as the pore fluid (Chen et al., 2022; Hunfeld et al., 2017). These experiments simulated M 3–4 earthquake slip pulse functions with rapid slip acceleration and deceleration (>15 m/s²) and peak seismic velocities (>1 m/s) within a few centimeters or decimeters of displacement (e.g. Wentinck, 2018). TP was effective to some extent in these cases. Although the peak velocity and slip acceleration in our study are significantly lower, the observed TP-

induced weakening behavior suggests potential differences in dynamic friction when applying seismic slip pulses to brine-saturated gouge, if the fault zone structures within the gas reservoirs are favorable for TP (e.g. low permeability and thermal conductivity of the wall rocks; Caine et al., 1996; Faulkner et al., 2010; Wibberley and Shimamto, 2005). In general, our results suggest that weakening during dynamic slip could be less than predicted from DI-water-saturated slip-pulse experiments if a more viscous fluid such as brine is present. This may have implications for rupture nucleation and growth above versus below the gas-water contact in gas fields, such as Groningen.

5.5 Conclusions

We conducted medium-velocity friction experiments on sandstone-derived fault gouges with four different types of pore fluids (DI water, in-situ brine, 1 cSt, and 5 cSt silicone oil) to investigate the effect of the thermal pressurization factor and hydraulic diffusivity on the efficiency and effectiveness of TP and the associated TP-induced weakening. All tests were performed under undrained conditions at an applied normal stress of 12 MPa, initial pore fluid pressures of 1 and 2 MPa, and a slip velocity of 0.05 m/s within ~0.7 m displacement. The main findings and conclusions are as follows:

1. Our results demonstrate that TP can be effective at this slip velocity, causing dynamic slip weakening for all fluids investigated.

2. A first stage of sharp weakening associated with flash pressurization, and a following TP-induced weakening stage, are highly dependent on the thermal and hydraulic properties of the pore fluid, specifically fluid expansivity and viscosity.

3. Based on a comparison between slip-on-plane model predictions and the experimental observations, we show that a fluid-saturated fault with a higher thermal pressurization factor and lower hydraulic diffusivity does not lead to more weakening by TP. This may be related to the effect of the fluid viscosity on gouge deformation during rapid slip, which influences the fault-zone permeability. When considering the potential changes in the permeability of the fault zone during slip, the difference in the predicted stress drops and temperature rises between different pore fluids are broadly similar to the experimental and microstructural observations.

4. Our results demonstrate that a gouge-filled fault saturated with brine exhibits reduced weakening and higher dynamic friction compared to a water-

saturated fault. This finding offers valuable insights into refining slip-weakening parameter values within rupture models, enabling better constraints on the maximum moment magnitude of future induced earthquakes in Groningen gas reservoir.

Supplementary information
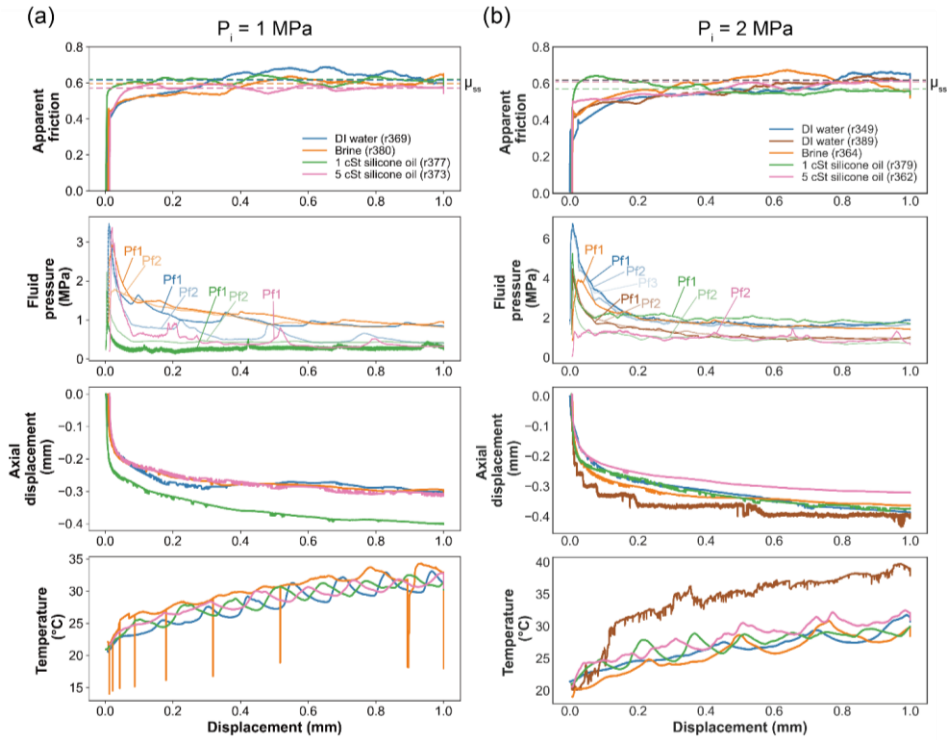
Figure S5.1: *Conditioning stage data plotted as apparent friction, fluid pressure, axial displacement, and temperature as a function of displacement for four different pore fluids at an initial pore fluid pressure of (a) 1 and (b) 2 MPa. The dashed lines indicate the level of the steady-state friction μ_{ss} of each experiment.*
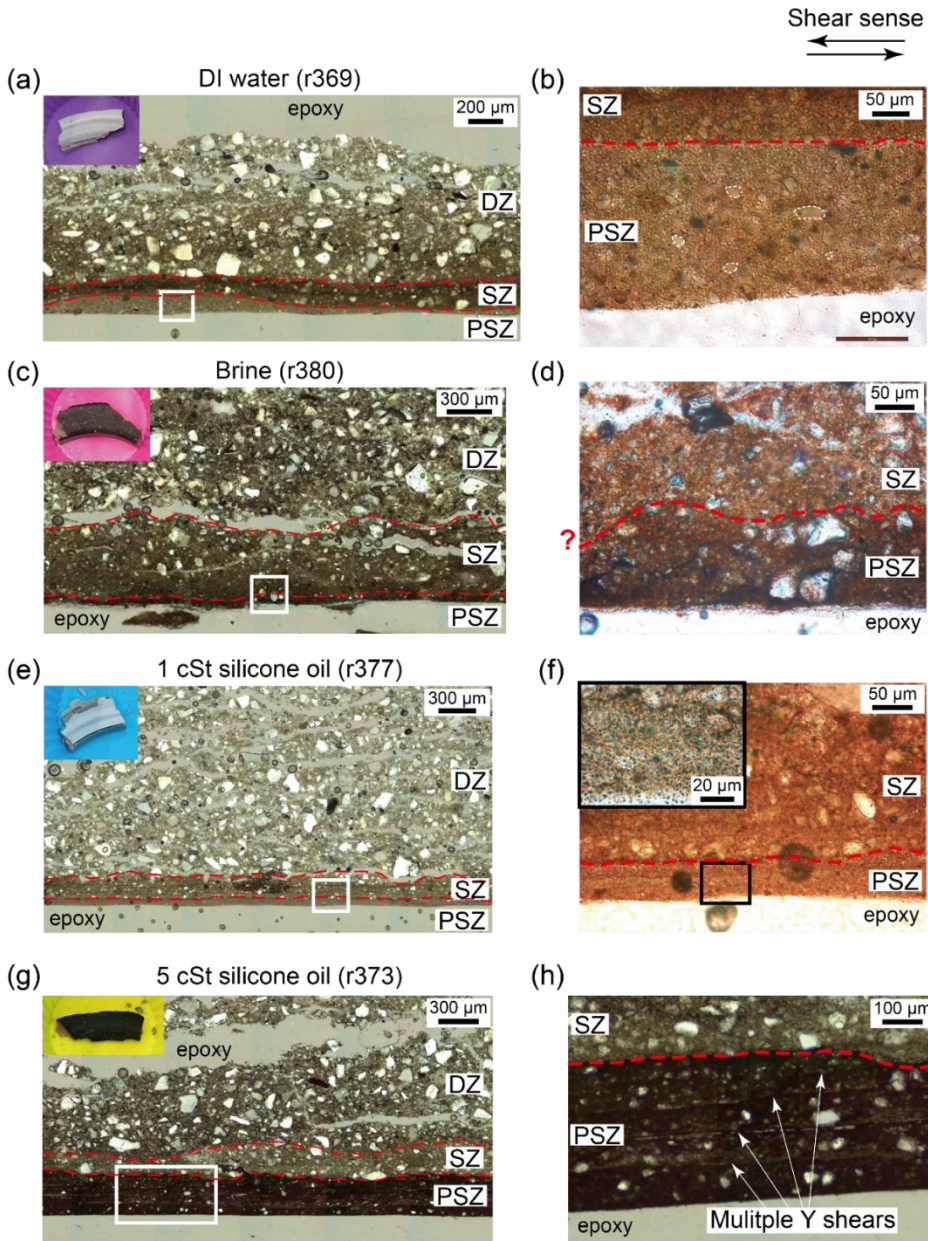
Figure S5.2: Plane-polarized optical micrographs of the deformed gouges for four different pore fluids at a P_i of 1 MPa, together with photographs of the air-dried deformed gouge sample with the slip surface (rotating side) facing up (corner inserts in the left column of images). The upward side of the optical micrographs shows the outer boundary while the downward side is the inner boundary. The full width of the gouge is 1.5 cm. (a, b) Water-saturated gouge sample (r369); (c, d) Brine-saturated gouge sample (r380); (e, f) 1 cSt oil-saturated gouge sample (r377); (g, h) 5 cSt oil-saturated gouge sample (r373). Red dashed lines indicate the boundaries of the damage zone (DZ), slip zone (SZ), and principle slip zone (PSZ).

Figure S5.3: *Main slip results for the water-saturated gouges at a Pi of 0.1, 1, and 2 MPa.*

Chapter 6

Effects of normal stress and slip acceleration on weakening in sandstone-derived fault gouges during simulated small-magnitude earthquakes

Chien-Cheng Hung, André R. Niemeijer, Stefano Aretusini, Elena Spagnuolo,
Jianye Chen, Maartje Hamers
To be submitted to Journal of Structural Geology

Abstract

Numerous experimental studies have shown that faults become dynamically weak during large displacements (>1 m) at seismic slip velocities (>0.1 m/s). However, the extent to which dynamic weakening plays a role in small-displacement (dm), induced earthquakes (magnitude 3 to 4), such as those occurring in the Groningen Gas Field (the Netherlands), has remained relatively unexplored. We performed seismic slip-pulse experiments on Slochteren sandstone gouges (SSG) using a rotary-shear apparatus. Conditioning (i.e. pre-sheared) gouge layers confined between ~1.5 mm thick sandstone host blocks (composed of three fan-shaped pieces) were subjected to a slip-pulse at initial effective normal stresses σ_{eff} of 4.9–16.6 MPa. Slip pulses featuring a peak velocity V_{pk} up to 1.8 m/s and slip accelerations up to 42 m/s^2 were applied over a total shear displacement of 7.5–15 cm, using either dry Argon or water as pore fluid, introduced at initially ambient temperature conditions. Pore fluid pressure was controlled at 0.1 and 1 MPa at the sample boundaries throughout the experiments. All water-saturated gouges revealed a similar evolution of apparent friction and volumetric behavior, showing rapid weakening from a peak value of ~0.7 to a minimum value of ~0.3, accompanied by initially rapid dilatancy followed by slower ongoing dilatation, during the acceleration phase. By contrast, weakening was subtle in the experiment with argon as pore fluid under similar conditions. Our results confirm earlier findings that water-saturated SSG slip-weaken substantially during seismic slip-pulse tests, with a minor dependence of weakening on normal stress, slip acceleration, and displacement, while dry (Argon-filled) samples do not. Microstructural observations on our wet/dry samples show that the width of the PSZ is not systematically correlated with the frictional work or frictional power input densities, suggesting that mechanical wear processes and/or heat production, enhanced by normal stress and slip rate, do not necessarily control the growth of the PSZ. The implication is that thermal pore fluid pressurization with liquid/vapor water phase transitions, on a shear-band or finer (asperity) scale, may play a key role in weakening short-displacement, induced earthquakes.

6.1 Introduction

Human-induced seismicity has been reported worldwide since activities in subsurface reservoirs, like fluid injection or hydrocarbon production, have increased in the past few decades (Elsworth, 2013; Ellsworth et al., 2016; McGarr et al., 2002; Nicol et al., 2011; Segall, 1989). Since the 1990s, induced earthquakes related to gas production have been recorded in the Groningen field, located in the northern Netherlands, with the largest event reaching $M_w = 3.6$. The depth of relocated hypocenters of these induced seismic events suggests that most, if not all, events occur on the pre-existing normal faults within the sandstone reservoir (Dost and Haak, 2007; Dost et al., 2020; Smith, 2019; Spetzler and Dost, 2017; Van Eijs et al., 2006). A thorough understanding of the mechanical behavior of these faults is needed to provide constraints on geomechanical rupture models (e.g. Buijze et al., 2019), and to assess the potential for induced fault activity and associated seismic hazard.

High-velocity friction experiments on simulated fault gouges have shown that fault strength dramatically drops when frictional heat is rapidly generated and accumulated within the simulated fault zone (see the summary in Di Toro et al., 2011; Niemeijer et al., 2012). Generally, flash heating at asperity contacts (e.g. Beeler et al., 2008; Goldsby and Tullis, 2011; Kohli et al., 2011; Rice, 1999, 2006) and thermal pressurization of the pore fluid (hereafter TP; e.g. Badt et al., 2020; Brantut et al., 2010; Lachenbruch, 1980; Rice, 2006), are the two major mechanisms which are commonly proposed to be plausible mechanisms for dynamic weakening at (sub)seismic rates within natural gouge-filled fault zones (e.g. Brantut and Platt, 2017). Recent high-velocity slip-pulse studies (Chen et al., 2023; Hunfeld et al., 2021) on gouges prepared from the key lithologies in the Groningen gas field have shown that wet faults significantly slip-weaken during a seismic slip pulse, independently of lithology. Hunfeld et al. (2021) proposed that the dynamic weakening observed in their low initial pore fluid pressure ($P_i <$ 0.1 MPa) experiments was likely attributable to TP of the pore fluid, accompanied by the water liquid/vapor phase transition, within the shearing sample (e.g. in a principal shear band).

To reduce uncertainties associated with gouge extrusion observed by Hunfeld et al. (2021), Chen et al. (2023) used a newly developed ring-shear assembly, with a pressure vessel to confine the gouge samples and to apply pore

fluid pressure, to perform both dry and high initial pore fluid pressure ($P_i > 0.5$ MPa) experiments. In addition, the new setup allowed for P–T measurements in near-direct contact with the active slip surface, achieved by reducing the roughness of the rotating piston face. These authors demonstrated that water must be present within the fault zone to cause significant weakening as dry faults do not weaken, again independently of lithology. The absence of significant weakening in dry samples also ruled out a conventional flash heating mechanism. In their high-P_i experiments, on the other hand, Chen et al observed shear-induced gouge dilatancy accompanied by a measured pore fluid pressure drop during dynamic weakening, which excludes the possibility of bulk sample TP and water vaporization. Based on the microstructural observation of abundant voids and shear-parallel "microslip zones" on the scale of a few tens to a few hundreds of μm, they proposed that TP might either occur at the scale of exceedingly localized slip bands, or at grain contact scale, induced by flash heating (e.g. Yao et al., 2018).

Overall, then, TP is presumably effective during small-displacement earthquakes on gouge-filled faults. However, questions remain regarding at what scale TP occurs and whether TP can explain the whole dynamic weakening process, i.e. whether other mechanisms may be involved in different stages of the weakening process as the effectiveness of TP changes with changing fluid transport properties like fluid viscosity and permeability (see Chapter 5). Another important question is whether the physical properties of the wall rocks, like thermal conductivity, permeability, and storage capacity, play a role in the efficiency of localized TP and hence weakening (e.g. Brantut and Mitchell, 2018), since only Ti-alloy pistons were used in the Hunfeld / Chen studies.

The aim of the present study is to investigate the effectiveness of TP and its influence on dynamic slip/shearing behavior of simulated Slochteren sandstone gouge under conditions close to the Groningen reservoir conditions, simulating M 3–4 earthquake slip. We performed seismic slip-pulse experiments under conditions comparable to Chen et al. (2023), using sandstone plates (composed of three fan-shaped pieces) as host-block materials. In addition, we imposed shorter displacements (7.5 cm vs. 15 cm) with a faster slip acceleration (42 m/s^2 vs. 15 m/s^2), maintaining a constant shear stress level (pre-shear stress) before the initiation of the slip pulse. We focus here on microstructural observations with

the aim of characterizing the shear band(s) and quantifying any correlation between the thickness of the shear bands and energy dissipation after seismic slip-pulse experiments. The latter is to explore whether the formation of shear bands is associated with mechanical wear processes and/or heat production (i.e. frictional power density vs. frictional power density, Di Toro et al., 2011) for a seismic slip pulse. Previous results of high-velocity friction experiments on both granular and clay-rich gouges sheared at long displacement (i.e. >1 m) suggested that the growth of the principle slip zone (PSZ) and the production of nano-particles is dominated by mechanical wear processes. (Aretusini et al., 2017; Kuo et al., 2022). We supplement this with numerical modeling to explore the spatial distributions of temperature and pore fluid pressure around the observed shear bands during dynamic weakening.

6.2 Methods

6.2.1 Starting materials

We used crushed Slochteren sandstone obtained from the Groningen gas reservoir, as the starting material (courtesy of the field operator, the Nederlandse Aardolie Maatschappij BV: NAM). The Slochteren sandstone was derived from the core of the Stedum 1 (SDM-1) borehole (Figure 6.1). We collected sandstone cores from both above and below the gas-water contact (GWC, at depth of ~2980m), crushed these into a bulk powder (~25 kg) using a jaw crusher, and used the resulting mixture ($d_{80} < 50$ μm) as a starting material. As noted in Chapter 2, the resulting powder, derived from the core below the GWC, may contain some salts because the high-salinity brine present in the core upon recovery resulted in salt precipitation in the pore space during core storage. The preparation of the powder is to simulate the fine-grained gouge product expected to be present in the principal slip zones of natural faults in the reservoir (Chester and Chester, 1998; Sibson, 1986). The mineral composition of the Slochteren sandstone gouge (SSG) consists of ~75 wt% quartz, ~12 wt% feldspar, and minor amounts of clay minerals (~5 wt%, kaolinite, and phengite), and carbonates (~5 wt%) (Hunfeld et al., 2017). Note that our sample is a mixture of the two sandstone samples used by Hunfeld et al. (2017) and thus slightly different from the two subsequent slip pulse studies by Hunfeld et al. (2021) and Chen et al. (2023).
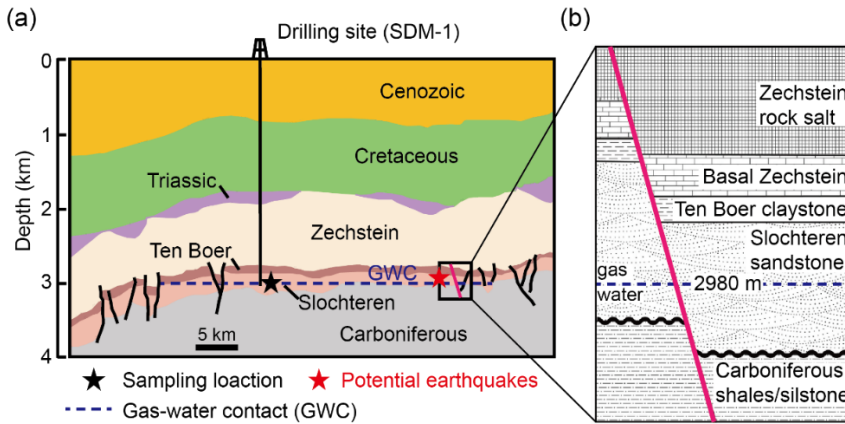
Figure 6.1: *Schematic cross section of the stratigraphy and fault systems in the Groningen gas field (Northern Netherlands). We used Slochteren sandstone retrieved from the borehole at a depth of ~3 km as starting material (black star) as the depth of relocated hypocenters of induced seismic events suggests that most, if not all, events occur within the reservoir (red star; Dost et al., 2020). After Hunfeld (2020).*

6.2.2 Seismic slip-pulse friction experiments

We conducted seismic slip-pulse friction experiments using the Slow to HIgh Velocity rotary-shear Apparatus (SHIVA) at the Istituto Nazionale di Geofisica e Vulcanologia (INGV, Rome), Italy (Figure 6.2a-d; Di Toro et al., 2010). The machine is equipped with a confined and pressurized gouge setup which allows control and measurement of pore fluid pressure and temperature close (described below) to the gouge layer during the experiment (Aretusini et al., 2021). We prepared ~2 mm thick gouge samples (12 g), confined between two solid cylindrical pistons (51.1-mm diameter). Each piston has three tolerance-fit sockets, which normally host three permeable stainless-steel frits that allow fluid access to the gouge layer through small channels in the pistons (Aretusini et al., 2021; Figure 6.2c). In this study, we used Indian sandstone frits (porosity $n \approx 12\%$, thermal conductivity $K = 3.87$ W/m/K, permeability $k \approx 3 \times 10^{-17}$ m^2; Tanikawa et al., 2010) as the main host-rock materials for all experiments, except for one control experiment, which was done with porous steel plates (Mottcorp; thermal conductivity $K = 15$ W/m/K, permeability $k \approx 1 \times 10^{-12}$ m^2) to investigate the effect of the host "rock" properties on frictional behavior (see Table 6.1). Pore fluid pressure is monitored on the rotating (downstream) side of the sample with a pressure transducer (10 MPa full range, with 0.0025 MPa resolution) and on the static (upstream) side with a (small) piezoresistive transducer (Keller, 2MI-PA210, 10 MPa full range, with 0.05 MPa resolution) located under the host-rock plate (~3.85 mm from the static boundary of the gouge layer – Figure 6.2). With

a water-filled pressure vessel, we can provide a confining pressure controlled with a syringe pump (25.86 MPa full range, with ~0.13 MPa resolution) to confine the PVC-wrapped gouge layer and to prevent gouge extrusion during the seismic slip pulse. To monitor temperature during the experiments, a K-type thermocouple was placed inside the static sample holder with the tip at ~1 mm from the static boundary of the gouge layer, located between the frits (Figure 6.2b, c). Additional details on sample preparation are described in supplementary information (see Text S6.1).
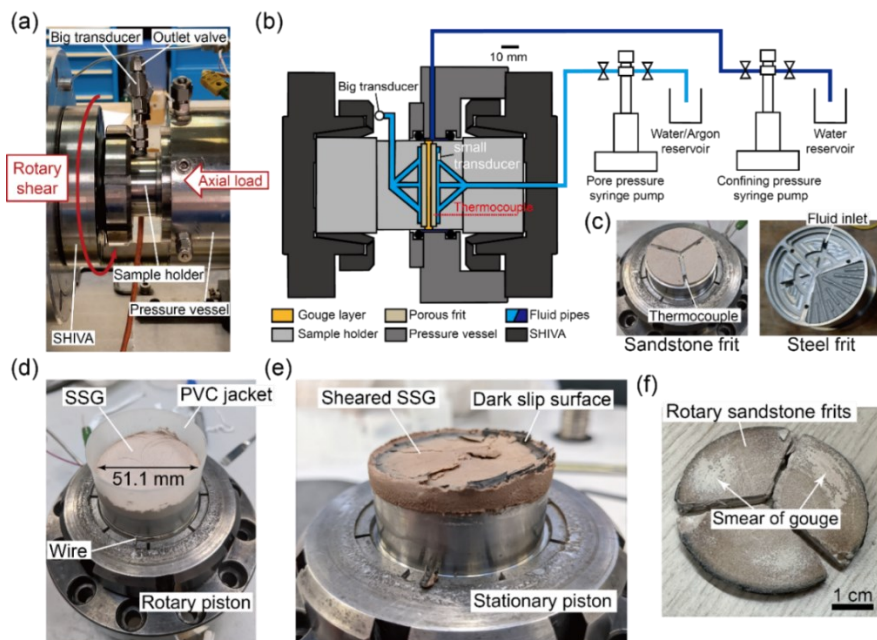
Figure 6.2: The rotary-shear apparatus with the pressurized gouge setup. (a) Photo of the pressurized gouge setup installed in SHIVA. (d) Photo of starting gouge layer in the sample holder. (c) Porous Indian sandstone frits and porous steel frits as host-rock materials. (b) Schematic diagram of the pressurized gouge setup for SHIVA. Large (downstream) and small (upstream) transducers were used to measure the fluid pressure at the rotary and stationary sides, respectively. Two syringe pumps were used to control the confining pressure and initial fluid pressure of the gouge layer. (e) Photo of a SSG sample sheared at 1.5 m/s. A dark ring was observed at the edge of the gouge-host block interface. (f) Photo of the sandstone frits from the rotary side after the experiment. A thin layer (PSZ) of the gouge is attached to the outer region of the gouge-host block interface.

Friction experiments were conducted at an initial effective normal stress σ_{eff} of 6–18 MPa, employing a peak velocity V_{pk} of 0.05–1.8 m/s, variable slip accelerations of 9.4–42 m/s^2 (triangular and Yoffe-type velocity functions, e.g. Harbord et al., 2021) and displacements of 7.5–15 cm, under undrained water- or argon-saturated conditions with an initial pore fluid pressure P_{i} of 0.1 and 1 MPa.

All the tests performed are listed in Table 6.1, along with the corresponding conditions and key observations. After mounting the pressure vessel with the dry gouge sample in SHIVA, we saturated the dry gouge sample with pure water (or argon) through the pore pressure syringe pump (Figure 6.2b). Then, we incrementally applied normal load and pore fluid pressure to achieve the target conditions. Before initiating the slip pulse, the saturated sample was pre-sheared at 5 mm/s for 0.4 m (80 seconds) displacement under drained conditions (i.e. conditioning stage, see also Chapter 5). After the conditioning stage, the shear torque was kept constant at the level of the pre-shear stress for 240 seconds. We then closed the fluid drainage port and waited for another 60 seconds before initiating slip pulse. All the experiments followed identical procedures before the slip pulse.

During the slip pulse, we note that some experiments did not achieve target peak velocity, slip acceleration, or displacement (values with bracket in Table 6.1), due to the combination of machine and sample effects. This occurred particularly in experiments in which a fast acceleration was imposed. For instance, the achieved maximum slip acceleration of ~42 m/s^2 in our experiments was measured at a requested value of 60 m/s^2. In addition, the achieved peak velocity and displacement in the dry gouges were smaller than in the wet gouges, suggesting that the rheology of the sample material influences the machine response. One experiment (s1937, Table 6.1) was taken as a reference experiment to investigate the effect of normal stress and slip acceleration.

After the slip pulse, the sample was held for 300 seconds and we then opened the outlet valve (Figure 6.2a). Throughout each experiment, various data including normal load, shear torque, axial displacement, temperature, confining pressure, pore fluid pressure (upstream and downstream), and pore fluid volume were collected at a logging rate of 200 Hz and 20000 Hz, for the conditioning and the slip-pulse stages, respectively. The apparent friction coefficient μ_{app} is then determined as the ratio of shear stress to initial effective normal stress (applied normal stress σ_n – initial pore fluid pressure measured from the downstream $P_{i\_downstream}$). Incremental displacement is obtained by combining measurements made using both a fine (629760 div, ~0.17 μm) and coarse (400 div, ~267.5 μm) optical encoder on the angular rotation axis of the motor, yielding slip velocity from the derivative with respect to time interval.

Table 6.1: *Experimental conditions and corresponding mechanical data. ID s1833 is the experiment with porous steel frits. ID s1929 and s1931 are the only two experiments without maintaining pre-shear stress. ID s1946 is the experiment using Argon as pore fluid, as indicated in brackets (Continued to the next page).*

ID	σ_{eff} (MPa)	P_{i} (MPa)	P_{c} (MPa)	V_{pk} (m/s)	Acc. / Dec. (m/s^2)	D (m)	μ_{pk} (-)	μ_{min} (-)	μ_{ss} (-)	ΔH_{dyn} (μm)	ΔH_{fin} (μm)	ΔP_{dyn} (MPa)	ΔP_{max} (MPa)	ΔP_{post} (MPa)
s1833 (steel frit)	5.0	0.18	2	1.36	15 / 15	0.13	0.70	0.59	0.58	13	-23	+0.051 / −0.008	0.05	0.01
s1834	4.9	0.13	2	1.37	15 / 15	0.13	0.91	0.41	0.38	-9	7	+0.279 / −0.039	0.28	-0.03
s1929 (no pre-stress)	11.0	1.00	1.97	1.56	15 / 15	0.15	0.79	0.27	0.28	35	12	−0.119 / −0.221	0.77	0.38
s1930	10.8	0.97	2	1.55	15 / 15	0.15	0.71	0.32	0.30	42	33	−0.006 / −0.024	0.69	0.35
s1931 (no pre-stress)	10.9	1.06	1.95	1.57	15 / 15	0.15	0.82	0.25	0.17	87	39	−0.145 / -0.206	1.15	0.26
s1932	10.8	0.96	2.5	1.54	15 / 15	0.15	0.73	0.35	0.35	13	-16	−0.013 / -0.165	1.09	0.61
s1933	11.7	0.12	2	1.55	15 / 15	0.15	0.69	0.29	0.25	16	-36	+0.066 / N/A	0.10	N/A
s1934	10.8	0.97	2.5	1.36 (1.5)	42 / 9.7	0.13	0.68	0.33	0.26	10	15	+0.055 / −0.018	0.71	0.16
s1935	10.1	1.64	2.5	0.9	30 / 30	0.02	0.76	0.56	0.51	18	23	−0.065 / -0.013	-0.05	0.58
s1936	10.8	0.97	2.5	1.21 (1.5)	42 / - (Yoffe)	0.13	0.76	0.48	0.43	3	-103	+0.018 / +0.008	0.30	0.07
s1937	10.8	0.97	2.5	1.53	30 / 30	0.07	0.69	0.38	0.30	16	10	+0.049 / +0.004	0.24	N/A
s1938	16.6	1.24	2.5	1.38 (1.5)	30 / 30	0.06	0.68	0.34	0.24	43	-26	−0.060 / −1.221	1.10	-2.90
s1939	4.9	0.98	2.5	1.52	30 / 30	0.07	0.64	0.45	0.44	1	-6	−0.027 / −0.172	0.88 (up)	0.28 (down)

s1941	10.8	0.96	2.5	1.8 (3)	42 / 12 (42)	0.17	0.70	0.32	0.33	10	8	+0.171 / −0.054	2.63	0.50
s1945	14.0	1.03	3.75	1.46	30 / 30	0.06	0.62	0.38	0.31	14	0	+0.140 / −0.009	1.39	0.64
s1946 (Argon)	10.8	0.98	2.5	1.31	30 / 30	0.05	0.75	0.60	0.48	-20	35	+0.021 / +0.008	0.06 (up)	N/A
s1947	7.9	0.99	2.5	1.53	30 / 30	0.07	0.77	0.40	0.41	12	16	+0.274 / −0.024	0.48	0.35

Note. σ_{eff} = the nominal effective normal stress (applied normal stress $\sigma_n - P_{i\_downstream}$). P_i = the initial pore fluid pressure measured from the downstream pressure transducer. P_c = the confining pressure. V_{pk} = the measured peak slip velocity where the value in brackets is the imposed value. Acc. and Dec. = the measured acceleration and deceleration, respectively, where the value in brackets is the imposed value. D = total displacement. τ_{pk} = the peak shear stress. μ_{pk} = the peak friction. μ_{min} = the minimum friction. μ_{ss} = the nominal steady-state friction determined by fitting the empirical equation of Mizoguchi et al. (2007). ΔH_{dyn} and ΔH_{fin} = the maximum change in axial displacement during the acceleration phase and the final thickness change, respectively, both with respect to the initial gouge thickness measured before the initiation of the slip pulse. ΔP_{dyn} = the maximum change in fluid pressure (downstream vs. upstream, separated with "/") during the acceleration phase. ΔP_{max} = the absolute maximum in fluid pressure change during the slip pulse, mostly measured at the downstream side where two of the experiments were measured at the upstream side as indicated in brackets. ΔP_{post} = the absolute maximum in fluid pressure change after the slip pulse and before the outlet valve opened, mostly measured at the upstream side where one of the experiments was measured at the upstream side as indicated in brackets. N/A means data either with no observable change or with strong oscillations. Frictional power density is calculated as $V_{pk} \times \tau_{min}$, and frictional work density is calculated as Disp. $\times \tau_{min}$.

To explore the total work dissipated in the slip zone and the total power dissipated within the gouge layer, per unit area of slip surface (e.g. Aretusini et al., 2017; Di Toro et al., 2011; Kuo et al., 2022), we introduce the frictional work density (FWD) and the frictional power density (FPD), respectively, which can be defined as:

$$FWD = \int_0^D \tau(x)dx, \qquad (6.1)$$

with D the total displacement and $\tau(x)$ the shear stress evolution with displacement x, and

$$FPD = FWD/\Delta t \qquad (6.2)$$

with Δt the duration of the experiment. The calculated FWD and FPD from the mechanical data will be correlated with the microstructure of the gouge layer described below.

6.2.3 Analytical methods

After the deformed gouge samples plus sandstone frits were extracted and completely dry (i.e. air-dried under room temperature), we impregnated the gouge together with the sandstone host blocks, if they were still complete and attached to the deformed gouge (3 out of 20), with epoxy resin. Then we prepared petrographic thin sections, cut axially ~3 mm away from the outer boundary towards the center of the sandstone frit. The sections were prepared with a thickness of 30 μm, mounted on silica glass, and polished with 0.3-μm-sized alumina powder for optical (OM), scanning electron microscopy (SEM), and transmission electron microscope (TEM) analysis. The analytical methods and associated instruments are listed as follows:

1. A ZEISS Axioscan 7 Microscope Slide Scanner and a Zeiss EVO 15 environmental SEM-EDS, both installed at Utrecht University, were used to investigate the microstructures, and to determine the semi-quantitative chemical composition of the minerals in the gouge layer. For SEM-EDS, the petrographic sections were sputtered with Pt/Pd at 5-nm thickness and semi-quantitatively analyzed at 15 kV with a focused beam of ~1 μm in diameter.

2. A Thermo Fisher Helios G3 Nanolab Focused Ion Beam-Scanning Electron Microscopy (FIB-SEM) and A Thermo Fisher Talos F200X transmission electron microscope (TEM) at the Utrecht University were used to retrieve information, including selected area diffraction patterns (SADP), on experimental products that could not be identified otherwise.

3. The software packages ilastik and ImageJ (available at https://www.ilastik.org/ and https://imagej.nih.gov/ij/, respectively) were used to process back scattered electron (BSE) images to quantify the particle size distribution (PSD) of the fragmented grains within the gouge layers. ilastik was first applied to identify grain boundaries within the fine-grained matrix based on various object feature selections (e.g. color, intensity, edge, and texture). Once we established a standard for grain boundary identification and output grain segmentation images, we applied batch processing to the rest of the images with the same standard. Then, ImageJ was used to measure the particle size distribution for all the segmented images.

6.3 Results

6.3.1 Frictional behavior

Figure 6.3 shows typical results on the frictional behavior, pore fluid pressure, and gouge thickness obtained during the conditioning and slip-pulse stages of the present tests. Here we present the data obtained from experiment s1930. Note that temperature data are not presented here because we do not observe visible temperature change (only 4–5°C) during the slip pulse, likely due to problems (noise) in measuring temperature, as shown in Figure S6.1. During the conditioning stage, the apparent friction coefficient μ_{app} increases from an initial value of ~0.5 to a steady-state value of ~0.7, accompanied by a decrease in both the gouge thickness and the downstream pore fluid pressure. The conditioning data at different effective normal stresses (5-17 MPa) are shown in Figure S6.2, similar to Figure 6.3. After the slip pulse was initiated and the slip started to accelerate, we observed strong oscillations in shear stress and thus μ_{app} (light grey curve) at the initial sliding after which the oscillations become smaller with increasing displacement. This is mainly due to machine effects related to the sudden application of the fast acceleration, which causes variation in the friction values that are particularly significant for the peak friction μ_{pk}. Taking this into account, to determine the peak friction μ_{pk} and minimum steady-state friction μ_{min}, we used the smoothed friction data using a moving average of 100 data points (= 10 ms), the black curve in Figure 6.3b, but also noted the upper and lower bounds of the entire friction envelope. We showed that the data smoothing with the choice of the window size does not influence how we determined the frictional parameters, in particular μ_{pk} (see Figure S6.3). This is important because the choice of the μ_{pk} and μ_{min} would further affect the determination of the weakening

distance and weakening rate, which are used to compare to previous slip-pulse data (Chen et al., 2023; Hunfeld et al., 2021). During the acceleration phase, the μ_{app} firstly overcome static friction μ_s within ~0.05 second and then constantly decreased, along with continuous gouge dilatation. Pore fluid pressures measured from both the downstream and upstream do not show significant changes until 80% of the shear strength was reduced at which point, they both increased almost simultaneously. During the deceleration phase, the μ_{app} continued to drop to a minimum value of ~0.3, reached within ~0.03 second after peak velocity was reached and began to increase to ~0.45 while the thickness of the gouge layer remains constant. In addition, the downstream and upstream pore fluid pressure kept increasing up to 1.5 and 1.2 MPa, respectively. After the experiment, the downstream and upstream fluid pressures were observed to continuously increase up to a peak value of ~1.66 and ~1.52 MPa (not fully shown in Figure 6.3) and began to decrease after reaching these peak values. Typically, the pressure increase and subsequent drop were observed to be more rapid in the downstream than in the upstream.
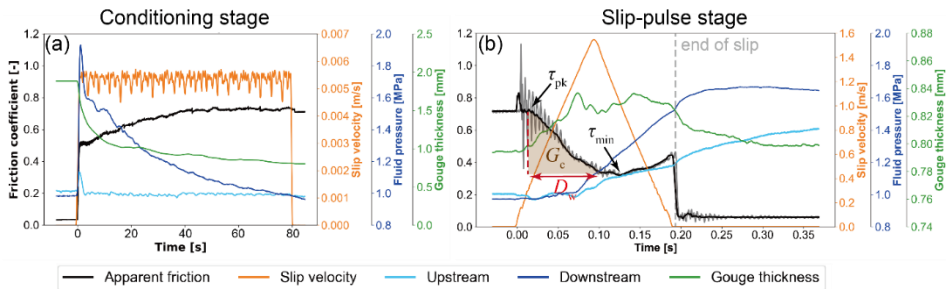
Figure 6.3: *Typical results of (a) the conditioning and (b) the slip-pulse stage and part of the post-slip stage obtained in the present experiments. The data here are for sample s1930 performed at an effective normal stress σ_{eff} of 10.8 MPa, and an initial water pressure P_i of 0.97 MPa. The gouge layer was deformed at a constant slip rate of ~5 mm/s and in a pulse reaching ~1.5 m/s for ~0.4 m and ~0.15 m displacement during the conditioning and slip-pulse stages, respectively. Fluid pressures were measured from both the upstream (stationary) side and the downstream (rotary) side. The apparent friction coefficient, $\mu_{app} = \tau/(\sigma_n - P_i)$ was calculated using P_i obtained from the downstream side before shearing. Pre-shear stress was kept constant at ~7.56 MPa (0.7 × 10.8 MPa) before the initiation of the seismic slip-pulse. Strong oscillations in slip-pulse friction data (gray curve) are mainly due to the sudden application of fast acceleration by the motor. The data was smoothed using a moving average of a window size of 100 data points (black curve). G_c refers to the breakdown work obtained from the area below the smoothed friction curve over a slip weakening distance D_w.*

A comparison of the mechanical data (apparent friction, slip velocity, downstream pore fluid pressure, and axial displacement) obtained under various conditions is shown in Figure 6.4. In general, all gouge samples show significant

slip-weakening when water is present with sandstone host rocks, with the exception of the dry/argon-filled sample, and the test with porous steel frits (Figure 6.4a, b). This weakening shows no sytematic dependence on normal stress, acceleration, or type of imposed velocity function (Figure 6.4c, d). Independent of environmental conditions, μ_{pk} lies within the range of 0.6–0.8 (after smoothing). For the wet gouges, all the μ_{min} – values with sandstone host rocks lie between 0.3–0.5, while μ_{min} for the wet gouge with steel host blocks (dark purple curve in Figure 6.4a) and the dry gouge with sandstone frits (red curve in Figure 6.4b) is ~0.6. Most wet gouges show dilatation (up to 0.04 mm) during the acceleration phase, except for the P_i = 0.1 and 2 MPa experiments, which show an almost instantaneous compaction of ~0.03 mm. On the other hand, the dry gouge only displays compaction behavior. In Figure 6.4d, we compare the wet gouges with triangular velocity function with different slip accelerations. We observe a similar μ_{min} – value of ~0.35, but this is achieved slightly faster in the high acceleration experiment. For the Yoffe function, the μ_{min} is 0.5 which is 0.15–0.2 larger than the experiments with the triangular function, while the initial weakening seems to follow the same slope as all the other experiments. In all experiments, a re-strenghting behavior can be observed during the deceleration phase.
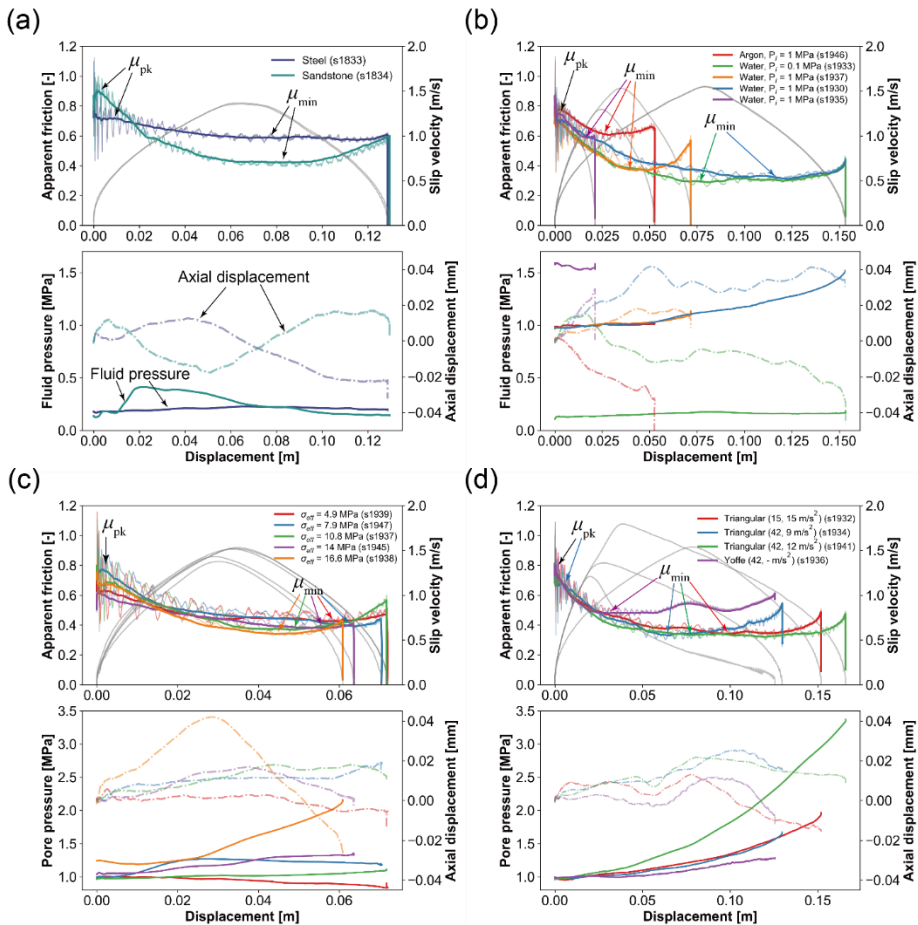
Figure 6.4: *Comparison of the friction, slip velocity, fluid type/pressure, and gouge thickness data versus displacement for all the high-velocity slip-pulse experiments under various conditions. (a) Effect of host-block material (P_i = 0.1 MPa); (b) Effect of the type of pore fluid, initial fluid pressure, and displacement; (c) Effect of initial effective normal stress; (d) Effect of velocity function. The dash-dot line represents axial displacement data and the solid line represents fluid pressure data measured at the downstream end/side of the sample.*

6.3.2 Slip-weakening and -restrengthening parameters

We observe slip-weakening behavior in all slip-pulse experiments and weakening curves that are comparable to previous results from high velocity experiments. Thus, the slip-weakening curve might be fitted by the empirical equation proposed by Mizoguchi et al. (2007), based on the post-peak slip weakening distance D_w over which shear stress (or apparent friction μ_{app}) drops to a conceptual 5% of the initial peak value:

$$\mu_{app} = \mu_{ss} + (\mu_{pk} - \mu_{ss})\, e^{\left[\frac{\ln 0.05(x - x_{pk})}{D_w}\right]} \tag{6.3}$$

Here x_{pk} the displacement measured up to the peak friction μ_{pk}. To obtain nominal steady-state friction parameters μ_{ss} and D_w for all experiments with restrengthening during the deceleration phase, we fitted equation 6.3 to the friction data between the μ_{pk} and μ_{min}, defined as the type I fitting method. Note that nominal steady state was not achieved in our runs, so that μ_{ss} obtained from the fitting method is always lower than the minimum friction reached in the experiments. As an alternative strategy, we also fitted (6.3) to the friction data by fixing μ_{ss} to equal μ_{min}, allowing D_w to be the only free parameter for fitting, defined as the type II fitting method. Based on the fitting curve, the breakdown work G_c (i.e. fracture energy) corresponding to each slip-pulse experiment was determined by taking the integral in equation 6.3 from μ_{pk} (or τ_{pk}) over D_w. Additionally, we followed the same concept to obtain a fit to the re-strengthening curve during the deceleration phase, using the modified equation:

$$\mu_{app} = \mu_{re} + (\mu_{ss} - \mu_{re})\, e^{\left[-\frac{\ln 0.05(x - x_{ss})}{D_{re}}\right]} \tag{6.4}$$

where μ_{re} is the final friction at the end of the re-strengthening phase, x_{ss} is the displacement measured up to the minimum friction μ_{min}, and D_{re} is the distance over which shear stress (or μ_{app}) increases to a conceptual 95% of the minimum value.

Figure 6.5 shows the slip-weakening parameters against effective normal stress and slip acceleration. The error bars shown for μ_{pk} and μ_{ss} are determined from the maximum and minimum values of the friction envelope curves. We find that μ_{pk} has large error bars and shows a relatively small or no trend with increasing effective normal stress and slip acceleration (Figure 6a, b). On the other hand, μ_{ss} shows a linearly decreasing trend with increasing effective normal stress, consistent with previous studies obtained for natural fault gouges (Mizoguchi et al., 2007; Yao et al., 2013; Figure 6a), while its dependence on slip acceleration is relatively small or absent in the range investigated (Figure 6.5b). Stress drop $\Delta\tau$ is also shown to be dependent on the effective normal stress, following a linear growth, but only weakly decreases with acceleration (Figure 6.5c, d). Both the D_w and the derived parameters G_c show a linear dependence on the effective normal stress where the D_w obtained from type II fitting shows much less dependence on effective normal stress (Figure 6.5e, g). On the other hand, D_{re} and G_{re} show more or less no dependence on effective normal stress (Figure

216

6.5e, g). All these four parameters (i.e. D_w, D_{re}, G_w, and G_{re}) do not reveal a clear dependence on slip acceleration (Figure 6.5f, h).
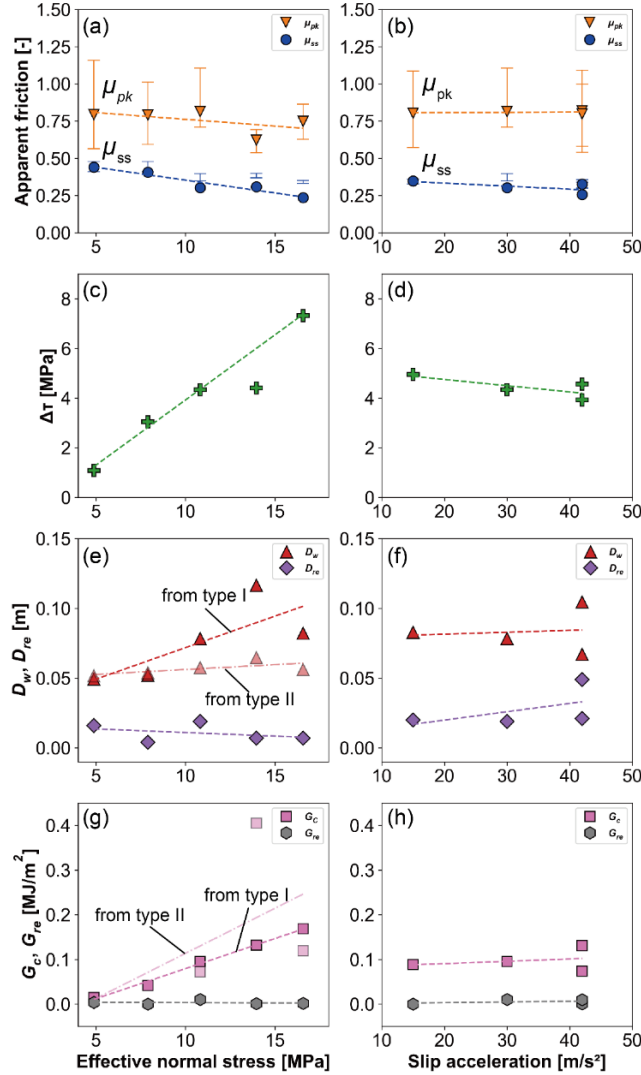
Figure 6.5: *Frictional parameters as a function of effective normal stress and slip acceleration. (a, b) Apparent peak friction μ_{pk} and nominal steady-state friction μ_{ss}. The error bars shown here are determined from the maximum and minimum values of the friction envelope curves instead of from the empirical fitting. Thus, in some cases, the fitted μ_{ss} are above the fitted data point; (c, d) Dynamic stress drop $\Delta\tau$; (e, f) Slip weakening distance D_w and slip strengthening distance D_{re}; (g, h) Breakdown work G_c and restrengthening work G_{re}. The upper and the lower bounds of the data were calculated based on the highest and lowest μ_{pk} and μ_{min} values, respectively, due to the strong friction oscillations at the initial slip. The obtained $\Delta\tau$ without error bar was calculated based on the smoothed shear stress curve. The data points and the dashed lines with lighter color in (e) and (g) indicate the fitted results obtained from type II fitting method (see the main text).*

6.3.3 Dilatation and fluid pressure data

We determined another four key parameters derived from the gouge thickness and fluid pressure data for each experiment, following the approach described by Chen et al. (2023). For the gouge thickness data, we determined the maximum change in axial displacement during the acceleration phase (ΔH_{dyn}) and the final thickness change (ΔH_{fin}), both with respect to initial gouge thickness measured before the initiation of the slip pulse. For the fluid pressure data, we took the maximum change in fluid pressure, measured at either the rotary (downstream) or stationary (upstream) side of the sample during the acceleration phase, as ΔP_{dyn}. The absolute maximum in fluid pressure change ΔP_{max} was mostly measured at the downstream side and usually reached after the end of the slip-pulse. All the measurement results are summarized in Table 6.1.

In all wet experiments, we observed a positive thickness change ΔH_{dyn} (dilatation) during the acceleration phase, followed by compaction at the later stage during, or after the slip pulse (Figure 6.4). On the other hand, the experiment with Argon fluid only showed continued compaction (Figure 6.4b). Overall, net dilatation ($\Delta H_{fin} > 0$) is observed in most wet experiments where ongoing compaction is always observed after the cessation of the slip-pulse.

Figure 6.6a and b shows the relationship between the dynamic fluid pressure change ΔP_{dyn} and the dilatation ΔH_{dyn} for both the downstream and upstream sensors from the wet experiments at high-P ($P_i \approx 1$ MPa) conditions. For the wet experiments with low acceleration (Acc. = 15 m/s^2, green squares), we observe a decrease in the dynamic fluid pressure change ΔP_{dyn} at both the downstream and the upstream sides upon imposing the slip-pulse, accompanied by dilatation. In contrast, most of the high-acceleration experiments (Acc. = 30 and 42 m/s^2, blue triangles and red circles) showed pore pressure increase at the downstream side, independently of the normal stress. Figure 6.6c and d show the maximum fluid pressure ΔP_{max} against normal stress and slip acceleration. Though data are few, ΔP_{max} does not appear to systematically correlate with normal stress or acceleration.
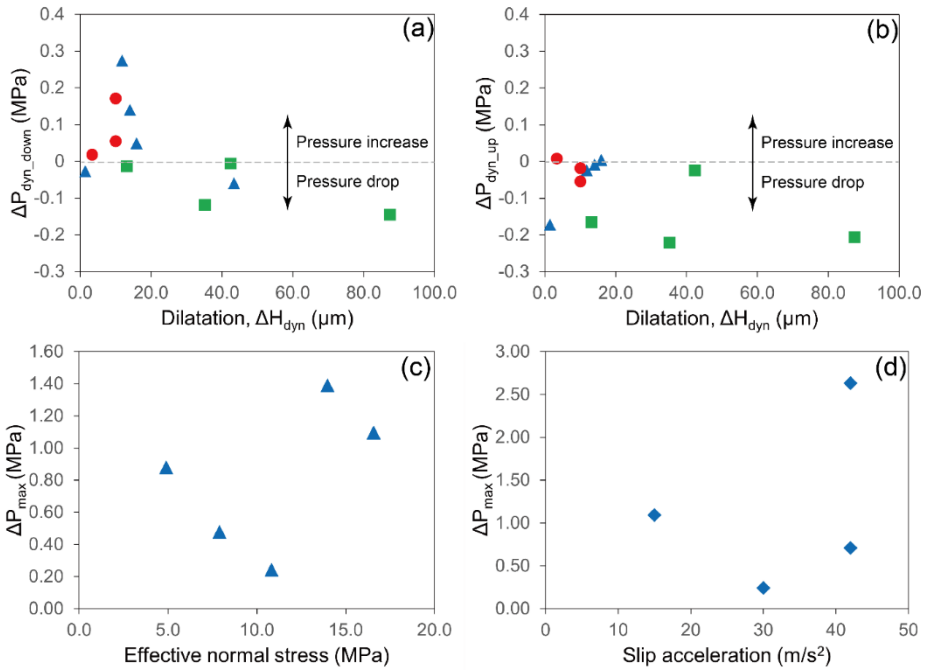
Figure 6.6: *Dynamic fluid pressure ΔP_{dyn} measured from (a) the rotary side (downstream) and (b) the stationary side (upstream) of the sample as a function of gouge dilatation ΔH_{dyn} during the slip acceleration phase. Maximum fluid pressure ΔP_{max}, measured from the downstream side, as a function of (c) normal stress and (d) slip acceleration. Green squares indicate the experiments performed at a slip acceleration of 15 m/s². Blue triangles indicate the experiments performed at a slip acceleration of 30 m/s². Red circles indicate the experiments performed at a slip acceleration of 42 m/s².*

6.3.4 Microstructural observations

6.3.4.1 Optical microscopy (OM)

Figure 6.7 shows the plane-polarized optical images for the conditioned gouge and the slip-pulse gouges deformed at different normal stresses. The wet gouge after the conditioning stage exhibited two distinct regions without a clearly distinguishable boundary (Figure 6.7a). The upper ~1/3 portion (i.e. rotary side) of the gouge layer exhibits a relatively low porosity and finer grain size as compared to the bottom region (i.e. stationary side). Here, we characterize the upper dense and fine-grained regime as slip zone (SZ) and the bottom porous and coarse-grained regime as damage zone (DZ), as indicated in Figure 6.7a. Similar microstructures are also observed in the wet slip-pulse gouges under different σ_{eff} (as indicated in Figure 6.7b, c, d, f), except for the $\sigma_{eff} \approx 17$ MPa experiment where the grain size and porosity within the bulk gouge layer is spatially homogeneous (Figure 6.7b-g). In the case of the wet slip-pulse gouges at σ_{eff} of 11 MPa (Figure

6.7d, e), we observe an extremely thin layer (<50 μm thick) with finer grain sizes as compared to the SZ at the top gouge-host rock boundary (rotary side) of the gouge sample. We characterized this zone as the principle slip zone (PSZ), defined as the finest distinguishable zones (finer than the SZ) within each sample (hence the zones with presumably the most shear strain). A PSZ can also be identified in the dry slip-pulse gouge, though a SZ is not distinguishable (Figure 6.7h). By contrast, under OM observations, a PSZ is difficult to identify (or absent) in the other wet gouge samples, which will be further characterized in SEM analyses as well as particle size analyses. Generally, the SZ contains a few randomly oriented angular to sub-rounded clasts ($d > 50$ μm) of quartz and minor feldspar and dolomite, and the DZ shows more abundant large quartz grains and shear-parallel fractures. Grains within the PSZ are too small to identify their size and shape from OM analysis. In addition, for all wet gouges, we observe a few continuous thin (< 100 μm) layers with black color oriented in the shear direction, which are generally randomly distributed across the width of the gouge layer. Dry gouge does not show clear layers of the black/opaque material (Figure 6.7h). Apart from sections cut along the slip direction and perpendicular to the shear plane, we also prepared one thin section cut perpendicular to the shear direction (i.e. across the center and the edge of the gouge disk) from reference gouge sample s1937 to observe any radial effects on wet gouge microstructure (see Figure S6.4). For the sample studied, the shear-parallel and shear-perpendicular microstructures were similar, with little variation in the thickness of the SZ and DZ, or in the distribution of black layers.
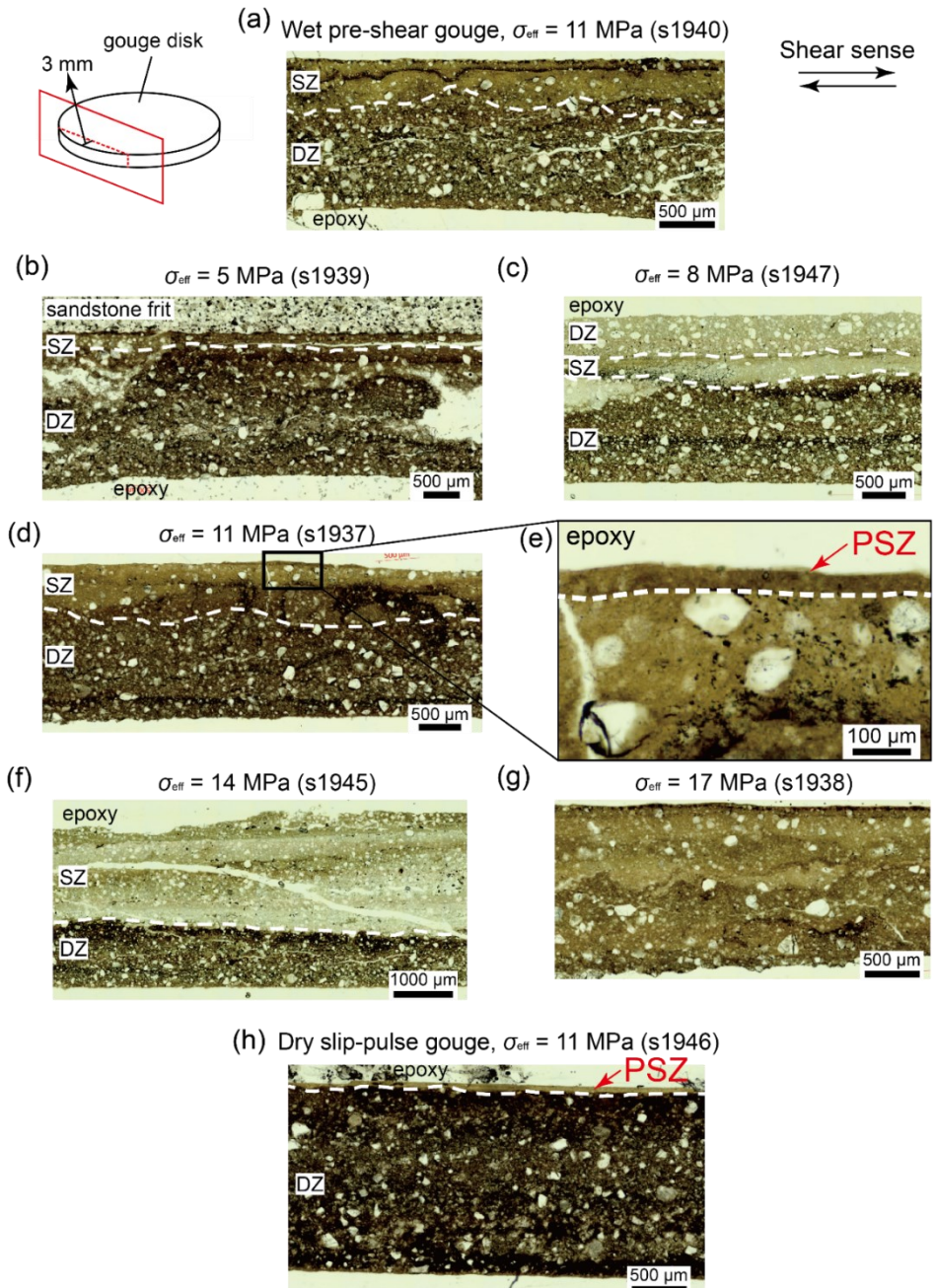
Figure 6.7: *Plane-polarized optical images of the deformed SSG layer. (a) Wet conditioned gouges deformed at σ_eff = 11 MPa (s1940, not presented in Table 6.1). (b-g) Wet slip-pulse gouges deformed at varied σ_eff in the range of 5–17 MPa, with (g) a zoom-in image of the PSZ. (h) Dry slip-pulse gouge deformed at σ_eff = 11 MPa.*

6.3.4.2 Scanning electron microscopy (SEM)

Figure 6.8 shows representative backscattered SEM images of the wet conditioned gouge and the wet slip-pulse gouges at different σ_{eff} (5 to 17 MPa). For the conditioned gouge, we can observe a gradual decrease in grain size from larger than 150 μm within the DZ in the lower half of the sample to a few micrometers within the SZ, near the upper boundary, consistent with the OM observations (Figure 6.7a). From low to high normal stress, the microstructures of the wet slip-pulse gouges do not show significant differences compared to the conditioned gouge, with the exception of the σ_{eff} = 8 MPa and σ_{eff} = 14 MPa experiments which show well-developed interlayer structures of fine- (i.e. SZ) and coarse-grained (i.e. DZ) layers (Figure 6.8b-f). At relatively low σ_{eff} (i.e. 5 MPa), a PSZ with <100 μm thickness at the gouge-host rock interface seems to be present though grains with a size of ~80–100 μm can still be observed (zoom-in in Figure 6.8b). At the highest normal stress (e.g. 18 MPa; Figure 6.8f), the grain size distribution in the bulk gouge layer is much more uniform. At σ_{eff} of 8 and 14 MPa, the gouge layer exhibits rather complicated layering structures compared to the other gouges. In other words, the observed further size reduction zone (or PSZ) is not at the boundary with the sandstone frits, which is possibly associated with breaking of the sandstone frits during the experiments as observed during the sample recovery. To characterize these interlayer structures and determine whether these further size reduction zones are PSZ and the corresponding thickness, we performed quantitative analyses of particle size distribution of these distinct layers.
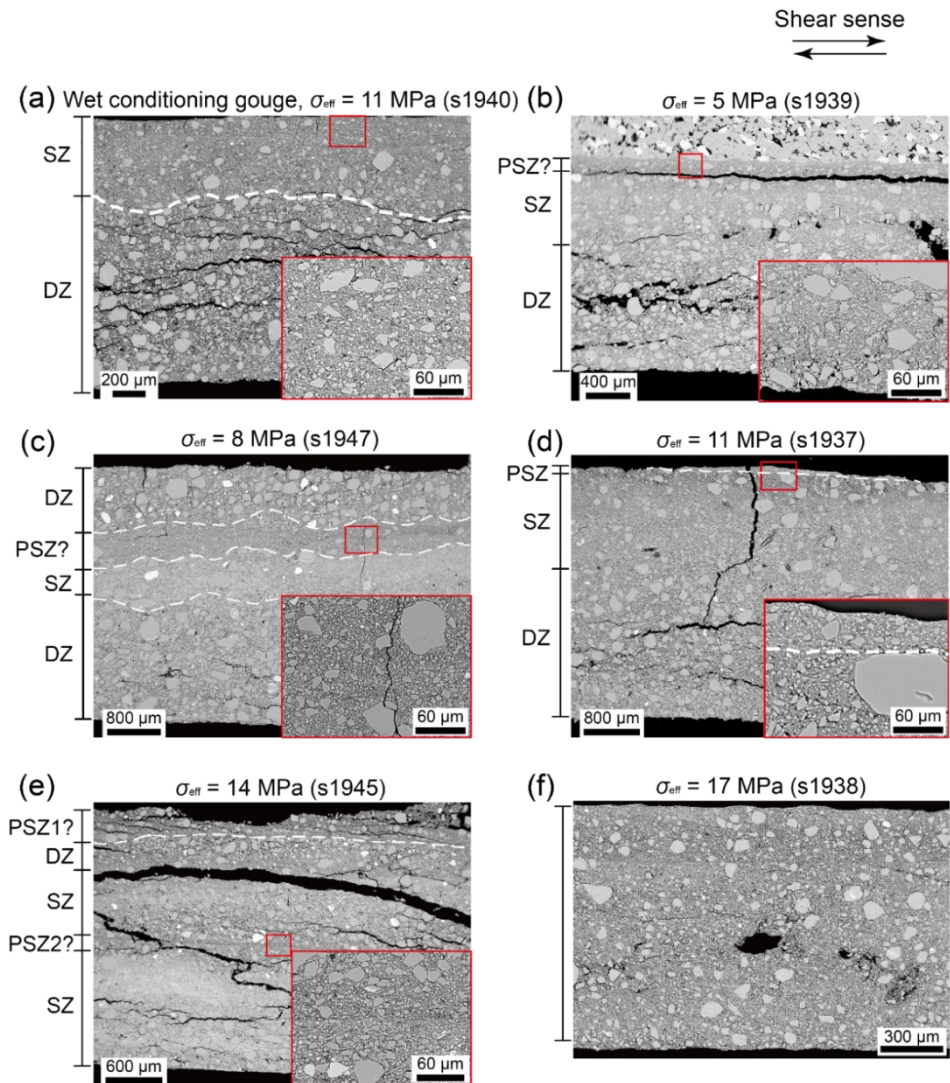
Figure 6.8: *Backscattered SEM images of the wet sheared gouge layer. (a) Starting material after the conditioning stage. The SZ and DZ domains can be identified with a transition zone, indicated by the black dashed line in between; (b) Slip-pulse gouge deformed at σ_{eff} of 5 MPa. A PSZ with <100 μm thickness seems to be present in between the SZ and the sandstone host rock; (c) At σ_{eff} of 8 MPa. A PSZ seems to be present in between the DZ and SZ. (d) At σ_{eff} of 11 MPa. A PSZ less than ~80 μm thickness is observed on the upper part of the SZ. (e) At σ_{eff} of 14 MPa. Multiple layers with variations in porosity and grain size can be observed. Two fine-grained layers (PSZ?) in contrast to the SZ might be identified. (f) At σ_{eff} of 17 MPa. The bulk gouge layer exhibits a relatively uniform PSD. The identification of the PSZ, SZ, and DZ is based on the preliminary visual observation of the SEM-BSE images without further PSD analysis.*

6.3.4.3. Focused ion beam–transmission electron microscopy (FIB-TEM)

We investigated the fine PSZ's seen in the SEM-BSE and OM images, and the black/opaque layers identified using OM, with FIB-TEM and selected area electron diffraction (SAED) - to retrieve information on the nature of the fine-grained materials within the wet samples (e.g. crystalline nanoparticles or amorphous). Figure 6.9 shows the selected locations of the FIB foils from the thin section cut perpendicular to the shear direction (see Figure S6.4) for analyzing the PSZ and the black layer and the associated SAED patterns. Based on the FIB foil observation, nanoparticles (d >100–200 nm) are crystalline and are pervasive within both the PSZ and the black layer. No amorphous material is present in either region (Figure 6.9d, e). It is likely that the PSZ is denser (less porous) than the black layer; however, the analyzed sample area (~150 μm^2) may not be representative enough.
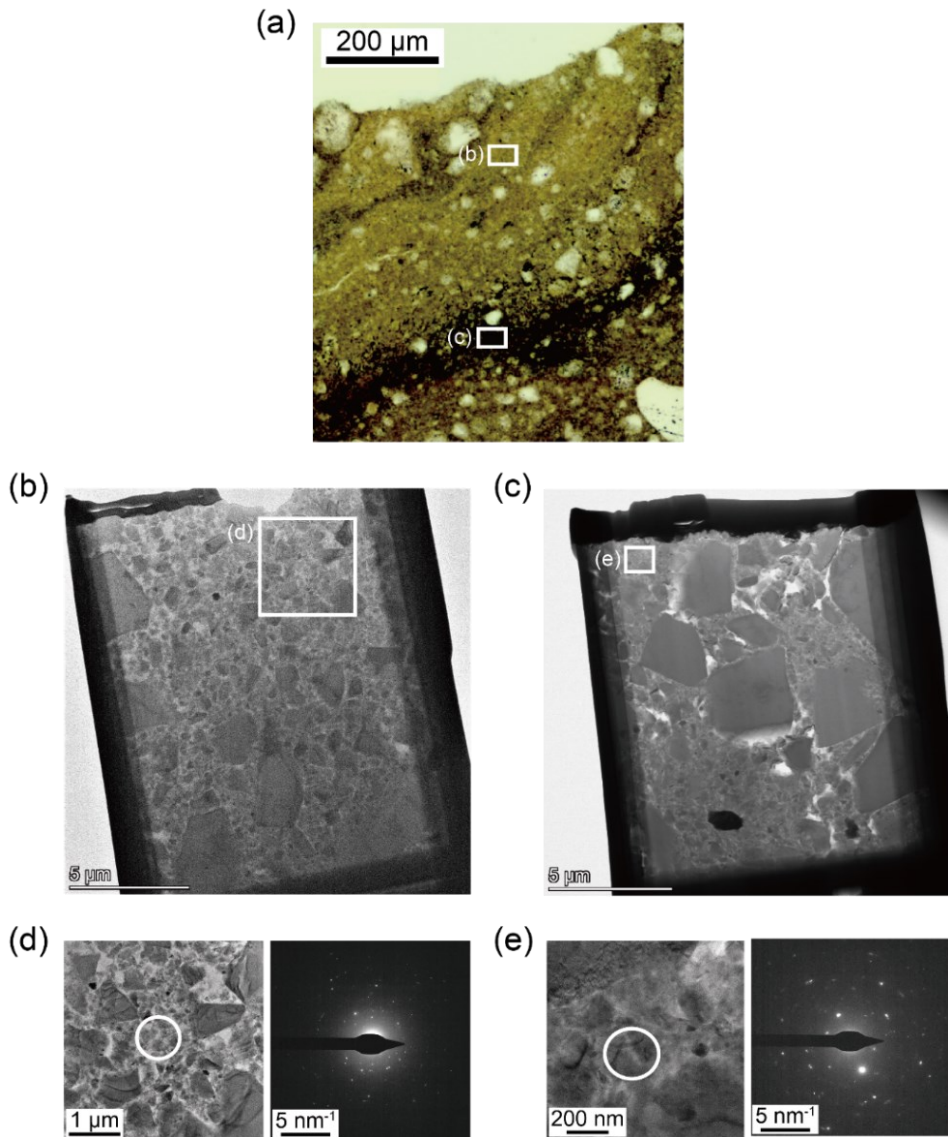
Figure 6.9: *A partial OM image recovered from wet reference experiment (s1937) and the bright field TEM images of the FIB foils collected from (b) the PSZ and (c) the black layer with (d, e) the SAED results from the corresponding white circle area.*

6.3.5 Particle size distribution (PSD)

To characterize the interlayer structures of the gouge layer and to determine the thickness of PSZ, we performed PSD analysis on the wet conditioned gouge (s1940) and wet slip-pulse gouges (s1935, s1937, and s1939). For each sample, we collected between 5–6 BSE images with magnification of x300-x700,

225

depending on the width of the PSZ and the grain sizes, for both PSZ and SZ. We have shown that the total analyzed area is representative enough to be used for PSD analysis (see Text S6.2, Figure S6.6, and S6.7 in for more details). We categorized the interlayer structures within the gouge layer, specifically based on the variation in grain size and the BSE grey-scale contrast between the PSZ and SZ as compared to the conditioning microstructure, into three types (Figure 6.10). Type I represents a gouge layer with a visible PSZ, adjacent to the sandstone frits, which has a sharp boundary and gray-scale intensity contrast against the SZ. In this case, the width of the PSZ can be easily quantified. Type II represents a gouge layer with a PSZ which is not at the boundary with the sandstone frits, but boundaries can be identified based on the contrast in the gray-scale intensity against the adjacent zone (i.e. SZ or DZ). Type III represents a gouge layer without a visible PSZ but with a PSZ that may be identified based on the grain size variation when compared with the SZ.

The PSD data are plotted as particle density (number of grains divided by total grain-count area, mm^2) distribution versus mean particle diameter, using a logarithmic scale. In general, our results show that the PSZ has more abundant fine grains (<2 μm) than the SZ for the conditioned gouge studied and for all types of the interlayer structures of the slip-pulse gouges. By comparison, the PSZ and DZ for the type I and III do not exhibit higher particle density than the conditioning SZ and DZ, respectively, while for the PSZ both the PSD curves shift to smaller grains, in particular for the type III. For the type II, the particle density of the slip-pulse gouges for both PSZ and SZ is higher than the conditioned gouges. The measured thicknesses of the PSZ are plotted versus both FWD and FPD (Figure 6.11). Generally, the PSZ thickness determined from the default displacement experiments (i.e. 7.5 cm displacement, experiment s1937) is approximately 30–60 μm, whereas the relatively long-displacement experiment (15 cm displacement, experiment s1932) produced a much thicker PSZ up to 200 μm. Note that the PSZ thickness determined from the slip-pulse gouge at σ_{eff} of 8 MPa (e.g. Figure 6.8c, experiment s1947) is anomalously thick (200 μm).
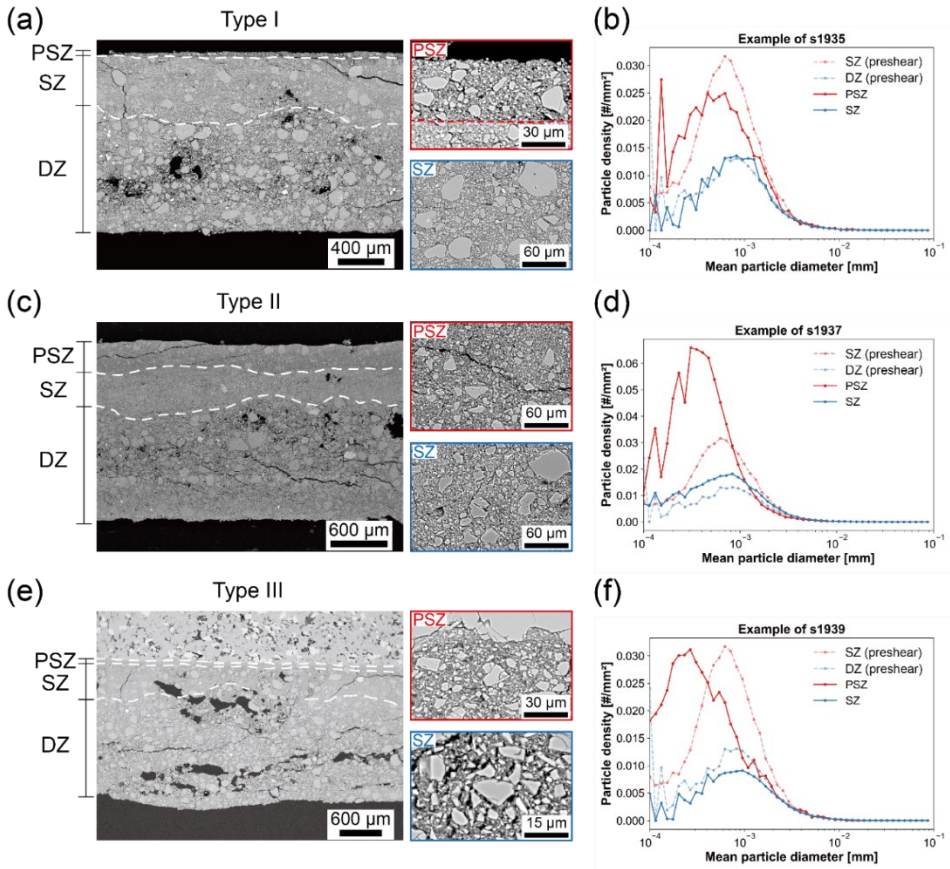
Figure 6.10: *Three different types of interlayer structures (a-c-e) based on the SEM-BSE images of samples s1935, s1937, and s1939. (b-d-f) Plots of the particle density against mean particle diameter for the SZ and DZ of the conditioned gouges and the PSZ and SZ for the slip-pulse gouges. The microstructure of the type I example was obtained from experiment s1935, which shows the gouge microstructure after a slip pulse with ~0.02 m displacement.*
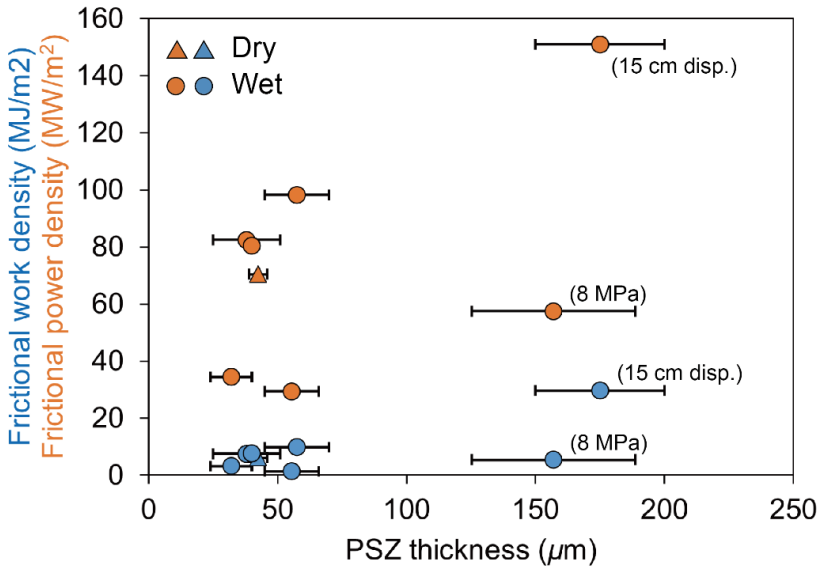
Figure 6.11: *Frictional work density (FWD) and frictional power density (FPD) against PSZ thickness. Error bars indicate the variation of PSZ width along the observed petrographic thin section.*

6.3.6 Numerical thermal modeling

Owing to the lack of an observable temperature change, to retrieve information of temperature and pore fluid pressure during the slip-pulse, and hence to assess the role of thermal pressurization (TP, Wibberley and Shimamoto, 2005), we developed a 2-D axisymmetric finite element model (FEM) using the COMSOL package, (Figure 6.12; e.g. Chen et al., 2013; Hunfeld et al., 2021; Kuo et al., 2022). With the modeling, we aim to directly compare the modeled pore fluid pressure to the measured data and then infer the slip-zone temperature. In the modeling, we assume all the frictional work was converted to heat during slip and distributed over the entire principal slip zone. We took 100 μm as the average PSZ thickness based on the microstructural observations. All the thermal and transport properties of the gouge sample, host-rock materials, and sample holder were set based on our best knowledge, as listed in Table S6.1. Since a large geometry of the sample assembly was simulated, we used a fixed temperature boundary condition with an initial temperature of 25°C and the fluid was assumed to be enclosed within the gouge layer and the porous sandstone host-rocks (i.e. no flux boundary conditions). We modeled both the local and PSZ-averaged temperature and pore pressure evolution at the location of $r = 2/3 \times r_0$ (upper monitoring point in Figure 6.12b; r_0 is the radius of the sample holder) and within

the PSZ, respectively. The radial location of the upper monitoring point is selected to be consistent with the radial location of the upstream (stationary) pressure sensor and thermocouple. The main differences are that the upstream pressure sensor is under the sandstone frit without contacting the gouge layer and the thermal couple is located between the sandstone frits, ~1 mm away from the PSZ (Figure 6.2c). The averaged temperature and pore pressure within the PSZ are calculated as $\int T, P(r,z)2\pi r dr/\pi r^2$, the integral of the local value within the PSZ over the area of the sliding surface. Thus, the modeled temperature and fluid pressure increase would always be higher from the local measurement than from the PSZ.

In the simulation of the reference experiment s1937 (Figure 6.12e, f), our results show that the wet gouge reaches a maximum temperature and pore pressure increase at the upper monitoring point of ~350°C and ~1.1 MPa, respectively, after ~0.07s of the slip-pulse. For the PSZ scale, the values are slightly lower at ~280°C and ~0.8 MPa. Compared to the measurement of the pore fluid pressure (the yellow and gray curves), it is shown that the maximum fluid pressure increase (0.2 MPa) is 0.6–0.9 MPa lower than the modeled results. The delay in the pressure signal due to drainage is not significant in the controlled experiment (s1937) which is absent in the model. The role of TP and whether vaporization occurred within the slip zone will be further discussed in section 5.4.2.2.
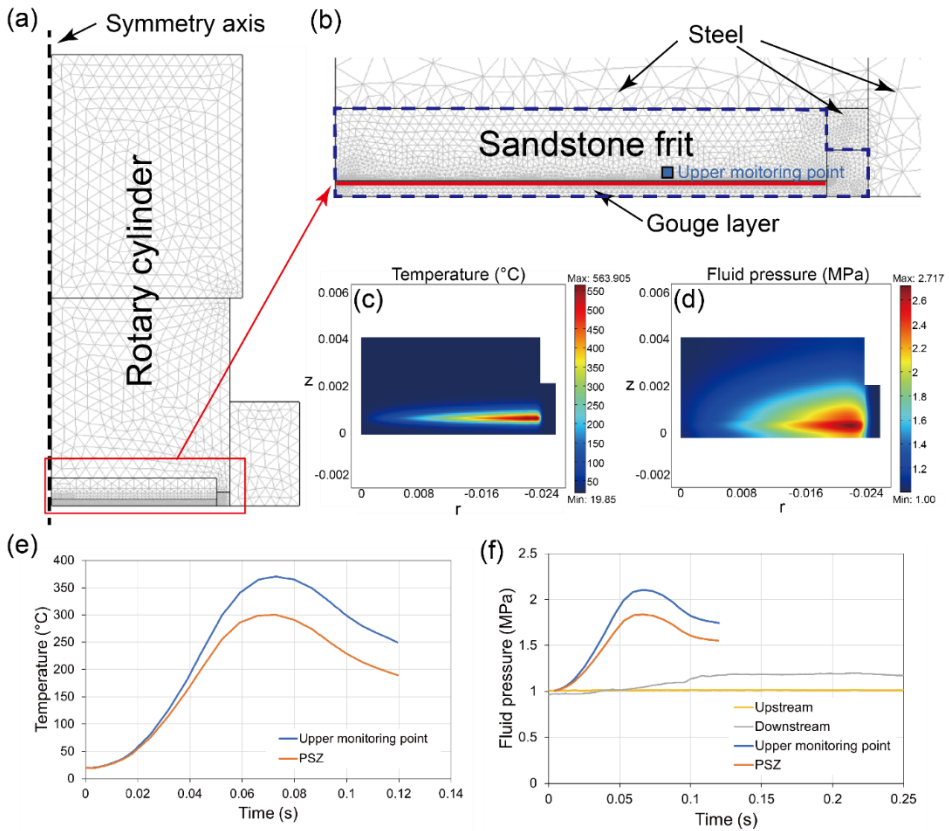
Figure 6.12: Setup and result of the 2-D FEM model. (a and b) Geometry, mesh, and material distribution for the 2-D symmetrical model domain as well as the boundary conditions of the fluid flux (no flux within the blue dashed line) and the heat source distribution over the PSZ thickness on the rotary boundary (thick red line). (c and d) Temperature and fluid pressure distribution at t = 0.074 s after initiation of the slip pulse. (e and f) Results of the temperature and pore fluid pressure evolution of the reference experiment s1937 as a function of time from the upper monitoring point, the PSZ, and measured data from the upstream and downstream sides.

6.4 Discussion

In the present study, we systematically investigated the dynamic frictional behavior of sandstone-derived fault gouges from the seismogenic zone of the Groningen gas reservoir. All experiments were performed under conditions that are comparable to recent studies by Hunfeld et al. (2021) and Chen et al. (2023) who simulated M3 to M4 earthquake slip under close-to-in-situ *P-T*-fluid conditions of the Groningen gas reservoir. To mimic in-situ earthquake conditions closer still, we used sandstone rock plates as host rocks, imposed short displacements down to 7.5 cm with a fast acceleration of up to 42 m/s^2, and kept a constant stress level (pre-shear stress) before the initiation of the slip pulse. In

the following, we first compare our results for wet samples with previous experimental observations of Hunfeld et al. (2021) and Chen et al. (2023), focusing on the evolution of shear stress as a function of slip velocity as well as slip weakening parameters. Second, we discuss the possible dynamic weakening mechanisms, especially the interplay between flash heating and thermal pressurization, based on the microstructural observations and numerical TP modeling of the simulated fault zones. Finally, we provide an interpretation on the controlling mechanisms for dynamic weakening in the sandstone-derived fault gouges and implications for induced seismicity in Groningen gas reservoir.

6.4.1 Comparison with previous experimental observations
6.4.1.1. Evolution of shear stress as a function of slip velocity

We compare the mechanical results of our wet experiments obtained from SHIVA with the experiments using the high-velocity rotary-shear apparatus (referred to as HV hereafter) in Beijing. The only one dry experiment performed in this study is comparable to the HV data (Chen et al., 2023), in which both dry samples do not show dramatic dynamic weakening (Figure 6.4b). All the comparison figures are plotted as shear stress against slip velocity (Figures 6.13, 6.14, and 6.15). This is because the slip acceleration and deceleration of the triangular slip-pulse function employed in the Beijing HV machine are lower than the values of 15, 30, and 45 m/s^2 targeted with SHIVA, which results in an incomparable amount of displacement between the HV and SHIVA data. Also, the measured pore fluid pressure changes during the slip-pulse are difficult to compare directly due to the differences in the distance between the pressure transducer(s) and the gouge layer in the different setups. Specifically, the HV experiments used an annular ring-shear assembly (40 mm and 28 mm for outer and inner diameters, respectively) for most tests and a solid cylinder (40 mm in diameter) for some other tests, while we only used a solid cylindrical setup (55.1 mm). The gouge layers were prepared to be ~1 mm and ~1.5 mm thick for the HV and SHIVA experiments after compaction, respectively. The HV tests therefore involved a smaller water volume in the gouge layer, and in the case of the HV ring shear assembly, an absence of shear torque contribution from the center part of the sliding surface. For the surface roughness, the host rocks used in the HV and SHIVA machines have roughly comparable surface roughness (ground with #80 SiC).

Overall, two main differences in wet experiments between the SHIVA and the HV data can be observed: one is that the shear stress supported at the very beginning and at the end of the slip pulse increases and decreases much faster in our experiments, and the other is that the initial weakening velocity V_w (i.e. the velocity at which the shear stress begins to drop, corresponding to the position of peak shear stress τ_{pk}) in our experiments (~0.16 m/s) is lower compared to that in the HV experiments (~0.3–0.4 m/s). These differences are likely due to the slightly faster slip acceleration at the start of our experiments, which results in higher heat production rate from sliding and faster weakening (Niemeijer et al., 2011), with the converse occurring at the end of our slip pulses. Below, we further discuss whether and how the host-block materials, pre-stress level, and effective normal stress affect the mechanical behavior.

Effect of host-rock materials

Thermal conductivity K of the host blocks has been reported to play an important role in determining the temperature rise from frictional heating and, thus, the dynamic weakening behavior of experimental faults at seismic slip rates (e.g. Yao et al., 2016b). With low-K host blocks, dynamic weakening becomes more pronounced as the temperature in the fault increases faster. In the SHIVA and HV experiments, three types of host blocks, composed of sandstone, solid Ti-alloy, and steel with thermal conductivities K (dry) of 3.87, 5.8, and 15 W/m/K, respectively, were used. Note that for (porous) sandstone, the effect of water saturation of pores would lead to a higher value of K of up to 4.5 W/m/K (Mielke et al., 2017), though the value is still lower than the K (dry) of Ti-alloy. Additionally, since the thickness of the sandstone plates is sufficiently thick (~3.5 mm) and the duration of the slip pulse applied in our experiment is extremely short (less than 0.2 seconds), the effect of thermal diffusivity and heat capacities of the host blocks might not influence the heat loss much during the slip pulse when comparing the data. In Figure 6.13, we compare our mechanical data, obtained using sandstone and steel blocks, to the HV data, obtained using Ti-alloy blocks, at a similar σ_{eff} of 5 MPa and with a low P_i of 0.1 MPa. Overall, we find that the weakening rate, defined as the slope of the shear stress drop from τ_{pk} to τ_{v_pk} (i.e. measured shear stress at V_{pk}) during acceleration, appears to become more significant as the K decreases, which is in agreement with the results of the previous study (Yao et al., 2016b). At the same time, the maximum fluid pressure increases (ΔP_{max}) measured in the sandstone (~0.28 MPa), Ti-alloy (~0.13 MPa),

and the steel experiments (~0.05 MPa) also suggest a higher temperature rise with lower λ_h host blocks. Here, we should note that the permeabilities of the sandstone and Ti-alloy host blocks are lower (~1–3×10^{-17} m^2) than that of the steel plates (~1×10^{-12} m^2) used for the SHIVA experiment. Thus, the observed fluid pressure changes are also consistent with the differences in the permeability of the host blocks, where the host blocks with low permeability can act as a barrier to fluid flow across the fault, which enhance built-up fluid pressure caused by heating.

On the other hand, during the deceleration phase, all the data show similar re-strengthening rates but the final strength is higher in our experiments (1.5–2 MPa vs 3 MPa). In addition, the dynamic shear stress in most of our experiments continuously decreased down to a minimum value τ_{min} while deceleration already started. The observation of the "prolonged" weakening as compared to the HV data, which shows immediate restrengthening when deceleration begins, may be associated with the different host blocks used. As sandstone has lower thermal conductivity than the Ti-alloy, the generated frictional heat (temperature rise) during the slip acceleration can be sustained within the gouge layer for a longer period and cause further weakening (or maintain low shear strength).
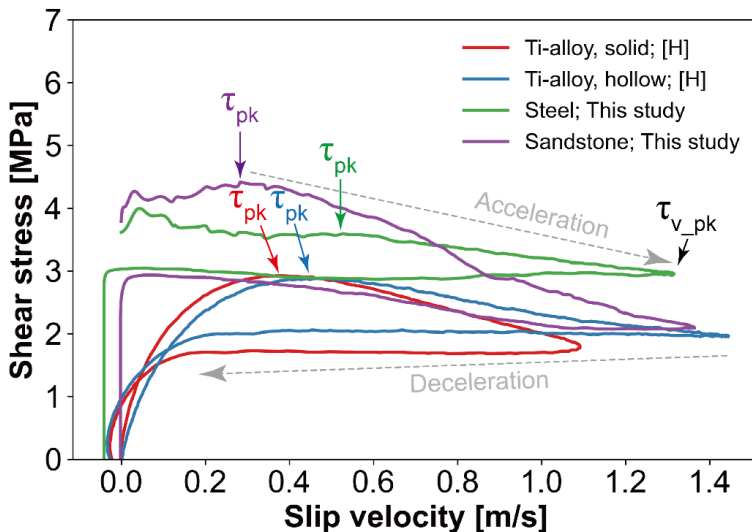
Figure 6.13: *Comparison of the mechanical data plotted as shear stress as a function of slip velocity for the host blocks with varied thermal conductivities. All experiments were performed at a similar effective normal stress of 5 MPa under water-saturated (P_i of 0.1–0.37 MPa) conditions.*

Effect of prestress level

Background stress (i.e. tectonic stress) is an important earthquake parameter controlling the dynamic rupture of earthquakes (Noda et al., 2009; Rice, 2006) because the background stress level together with how the fault dynamically weakens with increasing slip and slip rates determines whether earthquake slip can propagate or not. In our experiments, to simulate a fault with background stress in shear, we maintained the shear stress after the conditioning stage, defined as pre-stress, on the simulated SSG sample before initiating the slip pulse. We tested two different pre-stress ratios τ_b/τ_{pk}, one is nearly zero (i.e. without maintaining any pre-stress), and the other is close to one (i.e. the pre-stress τ_b is close to the peak strength τ_{pk}). Here, we do not show the comparison of our results to the HV data since many boundary conditions such as the initial pore fluid pressure, the host-block materials, and the geometry of the sample holder are slightly different. Thus, it becomes difficult to systematically discuss the effect of pre-stress on the mechanical behavior and the variations in the weakening rate. Figure 6.14 shows our mechanical data with and without pre-stress. We find that the experiments without pre-stress systematically produced larger peak strength (~0.79), lower dynamic friction (~0.26), and a faster weakening rate compared to the high-pre-stress experiments. In addition, sharp slip weakening seems to be more pronounced in the pre-stressed wet samples.

The observed variations in the level of friction suggest that the temperature rise and the associated weakening might be less significant in a high-pre-stress fault. We argue that, for a high-pre-stress fault, less frictional sliding is required to reach the yield strength because the grain contacts already sustain a certain amount of shear torque. Thus, less temperature in the bulk gouge zone would be generated. By contrast, more frictional sliding is required for a low-pre-stress fault to build up stress at grain contacts and to overcome the yield strength, and thus, might result in higher peak stress, higher temperatures, and more weakening. Previous numerical work of Platt et al. (2015) stated that pre-stress plays an important role in influencing the peak temperature in a gouge-filled fault. They showed that the peak temperatures when either thermal decomposition or thermal pressurization operate decreases with increasing pre-stress ratio. This concept might be used to explain our experimental observations, although their model had stress-driven boundary conditions instead of displacement-driven as in our experiments. To conclude, our results suggest that a fault zone with a lower level

of pre-stress could result in lower dynamic friction and larger weakening, which is expected to result from high peak temperature, during a slip-pulse rupture. More systematic tests with different levels of pre-stress ratios are needed to investigate the effect of the τ_b on dynamic weakening.
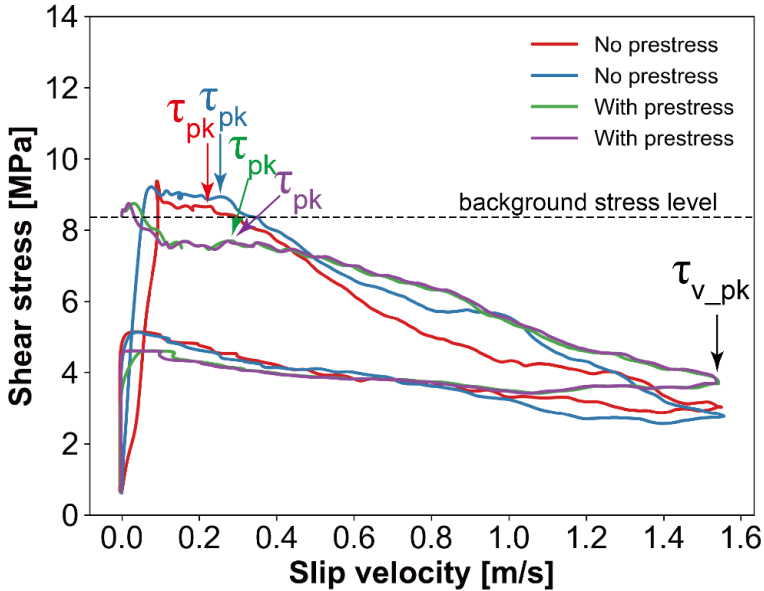
Figure 6.14: Comparison of the mechanical data plotted in terms of shear stress as a function of slip velocity for the experiments with and without pre-stress). The level of the pre-stress (~8.2 MPa) is indicated by the dashed line.

Influence of effective normal stress

The τ_{pk} and τ_{v_pk} data obtained in our wet tests at different initial effective normal stresses (black curves in Figure 6.15) are generally comparable to the HV results obtained using high initial pore fluid pressures (solid curve; $P_i > 0.5$ MPa), while systematically showing higher strength than HV results for low initial pore fluid pressures (dashed curve; $P_i < 0.5$ MPa, Figure 6.15). One thing to note is that our experiments involve twice the acceleration (30 m/s^2) and deceleration (30 m/s^2) and half of the imposed displacement (7.5 cm) compared to the HV data. Thus, the total amount of frictional work done in driving frictional sliding is less in our tests, while the heat production rate is faster. According to the shear stress-velocity plot (Figure 6.15), we observe that the initial slip behavior (before V reached 0.4 m/s) is different between the SHIVA and the HV data, where a sharp slip weakening following the initial slip strengthening (i.e. direct effect), defined

as "first weakening", can be identified in our wet experiments, in particular the experiments with pre-stress (Figure 6.14). We suggest that this initial weakening is likely due to the flash heating mechanism (Rice, 2006) together with local thermal pressurization (i.e. flash pressurization, Chen et al., 2023; Yao et al., 2018), the same mechanism as we proposed in the medium-velocity experiments (see Chapter 5). The first weakening appears to become pronounced when having high slip acceleration and with pre-stress, as further discussed in section 6.4.2.1.
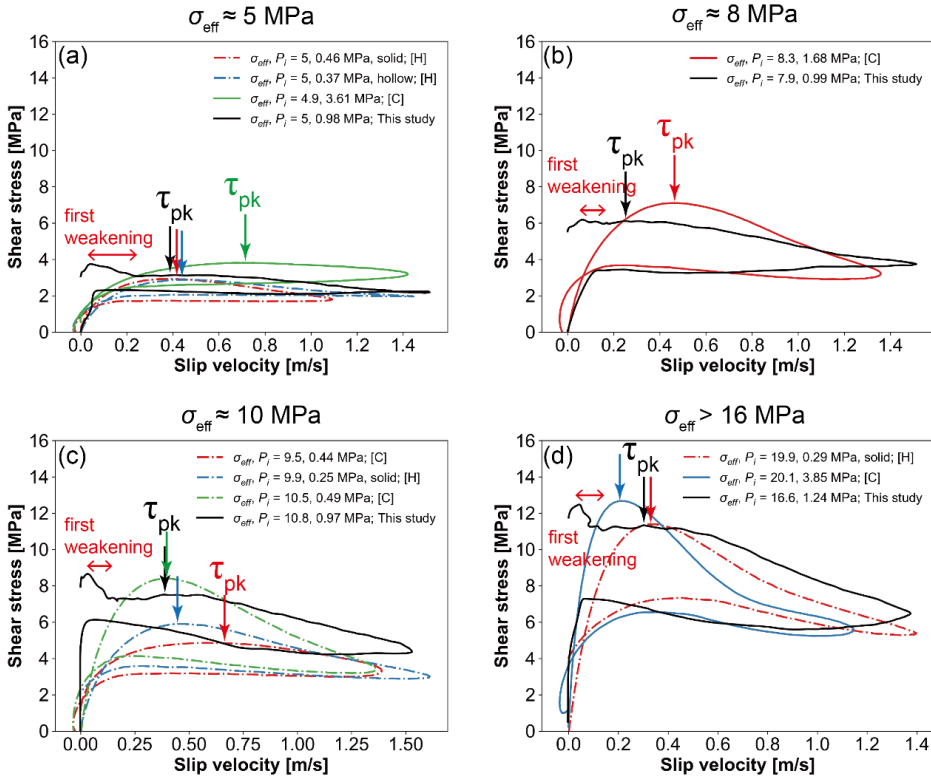
Figure 6.15: *Comparison of the mechanical data plotted as shear stress versus slip velocity under (a-d) different effective normal stresses σ_{eff} from 5 to up to 20 MPa. The dashed curves indicate the low-P_i (< 0.5 MPa) experiments and the solid curves indicate high-P_i ($\geq$ 0.5 MPa) experiments.*

6.4.1.2. Slip-weakening parameters – present vs. previous data

Dynamic friction (peak and steady-state friction), slip weakening distance D_w, and fracture energy G_c are critical parameters determining seismic radiation and rupture propagation (e.g. Kanamori and Brodsky, 2004; Beeler, 2006). Typically, the value of these parameters is shown to decrease with normal stress

owing to the larger amount of generated frictional heat (e.g. Niemeijer et al. 2011), as also reported from the HV data (Chen et al., 2023). In our study, we observe that the apparent friction (μ_{pk} and μ_{ss}) decreases with the applied normal stress while the D_w and G_c show an increase or a relatively neutral trend against normal stress, depending on the fitting choice of the friction parameters (Figure 6.5). We argue that this difference might be related to the following factors: first, the empirical fitting equation of Mizoguchi et al. (2007) is widely used to describe the full weakening curve (i.e. the shear stress or friction evolution) over a large seismic slip distance (few meters), towards a constant and stable steady-state value. In our data and the HV data, which both involve only a few tens of centimeters of slip, an almost immediate re-strengthening occurs when the slip starts to decelerate, and there is thus only a minimum value of dynamic friction and no steady state. In this case, the empirical fitting is based on this nominal minimum value, instead of a constant and stable value. If we constrain fitting with a fixed peak and steady-state values (type II fitting method), we can observe that the fitted D_w and G_c values change (see Figure 6.5e, g), and their dependence on effective normal stress becomes less or is absent. Thus, the choice of the fitting parameters and whether the shear strength fully weakened or not has a major influence on these slip-weakening parameters, especially for short slip pulses. Overall, we suggest that the type II fitting method might be a more reasonable way to fit the slip-pulse data because we observe that the deviation between the nominal steady-state friction μ_{ss} and the minimum friction μ_{min} becomes higher with increasing effective normal stress (Figure 6.5a), which leads to an overestimated (i.e. low) dynamic friction at high effective normal stress.

Second, we speculate that different experimental setups also have an influence on the dynamic friction and thus D_w and G_c. According to Hunfeld et al. (2021), they observed that the geometry of the setups, either a ring or a solid-cylinder setup, can potentially impact the evolution of dynamic weakening. Experiments using a solid-cylinder setup typically have less stress drop and slower weakening rates than those using a ring setup at higher normal stress (> 5 MPa), which is mainly due to the additional contribution of the shear torque from the center part of the gouge layer. This phenomenon can be observed in Figures 6.15b and d which show experiments that were all conducted at a high effective normal stress (> 5 MPa) under high-P_i (> 0.5 MPa) conditions. In addition, the slip velocity decreases towards the center which strongly influences the heat

generation by frictional sliding and, thus, the weakening. In this study, we used a solid-cylinder gouge setup which has a relatively large dimension (55.1 mm in diameter). Thus, the radial effect on the slip velocity becomes more significant and the associated triggered mechanism by frictional heating might become more complex due to the heterogeneous heat distribution along the slip surface. This may also explain why we do not observe a clear decreasing trend of D_w and G_c against normal stress. Despite this, we suggest that the values of the D_w and G_c obtained at high effective normal stress (i.e. 16.6 MPa) can directly be used as constraints for dynamic modeling because the dependence of these slip-weakening parameters on normal stress is minor or even becomes independent to some extent (Chen et al., 2023).

6.4.2 Dynamic weakening mechanism

Several weakening mechanisms have been proposed to explain the dynamic weakening of a wet gouge-filled fault at seismic slip rates (> mm/s). These include compaction-driven pore fluid pressurization (Oohashi et al., 2015), bulk thermal-mechanical pore fluid pressurization (Aretusini et al., 2021; Faulkner et al., 2011; Hunfeld et al., 2021; Togo et al., 2011), thermochemical pressurization (Brantut et al., 2010), bulk frictional melting lubrication (Di Toro et al., 2006; Tsutsumi and Shimamoto, 1997), silica gel production and lubrication (Rowe et al., 2019), thermally activated super-plasticity (Chen et al., 2021; De Paola et al., 2015), pore water phase transitions from the liquid to the gaseous or supercritical state (Chen et al., 2017; Ferri et al., 2010), and flash heating and weakening (Kohli et al., 2011; Proctor et al., 2014; Yao et al., 2018). For short seismic slip-pulses, Chen et al. (2023) excluded all the aforementioned mechanisms and proposed an alternative interpretation for thermal flash pressurization of the fluid phase which occurred at the intergranular contact (asperity) scale or/and at the scale of exceedingly localized slip bands, without a pore water phase transition. This conclusion was based on the following observations and experimental conditions: i) onset of shear-induced gouge dilatancy accompanied by measured pore pressure decrease which excludes bulk pore fluid thermal pressurization; ii) low measured temperature rises under wet conditions which excludes frictional melting; iii) weakening observed in different rock types, such as quartz- and clay-rich gouges, which excludes compositional-related mechanisms; iv) high initial pore fluid pressure (P_i > 0.5 MPa), which minimizes the possibility of vaporization of water and over-pressurization of fault gouges. Similar behavior

and conditions also characterize our study (Figure 6.6). In the following, we reconsider whether flash heating and weakening could have operated in our experiments since this mechanism has been eliminated in both dry and wet experiments in Chen et al. (2023), we assess whether the proposed flash/local thermal pressurization process is a candidate mechanism for dynamic weakening, and we evaluate whether a water phase transition possibly occurred in our experiments.

6.4.2.1. Flash heating

Flash heating and weakening is commonly reported to be a plausible mechanism for dynamic weakening at (sub)seismic rates (Rice et al., 2006). Before the initiation of frictional sliding, grain contacts support high stress due to the distribution of the force network from the applied normal stress. Once slip initiates, the high velocity combined with the high stress at the scale of grain contact asperities (<<1 mm) induce grain fragmentation, but also instantaneous elevated temperature rise driven by frictional heating within the contact lifetime (<< ms). This may result in thermal softening of the materials (e.g. microscopic melting in quartz-rich gouges) and, thus, a lowering of the macroscopic friction typically at the onset of the slip. In all our wet experiments with pre-stress, we observed an initially rapid increase and then a decrease in stress supported, when the stress pulse was first applied, followed by a slight increase towards a peak strength, corresponding to (apparent) peak friction μ_{pk}. The first weakening stage identified here does not seem to be an artifact resulting from the data smoothing and its magnitude is shown to increase with slip acceleration (see Figure S6.3b). Although the microstructural observations do not reveal any evidence (e.g. formation of rods of glass at the microscale: Brantut et al., 2016; Violay et al., 2014) for the activation of flash heating, we suggest that such evidence may have been overprinted or obliterated by ongoing shear beyond the peak friction. In addition, the absence of first slip weakening in both of our wet experiments conducted without pre-stress, and in the HV experiments, suggests that pre-stress at grain contacts might have played a significant role in causing the early weakening effect. Thus, flash heating could be responsible for the first sharp weakening seen in our wet experiments, or at least cannot be excluded.

At the same time, however, we do not observe either the early weakening or main weakening stages in our dry control experiment, suggesting that the

presence of pore water plays an important role in both the first and the second weakening. This makes flash heating seem unlikely in the dry or wet cases, though it still cannot be eliminated in the wet samples. This is because the lack of a weakening effect in the dry test may be associated with the number of fine particles and grain contact size within the PSZ, distributing the total imposed velocity. Based on the microstructural observations (see Figure S6.4), we observed more abundant fine particles in the PSZ of the dry gouge than in the wet gouge after the slip pulse, suggesting more extreme slip localization with enhanced grain size reduction under room-dry conditions. If this grain size effect also occurred during the conditioning stage at a slip velocity of mm/s, the conditioning dry gouge would have a larger number of finer particles which increases the number of asperity contact N_a sharing the total slip velocity and reduces the asperity diameter, D_a. These two are important parameters determining a characteristic weakening velocity of a gouge layer based on the flash heating model (Brantut and Platt, 2017; Platt et al., 2014; see equation 1.2). Both the changes of these two parameter values lead to a higher weakening velocity and, consequently, may cause the absence of flash heating and weakening in our dry experiment. Overall, flash heating and weakening appears to be not effective in the dry experiment. The importance of flash weakening might also be reduced in the wet experiments because of continuous grain size reduction (Figure 6.10), which reduces the average asperity size and contact lifetime, but cannot be eliminated. Another possible weakening mechanism responsible for the first weakening in the wet samples might be flash pressurization (Yao et al., 2018; Chen et al., 2023), the mechanism that combines flash heating and local thermal pressurization at intergranular contacts in the presence of pore water, as also inferred to be effective in the medium-velocity experiments (Chapter 5). This is the weakening mechanism proposed by Chen et al. (2023) to explain the main slip weakening in the wet HV data (second weakening in our cases), which cannot be ruled out in our study.

6.4.2.2. Pore fluid thermal pressurization (TP) and potential for vaporization

An important question in our experiments remains whether TP occurred in the bulk gouge, shear band, or even at the asperity scales (i.e. flash pressurization), and therefore to what extent the TP plays a role in dynamic weakening. We first note that in our wet, high acceleration (high-$Acc \geq 30$ m/s²) experiments, no fluid pressure drop was observed at the rotary (downstream) side of the sample where

slip tends to localize (Figure 6.6a), as what we observed in our wet, low acceleration (low-Acc < 30 m/s^2) experiments. This suggests that the dilatancy-induced pore pressure drop seen at the stationary side might be masked out at the rotary side by TP - due to faster heat generation. Here, we aim to better understand the role of TP in our experiments by combining the microstructures of the PSZ with our thermal modeling results for the high-P_i/high-Acc experiments, where the conditions are comparable to those applied in the HV experiments by Hunfeld, Chen, and coworkers.

First, we discuss how the experimental slip was distributed within the gouge layer during the wet experiments. We observed that a grain size reduction zone of half of the gouge thickness formed on the rotary side of the conditioned gouge, containing an additional ~100–120 μm thick PSZ with even finer grain sizes close to the boundary (Figure 6.7a and 5.8a). The presence of such a fine-grained layer could result in lower permeability which may delay fluid transport across the gouge layer. However, during the early acceleration stage (~0.01 m) of the slip pulse, we observed a pore pressure drop driven by shear-induced dilatancy at both the downstream (rotating) and upstream (stationary) sides, for accelerations < 30 m/s^2. This illustrates that short-lived pressure transients occurring in the gouge layer can be measured and that the pressure diffusion time in the downstream water reservoir might be negligible (Aretusini et al., 2021). Since the fine-grained layer likely acts as a barrier for fluid drainage, pore fluid pressure changes from local dilatancy (e.g. within the PSZ) are less likely to be measured simultaneously on both sides of the sample. Thus, shear-induced dilatancy is suggested to occur within the bulk gouge layer at the onset of slip. With increasing velocity and slip distance during dynamic weakening (~0.02 m of slip, sample s1935), a distinct and narrower PSZ (45–66 μm thick) developed, with more abundant fine grains compared to the PSZ of the conditioned gouge, whereas the particle size distribution (PSD) of the wider SZ in both gouges are nearly identical (Figure 6.10a). At the same time, the pore fluid pressure continued to drop, while the gouge continued to dilate (the purple curve in Figure 6.4b). During the late stage of the weakening (ranging from 0.02–0.05 m of slip), the pore pressure began to increase with continued gouge dilatancy, as observed in most of our wet high-P_i experiments (including high- and low-$Acc.$ experiments; Figure 6.4b, c, and d). This behavior is not observed in the HV tests with high-P_i and low-Acc where the pore pressure began to increase not until the gouge began to compact (as also

reported e.g. by Aretusini et al., 2021; Kuo et al., 2022). This might be due to the use of the sandstone plates as host blocks in our study, which facilitates temperature increase due to low thermal conductivity and thus, fluid pressure increases. Based on the above observations, we suggest that seismic slip in our wet experiments was primarily localized within a narrow PSZ where TP took place during the slip-pulse.

The following question is whether the liquid-vapor transition of water was involved in TP. Our thermal modeling indicates that the average temperature and pore fluid pressure within the PSZ of the wet gouge deformed at high-P_i (P_i = 1 MPa) (reference experiment s1937; Figure 6.12) increased to a maximum value of ~300°C (assuming 100% of the total heat input) and ~1.8 MPa, respectively. By comparing the evolution of the temperature and the pore fluid pressure curves with the water phase diagram (Chen et al., 2017; Weatherley and Henley, 2013), we find that the temperature reached at ~0.045 s or ~0.03 m of slip is estimated to be ~205°C which is about the temperature needed for water vaporization with a pore fluid pressure of ~1.6 MPa. Since the temperature increases faster than the pore fluid pressure during the acceleration phase, and since the modeled maximum bulk temperature is much higher than the temperature required for water vaporization, we infer that the pore water would be in the vapor phase throughout the later stage of the weakening regime (i.e. beyond a displacement of 0.03 m). The low-P_i (P_i = 0.1 MPa) experiment shown in Figure 6.4b (experiment s1933), shows faster dynamic weakening at slip initiation compared to high-P_i (P_i = 1 MPa) experiments (Figure 6.4b), which may further imply that water vaporization occurred earlier, enhancing weakening together with TP throughout the PSZ.

So far, it remains difficult to assess how much weakening can be attributed to vaporization since pore fluid thermal pressurization and vaporization may be triggered at the same time, in different spatial locations, during weakening. Due to the cylindrical disc-shape of the sample and variability in porosity within the gouge layer, heat production and vaporization would occur heterogeneously. In addition, the present modeling does not include the liquid-vapor transition heat (i.e. latent heat), which would buffer the temperature rise (Acosta et al., 2018; Chen et al., 2017), and thus limit the heating and weakening. To conclude, we suggest that water vaporization took place within the PSZ and played a role in the

dynamic weakening in our slip-pulse experiments despite being under high-P_i conditions. This inference highlights the importance of the properties (e.g. thermal conductivity) of the host-rock materials on temperature rise and, thus, the activated weakening mechanisms. In comparison, previous slip-pulse studies proposed different weakening mechanisms, either TP with water vaporization at shear-band scales under low-P_i conditions (i.e. $P_i = 0.1$ MPa; Hunfeld et al., 2021) or flash pressurization without water vaporization under high-P_i conditions (i.e. $P_i > 0.5$ MPa; Chen et al., 2023), for SSG samples both using host blocks (Ti-alloy) with a relatively high thermal conductivity. More detailed modeling is needed, taking into account variations in local microstructure (e.g. effect of interlayer structure with different grain sizes and permeability) and host-block materials to investigate the effectiveness and efficiency of water vaporization. In addition, since the measured fluid pressure and the gouge dilatation are limited, TP and water vaporization might occur at a smaller scale (i.e. asperity scales), the same mechanism (i.e. flash pressurization) as proposed in Chen et al. (2023). This requires numerical modeling at particle scales coupled with thermal-hydraulic-mechanical (THM) solutions to further demonstrate the possibility of local TP.

6.4.3 Implications for induced seismicity

Compared to the previous work of Hunfeld et al. (2021) and Chen et al. (2023), the present study has further investigated dynamic slip in laboratory experiments simulating induced earthquakes. We used sandstone as host blocks and applied slip at the rates, accelerations, and displacements close to those expected for earthquakes of magnitude 3–4 (Buijze et al., 2017b; Wentinck, 2018). One of the main findings is that all the wet gouges significantly weaken during the seismic slip pulse, except for the one with steel host blocks (Figure 6.4a), indicating that the thermal and hydraulic properties of the host-block materials play a critical role in TP-induced fault weakening. Our result shows that both the effectiveness and efficiency of TP could be enhanced if the host blocks possess relatively low thermal conductivity and permeability. In the Groningen gas reservoir, most fault segments are interpreted to crosscut the Slochteren sandstone reservoir, the overlying basal Zechstein (mainly composed of 48 wt% anhydrite and 32 wt% calcite and dolomite) and Ten Boer claystone (mainly composed of 48 wt% quartz and 39 wt% phyllosilicates) caprocks, as well as the underlying Carboniferous siltstone/shale source rocks (Van Eijs et al., 2006). Thus, the fault segments that crosscut the overlying and underlying rocks would have different

host-rock materials, which may potentially lead to different rupture behavior. In general, the mean thermal conductivities K of anhydrite, dolomite, and sandstone (~3–3.6 W/m K) are higher than that of shale (~2.5 W/m K; Tang et al., 2018), suggesting that the thermal conductivities of basal Zechstein and Slochteren sandstone should also be relatively higher than Ten Boer claystone and Carboniferous shale. However, such small variations in K between these lithologies likely have limited influences on fault weakening, since frictional heating is expected to be more efficient in natural seismic slip pulses, due to high normal stress and fast acceleration, and total durations of the small earthquakes are shorter. On the other hand, the permeability k of the Slochteren sandstone is reported to range from ~1×10^{-16} m^2 to ~1×10^{-12} m^2 at different reservoir locations (NAM, 2016), suggesting that the effectiveness of TP on faults could vary within the sandstone reservoir, due to the heterogeneous spatial distribution of permeability. However, we suggest that the permeability of the host blocks would become less influential on the effectiveness of TP on crosscutting fault segments, because the permeability below which TP is efficient for small-magnitude earthquakes is on the order of that of the most impermeable parts of the reservoir (i.e. $k \approx 1\times10^{-16}$ m^2, NAM, 2016, depending on PSZ thickness) and the permeability of the clay-rich lithologies (i.e. Ten Boer claystone and Carboniferous shale) is expected to be (much) lower than this.

In addition, the porosity of the sandstone, which is shown to vary considerably in both depth and across the field (NAM, 2013; Van Hulten et al., 2010), may also influence thermal conductivity and permeability. For a saturated sandstone, an increase in porosity would result in higher permeability (e.g. NAM, 2016) and lower thermal conductivity, which would in turn decrease more significantly in gas-saturated than in water-saturated conditions (e.g. Eppelbaum et al., 2014). This shows competing effects on TP and thus weakening. Overall, the vertically-average porosity of the sandstone in the gas reservoir is shown to vary from 18–22% at the central part of the gas field, decreasing to both the northern and the southern regions with less than 10% (see Figure 1.7) and the horizontally-average porosity of the sandstone (at a depth of ~3000 m) varies from 7% to over 20% towards shallow depths (NAM, 2013; Van Hulten et al., 2010). Within this range of porosity, the permeability could potentially increase by two orders of magnitudes (NAM, 2016), while the thermal conductivity remains low decreasing from 2.5–2.6 to 1.5–1.75 W/m K (Eppelbaum et al.,

2014), from the base to the top of the reservoir. The above observations imply that TP might be less effective on fault segments near the reservoir top and at the central field, while becoming more effective on the lower segments and towards the northern and southern regions, potentially leading to more weakening and thus bigger earthquakes.

Overall, the Slochteren sandstone reservoir rocks show dramatic dynamic weakening during the acceleration phase of the present tests, followed by re-strengthening behavior as slip decelerated, specifically under water-saturated conditions. In the reference experiment (s1937), the apparent friction drops from 0.75 to 0.25, then rises to ~0.6. Our results show that low dynamic friction can be achieved if the slip acceleration is sufficiently fast to reach seismic velocities (m/s), despite low frictional work in short displacement experiments (i.e. ~7.5 cm). In addition, re-strengthening rates and work input (i.e. G_{re}) do not show much dependence on normal stress (Figure 6.5) while they are enhanced by shorter displacement (Figure 6.4b). The observed re-strengthening trends are generally consistent with the previous study of Violay et al. (2019). These authors showed that the co-seismic re-strengthening of cohesive faults of Carrara marble during seismic slip deceleration becomes more pronounced under water-saturated conditions and increases with the power density (normal stress times slip velocity). By comparison, our results show that the re-strengthening in the Slochteren sandstone gouge is enhanced by shorter displacement. When applied to nature, the combined experimental observations imply that the amount of co-seismic re-strengthening may vary, depending on the preceding earthquake slip. More systematic tests are needed, such as with variable shear displacement, slip acceleration and deceleration, and gouge materials, to fully understand how a re-strengthening phase influences the earthquake cycle – in the context of both induced and natural earthquakes.

Our microstructural observations show that some slip-pulse gouges clearly formed a PSZ, indicating where deformation took place, while others show distributed cataclastic flow structures (Figure 6.7g, e.g. Niemeijer et al., 2012), likely suggesting a smaller degree of slip localization, though a fine-grained layer can still be identified. We focus on the characteristics of these PSZs, such as the particle size distribution and thickness, as these provide information on the mechanical wear process and mechanism (e.g. Aretusini et al 2017) and constrain

local heat production, temperature rise, and weakening (e.g. Rice, 2006). Generally, we do not observe a visible correlation between the PSZ thickness and frictional work density (FWD) or frictional power density (FPD) where the PSZ thickness remains at ~50 μm thick, regardless of the increase in the FWD and FPD (Figure 6.10). This suggests that within short seismic slip, comparable with induced seismic slip, the process of cataclasis and the associated growth of PSZ are not strongly influenced by either frictional work or frictional power densities, unlike previous high-velocity friction studies with long shear displacement (meter scale, e.g. Kuo et al., 2022), more akin to large earthquake slip trajectories. The above implications can be better constrained if the characteristics of the PSZ within the reactivated faults in the Groningen reservoir are understood from borehole core observations or other exhumed analog faults with a similar reservoir lithology as the Groningen gas reservoir.

6.5 Conclusions

We performed seismic slip-pulse experiments on simulated sandstone-derived fault gouges retrieved from the depth within the Groningen gas reservoir at which most induced events have been reported to occur. To simulate conditions of induced earthquakes of magnitude 3–4, we performed rotary-shear experiments using the SHIVA machine at INGV, with a newly designed pressurized gouge setup. We imposed short-displacement (7.5–15 cm), high-velocity slip pulses (up to ~1.8 m/s) on conditioned gouges subjected to (initial) effective normal stresses σ_{eff} in the range of 4.9–16.6 MPa and initial fluid pressures P_i of 0.1–1 MPa, using either dry Argon or water as pore fluid, and at initially ambient temperature conditions. In addition, microstructural analyses and numerical modeling were performed to quantify the characteristics of the active principal slip zone (PSZ) and the evolution of temperature and pore pressure in the experiments. The main findings are summarized as follows:

1. Water-saturated sandstone-derived fault gouges show significant dynamic weakening while dry gouges do not. The dynamic minimum friction values μ_{min} derived from the wet experiments show a decrease with increasing effective normal stress while the slip-weakening distance D_w, fracture energy G_c, and re-strengthening behavior show little dependence on normal stress. These parameters do not show visible dependence on slip acceleration.
2. Microstructures of the simulated fault zones generally reveal a thin PSZ. The width of the PSZ does not increase with the frictional work density (FWD)

or frictional power density (FPD), implying that the mechanical wear process, through normal stress and slip rate, has limited effects on the growth of the PSZ during seismic slip pulse.

3. Previous slip-pulse studies have proposed two different controlling weakening mechanisms responsible for the dynamic weakening in wet sandstone gouges using Ti-alloy as host blocks, either thermal pressurization (TP) with water vaporization at shear-band scales under low-P_i conditions (i.e. P_i = 0.1 MPa; Hunfeld et al., 2021) or TP at the scale of exceedingly localized slip bands, or at grain contact scale, induced by flash heating (i.e. flash pressurization) without water vaporization under high-P_i conditions (i.e. P_i > 0.5 MPa; Chen et al., 2023). In our study, fluid pressures and temperatures implied from numerical modeling show that TP is an effective dynamic weakening mechanism in the wet sandstone gouges and becomes much more efficient using sandstone as host blocks during the seismic slip pulse. In addition, water vaporization may occur within the PSZ and plays an additional role in dynamic weakening. We do not exclude flash pressurization as another possible weakening mechanism operating in our experiment due to the limited change in the measured fluid pressure increase and gouge dilatation. To test this, numerical modeling at particle scales coupled with thermal-hydraulic-mechanical (THM) solutions is needed.

Supplementary information

Text S6.1: Sample preparation

Before each experiment, the static sample holder was jacketed with a polyvinyl chloride (PVC) shrink tube fixed to the static holder with stainless-steel wire. We evenly distributed 12 g of Slochteren sandstone gouge on top of the entire stationary sample assembly and added few drops of deionized water on top of the gouge sample to dampen it to allow the installation of the assembly in the horizontal sample chamber. Following this, the axial piston was used to insert the rotary sample holder into the pressure vessel. The internal surface of the jacket was lubricated with MoS2-based solid lubricant to reduce friction between the rotary sample holder and the PVC jacket. We first applied a small normal load of 0.35 kN to the gouge layer to ensure the sample was under load. Then, we started with a gradual and simultaneous increase of the normal stress (σ_n) and confining pressure (P_c) followed by an increase of fluid pressure (P_f) step by step to ~2.68, 2.5, and 1 MPa, respectively.

Text S6.2: Representative area for particle size distribution (PSD) analysis

To find the size of the representative area, we determined at which scale the particle size distribution (PSD) no longer changes. To do this, we selected a x500 image (typical resolution that can fully cover the width of the PSZ) and cropped it stepwise to obtain images with a field of view similar to that of a higher magnification image (e.g. x660, x1000, x1500, and x2000). In order to obtain a field of view (FOV) with smaller magnification, we also combined four different x500 images to obtain an area which is equivalent to x250 image where the other three x500 images were randomly picked from other locations of the PSZ. Figure S6.6 shows that the particle density (number of grains / total grain area) at different scales is almost identical for grain sizes larger than 500 nm, except for the x2500 and x3000 images, while for the grain size smaller than 500 nm, the particle density decreases with increasing FOV (smaller magnification) until the FOV consists of more than two x500 images. This indicates that we should at least analyze more than two x500 images as the representative PSD for the PSZ in this case. We argue that the systematic change in the particle density with magnification at the grain size < 500 nm is caused by the effect of the number of grains that were cropped at the image boundaries. Since we do not consider the grains at the boundaries, the percentage of the number of the cropped grains with respect to the total number of analyzed grains would increase when having a

smaller FOV (higher magnification). This effect becomes significant for the finer grains as they are more abundant and, thus, the particle density would increase. On the other hand, it is worth noting that the particle resolution under the SEM-BSE analysis becomes less effective with decreasing grain size, especially for nanoparticles, because grain boundaries become difficult to resolve. Considering the above, we adopted 500 nm as the minimum value for the PSD and took at least five x500 images for PSD analysis.

The second issue addressed is whether the PSD of multiple images of a specific area of interest with identical magnification has strong variation or not. If the particle density varies by more than 10%, we then suggest that there is a substantial heterogeneity of PSD at this specific resolution, which is not suitable to be the representative area. To do this, we further analyzed five x500 and five x1000 images. Figure S6.7 shows the PSD for each x500 and x1000 image selected from five different locations. Generally, the PSD of x500 and x1000 images for each location are similar (within 10% variations) while some images (one out of five here) may show slightly out of range (> 10%; red curves in x1000). Although the results can be affected by selection bias or the number of images analyzed, it appears that the effect of grain size variation on PSD at different locations becomes less significant when using a larger FOV (i.e. x500 image). Thus, we argue that the PSD heterogeneity should have a minor influence on the choice of x500 magnification.
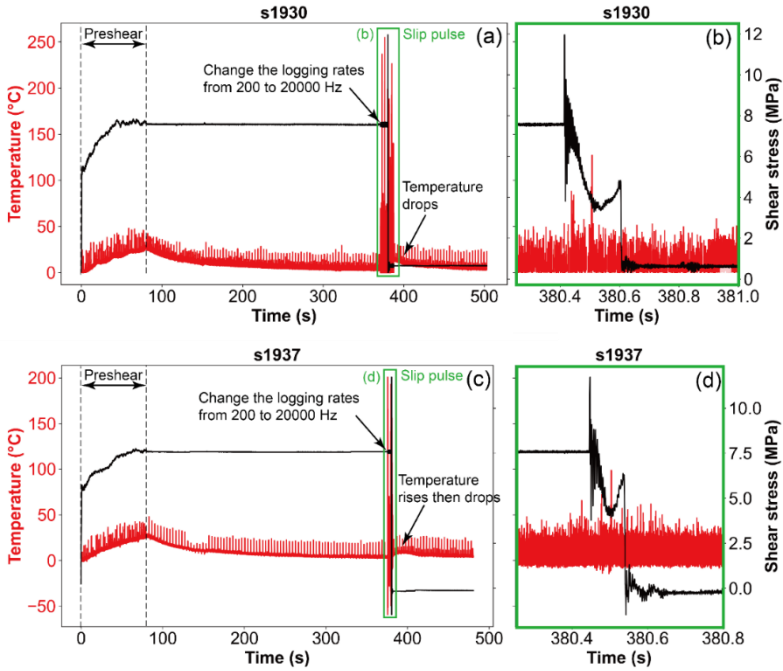
Figure S6.1: *Evolution of the measured temperature and shear stress as a function of time throughout the conditioning and slip-pulse stages for (a, b) the low-acceleration (s1930) and (c, d) the high-acceleration (s1937) experiments.*
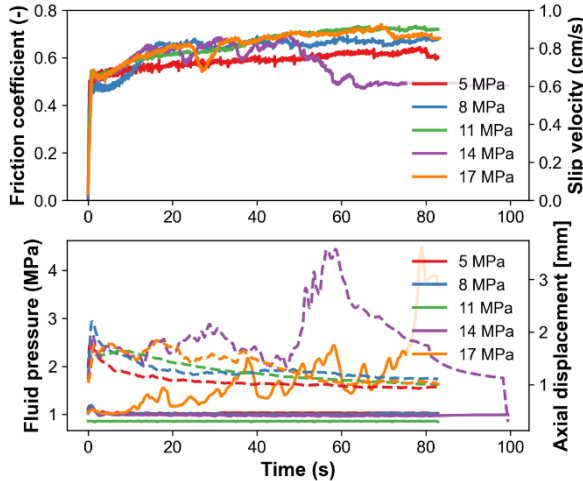
Figure S6.2: *Conditioning data at effective normal stress of 5–17 MPa plotted as shear stress as a function of time. It is noted that at 14 MPa, the friction coefficient began to decrease from ~0.7 to ~0.5 accompanied by large gouge dilatation (~2.5 mm) after 45 seconds of the slip initiation. We infer that these behaviors were caused by the damage of the sandstone frits, where the damaged frit was no longer parallel to the gouge layer and shear sense. The damaged (or broken) frits can be observed during sample recovery.*
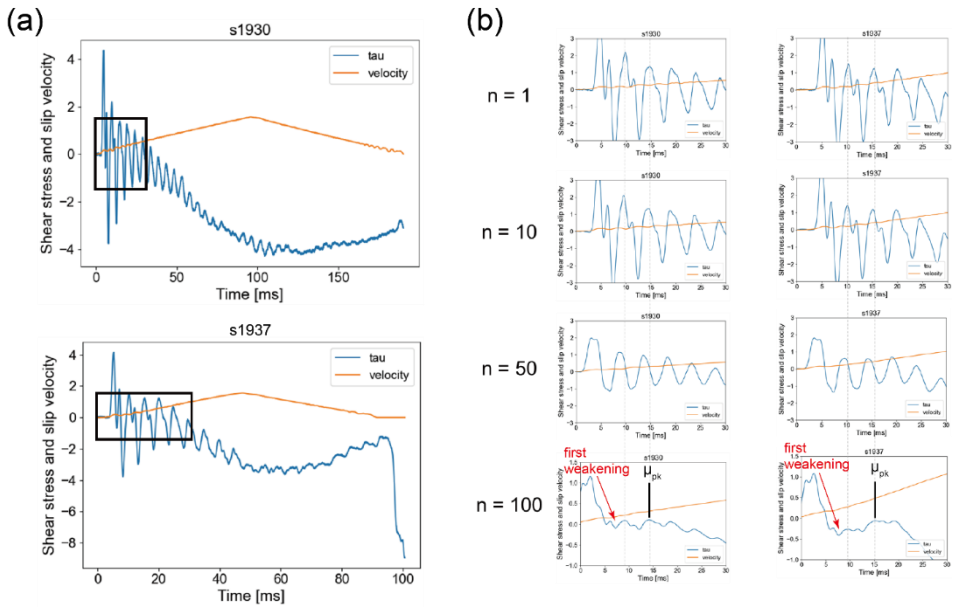
Figure S6.3: *Examples of data smoothing of the mechanical data (a) at slip acceleration of 15 m/s^2 (s1930) and 30 m/s^2 (s1937) with (b) variable moving average of 1–100 data points. We focused on the initial slip (black rectangle regions) with the strongest oscillations. The gray dashed lines indicate the range of μ_{pk} determined from the curve without smoothing (n = 1) to with smoothing (n = 100).*
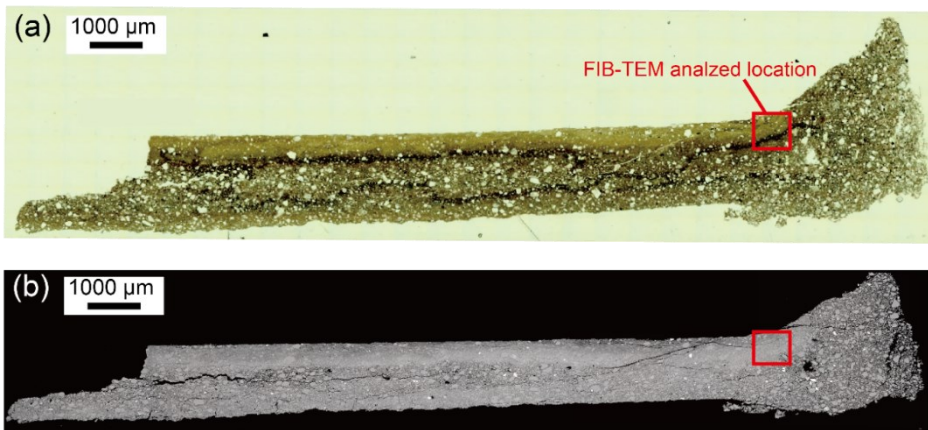
Figure S6.4: *Gouge microstructure prepared across the center and the edge of the gouge layer. (a) The OM image and (b) The SEM-BSE image. The red rectangle indicates the selected location for FIB-TEM analysis.*
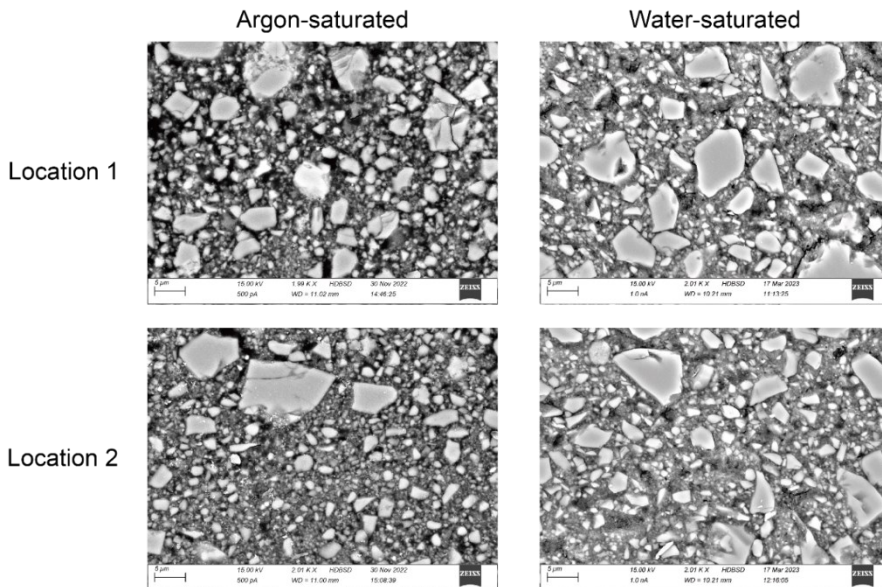
Figure S6.5: *SEM-BSE images between the argon-saturated (s1946) and water-saturated (s1937) gouges deformed at similar experimental conditions under x2000 magnification. Under this magnification, the wet gouge generally exhibits a greater number of grains with size ~10 µm than the dry gouge.*
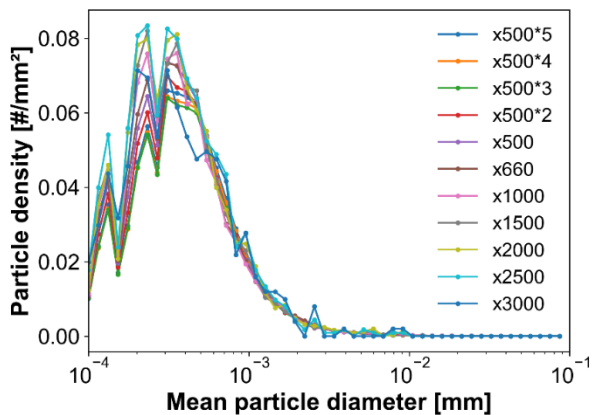
Figure S6.6: *Particle density as a function of mean particle diameter for images with different field of view. The magnification in the legend refers to the images with different FOVs.*
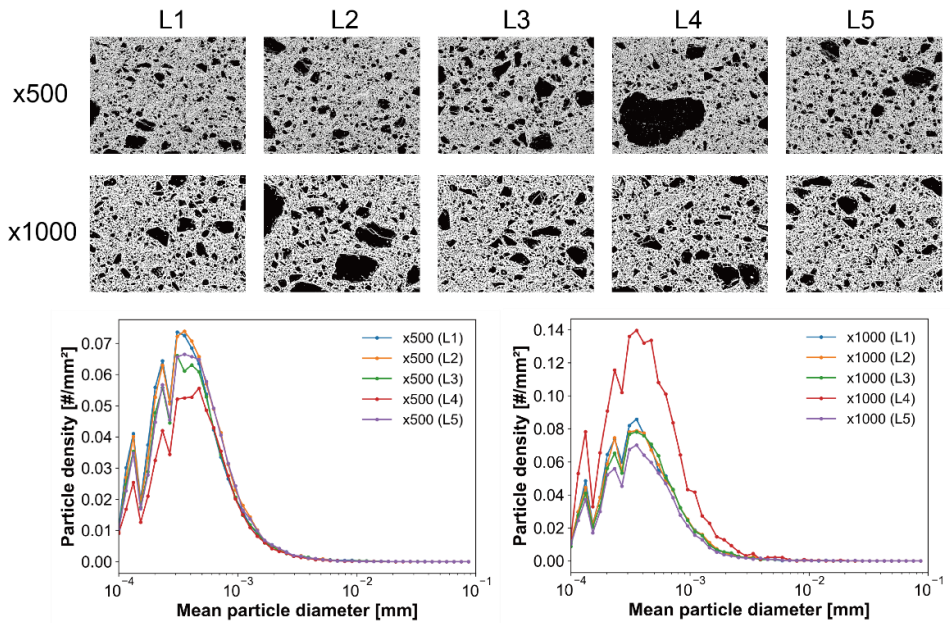
Figure S6.7: *Particle density as a function of mean particle diameter for images with different field of view (FOV similar to x500 and x1000 magnifications) obtained from five different locations (L1 to L5) of the PSZ. The magnification in the legend refers to the images with different FOVs.*
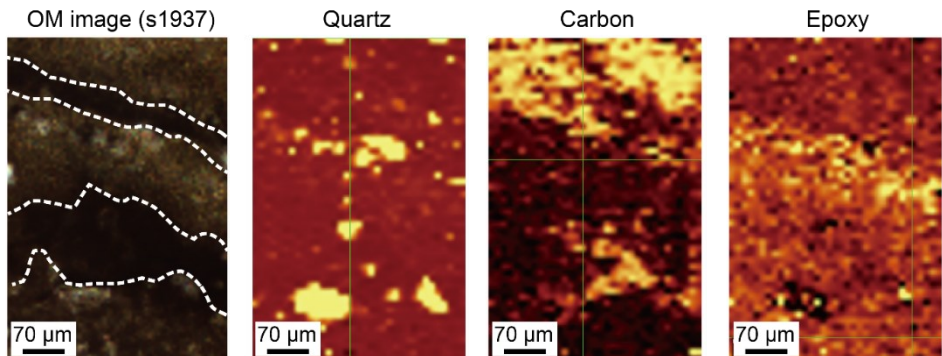
Figure S6.8: *Raman mapping of the region with black (opaque) layers (white dashed lines) for the gouge sample obtained from experiment s1937. The distribution of the black layers does not systematically correlate to the distribution of the quartz, carbon, and epoxy signals (brighter color).*

Table S6.1: *List of input parameters and values used in the thermal pressurization modelling.*

Parameter	Definition	Value	Source
	Frictional parameters and boundary conditions		
W	Gouge layer thickness (mm)	0.8	
W_{psz}	PSZ thickness (μm)	100	SEM observation
T_0	Initial temperature (°C)	25	
	Stainless steel		
ρ	Density (kg m^{-3})	8000	Kuo et al., (2022)
c	Specific heat capacity (J kg^{-1}K^{-1})	500	Kuo et al., (2022)
K	Thermal conductivity (W m^{-1}K^{-1})	16	Kuo et al., (2022)
	India sandstone		
ρ	Density (kg m^{-3})	2650	Tanikawa et al., (2010)
c	Specific heat capacity (J kg^{-1}K^{-1})	800	Tanikawa et al., (2010)
K	Thermal conductivity (W m^{-1}K^{-1})	3.87	Tanikawa et al., (2010)
n	Porosity (%)	12	Tanikawa et al., (2010)
k	Permeability (m^2) at 10 MPa	$3 \cdot 10^{-17}$	Tanikawa et al., (2010)
S_s	Specific storage (Pa^{-1})	6×10^{-9}	Tanikawa et al., (2010)
	Gouge		
ρ	Density (kg m^{-3})	2657	From pycnometer measurement
c	Specific heat capacity (J kg^{-1}K^{-1})	1160	Hunfeld et al., (2021)
K	Thermal conductivity (W m^{-1}K^{-1})	2.386	Hunfeld et al., (2021)
n	Porosity (%)	25	Hunfeld et al., (2021)
k	Permeability (m^2)	5×10^{-18}	Hunfeld et al., (2021)
S_s	Specific storage (Pa^{-1})	1×10^{-8}	Hunfeld et al., (2021)
α_{th}	Thermal diffusivity of the gouge (m^2/s)	8×10^{-7}	Hunfeld et al., (2021)
	Resulting material properties		
α_{hy}	Hydraulic diffusivity (mm^2/s)	0.5	

Chapter 7

Conclusions, implications, and suggestions for future research

In this thesis, I conducted a series of laboratory friction experiments on simulated, sandstone-derived fault gouges from low to high slip velocities, as well as 3-D discrete element modeling (DEM) simulations on a granular gouge layer at seismic slip rates, to investigate the role of localization and heating on the dynamic frictional behavior of quartz-rich, gouge-filled faults during small-displacement earthquake slip. I utilized crushed Slochteren sandstone core materials (SSG; quartz content > 75wt%), extracted from both above and below the gas-water contact (GWC), in the Groningen gas field, the Netherlands, as the starting material - which is one of the key lithologies in the reservoir and hosts most of the events induced by gas production (Dost and Haak, 2007; Dost et al., 2020; Smith, 2019; Spetzler and Dost, 2017; Van Eijs et al., 2006). The results of this thesis are not only relevant for the Groningen earthquakes but can also be applied to other small natural and other induced seismic events in quartz-rich faults under upper crustal conditions.

I explored how slip localizes within fault gouges and the effect of this on the associated mechanical (frictional) response during rupture nucleation **(Chapter 2)**. I investigated the evolution of the experimental shear zone and associated slip distribution over the localization features by conducting direct shear experiments, at subseismic slip rates, on a 1 mm thick SSG layer containing a thin segment of albite gouge (~10 wt%) as a strain marker. Slip distribution was analyzed at variable frictional stages and slip velocities, making use of machine-learning-based image analyses, conducted using X-ray CT scan. All the experiments were performed at an effective normal stress of 40 MPa, a pore fluid (DI water) pressure of 15 MPa, and an ambient temperature of 100 °C, which is comparable to the in-situ reservoir conditions in Groningen. The SSG layers were deformed at three different constant displacement rates of 1, 30, and 1000 μm/s and terminated at three successive frictional stages, namely the strain-hardening, strain-softening, and steady-state stages, at shear strains equivalent to 1.3, 3.3, and 5.5, respectively. An additional velocity-stepping experiment was conducted with velocity steps in the range 1-30-1000-30 μm/s (with each velocity covering a displacement interval of 1-2 mm), for control purposes regarding the frictional behavior of the pure SSG layer. To automatically determine the type of localization feature and quantify how much displacement is accommodated over each feature along the albite-SSG boundary, I developed a machine-learning-

based boundary detection method, based on the random forest approach, which I applied to hundreds to thousands of XCT images.

I then investigated how particle-scale parameters influence slip localization for a granular layer at seismic slip rates **(Chapter 3)**. I utilized 3-D DEM numerical simulations, representing a direct shear experiment (similar to the setup in Chapter 2) on a pack of unbreakable spherical grains. Particle-particle interactions follow the Hertz-Mindlin (HM) contact model with no micro-slip solution (Mindlin, 1949) which is appropriate for elastic contact bodies (Thornton, 2011). I employed a novel principal slip zone (PSZ) model, consisting of a layer of particles with a finer grain size (the PSZ), oriented parallel to the shear direction and overlying a homogeneous coarser granular pack, to investigate the impact of PSZ grain size and PSZ thickness on the amount of slip accommodated within the PSZ during numerical seismic slip. I varied the contrast in grain size between the PSZ and the remaining gouge zone from 10% to 50% as well as the contrast in thickness between the PSZ and the bulk gouge zone from 12.5% to 50%. In addition, I explored the role of interparticle sliding and rolling on slip distribution by reducing the interparticle (intrinsic) friction down to 0.1, as an analogue for phyllosilicate sliding, and by introducing a rolling resistance of 0.5 for the entire granular layer.

The role of localization and heating on dynamic frictional behavior during rupture propagation was investigated by performing rotary-shear friction experiments at slip velocities from 1 mm/s up to 1.8 m/s **(Chapters 4, 5, and 6)**. To constrain the mechanisms responsible for dynamic weakening at (sub)seismic slip velocities, I measured temperature (shear-band scale vs. asperity-contact scale) and fluid pressure evolution close to the actively slipping zone, and performed microstructural analyses of the deformed gouge samples. This involved medium-velocity (MV) rotary shear experiments conducted at 0.001 to 0.05 m/s **(Chapter 4)**, performed using nearly spherically grained, Ottawa quartz sand "gouges" as starting materials, plus a high-speed infrared camera to capture local, short-term temperature rises (i.e. flash temperatures) at asperity contacts A range of normal stress (1 to 7.5 MPa), slip velocities (0.001 to 0.05 mm/s), and initial grain sizes (250–300 μm, 300–425 μm, 425–500 μm, and 500–710 μm in diameter) was investigated, under room-dry and wet conditions, to characterize the dependence of flash temperature on these variables. To minimize initial grain

size reduction which would decrease the efficiency of flash heating and its duration, we did not perform a conditioning stage (i.e. pre-shear) in these experiments.

In another group of MV rotary tests at $V = 0.05$ m/s **(Chapter 5)**, I investigated the effect of thermal and hydraulic properties of the pore fluid on dynamic slip weakening induced by thermal pressurization (TP), using SSG as starting materials. I employed a pre-slip conditioning stage (1 mm/s for 1 m displacement) and used four different types of pore fluid, specifically deionized water, Dow Corning 200 silicone oils (1 and 5 centistokes), and synthetic brine with a composition (salinity) similar to the in-situ brine in the Groningen gas reservoir. These experiments were conducted at an applied normal stress of 12 MPa, and initial pore fluid pressures of 0.1, 1, and 2 MPa under undrained conditions.

All of the above MV friction experiments were imposed a relatively long shear displacement (e.g. 0.75 m at 0.05 m/s) to achieve a similar amount of total heat production (slip velocity × displacement) as applied in high-velocity (HV) experiments. However, the displacement and the velocity function are not comparable to small-magnitude earthquakes, which have a pulse-like slip behavior with only a few tens of centimeters of displacement (e.g. Wentick, 2018). To simulate more realistic small-earthquake slip velocity conditions, I performed HV friction experiments **(Chapter 6)** on ~1.5 mm thick SSG layers, applying a conditioning stage (pre-slip at 5 mm/s for 0.4 m) followed by a pulse-like velocity-time function (triangular vs. modified Yoffe velocity functions). The tests were performed at a range of initial effective normal stresses σ_{eff} between 4.9–16.6 MPa, reaching a peak velocity V_{pk} up to 1.8 m/s and slip accelerations of up to 42 m/s^2, over a displacement of 7.5–15 cm, using either Argon or water as pore fluid, at ambient temperature conditions. The SSG layers were confined between ~1.5 mm thick sandstone host blocks (cylindrical discs) which have similar thermal and hydraulic properties to the Groningen (Slochteren) reservoir sandstone. In addition, I tested two different pre-stress ratios (pre-stress τ_b/peak strength τ_{pk}), one being nearly zero (i.e. without keeping any pre-stress) and the other being close to one (i.e. the pre-stress τ_b is close to the peak strength τ_{pk}). I characterized the particle size distribution (PSD) of the pre-deformed (conditioning stage) and slip-pulse gouge products, as well as the corresponding

PSZ thicknesses, as well as their relation to frictional work density (FWD) and frictional power density (FPD). Finite element modeling (FEM) thermal modeling (COMSOL package) was further utilized to retrieve information on the evolution of temperature and pore fluid pressure within the active shear zone, and hence to provide constraints on possible dynamic weakening mechanisms.

The combined results of the experimental, microstructural, and numerical studies shed light on the (micro)mechanics of small-magnitude earthquakes, providing better constraints on the development (thickness) of the active fault zone, the level of dynamic friction, and the controlling dynamic weakening mechanisms providing useful input for geo-mechanical rupture models aimed at estimating maximum possible moment magnitude (e.g. Buijze et al., 2019). Below, I summarize the main findings of each chapter and discuss implications for induced seismicity in the Groningen gas reservoir, as well as broader implications for small-magnitude earthquakes. Finally, I identify remaining unsolved questions and list suggestions for future work.

7.1 Main findings

The main results of the mechanical data and quantification of localization, as derived from each chapter, are compiled in Figure 7.1. Below, all the mentioned terms for friction coefficient (i.e. static friction μ_s, peak friction μ_{pk}, minimum friction μ_{min}, steady-state friction μ_{ss}, and dynamic friction μ_{dyn}) are expressed as apparent values, determined as shear stress τ / initial effective normal stress σ_{eff} (applied normal stress σ_n – initial pore fluid pressure P_i).
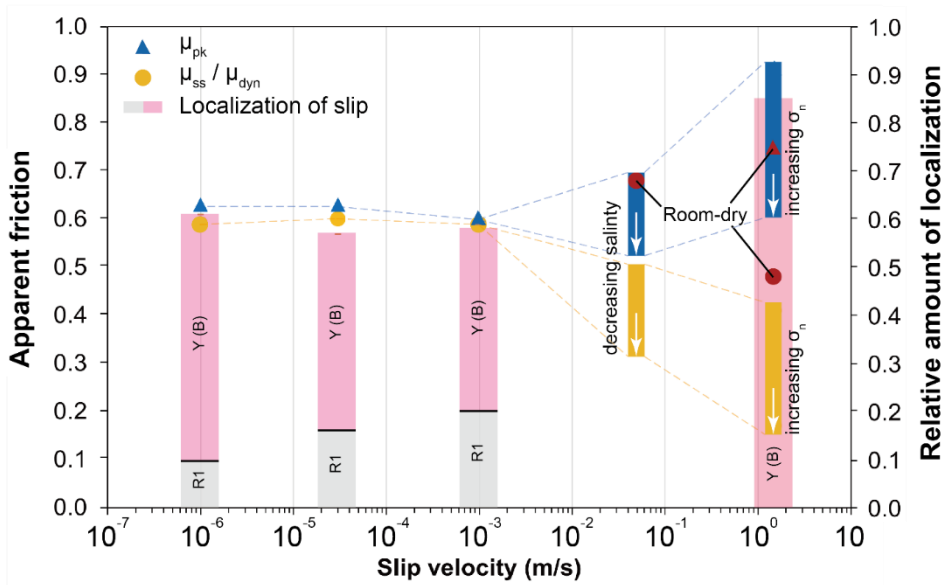
Figure 7.1: *Compiled data on mechanical behavior and the quantification of slip localization obtained from the work reported in Chapters 2, 3, 5, and 6 of this thesis, from slip velocities relevant to rupture nucleation (1 µm/s) to seismic slip velocities (1.5 m/s). The relative amount of localization on R_1 and Y (including boundary shear) shears, shown at slip velocities of 1, 30, and 1000 µm/s, are the results obtained at the steady-state stage with a total displacement of 5.5 mm (Chapter 2). The result at the slip velocity of 1 m/s was obtained from the DEM numerical modeling with a total displacement of 18.75 mm (Chapter 3). The μ_{ss} data represent the apparent "steady-state" friction obtained at subseimic slip rates (Chapter 2) and the μ_{dyn} data represents the apparent minimum friction μ_{min} reached during dynamic weakening at seismic slip rates (≥5 cm/s, Chapters 5 and 6). The white arrows at a slip velocity of 0.05 m/s and 1.5 m/s indicate a decrease in salinity and an increase in normal stress (σ_n), respectively.*

7.1.1 Experimental constraints on the relationship between mechanical response, strain localization and displacement partitioning at low-sliding velocities

As shown in Chapter 2, our quartz-rich gouges sheared under in-situ reservoir conditions exhibit a similar evolution of mechanical response, localization features and partitioning of displacement, with increasing shear strain of up to 5.5, at all tested displacement rates of 1, 30, and 1000 µm/s. The apparent sliding friction μ_{app} first reached a broad peak friction μ_{pk} (0.6–0.64) and then evolved towards a "steady-state" friction μ_{ss} of ~0.6, which follows a roughly linear slip-weakening curve. The additional velocity-stepping experiment with velocity steps of 1-30-1000-30 µm/s demonstrated velocity-weakening behavior of the SSG across this velocity regime. The attainment of the peak friction μ_{pk} (i.e. the strain-hardening stage) is mainly associated with homogeneous gouge deformation, whereby up to 85% of the total displacement is uniformly

260

distributed within the bulk gouge layer. I found that shear fabrics orientated along R_1 and boundary (B) shears already formed at the strain-hardening stage, with these fabrics accommodating 16–34% of total displacement, and that their contribution increased with displacement rate. In the subsequent strain-softening stage, I observed that R_1 shears rotated towards a lower angle relative to the shear direction, and Y (including B) shears became more developed in the gouge layer. Other localization fabrics, such as R_2 and P shears, were not identified in any stages. In addition, the relative amount of localization of displacement along both the R_1 and Y (including B) shears continuously increased to an average value of ~60% at the steady-state stage at all rates. With the total imposed displacement of 5.5 mm, our results suggest that roughly 2 mm of fault slip will be accommodated through homogeneous shearing during rupture nucleation, at least up to slip velocities of 1 mm/s.

7.1.2 Numerical constraints on strain localization and displacement partitioning at high-sliding velocities

The 3-D DEM simulations of the direct-shear PSZ model sheared to a shear strain of 5 (18.75 mm displacement) showed that the localization of slip is sensitive to the relative grain size and thickness of the PSZ compared to the remainder of the bulk gouge zone (Chapter 3). For identical PSZ thickness, I found that the absolute amount of localization increases with decreasing relative grain size of the PSZ, with up to 90% of the displacement being localized when the grain size in the PSZ is 50% of the bulk grain size. This indicates that roughly 2 mm displacement was attributed to homogeneous deformation of the gouge layer during seismic slip, which is similar to the experimental results obtained at subseismic slip rates (Chapter 2). For an identical contrast ratio of the PSZ to bulk grain size, the amount of localization does not show much variation with PSZ thickness. However, the shear displacement gradient in the fine-grained layer evolves from uniform (linear) to convex up with increasing thickness contrast, indicating that more slip is localized near the fine- and coarse-grained (FCG) interface. These results revealed that slip is prone to be largely accommodated near the grain-size contrast boundary because the boundary represents a contrast in contact stiffness and contact force between the fine- and coarse-grained layers. The main findings in Chapter 3 are that i) slip is prone to be localized within the fine-grained layer and the amount of localization is sensitive to the relative grain size and layer thickness of the PSZ, ii) the presence of a weaker, fine-grained

layer within a dense fault zone is likely to result in self-enhanced weakening of the fault zone, and iii) the absence of slip-weakening behavior in our numerical results suggests that thermal mechanisms (e.g. flash heating and weakening) are needed to induce dynamic weakening of a fault and localization alone is not sufficient to cause slip weakening.

7.1.3 The role of flash heating and thermal pressurization at medium-sliding velocities

My temperature measurement data obtained in Chapters 4 and 5 indicate that frictional heating becomes active at both the asperity-contact (Chapter 4) and bulk shear-zone scales (Chapter 5), when the sliding velocity approaches the MV range of 1 mm/s to 50 mm/s. In Chapter 4, I showed that the rotary-shear experiments equipped with a high-speed infrared camera can successfully capture flash temperatures of up to 220°C and 80°C in the actual shear zone under room-dry and wet conditions, respectively. Although the actual location of the flashes (i.e. grain-grain contact vs. grain-window contact) requires more tests and better discrimination, I found that the magnitude of the flashes showed some correlation with slip velocity and normal stress, comparable to the trends predicted by the Rice flash-weakening model (Rice, 2006). For the dry quartz gouges, I showed that flash heating can be an efficient mechanism at velocities of mm/s to cm/s while failing to induce dynamic weakening, presumably because the flash temperature did not reach the softening temperature of the SSG material ($T >$ 1700°C for quartz, Spray, 1992). On the other hand, the controlling weakening mechanism for the dynamic stress drop observed in the wet gouges is suggested to be compaction-induced pressurization due to the observed significant gouge compaction and pore fluid pressure increase.

In the MV experiments using SSG with different pore fluids under conditions favorable for TP (Chapter 5), I found that wet gouges exhibited two stages of dynamic slip weakening, a first sharp but minor weakening and a second major weakening, in all the experiments, while the room-dry gouge does not reveal any weakening (even strengthening to a friction of 0.68; Figure 7.1). The pore fluid properties, the initial pore fluid pressures, and the holding time (i.e. the waiting time between the pre-slip conditioning and main slip stages) have major impacts on both weakening stages. The magnitude of weakening seen in the two weakening stages increased with fluid type in the order of in-situ brine, DI water,

1 cSt silicone oil, and 5 cSt silicone oil gouges. The experiments with a longer holding time showed a more significant weakening in the first and second stages. Based on the estimated range of flash temperatures of 290–450°C, I inferred that the first sharp weakening stage is mainly associated with "flash pressurization/vaporization" (Yao et al., 2018; Chen et al., 2023), a mechanism combining flash heating and local thermal pressurization at grain-grain contacts. The estimated flash temperatures are broadly higher than the measurement (T_{max} = 220°C, Chapter 4), which is likely related to the small asperity contact size D_a (assuming 10–25 μm for Ottawa quartz sand gouges) between grains, exceeding the limitation of the spatial resolution (25 μm) of the IR. Considering the smaller grain size of the SSG (<150 μm) versus the Ottawa sand, both the decrease in contact size (D_a of 5 μm) and contact lifetime should lead to a lower measured and predicted flash temperature rise. This will be further tested in a future study, as suggested in section 7.3.2.8. With the support of the measurement data, I infer that flash pressurization could be active and responsible for the first sharp weakening. Based on the different local pore pressures measured during the conditioning stage, I further suggest that an initial heterogeneous distribution of the pore fluid pressure within the gouge layer, after the conditioning stage, is one of the reasons for buffering of the extent of the first weakening in the short-holding-time experiment - due to the inhibition of vaporization at regions with a relatively high background fluid pressure generated during the conditioning stage, which did not have enough time to dissipate. In addition, I propose that flash heating might be less effective in the presence of water or brine than oil, because grain size reduction during the pre-slip conditioning stage may be promoted by water, thus decreasing the flash temperature due to the decrease in asperity sizes.

The second slip-weakening stage is inferred to be caused by bulk TP in the shear zone, as suggested by the measurements of fluid pressure increases. I compared the evolution of strength, fluid pressure, and temperature, in the second slip-weakening stage with the predictions of the slip-on-plane model coupled with TP (Rice, 2006; Rempel and Rice, 2006) and found that the model does not reproduce the systematic differences in the extent of the weakening and the temperature rise observed in my experiments. I showed that the degrees of the weakening predicted by the model are similar to the experimental observations only if I allow orders of magnitude decrease in the permeability of the shear zone, based on the microstructural observations (grain size reduction). The brine and 5

cSt oil gouges, with a relatively high fluid viscosity, typically exhibit more abundant coarse grains in the PSZ (comparing brine with water, and 5 cSt oil with 1 cSt oil), suggesting a lower degree of grain size reduction in the presence of high-viscosity fluid. This observation implies that the permeability of the shear zones with a high-viscosity fluid should be higher than those with a low-viscosity fluid. In addition, I found that experiments with a high-viscosity fluid tend to generate higher temperatures.

In summary, the main findings in Chapter 5 are that i) a gouge-filled fault saturated with brine exhibits reduced weakening and higher dynamic friction compared to a water-saturated fault even though brine has a larger thermal pressurization factor , a lower hydraulic diffusivity, and a higher temperature rise; ii) the manner in which the permeability of a fault zone evolves in the presence of fluids with different viscosities may play a significant role in predicting or fitting the slip-weakening curve using coupled TP analytical models, and may govern the slip behavior of a fault in which TP is the main weakening mechanism.

7.1.4 Dynamic frictional behavior at high-sliding velocities

The results of the HV rotary-shear slip-pulse experiments, presented in Chapter 6, revealed that the evolution of the friction coefficient at seismic slip rates is strongly velocity-dependent (Sone and Shimamoto, 2009; Liao et al., 2014), for both the triangular and Yoffe-type velocity functions, with slip-weakening and restrengthening behavior occurring during the acceleration and the deceleration phases, respectively. The dry (argon-filled) SSG sample exhibits a single slip-weakening stage from a peak friction μ_{pk} of 0.75 to a minimum friction μ_{min} of 0.48. For the water-saturated SSG, the slip-weakening can be divided into two stages (first a sharp minor weakening vs. second main weakening), similar to the observed slip behavior in the MV experiments. The μ_{pk} (attained after the first weakening) lies within a relatively wide range of 0.6–0.8, due to initial strong friction oscillations, whereas the μ_{min} (0.25–0.41) generally decreases with increasing normal stress and shows minor dependence on slip acceleration and imposed displacement (Figure 7.1). During the deceleration phase, μ_{app} began to restrengthen to ~0.47–0.56 where the re-strengthening rates and work input increase slightly with normal stress and decrease with shear displacement.

I first showed that the physical properties of the host- or wall-rock materials have a major impact on the amount of weakening. Specifically, a minor amount of weakening is observed using porous steel plates with a relatively high thermal conductivity K (15 W/m/K) and a high permeability k ($\approx 1 \times 10^{-12}$ m^2), while the experiments with sandstone host blocks (K = 3.87 W/m/K and $k \approx 3 \times 10^{-17}$ m^2) reveal significant weakening. Another interesting finding is that the experiments conducted with little or no shear prestress systematically produced higher peak strength (~0.79), lower dynamic friction (~0.26), and a faster weakening rate compared to the high-pre-stress experiments. This suggests that the temperature rise and the associated weakening might be less significant in a highly pre-stressed fault. Moreover, I do not find systematic correlations between the PSZ thickness and the frictional work and power densities (FWD and FPD), which suggests that the mechanical wear process has limited effects on the growth of the PSZ for small-displacement earthquakes.

For the first slip-weakening stage observed in the wet gouges in the slip-pulse experiments (Chapter 6), I inferred that flash heating or flash pressurization/vaporization could be the dominant weakening mechanism, as also inferred in the MV experiments described in Chapter 5. The absence of the first weakening in Argon-dry gouge might be due to the high compressibility of argon, which inhibits the build-up of pore pressure. In addition, vaporization does not play a role under a gas-phase environment. The reduced main slip-weakening observed in the Argon-dry gouge might be associated with the finer grain sizes observed in the PSZ, which reduces the effectiveness and/or efficiency of flash heating. For the second or main slip weakening stage in the wet gouges, I excluded the possibility of TP in the bulk gouge zone from being the controlling weakening mechanism, on the basis of the observed onset of shear-induced gouge dilatancy accompanied by a measured pore pressure decrease (similar observations reported in Chen et al., 2023). The results of thermal modeling provided estimates of the temperature reached, after ~0.045 s or at ~0.03 m of slip (i.e. dynamic second stage weakening regime) of ~205°C, which is about the temperature needed for water vaporization at the measured pore fluid pressure of ~1.6 MPa, suggesting that the pore water could be in the vapor phase throughout the later stages of the main weakening. I inferred that local TP together with water vaporization took place within the PSZ and may have played a central role in the second stage dynamic weakening seen in my slip-pulse experiments.

7.2 Implications for small-magnitude earthquakes

7.2.1 Implications for induced seismicity in the Groningen gas reservoir

The work presented in this thesis can be directly used to provide constraints on slip-weakening parameters (e.g. heat budget, the level of dynamic friction, weakening rate) of induced seismicity in the Groningen gas reservoir. In addition, the results are relevant to natural and induced earthquakes occurring under upper crustal conditions and in lithologies resembling the Groningen units, and can provide input for feasibility studies of future projects in the subsurface (e.g. geothermal energy production, CO_2 storage, H_2 storage).

First, my observations on shear zone development, and my quantitative results on slip distribution within SSG layers, provide important constraints on the development (thickness) of the active principal slip zone, and on the heat budget for the induced seismicity in the Groningen gas reservoir (Chapters 2, 5, and 6). At subseimic slip velocities, I observed that more than one boundary-parallel shear (i.e. Y and B shears) developed in the gouge zone after 5.5 mm displacement. B shears (PSZs) were the most well-developed localization features, typically dominating at one side of the gouge layer, with an overall thickness of less than 150 μm. Previous friction experiments have documented that the formation of such a thin zone (PSZ) at subseismic rates could be a prerequisite for the accumulation of ongoing fault slip during rupture propagation (Ikari, 2015). Additionally, numerical simulations have shown that the thickness of the PSZ has a major influence on various earthquake parameters (e.g. slip duration, rupture velocity) for a fault zone dominated by TP (Platt et al., 2015). Based on these two studies and the observed slip localization feature (also thickness) in the low-sliding-velocity fault gouges, it is suggested that the rupture velocity of the fault, for example, could increase at least 3–4 times faster than a 1 mm thick layer of a homogeneously deforming fault gouge during rupture propagation. The above discussion can provide important constraints on heat generation for Groningen earthquakes if the characteristics of the PSZ (i.e. thickness and grain size) in natural pre-existing fault (both faults that have slipped in an induced event or experienced fault slip or as-yet silent faults) are better understood from borehole core observations or other exhumed analog faults with a similar lithology.

Second, the results of quantifying localization in Chapter 2 showed that about 60% of the total fault slip occurs on localization features developed in the simulated gouge zone, with 40–50% of the total slip being localized on Y and B shears. The amount of localization between R_1 and Y (including B) shears has a minor dependence on displacement rate in the range from 1 μm/s to 1000 μm/s. If the dependence of strain partitioning on velocity remains small, and if fault slip is localized along one Y shear (i.e. a PSZ), then when a fault subsequently accelerates to seismic slip rates (> 1 cm/s), the results of the localization quantification (Chapter 2) suggests that about 40% of total fault slip before the onset of dynamic weakening could still be accommodated by distributed shearing. The experimental results are comparable to my numerical DEM simulations of the PSZ behavior when sheared at seismic slip rate (1 m/s) to a total shear displacement of 18.75 mm (i.e. to a shear strain of 5; Chapter 3). I found that the absolute amount of distributed slip at seismic slip rates ranges from ~2–4 mm (~10–20% of the total slip) which remains similar to those (2.2 mm) obtained at low sliding velocities. The combined results of the experimental and DEM studies imply that the amount of distributed slip in the gouge layer might not show much variation from rupture nucleation to propagation for a short-displacement earthquake. For small earthquakes (M3–M4), seismological data indicates that fault slip is limited to a few centimeters or decimeters, following a similar pulse-like slip behavior featuring rapid accelerations and immediate/moderate decelerations (Buijze et al., 2019; Dost and Kraaijpoel, 2013; Heaton, 1990; Tomic et al., 2009; Wentinck, 2018; Zoback and Gorelick, 2012). If fault slip is ~10 cm (a displacement typically suggested to occur for M 3–4 earthquakes), then over 95% of the total displacement (assuming 4 mm contributes to uniform deformation) could be converted to frictional heat, which provides constraints on the heat budget of cm-scale seismic slip events, and hence on effects such as thermal pressurization or flash heating that may control dynamic slip weakening during seismic slip (*cf.* Hunfeld et al 2021; Chen et al 2023).

Third, the MV and HV experiments, presented in Chapters 5 and 6, revealed that the SSG slip-weakened (μ_{dyn} = 0.33–0.45 and 0.25–0.38, respectively, at σ_n = 12 MPa) as long as water/brine is present within the fault zone while remaining relatively strong (μ_{dyn} = 0.68 and 0.48, respectively, at σ_n = 12 MPa) under dry conditions. This suggests that the strength of the Groningen faults would be dynamically reduced during rupture propagation. In the MV experiments, we

showed that faults saturated with water and in-situ brine can both experience slip weakening through TP, with the brine-filled faults exhibiting the least amount of weakening and higher dynamic friction values (0.42–0.49) compared to water-saturated faults (0.33–0.45). TP was inferred to dominate dynamic weakening in these cases. Thus, if the fault zone structures within the gas reservoirs are favorable for TP (e.g. if the fault zones have a permeability $k < 10^{-16}$ m^2 and the wall rocks have sufficiently low thermal conductivity; Caine et al., 1996; Faulkner et al., 2010; Wibberley and Shimamto, 2005), our results imply that the viscosity and salinity of the pore fluid should play an important role in affecting fault weakening during Groningen earthquakes. This is considered further below.

In our HV experiments, we found that both the effectiveness and efficiency of TP could be enhanced if the wall rock blocks possess relatively low thermal conductivity and permeability. In the Groningen gas reservoir, most fault segments are interpreted to crosscut the Slochteren sandstone reservoir, the overlying basal Zechstein (mainly composed of 48 wt% anhydrite and 32 wt% calcite and dolomite) and Ten Boer claystone (mainly composed of 48 wt% quartz and 39 wt% phyllosilicates) caprocks, and the underlying Carboniferous siltstone/shale source rocks (Van Eijs et al., 2006). Thus, the fault segments that crosscut the overlying and underlying rocks would lead to different combinations of wall rocks, at different depths on each side of the fault, which may potentially lead to different rupture behavior. Generally, I argue that thermal conductivity K and permeability k of the host rocks likely have limited influence on fault weakening at fault segments juxtaposing like and unlike formations. This is because i) the variations in K between the various key lithologies are small (~3–3.6 W/m K for anhydrite, dolomite, and sandstone and ~2.5 W/m K for shale; Tang et al., 2018) and ii) the permeability below which TP is efficient for small-magnitude earthquakes is of the order of that of the most impermeable parts of the reservoir (i.e. $k \approx 1 \times 10^{-16}$ m^2, NAM, 2016, depending on PSZ thickness), while the permeability of the clay-rich lithologies (i.e. Ten Boer claystone and Carboniferous shale) is expected to be (much) lower than this. For point (ii), I argue that the effectiveness of TP could still be variable within the sandstone segments due to the heterogeneous spatial distribution of permeability ($k \approx 1 \times 10^{-16}$ m^2 to 1×10^{-12} m^2, NAM, 2016). The porosity distribution within the sandstone reservoir varies considerably both laterally in the reservoir (18–22% at the central part of the gas field, decreasing in both the northern and the southern regions

which have less than 10%, see Figure 1.7) and vertically (7% to over 20% towards shallow depths; NAM, 2013; Van Hulten et al., 2010). Hence, the permeability could concomitantly vary by two orders of magnitudes (NAM, 2016) while the thermal conductivity is low, decreasing from 2.5–2.6 to 1.5–1.75 W/m K (Eppelbaum et al., 2014). These observations imply that, due to the spatial variability in the physical properties of the sandstone reservoir, the efficiency of TP might decrease at the center of the field and towards the upper fault segments, while increasing towards the northern and southern regions and on deeper segments.

Fourth, the results of the HV friction experiments (Chapter 6) show that the evolution of friction has a strong dependence on the applied slip history (e.g. Sone and Shimamoto, 2009; Harbord et al., 2021; Rubino et al., 2022), using both triangular and Yoffe-type velocity functions, with dynamic slip weakening and re-strengthening behavior occurring as a function of the imposed slip velocity, with a nearly linear strength-velocity relationship. This finding provides clear insight into fault strength evolution with the slip-velocity history for Groningen earthquakes. It also highlights the significance of understanding whether fault acceleration and deceleration vary during dynamic slip in rupture propagation throughout the reservoir. In natural settings, rupture propagation associated with an earthquake (i.e. crack-like vs. pulse-like, Lu et al., 2007) is spontaneous, whereby slip, slip rate, and shear stress evolution are not imposed (i.e. like conventional friction experiments) but rather determined by the state of fault shear prestress, fault friction, and dynamic stress transfer (i.e. stress drop) during rupture. The duration of seismic slip (called the rise time) may be expected to be shorter, leading to a higher slip rate and faster acceleration, if i) there is a high shear prestress or a low initial static friction (because less energy is needed to drive the fault to failure, facilitating the energy available for acceleration), or ii) there is a large stress drop due to high initial friction and a large amount of dynamic weakening. Similar concepts have been suggested in previous experimental and numerical studies (e.g. Bizzarri et al., 2001; Cocco et al., 2009; Lu et al., 2010; Rubino et al., 2017). Based on the above, the results of the MV experiments presented in Chapter 5, showing the variations in dynamic weakening between the water- and brine-filled experiments, may imply that the acceleration of seismic slip varies between the upper and lower part of the sandstone reservoir – because the top part of the reservoir (50–150 m) is gas-

bearing while the lower portion (~1/3) is fully saturated with highly saline brine (with a gas-water contact (GWC) at depths of ~2971 m, Waldmann, 2012). Although the role of methane (gas, liquid, or supercritical phase) on dynamic weakening remains unknown (as further discussed in section 7.3.2.2), we may expect different amounts of stress drop above and below the GWC, potentially resulting in different fault slip velocity history.

The restrengthening behavior observed during the deceleration phase of the water-saturated slip pulse experiments of Chapter 6 has some implications for how Groningen earthquake ruptures arrest (Beeler and Tullis, 1996). In our water-saturated quartz-rich gouges, the re-strengthening rates and work input do not show much dependence on normal stress, whereas they are enhanced by shorter displacement, which is generally consistent with the study by Violay et al. (2019) of cohesive rocks (Carrara marble) under water-saturated conditions. When applied to nature, the combined experimental observations imply that the amount of co-seismic re-strengthening may vary, depending on the magnitude of earthquake slip. This effect may further influence post-seismic healing and initial stress conditions for the next seismic event, and again would likely influence the duration of the seismic slip, as discussed previously.

Finally, the values of the slip-weakening parameters (e.g. dynamic friction, weakening distance D_w, weakening rate W, and fracture energy G_c), obtained from the HV experiments, presented in Chapter 6, can be considered as new input for dynamic rupture models (e.g. Buijze et al., 2019), as well as linear elastic fracture mechanics (LEFM) models (Weng and Ampuero, 2019; Weng et al., 2021), to provide a more reliable estimate of the maximum possible moment magnitude for the induced events that might occur in the Groningen field the future (Figure 7.2). Current modeling studies of induced earthquakes in Groningen typically assume a linear slip-weakening model for individual faults, featuring a uniform fault-wide friction drop from 0.6 to values in the range of 0.2–0.5, to facilitate earthquake generation (Buijze et al., 2017b, 2019). In our HV slip-pulse data, we found that the water-saturated gouge significantly slip-weakens, following a power-law exponential decay (Mizoguchi et al., 2007), within only 0.03 m displacement while the fault accelerates to velocities > 0.16 m/s. This provides an alternative coseismic slip-weakening history that could be implemented in rupture models. At $\sigma_n^{eff} \approx 17$ MPa, the apparent friction drops

from ~0.68 (peak friction) to ~0.34 (minimum friction), with a weakening distance D_w of ~0.044 m, resulting in a slip weakening rate W of ~0.09 MPa/mm. Since the dependence of these frictional parameters on normal stress is minor or negligible/non-existent (Chen et al., 2023), we suggest that these values can directly be used as constraints for dynamic rupture modeling. Overall, the observed slip-weakening curves and the associated frictional parameters (i.e. μ_{pk} and μ_{dyn}) derived from the empirical function (i.e. power-law) are similar to the previous results of the slip-pulse experiments on the Groningen reservoir rocks (Chen et al., 2023; Hunfeld et al., 2021), even with the application of more realistic conditions (high pre-stress as well as the use of sandstone host blocks) in our experiments. One main difference is that the D_w is shorter and W is smaller in our study, due to the faster slip acceleration and shorter displacement that we applied. This highlights the importance of determining true slip and stress drop magnitude associated with Groningen earthquakes, as typically estimated from seismic analysis (e.g. Dost and Kraaijpoel, 2013). The present constraints from my experiments might be further verified by seismic analysis of stress drop and slip magnitude during small slip events in Groningen.
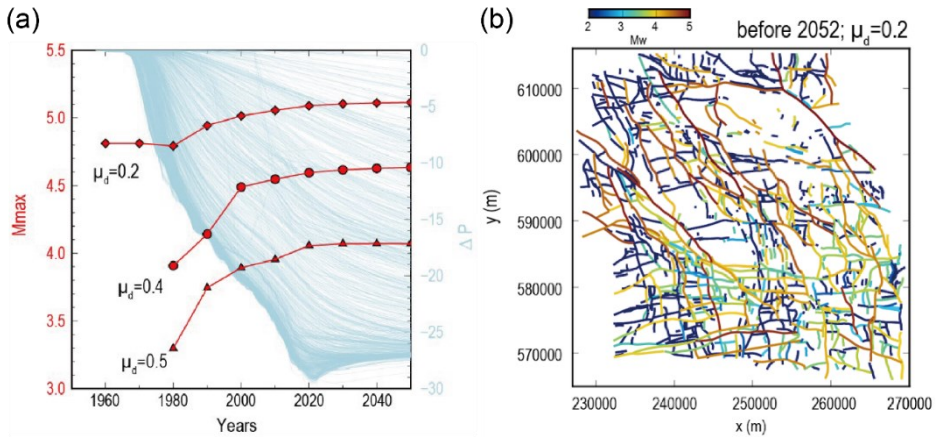
Figure 7.2: *M_{max} predictions for the Groningen gas field. (a) Estimated maximum moment magnitude M_{max} over time (years), for different values of dynamic friction μ_d, calculated for stress changes, on the main (i.e. largest) faults mapped in the Groningen field, resulting from fluid pressure changes ΔP due to gas depletion. (b) Along dip 2D LEFM and along-strike 2.5D LEFM giving M_{max} on the main faults in the Groningen field, assuming $\mu_{dyn}=0.2$ before 2052. Adapted from NAM (2022).*

7.2.2 Broader implications

The velocity dependence of friction of fault materials has a strong correlation to shear localization and the associated development of localization

features within the fault zone (Logan et al., 1992; Marone, 1998, Beeler et al., 1996). The transition from velocity strengthening or velocity neutral behavior to velocity weakening behavior is typically associated with the transition of distributed deformation and slip localized along R_1 shears to a well-developed set of Y or B shears (Beeler et al., 1996; Ikari, 2015). My results obtained from the velocity-stepping experiment reported in Chapter 2 showed that SSG exhibits velocity-weakening behavior during velocity transitions from 1 to 30 to 1000 μm/s, which is opposite to the velocity-strengthening behavior reported for SSC in the previous study by Hunfeld et al. (2017) who conducted velocity-stepping experiments at a lower velocities, i.e. ranging from 0.1 to 10 μm/s, using identical materials, experimental setup and conditions. This difference in the velocity-dependence behavior suggests that a transition from velocity-strengthening to velocity-weakening behavior could be associated with the size of (up)step velocities employed. In addition, the gouge microstructures at the higher sliding velocities (i.e. 30 and 1000 μm/s) do not show well-developed boundary-parallel localization features, and the amount of localization along Y and B shears is even lower than those at low sliding velocity (i.e. 1 μm/s; see Figure 7.1). Similar frictional behavior and gouge microstructures have also been experimentally documented in simulated calcite fault gouges deformed at a velocity range from 0.1 to 300 μm/s under an ambient temperature of 550°C as well as being reproduced in microphysical modeling (Chen et al., 2020). The result of our work further implies that the occurrence of velocity-weakening behavior might not necessarily require well-developed boundary-parallel shears or an extreme amount of slip localization along these features. In turn, the environmental conditions (i.e. ambient temperature and normal stress) and sliding velocities, which control the granular flow of the bulk gouge volume (i.e. dilatation versus compaction; Hunfeld et al., 2017), may play an important role in determining the velocity dependence of the gouge materials.

The results of the MV experiments of Chapter 5 highlight the importance of pore fluid properties, especially fluid viscosity and salinity, in influencing the shear zone development and the efficiency of TP in gouge-filled faults during rupture. In natural settings, formation waters in sedimentary sequences display a range of salinity of about 5 orders of magnitude, varying between 72 - 600 g/l total dissolved solids (Case, 1945; Hanor, 1994), which influence the fluid viscosity. In addition, in geoengineering practice, the viscosity of the injected

fluids varies over 4 orders in magnitude, from 1 mPa s for liquid water to 10 Pa s for fracturing fluids (Economides and Boney, 2000), though the actual fluid viscosity at shallow depths (i.e. 3 km) might change under in-situ PT conditions (e.g. P_f = 15 MPa, T = 100 °C in the case of the Groningen gas field). Since most previous experimental studies of dynamic frictional properties of fault gouges were done using DI water as pore fluid (e.g. Aretusini et al., 2021; Chen et al., 2023; Ferri et al., 2010; Hunfeld et al., 2021; Kuo et al., 2021, 2022; Remitti et al., 2015; Ujiie et al., 2010, 2013; Yao et al., 2018), it is important to consider the effect of pore fluid properties when assessing the dynamic rupture behavior of both natural and induced earthquakes (Cornelio et al., 2019, 2020). Moreover, we showed that the coupled TP model predictions are more comparable to experimental observations when taking shear zone development and associated changes in permeability into account. This further highlights the importance of shear localization and microstructure, as well as the slip history effect of faults during the seismic cycle, in controlling the effectiveness and efficiency of TP. History effects include whether faults become cemented and fractures become healed during the post-seismic period, which will cause a decrease in fault-zone permeability over geological time, as well as cohesion development and restrengthening. Importantly, these time-dependent healing and sealing processes are typically not considered in seismic cycle simulations (e.g. Lapusta and Rice, 2003; Li et al., 2022) or in geomechanical models (e.g. Buijze et al., 2019).

7.3 Suggestions for future research

The work done in this thesis provides experimental and numerical perspectives on the role of slip localization, frictional heating, and dynamic weakening in quartz-rich fault gouges during small-magnitude earthquakes, from the rupture nucleation to propagation stages. Still, there are unresolved issues that should be addressed to further improve our understanding of small slip events. Below, I list the remaining unresolved questions and data needed of work reported, as well as suggestions for improvements in both experimental methods and conditions for future work.

7.3.1 Unresolved issues and remaining data needs
7.3.1.1 Spatial heterogeneity of slip localization at low sliding velocities

In the direct shear experiments of Chapter 2, I found that the pattern of gouge deformation is generally consistent (uniform) throughout the analyzed

gouge zone (from one end toward the center), for most experiments. However, the deformation of the albite marker boundaries in two experiments, one at 1 μm/s in the strain-softening stage and the other at 1000 μm/s in the steady-state stage, show a clear variation from the ends towards the center of the analyzed gouge layer segment. In both cases, more deformation appears to be accommodated by a boundary shear, and less by R_1 shears, at one end of the analyzed gouge segment (only one end is included), whereas the deformation looks more "distributed" closer to the center. However, I do not see a clear trend in the amount of slip computed for either the R_1 shears or Y (or B) shears (Figure 2.7 in Chapter 2). Despite the insignificant difference in displacement partitioning obtained from my automated analyses, I argue that this change in the deformation pattern is real and could be related to the cylindrical or interlocking L shape of the direct shear setup. Detailed FEM modeling (e.g. Logan et al, 1992) is required to link the pattern of the gouge deformation to variations in normal stress or rotation of the principal stress axes, related to the imperfect direct-shear boundary conditions imposed by the shear setup. In addition, microstructural observations on natural fault-zone gouges derived from either borehole cores or exhumed analogue faults are needed to provide a direct comparison with the experimental products as well as constraints on the initial state of the gouge microstructure of faults in the Groningen reservoir system prior to induced slip.

7.3.1.2 The role of FCG interface on initiation of slip localization

In the DEM modeling of Chapter 3, I observed that slip localization tends to initiate at the fine- to coarse-grained (FCG) gouge interface, even though the strain is nearly fully localized within the fine-grained layer. I suggested that this is due to the difference in the properties at the FCG interface as compared to both fine- and coarse-grained layers. At the FCG interface before shearing, the mixture of fine and coarse grains provides a lower local porosity and an increase in the average coordination number of large grains. The interface region also becomes a contrasting boundary in terms of grain size, contact stiffness, and contact force. The above factors likely trigger the initial slip at grain contacts in the interface. However, the controlling role of each variable remains unclear. More detailed analyses are needed, such as the evolution of contact forces over each timestep.

7.3.1.3 Effect of pore fluid properties on slip localization and other possible dynamic weakening mechanisms at medium sliding velocities

In the microstructural observations of the MV gouge samples presented in Chapter 5, the cause of the observed differences in shear zone development in the fault gouges tested with different fluid viscosities remains unclear. A more systematic analysis of the particle size distribution of the principle slip zone is required to determine how much variation in grain sizes exists, as well as how this leads to potential changes in gouge permeability. Alternatively, the latter can be done by measuring the permeability before and after the slip pulse. In addition, it is also necessary to conduct microstructural observations on the deformed gouge layer, after the conditioning stage, as the ongoing fault slip localization and slip distribution could be strongly dependent on the initial gouge state (Ikari, 2015), as mentioned in the previous section 7.3.1.1. Finally, we note that the brine pore fluid has different salinity and pH compared to water, which could influence the subcritical crack growth and, thus, the process of grain fragmentation. More systematic experiments, varying viscosity, salinity, and pH to determine which of the fluid properties is most crucial in controlling the efficiency of thermal pressurization, are needed.

Another question is whether other dynamic weakening mechanisms, besides TP (at shear band scales or asperity contact scales), might also play a role in the second slip weakening stage that I observed under undrained fluid conditions. In some water and brine experiments, I observed that the measured fluid pressure increase cannot explain the full amount of the weakening. Other mechanisms such as Elastohydrodynamic lubrication (EHD; Brodsky and Kanamori, 2001), or silica gel lubrication in wet quartz-dominated materials (Di Toro et al., 2004), have also been proposed to be an effective dynamic weakening mechanism in a fluid-saturated fault. To investigate the effectiveness of these two mechanisms in our quartz-rich fault gouges, a wider range of fluid viscosities (e.g. 100 times higher than water) as well as drained boundary conditions should be considered in future research.

7.3.1.4 Thin black layers: Shear localization features or artifacts?

In the HV slip-pulse experiments of Chapter 6, I observed that most wet deformed gouges display several continuous, thin (< 100 μm black-colored (i.e. opaque) layers, oriented roughly along the shear plane in plane-polarized optical

images, and generally randomly distributed across the thickness of the gouge layer (e.g. Figure 6.7d in Chapter 6). On the other hand, the bulk spectator region (i.e. the damage zone beyond the PSZ) in the dry-deformed, slip-pulse gouge samples generally exhibits colors as dark as these thin layers, while the PSZ is much lighter. I further showed that the black materials are not related to either variations in chemical composition (SEM-BSE analysis), the formation of amorphous materials (FIB-TEM analysis), or the formation of carbonaceous materials (Raman analysis). The origin and nature of these shear-parallel features, and whether they are another form of Y shear, which acts as a relatively impermeable layering structure, remains unknown. Alternatively, dark features observed in plane-polarized optical images may be simply due to the blocking of light by ultrafine gouge materials if the thin section is too thick. Another possibility for the observed black layers might be artifacts due to thin-section preparation (i.e. polishing), resulting in variations in the local thickness of the thin section. To further investigate whether these black layers are localization features or artifacts, future analyses on i) surface topography and chemical composition with a higher resolution SEM-BSE (e.g. Zeiss Gemini 450 SEM), ii) TEM studies to determine if these bands are simply ultrafine (nano) grained bands, and iii) additional careful polishing on these thin sections, can be included.

7.3.1.5 Dynamic weakening mechanisms during seismic slip pulses: At what scale did TP occur and how effective was vaporization?

Based on the results of the thermal modeling presented in Chapter 6, I inferred that TP together with water vaporization could occur within the PSZ during the main dynamic weakening, even with a high initial fluid pressure ($P_i =$ 1 MPa). However, I found that the increase in the measured fluid pressure and the gouge dilatation are limited, which suggests that TP might occur at a smaller scale (i.e. asperity scales), the same mechanism (i.e. flash pressurization) as proposed by Chen et al. (2023). Numerical modeling at particle scales coupled with thermal-hydraulic-mechanical (THM) solutions is needed to further demonstrate the possibility of local TP. In addition, it remains difficult to assess how much weakening can be attributed to vaporization, since pore fluid thermal pressurization and vaporization may be triggered at the same time in different locations throughout the weakening regime. Currently, my modeling does not include the latent heat of water vaporization, which would buffer the temperature rise (Acosta et al., 2018; Chen et al., 2017), and should limit the heating and

weakening. More detailed modeling is needed, taking into account variations in local microstructure and host-block materials to investigate the effectiveness and efficiency of water vaporization. Finally, to investigate whether water vaporization did occur and caused additional weakening in the present slip-pulse tests, experiments with higher initial pore fluid pressures ($P_i > 2$ MPa) should be performed in future studies.

7.3.2 Broader challenges for future studies

7.3.2.1 *Effect of fault gouge heterogeneity on localization and dynamic weakening*

The pre-existing faults that host induced seismic events in the Groningen field are characterized by ancient offsets in the tens to hundreds of meters (e.g. 50 m; Buijze et al., 2019). As already discussed, this leads to the juxtaposition of the reservoir sandstone against the overlying caprocks (i.e. Ten Boer Claystone, Basal Zechstein) as well as the underlying source rock (i.e. Carboniferous shale/siltstone substrate). Experimental studies of fault gouges containing strong (quartz) and weak (clay) gouge segments, at subseismic slip rates, have shown that the fault strength can significantly decrease with displacement, due to shear localization within a thin weak clay-rich layer, developed due to smearing (Bedford et al., 2021; Arts et al., 2023, in review). When shear heating is involved during seismic slip pulse, this might activate variable/additional thermal processes (e.g. thermal dehydration or decomposition of clay minerals) for a heterogenous fault gouge as compared to a pure SSG layer. Additionally, the smearing process will affect the local permeability and porosity of the bulk gouge layer, which will affect the hydraulic properties and the compressibility, which in turn affect TP (see equations 1.6 and 1.10). To fully understand the dynamic rupture behavior of pre-existing faults and associated weakening mechanisms, across an entire fault segment, the heterogeneous spatial distribution of different fault gouge materials should be considered in future HV experiments, by introducing a segmented layer of the overlying and underlying fault gouges together with SSG, with detailed microstructural analyses of grain size, porosity and PSZ thickness.

7.3.2.2 *Dynamic slip behavior of reservoir rocks in the presence of gas (methane)*

Brine and methane (plus 15% Nitrogen) were reported to be the dominant fluids that exist within the sandstone reservoir (De Jager and Geluk, 2007). I have

shown that dynamic weakening would be reduced in the presence of in-situ brine if TP is dominant. How dynamic weakening varies in the presence of methane (gas or supercritical phase) and/or nitrogen remains unknown and is challenging to test in HV friction experiments. This type of knowledge requires a full understanding of the thermal, thermodynamic, hydraulic, and phase properties (equation of state) of methane and methane/nitrogen mixtures. In addition, as discussed previously, more systematic friction experiments with variable pore fluids with different fluid viscosities, compressibilities, and expansivities are required to constrain how these parameters influence TP-induced weakening, together with a comparison with the predictions from analytical solutions of the coupled TP problem (Rice, 2006).

7.3.2.3 Mechanism for co-seismic restrengthening behavior

In Chapter 6, the observed slip restrengthening during slip-pulse deceleration provides a first insight into the amount of strength that the fault would gain during a single seismic slip-pulse event. The presence or absence of re-strengthening is expected to impact many aspects of the earthquake cycle, including the slip rate evolution during faulting, the pattern of rupture propagation (crack- or pulse-like), the release of seismic waves, the energy budget, as well as rupture arrest, post-seismic fault healing and repeat time (Sone and Shimamoto, 2009; Violay et al., 2019). In the present work, I have shown that the re-strengthening rates of, and work input into, our wet SSG increase slightly with normal stress, while they decrease with shear displacement in the presence of water, in general agreement with previous experiments on cohesive rocks (Violay et al., 2019). However, it remains unclear whether the restrengthening mechanisms proposed by Violay et al. (e.g. change in rate-dependent crystal-plastic and grain size-dependent deformation mechanisms in the presence of water for Carrara marble and water-cooling of the frictional interface for micro-gabbro) are applicable to our wet SSG sample. On the other hand, Chen et al. (2023) demonstrated the opposite trend in the dependence of restrengthening on shear displacement, with their results showing that re-strengthening in the wet SSG sample is favored by larger displacement. Since the geometry of the pressurized gouge setup (an annular ring-shear assembly versus solid cylinder) and host-block materials (Ti-alloy vs. sandstone) are different from mine, whether these properties influence restrengthening remains to be further tested. More systematic tests are needed such as with variable shear

displacement, slip acceleration/deceleration, host-block materials, and gouge materials to fully understand the mechanism of restrengthening and how re-strengthening influences the earthquake cycle.

7.3.2.4 Scaling and extrapolation of laboratory results to nature

Whether the laboratory-derived frictional properties of the SSG obtained on a centimeter scale can be applied to the context of fault reactivation in the Groningen reservoir, with the dimensions of kilometer scales, remains a challenging and important question. One potential and straightforward approach is to directly compare the temperature anomalies measured in the experiments (Chapters 4, 5, and 6) with those estimated from fault rock samples recovered from the field. The temperature anomalies in both experimental and natural samples will be further approached by using the quantum diamond magnetometer (QDM), which can probe microscale magnetization in three dimensions (i.e., the full magnetic vector) with a spatial resolution down to 1–2 microns and will be sensitive enough to detect the weak magnetization effects in the Groningen sandstone that may be associated with elevated temperature and/or fluid motion tied to seismic activity (Fu et al., in progress). Besides the direct comparison of temperature rise, an integrated approach, including studies on fault geometry (e.g. surface roughness, dimensions), fault offset, and materials heterogeneity (e.g. elastic modulus, permeability, softening temperature, mineral, and chemical composition, etc.) along fault strike, are required to bridge the gaps between the lab and natural scales (e.g. Niemeijer et al., 2012). In addition to experiments at the cm-scale (such as the present research), fault shearing experiments at single-grain scale (Mishra et al., in progress), as well as dm- and m-scale (Buijze et al., 2021; Ji et al., in progress; Togo et al., 2015; Yamashita et al., 2015), are needed to validate theoretical (Rice et al., 2014) and numerical models, including finite element models (FEM; Ma et al., 2006) as well as DEM modeling, which can serve as an upscaling tool from particle to borehole core scales (Chapter 3).

7.3.2.5 Advances in experimental methodology I: Low-velocity experiments with XCT analysis

In Chapter 2, the evolution of gouge microstructures at three different frictional stages was obtained, at a specific slip velocity, by conducting three individual experiments each with XCT scanning of the deformed gouge layer recovered after dismantling the direct shear pistons used. To avoid bias or

disruption from sample extraction and preparation, and to avoid effects of sample variability, it would be better to analyze the same gouge layer at different shear strains. This can be done by employing a direct-shear setup made of materials such as PEEK (polyetheretherketone) or aluminium, which can support high confining stress as well as allow X-rays to penetrate through the piston and gouge sample. Another alternative is to perform the experiments using dynamic synchrotron X-ray microtomography (4-D XCT), enabling linking of the macroscale behavior to the processes active under in situ conditions, as already done for compaction (e.g. Renard et al., 2020) and dehydration experiments (e.g. Fusseis et al., 2022). With this kind of setup, we could conduct incremental XCT scans for a single direct-shear setup and the entire sample (from one end to the other end), without taking apart the piston at different frictional stages. In addition, sample damage during recovery could be avoided.

7.3.2.6 Advances in ML-training methodology: Boundary segmentation

The present ML-based boundary detection method presented in Chapter 2 offers a reliable method of boundary detection, with less than 10% of detections being rejected by the outlier filter. To further improve the segmentation quality, future improvements in image pre-processing could be made within the framework of automatic boundary method; for example, by employing fracture suturing or intensity adjustment. This, in principle, can be done relatively easily, if only by processing a few images, but becomes more challenging when dealing with more than hundreds or thousands of images – thus demanding further application of efficient machine learning tools for these purposes.

7.3.2.7 Advances in DEM modeling: The effect of time-dependent mechanisms on localization and mechanical response

The present numerical DEM PSZ model is a simple representation of a fault zone gouge with a preexisting PSZ, applied without introducing any time-dependent mechanism such as grain size reduction or contact healing. Previous studies have shown that strain localization is strongly correlated with enhanced grain size reduction (Mair and Abe, 2008), the presence of time-dependent contact healing (Morgan, 2004), as well as an increase in interparticle bond strength (Casas et al., 2022), which caused a further reduction in friction, or unstable slip. Thus, it is also important to investigate how time-dependent effects and interparticle bonds play a role in the localization and frictional response in

our PSZ model. A future challenge is to couple DEM modeling with contact heating and pore network modeling (Mahmoodlu et al., 2016; Raoof and Hassanizadeh, 2010) to investigate the effect of the presence of multi-phase pore fluids on the heat generation at grain contact and bulk shear zone scales, and thus on weakening.

7.3.2.8 Advances in Experimental Methodology I: MV Experiments with a High-Speed Infrared Camera

One of the main issues in the experimental quantification of flash temperatures is the uncertainty of the location of flashes, whether resulting from grain-window or grain-grain contacts. To reduce the possibility of grain-window flashes, I aim to conduct further tests using a window with a curved surface instead of a flat surface together with depositing a low-friction material on the surface. Apart from determining flash temperatures, we can also employ the high-speed infrared camera with a full-frame analysis to quantify the evolution of the bulk temperature across the entire gouge layer for the experiments using SSG. This can be combined with the experiments using different pore fluids to provide further information on the relationship between localization and heat generation as well as heat diffusion.

7.3.2.9 Advances in Experimental Methodology II: HV Experiments

The present HV experiments were performed at a normal stress σ_n of up to 17 MPa, a pore fluid pressure P_f of 1 MPa, and under room temperature T conditions, which are not as extreme as the in-situ reservoir conditions ($\sigma_n = 55$ MPa, $P_f = 15$ MPa, and $T = 100°C$). It is also important to understand whether or when the level of the dynamic friction is no longer dependent on normal stress as well as the effect of background fluid pressure and temperature on the frictional behavior since temperature and pressure directly influence the state of the fluid, which has been shown to play a crucial role in controlling the dynamic slip of a cohesive fault (e.g. Feng et al., 2023). It remains challenging to impose seismic slip pulses on fluid-saturated gouges under such extreme conditions, due to the technical issue of the confinement of fluid and gouges.

References

Abe, S., & Mair, K. (2009). Effects of gouge fragment shape on fault friction: New 3D modelling results. Geophysical Research Letters, 36(23).

Acosta, M., Passelègue, F. X., Schubnel, A., & Violay, M. (2018). Dynamic weakening during earthquakes controlled by fluid thermodynamics. Nature communications, 9(1), 3074.

Atkinson, B. K. (1984). Subcritical crack growth in geological materials. Journal of Geophysical Research: Solid Earth, 89(B6), 4077-4114.

An, L. J., & Sammis, C. G. (1994). Particle size distribution of cataclastic fault materials from southern California: A 3-D study. Pure and Applied Geophysics, 143(1), 203-227.

Aretusini, S., Mittempergher, S., Plümper, O., Spagnuolo, E., Gualtieri, A. F., & Di Toro, G. (2017). Production of nanoparticles during experimental deformation of smectite and implications for seismic slip. Earth and Planetary Science Letters, 463, 221-231.

Aretusini, S., Meneghini, F., Spagnuolo, E., Harbord, C. W., & Di Toro, G. (2021). Fluid pressurisation and earthquake propagation in the Hikurangi subduction zone. Nature communications, 12(1), 2481.

Badt, N. Z., Tullis, T. E., Hirth, G., & Goldsby, D. L. (2020). Thermal pressurization weakening in laboratory experiments. Journal of Geophysical Research: Solid Earth, 125(5), e2019JB018872.

Bakker, E., Hangx, S. J., Niemeijer, A. R., & Spiers, C. J. (2016). Frictional behaviour and transport properties of simulated fault gouges derived from a natural CO_2 reservoir. International Journal of Greenhouse Gas Control, 54, 70-83.

Barbery, M. R., Chester, F. M., & Chester, J. S. (2021). Characterizing the distribution of temperature and normal stress on flash heated granite surfaces at seismic slip rates. Journal of Geophysical Research: Solid Earth, 126(5), e2020JB021353.

Beeler, N. M., Tullis, T. E., Blanpied, M. L., & Weeks, J. D. (1996). Frictional behavior of large displacement experimental faults. Journal of Geophysical Research: Solid Earth, 101(B4), 8697-8715.

Beeler, N. M., & Tullis, T. E. (1996). Self-healing slip pulses in dynamic rupture models due to velocity-dependent strength. Bulletin of the Seismological Society of America, 86(4), 1130-1148.

Beeler, N. M., Tullis, T. E., & Goldsby, D. L. (2008). Constitutive relationships and physical basis of fault strength due to flash heating. Journal of Geophysical Research: Solid Earth, 113(B1).

Bedford, J. D., & Faulkner, D. R. (2021). The role of grain size and effective normal stress on localization and the frictional stability of simulated quartz gouge. Geophysical Research Letters, 48(7), e2020GL092023.

Bedford, J. D., Faulkner, D. R., & Lapusta, N. (2022). Fault rock heterogeneity can produce fault weakness and reduce fault stability. Nature Communications, 13(1), 326.

Bizzarri, A., Cocco, M., Andrews, D. J., & Boschi, E. (2001). Solving the dynamic rupture problem with different numerical approaches and constitutive laws. Geophysical Journal International, 144(3), 656-678.

Bos, B., & Spiers, C. J. (2000). Effect of phyllosilicates on fluid-assisted healing of gouge-bearing faults. Earth and Planetary Science Letters, 184(1), 199-210.

Bos, B., & Spiers, C. J. (2001). Experimental investigation into the microstructural and mechanical evolution of phyllosilicate-bearing fault rock under conditions favouring pressure solution. Journal of Structural Geology, 23(8), 1187-1202.

Boullier, A. M., Yeh, E. C., Boutareaud, S., Song, S. R., & Tsai, C. H. (2009). Microscale anatomy of the 1999 Chi-Chi earthquake fault zone. Geochemistry, Geophysics, Geosystems, 10(3).

Boullier, A. M. (2011). Fault-zone geology: lessons from drilling through the Nojima and Chelungpu faults. Geological Society, London, Special Publications, 359(1), 17-37.

Boulton, C., Yao, L., Faulkner, D. R., Townend, J., Toy, V. G., Sutherland, R., ... & Shimamoto, T. (2017). High-velocity frictional properties of Alpine Fault rocks: Mechanical data, microstructural analysis, and implications for rupture propagation. Journal of Structural Geology, 97, 71-92.

Brantut, N., Schubnel, A., Corvisier, J., & Sarout, J. (2010). Thermochemical pressurization of faults during coseismic slip. Journal of Geophysical Research: Solid Earth, 115(B5).

Brantut, N., & Platt, J. D. (2017). Dynamic weakening and the depth dependence of earthquake faulting. Fault zone dynamic processes: Evolution of fault properties during seismic rupture, 171-194.

Brantut, N., & Mitchell, T. M. (2018). Assessing the efficiency of thermal pressurization using natural pseudotachylyte-bearing rocks. Geophysical Research Letters, 45(18), 9533-9541.

Brantut, N., Passelègue, F. X., Deldicque, D., Rouzaud, J. N., & Schubnel, A. (2016). Dynamic weakening and amorphization in serpentinite during laboratory earthquakes. Geology, 44(8), 607-610.

Breckels, I. M., & Van Eekelen, H. A. M. (1982). Relationship between horizontal stress and depth in sedimentary basins. Journal of Petroleum Technology, 34(09), 2191-2199.

References

Brodsky, E. E., & Kanamori, H. (2001). Elastohydrodynamic lubrication of faults. Journal of Geophysical Research: Solid Earth, 106(B8), 16357-16374.

Buijze, L., Niemeijer, A. R., Han, R., Shimamoto, T., & Spiers, C. J. (2017a). Friction properties and deformation mechanisms of halite (-mica) gouges from low to high sliding velocities. Earth and Planetary Science Letters, 458, 107-119.

Buijze, L., van den Bogert, P. A., Wassing, B. B., Orlic, B., & ten Veen, J. (2017b). Fault reactivation mechanisms and dynamic rupture modelling of depletion-induced seismic events in a Rotliegend gas reservoir. Netherlands Journal of Geosciences, 96(5), s131-s148.

Buijze, L., van den Bogert, P. A. J., Wassing, B. B. T., & Orlic, B. (2019). Nucleation and arrest of dynamic rupture induced by reservoir depletion. Journal of Geophysical Research: Solid Earth, 124, 3620–3645. https://doi.org/10.1029/2018JB016941

Buijze, L., Guo, Y., Niemeijer, A. R., Ma, S., & Spiers, C. J. (2021). Effects of heterogeneous gouge segments on the slip behavior of experimental faults at dm scale. Earth and Planetary Science Letters, 554, 116652.

Byerlee, J. (1978). Friction of rocks. In Rock friction and earthquake prediction (pp. 615-626). Birkhäuser, Basel.

Caine, J. S., Evans, J. P., & Forster, C. B. (1996). Fault zone architecture and permeability structure. Geology, 24(11), 1025-1028.

Casas, N., Mollon, G., & Daouadji, A. (2022). DEM analyses of cemented granular fault gouges at the onset of seismic sliding: peak strength, development of shear zones and kinematics. Pure and Applied Geophysics, 179(2), 679-707.

Case, L. C. (1945). Exceptional Silurian brine near Bay City, Michigan. AAPG Bulletin, 29(5), 567-570.

Catalano, E., Chareyre, B., & Barthélémy, E. (2014). Pore-scale modeling of fluid-particles interaction and emerging poromechanical effects. International Journal for Numerical and Analytical Methods in Geomechanics, 38(1), 51-71. doi:10.1002/nag.2198

Chen, J., Yang, X., Duan, Q., Shimamoto, T., & Spiers, C. J. (2013). Importance of thermochemical pressurization in the dynamic weakening of the Longmenshan Fault during the 2008 Wenchuan earthquake: Inferences from experiments and modeling. Journal of Geophysical Research: Solid Earth, 118(8), 4145-4169.

Chen, J., Niemeijer, A., Yao, L., & Ma, S. (2017). Water vaporization promotes coseismic fluid pressurization and buffers temperature rise. Geophysical Research Letters, 44(5), 2177-2185.

Chen, J., Verberne, B. A., & Niemeijer, A. R. (2020). Flow-to-friction transition in simulated calcite gouge: Experiments and microphysical modeling. Journal of Geophysical Research: Solid Earth, 125(11), e2020JB019970.

Chen, J., Niemeijer, A. R., & Spiers, C. J. (2021). Microphysical modeling of carbonate fault friction at slip rates spanning the full seismic cycle. Journal of Geophysical Research: Solid Earth, 126(3), e2020JB021024.

Chen, J., Hunfeld, L. B., Niemeijer, A. R., & Spiers, C. J. (2023). Fault weakening during short seismic slip pulse experiments: The role of pressurized water and implications for induced earthquakes in the Groningen gas field. Journal of Geophysical Research: Solid Earth, 128(2), e2022JB025729.

Chester, F. M., & Logan, J. M. (1986). Implications for mechanical properties of brittle faults from observations of the Punchbowl fault zone, California. Pure and applied geophysics, 124, 79-106.

Chester, F. M., & Logan, J. M. (1990). Frictional faulting in polycrystalline halite: Correlation of microstructure, mechanisms of slip, and constitutive behavior. The Brittle-Ductile Transition in Rocks, 56, 49-65.

Chester, F. M., Eva–ns, J. P., & Biegel, R. L. (1993). Internal structure and weakening mechanisms of the San Andreas fault. Journal of Geophysical Research: Solid Earth, 98(B1), 771-786.

Chester, F. M., & Chester, J. S. (1998). Ultracataclasite structure and friction processes of the Punchbowl fault, San Andreas system, California. Tectonophysics, 295(1-2), 199-221.

Chester, J. S., Chester, F. M., & Kronenberg, A. K. (2005). Fracture surface energy of the Punchbowl fault, San Andreas system. Nature, 437(7055), 133-136.

Chester, F. M., Rowe, C., Ujiie, K., Kirkpatrick, J., Regalla, C., Remitti, F., ... & Expedition 343 and 343T Scientists. (2013). Structure and composition of the plate-boundary slip zone for the 2011 Tohoku-Oki earthquake. Science, 342(6163), 1208-1211.

Cocco, M., Tinti, E., Marone, C., & Piatanesi, A. (2009). Scaling of slip weakening distance with final slip during dynamic earthquake rupture. International Geophysics, 94, 163-186.

Collettini, C., Niemeijer, A., Viti, C., & Marone, C. (2009). Fault zone fabric and fault weakness. Nature, 462(7275), 907-910.

Cornelio, C., Spagnuolo, E., Di Toro, G., Nielsen, S., & Violay, M. (2019). Mechanical behaviour of fluid-lubricated faults. Nature communications, 10(1), 1274.

Cornelio, C., Passelègue, F. X., Spagnuolo, E., Di Toro, G., & Violay, M. (2020). Effect of fluid viscosity on fault reactivation and coseismic weakening. Journal of Geophysical Research: Solid Earth, 125(1), e2019JB018883.

De Jager, J., & Geluk, M. C. (2007). Petroleum geology. Geology of the Netherlands, 241-264.

De Jager, J., & Visser, C. (2017). Geology of the Groningen field–an overview. Netherlands Journal of Geosciences, 96(5), s3-s15.

References

De Paola, N., Collettini, C., Faulkner, D. R., & Trippetta, F. (2008). Fault zone architecture and deformation processes within evaporitic rocks in the upper crust. Tectonics, 27(4).

De Paola, N., Hirose, T., Mitchell, T., Di Toro, G., Viti, C., & Shimamoto, T. (2011). Fault lubrication and earthquake propagation in thermally unstable rocks. Geology, 39(1), 35-38.

De Paola, N., Holdsworth, R. E., Viti, C., Collettini, C., & Bullock, R. (2015). Can grain size sensitive flow lubricate faults during the initial stages of earthquake propagation?. Earth and Planetary Science Letters, 431, 48-58.

Dieterich, J. H. (1979). Modeling of rock friction: 1. Experimental results and constitutive equations. Journal of Geophysical Research: Solid Earth, 84(B5), 2161-2168.

Di Toro, G., Goldsby, D. L., & Tullis, T. E. (2004). Friction falls towards zero in quartz rock as slip velocity approaches seismic rates. Nature, 427(6973), 436-439.

Di Toro, G., Hirose, T., Nielsen, S., Pennacchioni, G., & Shimamoto, T. (2006). Natural and experimental evidence of melt lubrication of faults during earthquakes. science, 311(5761), 647-649.

Di Toro, G., Niemeijer, A., Tripoli, A., Nielsen, S., Di Felice, F., Scarlato, P., ... & Mariano, S. (2010). From field geology to earthquake simulation: a new state-of-the-art tool to investigate rock friction during the seismic cycle (SHIVA). Rendiconti Lincei, 21, 95-114.

Di Toro, G., Han, R., Hirose, T., De Paola, N., Nielsen, S., Mizoguchi, K., ... & Shimamoto, T. (2011). Fault lubrication during earthquakes. Nature, 471(7339), 494-498.

Dost, B., & Haak, H. W. (2007). Natural and induced seismicity. Royal Netherlands Academy of Arts and Sciences.

Dost, B., & Kraaijpoel, D. (2013). The August 16, 2012 earthquake near Huizinge (Groningen). KNMI, de Bilt, the Netherlands.

Dost, B., van Stiphout, A., Kühn, D., Kortekaas, M., Ruigrok, E., & Heimann, S. (2020). Probabilistic moment tensor inversion for hydrocarbon-induced seismicity in the Groningen gas field, the Netherlands, part 2: Application. Bulletin of the Seismological Society of America, 110(5), 2112-2123.

Douglas, D. H., & Peucker, T. K. (1973). Algorithms for the reduction of the number of points required to represent a digitized line or its caricature. Cartographica: the international journal for geographic information and geovisualization, 10(2), 112-122.

Economides, M. J., & Boney, C. (2000). Reservoir stimulation in Petroleum Production. In Reservoir Stimulation (3rd ed., pp. 1-1,1-18). John Wiley & Sons, University of Houston, USA.

Ellsworth, W. L. (2013). Injection-induced earthquakes. Science, 341(6142), 1225942.

Elsworth, D., Spiers, C. J., & Niemeijer, A. R. (2016). Understanding induced seismicity. Science, 354(6318), 1380-1381.

Erdoğan, S. T., Forster, A. M., Stutzman, P. E., & Garboczi, E. J. (2017). Particle-based characterization of Ottawa sand: Shape, size, mineralogy, and elastic moduli. Cement and concrete composites, 83, 36-44.

Eppelbaum, L., Kutasov, I., Pilchin, A., Eppelbaum, L., Kutasov, I., & Pilchin, A. (2014). Thermal properties of rocks and density of fluids. Applied geothermics, 99-149.

Ester, M., Kriegel, H. P., Sander, J., & Xu, X. (1996, August). A density-based algorithm for discovering clusters in large spatial databases with noise. In kdd (Vol. 96, No. 34, pp. 226-231).

Faulkner, D. R., Lewis, A. C., & Rutter, E. H. (2003). On the internal structure and mechanics of large strike-slip fault zones: field observations of the Carboneras fault in southeastern Spain. Tectonophysics, 367(3-4), 235-251.

Faulkner, D. R., Jackson, C. A. L., Lunn, R. J., Schlische, R. W., Shipton, Z. K., Wibberley, C. A. J., & Withjack, M. O. (2010). A review of recent developments concerning the structure, mechanics and fluid flow properties of fault zones. Journal of Structural Geology, 32(11), 1557-1575.

Faulkner, D. R., Mitchell, T. M., Behnsen, J., Hirose, T., & Shimamoto, T. (2011). Stuck in the mud? Earthquake nucleation and propagation through accretionary forearcs. Geophysical Research Letters, 38(18).

Faulkner, D. R., Sanchez-Roa, C., Boulton, C., & Den Hartog, S. A. M. (2018). Pore fluid pressure development in compacting fault gouge in theory, experiments, and nature. Journal of Geophysical Research: Solid Earth, 123(1), 226-241.

Feng, W., Yao, L., Cornelio, C., Gomila, R., Ma, S., Yang, C., ... & Di Toro, G. (2023). Physical state of water controls friction of gabbro-built faults. Nature Communications, 14(1), 4612.

Ferdowsi, B., & Rubin, A. M. (2020). A Granular Physics-Based View of Fault Friction Experiments. Journal of Geophysical Research: Solid Earth, 125(6), e2019JB019016.

Ferri, F., Di Toro, G., Hirose, T., & Shimamoto, T. (2010). Evidence of thermal pressurization in high-velocity friction experiments on smectite-rich gouges. Terra Nova, 22(5), 347-353.

Fondriest, M., Smith, S. A., Di Toro, G., Zampieri, D., & Mittempergher, S. (2012). Fault zone structure and seismic slip localization in dolostones, an example from the Southern Alps, Italy. Journal of structural Geology, 45, 52-67.

Fondriest, M., Smith, S. A., Candela, T., Nielsen, S. B., Mair, K., & Di Toro, G. (2013). Mirror-like faults and power dissipation during earthquakes. Geology, 41(11), 1175-1178.

References

French, M. E., Zhu, W., & Banker, J. (2016). Fault slip controlled by stress path and fluid pressurization rate. Geophysical Research Letters, 43(9), 4330-4339.

Friedman, M., & Higgs, N. G. (1981). Calcite fabrics in experimental shear zones. Washington DC American Geophysical Union Geophysical Monograph Series, 24, 11-27.

Fukuyama, E., & Mizoguchi, K. (2010). Constitutive parameters for earthquake rupture dynamics based on high-velocity friction tests with variable sliprate. International Journal of Fracture, 163, 15-26.

Fusseis, F., Butler, I. B., Freitas, D., Cartwright-Taylor, A., Elphick, S., & Andó, E. (2022). 4-dimensional in-situ/in-operando μ-CT imaging of geological processes at elevated temperatures and pressures using x-rays. In Proceedings of the 11th Conference on Industrial Computed Tomography (iCT).

Goldsby, D. L., & Tullis, T. E. (2002). Low frictional strength of quartz rocks at subseismic slip rates. Geophysical research letters, 29(17), 25-1.

Goldsby, D. L., & Tullis, T. E. (2011). Flash heating leads to low frictional strength of crustal rocks at earthquake slip rates. Science, 334(6053), 216-218.

Gomila, R., Fondriest, M., Jensen, E., Spagnuolo, E., Masoch, S., Mitchell, T. M., ... & Di Toro, G. (2021). Frictional melting in Hydrothermal fluid-rich faults: Field and experimental evidence from the Bolfin fault zone (Chile). Geochemistry, Geophysics, Geosystems, 22(7), e2021GC009743.

Hadizadeh, J., Sehhati, R., & Tullis, T. (2010). Porosity and particle shape changes leading to shear localization in small-displacement faults. Journal of Structural Geology, 32(11), 1712-1720.

Haines, S. H., Kaproth, B., Marone, C., Saffer, D., & Van der Pluijm, B. (2013). Shear zones in clay-rich fault gouge: A laboratory study of fabric development and evolution. Journal of Structural Geology, 51, 206-225.

Han, R., Hirose, T., & Shimamoto, T. (2010). Strong velocity weakening and powder lubrication of simulated carbonate faults at seismic slip rates. Journal of Geophysical Research: Solid Earth, 115(B3).

Hangx, S. J., & Brantut, N. (2019). Micromechanics of high-pressure compaction in granular quartz aggregates. Journal of Geophysical Research: Solid Earth, 124(7), 6560-6580.

Hanor, J. S. (1994). Origin of saline fluids in sedimentary basins. Geological Society, London, Special Publications, 78(1), 151-174.

Harbord, C., Brantut, N., Spagnuolo, E., & Di Toro, G. (2021). Fault friction during simulated seismic slip pulses. Journal of Geophysical Research: Solid Earth, 126(8), e2021JB022149.

Hayward, K. S., Le Losq, C., & Cox, S. F. (2021). Quantifying dynamic pressure and temperature conditions on fault asperities during earthquake slip. Earth and Planetary Science Letters, 555, 116701.

Hazzard, J. F., & Mair, K. (2003). The importance of the third dimension in granular shear. Geophysical Research Letters, 30(13).

He, X. L., Li, H. B., Wang, H., Zhang, L., Xu, Z. Q., & Si, J. L. (2018). Creeping along the Guanxian-Anxian fault of the 2008 Mw 7.9 Wenchuan earthquake in the Longmen Shan, China. Tectonics, 37(7), 2124-2141.

Heaton, T. H. (1990). Evidence for and implications of self-healing pulses of slip in earthquake rupture. Physics of the Earth and Planetary Interiors, 64(1), 1-20.

Heermance, R., Shipton, Z. K., & Evans, J. P. (2003). Fault structure control on fault slip and ground motion during the 1999 rupture of the Chelungpu fault, Taiwan. Bulletin of the Seismological Society of America, 93(3), 1034-1050.

Heermance, R. V., Chen, J., Burbank, D. W., & Miao, J. (2008). Temporal constraints and pulsed Late Cenozoic deformation during the structural disruption of the active Kashi foreland, northwest China. Tectonics, 27(6).

Heesakkers, V., Murphy, S., & Reches, Z. (2011). Earthquake rupture at focal depth, Part I: Structure and rupture of the Pretorius fault, TauTona mine, South Africa. Pure and Applied Geophysics, 168(12), 2395-2425.

Hettema, M., Papamichos, E., & Schutjens, P. M. T. M. (2002). Subsidence delay: field observations and analysis. Oil & Gas Science and Technology, 57(5), 443-458.

Higgs, N. G. (1981). Mechanical properties of ultrafine quartz, chlorite and bentonite in environments appropriate to upper-crustal earthquakes. Texas A&M University.

Hirose, T., & Shimamoto, T. (2005). Growth of molten zone as a mechanism of slip weakening of simulated faults in gabbro during frictional melting. Journal of Geophysical Research: Solid Earth, 110(B5).

Ho, T. K. (1995, August). Random decision forests. In Proceedings of 3rd international conference on document analysis and recognition (Vol. 1, pp. 278-282). IEEE.

Hunfeld, L. B., Niemeijer, A. R., & Spiers, C. J. (2017). Frictional properties of simulated fault gouges from the seismogenic Groningen gas field under in situ P–T-chemical conditions. Journal of Geophysical Research: Solid Earth, 122(11), 8969-8989.

Hunfeld, L. B., Chen, J., Niemeijer, A. R., & Spiers, C. J. (2019). Temperature and gas/brine content affect seismogenic potential of simulated fault gouges derived from Groningen gas field caprock. Geochemistry, Geophysics, Geosystems, 20(6), 2827-2847.

Hunfeld, L. B. (2020). Frictional properties of simulated fault gouges from the Groningen gas field and implications for induced seismicity (Doctoral dissertation, Utrecht University).

Hunfeld, L. B., Chen, J., Niemeijer, A. R., Ma, S., & Spiers, C. J. (2021). Seismic slip-pulse experiments simulate induced earthquake rupture in the Groningen gas field. Geophysical research letters, 48(11), e2021GL092417.

References

Hung, C.-C., Niemeijer, A. R., & Vasconcelos, I. (2023). Strain Localization in Sandstone-Derived Fault Gouges Under Conditions Relevant to Earthquake Nucleation, Dryad, Dataset, https://doi.org/10.5061/dryad.f7m0cfz2d.

Ide, S., & Beroza, G. C. (2001). Does apparent stress vary with earthquake size?. Geophysical Research Letters, 28(17), 3349-3352.

Ikari, M. J. (2015). Principal slip zones: Precursors but not recorders of earthquake slip. Geology, 43(11), 955-958.

Ikari, M. J., Niemeijer, A. R., & Marone, C. (2015). Experimental investigation of incipient shear failure in foliated rock. Journal of Structural Geology, 77, 82-91.

Itasca, C. (1999). PFC 3D-User manual. Itasca Consulting Group, Minneapolis, 435.

Iwashita, K., & Oda, M. (1998). Rolling resistance at contacts in simulation of shear band development by DEM. Journal of engineering mechanics, 124(3), 285-292.

Ji, Y., Niemeijer, A., Baden, D., Yamashita, F., Xu, S., Hunfeld, L., ... & Spiers, C. (2022). Friction law for earthquake nucleation: size doesn't matter.

Jing, L., Kwok, C. Y., & Leung, Y. F. (2017). Micromechanical origin of particle size segregation. Physical review letters, 118(11), 118001.

Kanamori, H., & Brodsky, E. E. (2004). The physics of earthquakes. Reports on progress in physics, 67(8), 1429.

Kitajima, H., Chester, J. S., Chester, F. M., & Shimamoto, T. (2010). High-speed friction of disaggregated ultracataclasite in rotary shear: Characterization of frictional heating, mechanical behavior, and microstructure evolution. Journal of Geophysical Research: Solid Earth, 115(B8).

Kohli, A. H., Goldsby, D. L., Hirth, G., & Tullis, T. (2011). Flash weakening of serpentinite at near-seismic slip rates. Journal of Geophysical Research: Solid Earth, 116(B3).

Korkolis, E. (2019). Rotary shear experiments on glass bead aggregates: Stick-slip statistics and parallels with natural seismicity (Doctoral dissertation, UU Dept. of Earth Sciences).

Kreshuk, A., & Zhang, C. (2019). Machine learning: advanced image segmentation using ilastik. Computer Optimized Microscopy: Methods and Protocols, 449-463.

Kuo, L. W., Li, H., Smith, S. A., Di Toro, G., Suppe, J., Song, S. R., ... & Si, J. (2014). Gouge graphitization and dynamic fault weakening during the 2008 Mw 7.9 Wenchuan earthquake. Geology, 42(1), 47-50.

Kuo, L. W., Song, S. R., Suppe, J., & Yeh, E. C. (2016). Fault mirrors in seismically active fault zones: A fossil of small earthquakes at shallow depths. Geophysical Research Letters, 43(5), 1950-1959.

Kuo, L. W., Wu, W. J., Kuo, C. W., Smith, S. A., Lin, W. T., Wu, W. H., & Huang, Y. H. (2021). Frictional strength and fluidization of water-saturated kaolinite gouges at seismic slip velocities. Journal of Structural Geology, 150, 104419.

Kuo, L. W., Hung, C. C., Li, H., Aretusini, S., Chen, J., Di Toro, G., ... & Sheu, H. S. (2022). Frictional Properties of the Longmenshan Fault Belt Gouges From WFSD-3 and Implications for Earthquake Rupture Propagation. Journal of Geophysical Research: Solid Earth, 127(5), e2022JB024081.

Kuo, L. W., Sone, H., Luzin, V., Yeh, E. C., Hsu, Y. J., & Tan, E. (2022). Gouge fabrics reset by thermal pressurization record stress on faults after earthquakes. Geology, 50(9), 1033-1037.

Lai, Z., Vallejo, L. E., Zhou, W., Ma, G., Espitia, J. M., Caicedo, B., & Chang, X. (2017). Collapse of granular columns with fractal particle size distribution: Implications for understanding the role of small particles in granular flows. Geophysical Research Letters, 44(24), 12-181.

Lachenbruch, A. H. (1980). Frictional heating, fluid pressure, and the resistance to fault motion. Journal of Geophysical Research: Solid Earth, 85(B11), 6097-6112.

Lapusta, N., & Rice, J. R. (2003). Nucleation and early seismic propagation of small and large events in a crustal earthquake model. Journal of Geophysical Research: Solid Earth, 108(B4).

Leeman, J. R., Saffer, D. M., Scuderi, M. M., & Marone, C. (2016). Laboratory observations of slow earthquakes and the spectrum of tectonic fault slip modes. Nature communications, 7(1), 1-6.

Li, M., Pranger, C., & van Dinther, Y. (2022). Characteristics of earthquake cycles: A cross-dimensional comparison of 0D to 3D numerical models. Journal of Geophysical Research: Solid Earth, 127(8), e2021JB023726.

Li, H., Wang, H., Xu, Z., Si, J., Pei, J., Li, T., ... & Liu, D. (2013). Characteristics of the fault-related rocks, fault zones and the principal slip zone in the Wenchuan Earthquake Fault Scientific Drilling Project Hole-1 (WFSD-1). Tectonophysics, 584, 23-42.

Liao, Z., Chang, J. C., & Reches, Z. E. (2014). Fault strength evolution during high velocity friction experiments with slip-pulse and constant-velocity loading. Earth and Planetary Science Letters, 406, 93-101.

Linker, M. F., & Dieterich, J. H. (1992). Effects of variable normal stress on rock friction: Observations and constitutive equations. Journal of Geophysical Research: Solid Earth, 97(B4), 4923-4940.

Lockner, D. A., Kilgore, B. D., Beeler, N. M., & Moore, D. E. (2017). The transition from frictional sliding to shear melting in laboratory stick-slip experiments. Fault zone dynamic processes: Evolution of fault properties during seismic rupture, 103-131.

Logan, J. M. (1979). Experimental studies of simulated gouge and their application to studies of natural fault zones. In Proceedings of conference VIII-analysis of actual fault zones in bedrock (pp. 305-343).

References

Logan, J. M., & Rauenzahn, K. A. (1987). Frictional dependence of gouge mixtures of quartz and montmorillonite on velocity, composition and fabric. Tectonophysics, 144(1-3), 87-108.

Logan, J. M., Dengo, C. A., Higgs, N. G., & Wang, Z. Z. (1992). Fabrics of experimental fault zones: Their development and relationship to mechanical behavior. In International geophysics (Vol. 51, pp. 33-67). Academic Press.

Logan, J. M. (2007). The progression from damage to localization of displacement observed in laboratory testing of porous rocks. Geological Society, London, Special Publications, 289(1), 75-87.

Lu, X., Lapusta, N., & Rosakis, A. J. (2007). Pulse-like and crack-like ruptures in experiments mimicking crustal earthquakes. Proceedings of the National Academy of Sciences, 104(48), 18931-18936.

Lu, X., Rosakis, A. J., & Lapusta, N. (2010). Rupture modes in laboratory earthquakes: Effect of fault prestress and nucleation conditions. Journal of Geophysical Research: Solid Earth, 115(B12).

Ma, J., Couples, G. D., & Harris, S. D. (2006). A mixed finite element technique based on implicit discretization of faults for permeability upscaling in fault damage zones. Water resources research, 42(8).

Ma, K. F., Tanaka, H., Song, S. R., Wang, C. Y., Hung, J. H., Tsai, Y. B., ... & Wu, H. Y. (2006). Slip zone and energetics of a large earthquake from the Taiwan Chelungpu-fault Drilling Project. Nature, 444(7118), 473-476.

Ma, G., Zou, Y., Gao, K., Zhao, J., & Zhou, W. (2020). Size polydispersity tunes slip avalanches of granular gouge. Geophysical Research Letters, 47(23), e2020GL090458.

Ma, J., Li, D., Du, S., Han, Z., Luo, P., & Zhao, J. (2023). Comparison of subcritical crack growth and dynamic fracture propagation in rocks under double-torsion tests. International Journal of Rock Mechanics and Mining Sciences, 170, 105481.

Madding, R. P., Orlove, G. L., & Lyon, B. R. (2007, April). The importance of spatial resolution in IR thermography temperature measurement: three brief case studies. In Proceedings of SPIE, the International Society for Optical Engineering (pp. 654108-1). Society of Photo-Optical Instrumentation Engineers.

Mair, K., Frye, K. M., & Marone, C. (2002). Influence of grain characteristics on the friction of granular shear zones. Journal of Geophysical Research: Solid Earth, 107(B10), ECV 4-9. doi:10.1029/2001JB000516.

Mair, K., Marone, C., & Young, R. P. (2007). Rate dependence of acoustic emissions generated during shear of simulated fault gouge. Bulletin of the seismological Society of America, 97(6), 1841-1849.

Mair, K., & Hazzard, J. F. (2007). Nature of stress accommodation in sheared granular material: Insights from 3D numerical modeling. Earth and Planetary Science Letters, 259(3), 469-485. doi:10.1016/j.epsl.2007.05.006.

Mair, K., & Abe, S. (2008). 3D numerical simulations of fault gouge evolution during shear: Grain size reduction and strain localization. Earth and Planetary Science Letters, 274(1-2), 72-81. doi:10.1016/j.epsl.2008.07.010.

Mandl, G., De Jong, L. N. J., & Maltha, A. (1977). Shear zones in granular material. Rock mechanics, 9(2), 95-144.

Marone, C., & Scholz, C. H. (1989). Particle-size distribution and microstructures within simulated fault gouge. Journal of Structural Geology, 11(7), 799-814.

Marone, C. J., Scholtz, C. H., & Bilham, R. (1991). On the mechanics of earthquake afterslip. Journal of Geophysical Research: Solid Earth, 96(B5), 8441-8452.

Marone, C. (1998). Laboratory-derived friction laws and their application to seismic faulting. Annual Review of Earth and Planetary Sciences, 26(1), 643-696.

Mase, C. W., & Smith, L. (1984). Pore-fluid pressures and frictional heating on a fault surface. Pure and Applied Geophysics, 122, 583-607.

Mase, C. W., & Smith, L. (1987). Effects of frictional heating on the thermal, hydrologic, and mechanical response of a fault. Journal of Geophysical Research: Solid Earth, 92(B7), 6249-6272.

Masuda, K., Arai, T., & Takahashi, M. (2019). Effects of frictional properties of quartz and feldspar in the crust on the depth extent of the seismogenic zone. Progress in Earth and Planetary Science, 6, 1-8.

McDermott, R. G., Ault, A. K., Evans, J. P., & Reiners, P. W. (2017). Thermochronometric and textural evidence for seismicity via asperity flash heating on exhumed hematite fault mirrors, Wasatch fault zone, UT, USA. Earth and Planetary Science Letters, 471, 85-93.

McGarr, A., Simpson, D., & Seeber, L. (2002). 40 case histories of induced and triggered seismicity. In International handbook of earthquake and engineering seismology (pp. 647–661). https://doi.org/10.1016/s0074-6142(02)80243-1

Mercuri, M., Scuderi, M. M., Tesei, T., Carminati, E., & Collettini, C. (2018). Strength evolution of simulated carbonate-bearing faults: The role of normal stress and slip velocity. Journal of Structural Geology, 109, 1-9.

Mielke, P., Bär, K., & Sass, I. (2017). Determining the relationship of thermal conductivity and compressional wave velocity of common rock types as a basis for reservoir characterization. Journal of Applied Geophysics, 140, 135-144.

Miller, S. A. (2013). The role of fluids in tectonic and earthquake processes. Advances in geophysics, 54, 1-46.

Mijnlieff, H. F., & Geluk, M. (2011). Palaeotopography-governed sediment distribution—a new predictive model for the Permian Upper Rotliegend in the Dutch sector of the southern Permian Basin.

Mitchell, T. M., & Faulkner, D. R. (2009). The nature and origin of off-fault damage surrounding strike-slip fault zones with a wide range of displacements: A field

study from the Atacama fault system, northern Chile. Journal of Structural Geology, 31(8), 802-816.

Mizoguchi, K., Hirose, T., Shimamoto, T., & Fukuyama, E. (2007). Reconstruction of seismic faulting by high-velocity friction experiments: An example of the 1995 Kobe earthquake. Geophysical Research Letters, 34(1).

Modenese, C. (2013). Numerical study of the mechanical properties of lunar soil by the discrete element method (Doctoral dissertation, Oxford University, UK).

Moore, D. E., Summers, R., & Byerlee, J. D. (1989). Sliding behavior and deformation textures of heated illite gouge. Journal of Structural Geology, 11(3), 329-342.

Moore, D. E., & Byerlee, J. D. (1991). Comparative geometry of the San Andreas fault, California, and laboratory fault zones. Geological Society of America Bulletin, 103(6), 762-774.

Moore, D. E., & Byerlee, J. (1992). Relationships between sliding behavior and internal geometry of laboratory fault zones and some creeping and locked strike-slip faults of California. Tectonophysics, 211(1-4), 305-316.

Morgan, J. K., & Boettcher, M. S. (1999). Numerical simulations of granular shear zones using the distinct element method: 1. Shear zone kinematics and the micromechanics of localization. Journal of Geophysical Research: Solid Earth, 104(B2), 2703-2719.

Morgan, J. K. (1999). Numerical simulations of granular shear zones using the distinct element method: 2. Effects of particle size distribution and interparticle friction on mechanical behavior. Journal of Geophysical Research: Solid Earth, 104(B2), 2721-2732.

Morgan, J. K. (2004). Particle dynamics simulations of rate- and state-dependent frictional sliding of granular fault gouge. Pure and Applied Geophysics, 161(9), 1877-1891. doi:10.1007/s00024-004-2537-y.

Mindlin, R. D. (1949). Compliance of elastic bodies in contact.

NAM (2013). Technical addendum to the Winningsplan Groningen 2013 subsidence, induced earthquakes and seismic hazard analysis in the Groningen field

NAM (2016). On the implementation of Sedimentological data in Porosity Modelling for the Groningen field

NAM (2020), Seismic Hazard and Risk Assessment Groningen Field update for Production Profile GTS - raming 2020.

NAM (2022), Report on the Second Workshop on Mmax for Seismic Hazard and Risk Analysis in the Groningen Gas Field (Full Report)

Nguyen, H. N. G., Scholtès, L., Guglielmi, Y., Donzé, F. V., Ouraga, Z., & Souley, M. (2021). Micromechanics of sheared granular layers activated by fluid pressurization. Geophysical Research Letters, 48(14), e2021GL093222.

Nicol, A., Carne, R., Gerstenberger, M., & Christophersen, A. (2011). Induced seismicity and its implications for CO2 storage risk. Energy Procedia, 4, 3699–3706. https://doi.org/10.1016/j.egypro.2011.02.302

Niemeijer, A., Di Toro, G., Nielsen, S., & Di Felice, F. (2011). Frictional melting of gabbro under extreme experimental conditions of normal stress, acceleration, and sliding velocity. Journal of Geophysical Research: Solid Earth, 116(B7)

Niemeijer, A., Di Toro, G., Griffith, W. A., Bistacchi, A., Smith, S. A., & Nielsen, S. (2012). Inferring earthquake physics and chemistry using an integrated field and laboratory approach. Journal of Structural Geology, 39, 2-36.

Niemeijer, A., Fagereng, Å., Ikari, M., Nielsen, S., & Willingshofer, E. (2020). Faulting in the laboratory. In Understanding Faults (pp. 167-220). Elsevier.

Numbere, D., Brigham, W. E., & Standing, M. B. (1977). Correlations for Physical Properties of petroleum reservoir Brines (No. DOE/ET/12056-T3; SUPRI-TR-1). Stanford Univ., CA (USA). Petroleum Research Inst.

Noda, H., & Shimamoto, T. (2005). Thermal pressurization and slip-weakening distance of a fault: An example of the Hanaore fault, southwest Japan. Bulletin of the Seismological Society of America, 95(4), 1224-1233.

Noda, H., Dunham, E. M., & Rice, J. R. (2009). Earthquake ruptures with thermal weakening and the operation of major faults at low overall stress levels. Journal of Geophysical Research: Solid Earth, 114(B7).

Noël, C., Giorgetti, C., Scuderi, M. M., Collettini, C., & Marone, C. (2023). The effect of shear displacement and wear on fault stability: Laboratory constraints. Journal of Geophysical Research: Solid Earth, e2022JB026191.

Oohashi, K., Hirose, T., & Shimamoto, T. (2011). Shear-induced graphitization of carbonaceous materials during seismic fault motion: Experiments and possible implications for fault mechanics. Journal of Structural Geology, 33(6), 1122-1134.

Oohashi, K., Hirose, T., Takahashi, M., & Tanikawa, W. (2015). Dynamic weakening of smectite-bearing faults at intermediate velocities: Implications for subduction zone earthquakes. Journal of Geophysical Research: Solid Earth, 120(3), 1572-1586.

Papachristos, E., Stefanou, I., & Sulem, J. (2023). A discrete elements study of the frictional behavior of fault gouges. Journal of Geophysical Research: Solid Earth, 128(1), e2022JB025209.

Passelègue, F. X., Schubnel, A., Nielsen, S., Bhat, H. S., & Madariaga, R. (2013). From sub-Rayleigh to supershear ruptures during stick-slip experiments on crustal rocks. Science, 340(6137), 1208-1211.

Pedregosa, F., Varoquaux, G., Gramfort, A., Michel, V., Thirion, B., Grisel, O., ... & Duchesnay, E. (2011). Scikit-learn: Machine learning in Python. the Journal of machine Learning research, 12, 2825-2830.

References

Pitzer, K. S., Peiper, J. C., & Busey, R. H. (1984). Thermodynamic properties of aqueous sodium chloride solutions. Journal of Physical and Chemical Reference Data, 13(1), 1-102.

Platt, J. D., Rudnicki, J. W., & Rice, J. R. (2014). Stability and localization of rapid shear in fluid-saturated fault gouge: 2. Localized zone width and strength evolution. Journal of Geophysical Research: Solid Earth, 119(5), 4334-4359.

Platt, J. D., Viesca, R. C., & Garagash, D. I. (2015). Steadily propagating slip pulses driven by thermal decomposition. Journal of Geophysical Research: Solid Earth, 120(9), 6558-6591.

Proctor, B. P., Mitchell, T. M., Hirth, G., Goldsby, D., Zorzi, F., Platt, J. D., & Di Toro, G. (2014). Dynamic weakening of serpentinite gouges and bare surfaces at seismic slip rates. Journal of Geophysical Research: Solid Earth, 119(11), 8107-8131.

Qasem, N. A., Generous, M. M., Qureshi, B. A., & Zubair, S. M. (2021). A comprehensive review of saline water correlations and data: part II—thermophysical properties. Arabian Journal for Science and Engineering, 46, 1941-1979.

Ramer, U. (1972). An iterative procedure for the polygonal approximation of plane curves. Computer graphics and image processing, 1(3), 244-256.

Raoof, A., & Hassanizadeh, S. M. (2010). A new method for generating pore-network models of porous media. Transport in porous media, 81, 391-407.

Reches, Z. E., & Lockner, D. A. (2010). Fault weakening and earthquake instability by powder lubrication. Nature, 467(7314), 452-455.

Remitti, F., Smith, S. A. F., Mittempergher, S., Gualtieri, A. F., & Di Toro, G. (2015). Frictional properties of fault zone gouges from the J-FAST drilling project (Mw 9.0 2011 Tohoku-Oki earthquake). Geophysical Research Letters, 42(8), 2691-2699.

Rempel, A. W., & Rice, J. R. (2006). Thermal pressurization and onset of melting in fault zones. Journal of Geophysical Research: Solid Earth, 111(B9).

Renard, F., Kandula, N., McBeck, J., & Cordonnier, B. (2020). Creep burst coincident with faulting in marble observed in 4-D synchrotron X-ray imaging triaxial compression experiments. Journal of Geophysical Research: Solid Earth, 125(9), e2020JB020354.

Rice, J. R. (1992). Fault stress states, pore pressure distributions, and the weakness of the San Andreas fault. In International geophysics (Vol. 51, pp. 475-503). Academic Press.

Rice, J. R. (1999). Flash heating at asperity contacts and rate-dependent friction. Eos Trans. AGU, 80(46), F471.

Rice, J. R. (2006). Heating and weakening of faults during earthquake slip. Journal of Geophysical Research: Solid Earth, 111(B5).

Rice, J. R., Rudnicki, J. W., & Platt, J. D. (2014). Stability and localization of rapid shear in fluid-saturated fault gouge: 1. Linearized stability analysis. Journal of Geophysical Research: Solid Earth, 119(5), 4311-4333.

Riedel, W. (1929). Zur Mechanik geologischer Brucherscheinungen ein Beitrag zum Problem der Fiederspatten. Zentbl. Miner. Geol. Palaont. Abt., 354-368.

Rowe, C. D., Lamothe, K., Rempe, M., Andrews, M., Mitchell, T. M., Di Toro, G., ... & Aretusini, S. (2019). Earthquake lubrication and healing explained by amorphous nanosilica. Nature Communications, 10(1), 320.

Rubino, V., Rosakis, A. J., & Lapusta, N. (2017). Understanding dynamic friction through spontaneously evolving laboratory earthquakes. Nature communications, 8(1), 15991.

Rubino, V., Lapusta, N., & Rosakis, A. J. (2022). Intermittent lab earthquakes in dynamically weakening fault gouge. Nature, 606(7916), 922-929.

Rutter, E. H., Maddock, R. H., Hall, S. H., & White, S. H. (1986). Comparative microstructures of natural and experimentally produced clay-bearing fault gouges. Pure and applied geophysics, 124, 3-30.

Saber, O. (2017). Development and Characterization of a high-speed material-testing machine, and experimental Analysis of frictional flash Heating and dynamic Weakening in rock (Doctoral dissertation).

Sammis, C., King, G., & Biegel, R. (1987). The kinematics of gouge deformation. Pure and Applied Geophysics, 125(5), 777-812.

Samuelson, J., & Spiers, C. J. (2012). Fault friction and slip stability not affected by CO_2 storage: Evidence from short-term laboratory experiments on North Sea reservoir sandstones and caprocks. International Journal of Greenhouse Gas Control, 11, S78-S90.

Sandberg, O., & Sundqvist, B. (1982). Thermal properties of two low viscosity silicon oils as functions of temperature and pressure. Journal of Applied Physics, 53(12), 8751-8755.

Scholz, C. H. (2002). Earthquakes and faulting.

Scuderi, M. M., Collettini, C., & Marone, C. (2017a). Frictional stability and earthquake triggering during fluid pressure stimulation of an experimental fault. Earth and Planetary Science Letters, 477, 84-96.

Scuderi, M. M., Collettini, C., Viti, C., Tinti, E., & Marone, C. (2017b). Evolution of shear fabric in granular fault gouge from stable sliding to stick slip and implications for fault slip mode. Geology, 45(8), 731-734.

Scuderi, M. M., Tinti, E., Cocco, M., & Collettini, C. (2020). The role of shear fabric in controlling breakdown processes during laboratory slow-slip events. Journal of Geophysical Research: Solid Earth, 125(11), e2020JB020405.

Segall, P. (1989). Earthquakes triggered by fluid extraction. Geology, 17, 942–946. https://doi.org/10.1130/0091-7613(1989)017<0942: ETBFE>2.3

References

Shimamoto, T., & Logan, J. M. (1981). Effects of simulated fault gouge on the sliding behavior of Tennessee sandstone: nonclay gouges. Journal of Geophysical Research: Solid Earth, 86(B4), 2902-2914.

Spagnuolo, E., Plümper, O., Violay, M., Cavallo, A., & Di Toro, G. (2015). Fast-moving dislocations trigger flash weakening in carbonate-bearing faults during earthquakes. Scientific Reports, 5(1), 16112.

Spiers, C. J., Hangx, S. J., & Niemeijer, A. R. (2017). New approaches in experimental research on rock and fault behaviour in the Groningen gas field. Netherlands Journal of Geosciences, 96(5), s55-s69.

Sibson, R. H. (1973). Interactions between temperature and pore-fluid pressure during earthquake faulting and a mechanism for partial or total stress relief. Nature Physical Science, 243(126), 66-68.

Sibson, R. H. (1977). Fault rocks and fault mechanisms. Journal of the Geological Society, 133(3), 191-213.

Sibson, R. H. (1986). Earthquakes and rock deformation in crustal fault zones. Annual Review of Earth and Planetary Sciences, 14, 149.

Sibson, R. H. (2003). Thickness of the seismic slip zone. Bulletin of the Seismological Society of America, 93(3), 1169-1178.

Smith, S. A., Billi, A., Toro, G. D., & Spiess, R. (2011). Principal slip zones in limestone: microstructural characterization and implications for the seismic cycle (Tre Monti Fault, Central Apennines, Italy). Pure and Applied Geophysics, 168(12), 2365-2393.

Smith, S. A. F., Di Toro, G., Kim, S., Ree, J. H., Nielsen, S., Billi, A., & Spiess, R. (2013). Coseismic recrystallization during shallow earthquake slip. Geology, 41(1), 63-66.

Smith, S. A., Nielsen, S., & Di Toro, G. (2015). Strain localization and the onset of dynamic weakening in calcite fault gouge. Earth and Planetary Science Letters, 413, 25-36.

Smith, J. D. (2019). Geomechanical properties of the Groningen reservoir. University of Cambridge

Smith, J. D., White, R. S., Avouac, J. P., & Bourne, S. (2020). Probabilistic earthquake locations of induced seismicity in the Groningen region, the Netherlands. Geophysical Journal International, 222(1), 507-516.

Šmilauer, V., Catalano, E., Chareyre, B., Dorofeenko, S., Duriez, J., Gladky, A., ... & Thoeni, K. (2010). Yade reference documentation. Yade Documentation, 474(1).

Sone, H., & Shimamoto, T. (2009). Frictional resistance of faults during accelerating and decelerating earthquake slip. Nature Geoscience, 2(10), 705-708.

Spetzler, J., & Dost, B. (2017). Hypocenter estimation of induced earthquakes in Groningen. Geophysical Journal International, 209(1), 453–465.

Spray, J. G. (1992). A physical basis for the frictional melting of some rock-forming minerals. Tectonophysics, 204(3-4), 205-221.

Stathas, A., & Stefanou, I. (2023). Fault friction under thermal pressurization during large seismic-slip: Numerical analyses and extension of the model of frictional slip. International Journal of Mechanical Sciences, 248, 108184.

Tanikawa, W., Sakaguchi, M., Tadai, O., & Hirose, T. (2010). Influence of fault slip rate on shear-induced permeability. Journal of Geophysical Research: Solid Earth, 115(B7).

Tembe, S., Lockner, D. A., & Wong, T. F. (2010). Effect of clay content and mineralogy on frictional sliding behavior of simulated gouges: Binary and ternary mixtures of quartz, illite, and montmorillonite. Journal of Geophysical Research: Solid Earth, 115(B3).

The Engineering ToolBox (2009). Liquids - Volumetric Expansion Coefficients. [online] Available at: https://www.engineeringtoolbox.com/cubical-expansion-coefficients-d_1262.html [Accessed Day Month Year].

Thornton, C., Cummins, S. J., & Cleary, P. W. (2011). An investigation of the comparative behaviour of alternative contact force models during elastic collisions. Powder Technology, 210(3), 189-197.

Togo, T., Shimamoto, T., Ma, S., Wen, X., & He, H. (2011). Internal structure of Longmenshan fault zone at Hongkou outcrop, Sichuan, China, that caused the 2008 Wenchuan earthquake. Earthquake Science, 24, 249-265.

Togo, T., Shimamoto, T., Yamashita, F., Fukuyama, E., Mizoguchi, K., & Urata, Y. (2015). Stick–slip behavior of Indian gabbro as studied using a NIED large-scale biaxial friction apparatus. Earthquake Science, 28, 97-118.

Tomic, J., Abercrombie, R. E., & Do Nascimento, A. F. (2009). Source parameters and rupture velocity of small M≤ 2.1 reservoir induced earthquakes. Geophysical Journal International, 179(2), 1013-1023.

Tsutsumi, A., & Shimamoto, T. (1997). High-velocity frictional properties of gabbro. Geophysical Research Letters, 24(6), 699-702.

Tullis, T. E. (2015). Mechanisms for friction of rock at earthquake slip rates.

Ujiie, K., & Tsutsumi, A. (2010). High-velocity frictional properties of clay-rich fault gouge in a megasplay fault zone, Nankai subduction zone. Geophysical Research Letters, 37(24).

Ujiie, K., Tanaka, H., Saito, T., Tsutsumi, A., Mori, J. J., Kameda, J., ... & Expedition 343 and 343T Scientists. (2013). Low coseismic shear stress on the Tohoku-Oki megathrust determined from laboratory experiments. Science, 342(6163), 1211-1214.

Van der Walt, S., Sch"onberger, Johannes L, Nunez-Iglesias, J., Boulogne, Franccois, Warner, J. D., Yager, N., … Yu, T. (2014). scikit-image: image processing in Python. PeerJ, 2, e453.

References

Van den Ende, M. P. A., & Niemeijer, A. R. (2018). Time-dependent compaction as a mechanism for regular stick-slips. Geophysical Research Letters, 45(12), 5959-5967.

Van Eijs, R. M. H. E., Mulders, F. M. M., Nepveu, M., Kenter, C. J., & Scheffers, B. C. (2006). Correlation between hydrocarbon reservoir properties and induced seismicity in the Netherlands. Engineering Geology, 84, 99–111. https://doi.org/10.1016/j.enggeo.2006.01.002.

Van Eijs, R. M. H. E. (2015). Neotectonic stresses in the Permian Slochteren formation of the Groningen field. KNMI Scientific Report. Report No. EP201510210531. NAM (Assen).

Van Hulten, F. F. N. (2010). Geological factors effecting compartmentalization of Rotliegend gas fields in the Netherlands. Geological Society, London, Special Publications, 347(1), 301-315.

Van Ojik, K., Böhm, A. R., Cremer, H., Geluk, M. C., De Jong, M. G., Mijnlieff, H. F., & Nio, S. D. (2011). The rationale for an integrated stratigraphic framework of the Upper Rotliegend II depositional system in The Netherlands.

van Thienen-Visser, K., & Breunese, J. N. (2015). Induced seismicity of the Groningen gas field: History and recent developments. The Leading Edge, 34(6), 664-671.

Van Wees, J. D., Fokker, P. A., Van Thienen-Visser, K., Wassing, B. B., Osinga, S., Orlic, B., ... & Pluymaekers, M. (2017). Geomechanical models for induced seismicity in the Netherlands: Inferences from simplified analytical, finite element and rupture model approaches. Netherlands Journal of Geosciences, 96(5), s183-s202.

Verberne, B. A., He, C., & Spiers, C. J. (2010). Frictional Properties of Sedimentary Rocks and Natural Fault Gouge from the Longmen Shan Fault Zone, Sichuan, China. Bulletin of the Seismological Society of America, 100(5B), 2767-2790.

Verberne, B. A., Plümper, O., Matthijs de Winter, D. A., & Spiers, C. J. (2014a). Superplastic nanofibrous slip zones control seismogenic fault friction. Science, 346(6215), 1342-1344.

Verberne, B. A., Spiers, C. J., Niemeijer, A. R., De Bresser, J. H. P., De Winter, D. A. M., & Plümper, O. (2014b). Frictional properties and microstructure of calcite-rich fault gouges sheared at sub-seismic sliding velocities. Pure and Applied Geophysics, 171(10), 2617-2640.

Violay, M., Nielsen, S., Spagnuolo, E., Cinti, D., Di Toro, G., & Di Stefano, G. (2013). Pore fluid in experimental calcite-bearing faults: Abrupt weakening and geochemical signature of co-seismic processes. Earth and planetary science letters, 361, 74-84.

Violay, M., Nielsen, S., Gibert, B., Spagnuolo, E., Cavallo, A., Azais, P., ... & Di Toro, G. (2014). Effect of water on the frictional behavior of cohesive rocks during earthquakes. Geology, 42(1), 27-30.

Violay, M., Di Toro, G., Nielsen, S., Spagnuolo, E., & Burg, J. P. (2015). Thermo-mechanical pressurization of experimental faults in cohesive rocks during seismic slip. Earth and Planetary Science Letters, 429, 1-10.

Violay, M., Passelègue, F., Spagnuolo, E., Di Toro, G., & Cornelio, C. (2019). Effect of water and rock composition on re-strengthening of cohesive faults during the deceleration phase of seismic slip pulses. Earth and Planetary Science Letters, 522, 55-64.

Volpe, G., Pozzi, G., & Collettini, C. (2022). YBPR or SCC′? Suggestion for the nomenclature of experimental brittle fault fabric in phyllosilicate-granular mixtures. Journal of Structural Geology, 165, 104743.

Waldmann, S. (2012). Geological and mineralogical investigation of Rotliegend gas reservoirs in the Netherlands and their potential for CO_2 storage (Doctoral dissertation).

Waldmann, S., B. A. Verberne, and C. J. Spiers (2017), Physical mechanisms and mechanics governing compaction of the Slochteren sandstone: Progress report on the potential impact of the shifting GWC on water-rock interactions, Confidential Rep. work performed within Research Agreement UI49358, 29 pp, Utrecht University.

Wang, Z. Z. (1989). Frictional sliding and the fabric developed in experimental shear zones. Texas A&M University.

Wang, H., Li, H. B., Di Toro, G., Kuo, L. W., Spagnuolo, E., Aretusini, S., ... & Song, S. R. (2023). Melting of fault gouge at shallow depth during the 2008 MW 7.9 Wenchuan earthquake, China. Geology, 51(4), 345-350.

Waza, T., Kurita, K., & Mizutani, H. (1980). The effect of water on the subcritical crack growth in silicate rocks. Tectonophysics, 67(1-2), 25-34.

Weatherley, D. K., & Henley, R. W. (2013). Flash vaporization during earthquakes evidenced by gold deposits. Nature Geoscience, 6(4), 294-298.

Weng, H., & Ampuero, J. P. (2019). The dynamics of elongated earthquake ruptures. Journal of Geophysical Research: Solid Earth, 124(8), 8584-8610.

Weng, H., Ampuero, J.-P., and Buijze, L.: Physics-Based Estimates of the Maximum Magnitude of Induced Earthquakes in the Groningen Gas Field, EGU General Assembly 2021, online, 19–30 Apr 2021, EGU21-6144, https://doi.org/10.5194/egusphere-egu21-6144, 2021.

Wentinck, H. M. (2018). Dynamic modelling of large tremors in the Groningen field using extended seismic sources (Report for NAM). Shell Global Solutions International B.V. Retrieved from https://nam-feitenencijfers.data-app.nl/download/rapport/996f9a6e-9ef0-47e5-872dfda8de45be8d?open=true

Wibberley, C. A. (2002). Hydraulic diffusivity of fault gouge zones and implications for thermal pressurization during seismic slip. Earth, planets and space, 54(11), 1153-1171.

References

Wibberley, C. A., & Shimamoto, T. (2005). Earthquake slip weakening and asperities explained by thermal pressurization. Nature, 436(7051), 689-692.

Wojatschke, J., Scuderi, M. M., Warr, L. N., Carpenter, B. M., Saffer, D., & Marone, C. (2016). Experimental constraints on the relationship between clay abundance, clay fabric, and frictional behavior for the C entral D eforming Z one of the S an A ndreas F ault. Geochemistry, Geophysics, Geosystems, 17(10), 3865-3881.

Xing, T., Zhu, W., French, M., & Belzer, B. (2019). Stabilizing effect of high pore fluid pressure on slip behaviors of gouge-bearing faults. Journal of Geophysical Research: Solid Earth, 124(9), 9526-9545.

Yamashita, F., Fukuyama, E., Mizoguchi, K., Takizawa, S., Xu, S., & Kawakata, H. (2015). Scale dependence of rock friction at high work rate. Nature, 528(7581), 254-257.

Yao, L., Shimamoto, T., Ma, S., Han, R., & Mizoguchi, K. (2013). Rapid postseismic strength recovery of Pingxi fault gouge from the Longmenshan fault system: Experiments and implications for the mechanisms of high-velocity weakening of faults. Journal of Geophysical Research: Solid Earth, 118(8), 4547-4563.

Yao, L., Ma, S., Niemeijer, A. R., Shimamoto, T., & Platt, J. D. (2016a). Is frictional heating needed to cause dramatic weakening of nanoparticle gouge during seismic slip? Insights from friction experiments with variable thermal evolutions. Geophysical Research Letters, 43(13), 6852-6860.

Yao, L., Ma, S., Platt, J. D., Niemeijer, A. R., & Shimamoto, T. (2016b). The crucial role of temperature in high-velocity weakening of faults: Experiments on gouge using host blocks with different thermal conductivities. Geology, 44(1), 63-66.

Yao, L., Ma, S., Chen, J., Shimamoto, T., & He, H. (2018). Flash heating and local fluid pressurization lead to rapid weakening in water-saturated fault gouges. Journal of Geophysical Research: Solid Earth, 123(10), 9084-9100.

Yao, L., Ma, S., & Di Toro, G. (2023). Coseismic fault sealing and fluid pressurization during earthquakes. Nature Communications, 14(1), 1136.

Zhang, S., & Tullis, T. E. (1998). The effect of fault slip on permeability and permeability anisotropy in quartz gouge. Tectonophysics, 295(1-2), 41-52.

Zhu, H., Zhou, W. H., & Yin, Z. Y. (2018). Deformation mechanism of strain localization in 2D numerical interface tests. Acta Geotechnica, 13(3), 557-573.

Zoback, M. D. (2010). Reservoir geomechanics. Cambridge university press.

Zoback, M. D., & Gorelick, S. M. (2012). Earthquake triggering and large-scale geologic storage of carbon dioxide. Proceedings of the National Academy of Sciences, 109(26), 10164-10168.

Lekensamenvatting

Kleine aardbevingen (M<4) hebben de laatste jaren veel aandacht gekregen vanwege de wereldwijde toename van door de mens veroorzaakte seismische activiteit. in de diepe ondergrond (~ 2-3 km). De productie van olie en gas, bijvoorbeeld, kan leiden tot seismische activatie van breuken die het reservoir doorsnijden. Deze geïnduceerde aardbevingen kunnen aanzienlijke maatschappelijke onrust veroorzaken. Om het risico van geïnduceerde aardbevingen te beoordelen, is het belangrijk om de sterkte en het gedrag van breuken tijdens snelle beweging (> 1 m/s) te begrijpen. Dit vereist volledige karakterisering van de plek waar slip optreedt en inzicht in de ontwikkeling van breuksterkte vanaf de initiatie van de breuk tot de voortplanting ervan. Dit proefschrift richt zich op het grootste gasveld van Europa, het Groningen-gasveld in Nederland, als casestudy voor kleine aardbevingen in de bovenste korst.

Om aardbevingen in Groningen te simuleren heb ik laboratoriumexperimenten uitgevoerd op breukmeel van reservoirzandsteen, en gecombineerd met numerieke modellering. Een belangrijke bevinding is de cruciale rol van poriënvloeistof bij de afname van breuksterkte tijdens seismische beweging, als gevolg van thermische uitzetting van de poriënvloeistof. Dit proces werkt op verschillende schalen, van schuifzones op schaal van millimeters tot micrometer-schaal korrelcontacten, wat leidt tot verschillende stadia van verzwakking van de breuk. De eigenschappen van de poriënvloeistof en het breukmateriaal beïnvloeden de efficiëntie van de verzwakking. De resultaten van dit proefschrift geven een betere bepaling van de sterkteparameters die nodig zijn voor betrouwbare geomechanische modellen voor het Groningen-reservoirsysteem. Ze leveren daarnaast input voor haalbaarheidsstudies van toekomstige projecten in de ondergrond.

(translated from the original by André Niemeijer and Hans de Bresser)

Acknowledgment / 致謝

Time flies… It has been four years and six months since I came to the Netherlands in August 2019 to start my PhD life. Due to the COVID-19 pandemic, I feel like this period is even shorter. During this journey, I have encountered many difficulties and challenges in terms of research and daily life. Luckily, I have had the privilege of meeting many wonderful and remarkable people who have supported me in successfully completing my research and who have also been great company. I am exceptionally grateful to them.

First and foremost, I would like to show my biggest gratitude towards my supervisor André Niemeijer for giving me such an amazing opportunity to work on this PhD project and to become one of the members within the DeepNL program. Whenever I encounter any issues, you can also quickly and patiently provide brilliant ideas and solutions, despite stupid questions. I still remember that you once told me I could always go to knock at your office door whenever I got stuck. Those words really make me feel supportive during my research and unforgettable. For this, I am extremely grateful. Aside from research wise, we also played quite a few tennis and squash games during the pandemic period, which was very enjoyable, though I haven't gotten any chance to defeat you on squash at all… It is a pleasure working with you to and I truly enjoy our working relationship, which is very dynamic, interesting, innovative, and stress-free. I would also like to thank you for trusting me to take care of Iggy. For me, it is a unique and interesting experience.

Secondly, I would like to greatly thank my promotor Chris Spiers for welcoming me to become one of the members in the High Pressure and Temperature (HPT) Lab. It is a pleasure working in this big HPT family with you as a leader, who brings joy and motivation to everyone. You always provided me with very insightful feedback and suggestions during my lunch meeting presentation, which strongly helped me understand my knowledge gaps. You also motivate and inspire me to become more rigorous in science in a humorous way. I truly appreciate that you were dedicated to helping me review my thesis at the late stage of my PhD and make everything happen as planned. I will never forget this experience and the time having chats with you.

Thirdly, I would like to express my gratitude to my co-supervisors, Amir Raoof, and co-author, Thomas Sweijen, for introducing me to the world of numerical modeling. Amir, I want to thank you for providing brilliant ideas to resolve various conceptual issues in my modeling chapter, even though we didn't have too many opportunities for in-depth discussions. Thomas, I am immensely grateful to you for introducing me to the world of Yade-DEM when I had no prior experience with it. You helped me overcome one of the most challenging obstacles during my PhD by patiently addressing all the technical issues I encountered in model design and coding. I am delighted to have had such a pleasant and productive working experience with you.

Next, I would like to thank all the (former and current) members of the HPT lab Group at Utrecht University that I have met for providing much support and feedback for my research: Magda, you are the kindest, most caring, and gracious secretary I have ever met. Thank you for helping me with numerous errands I had no clue how to handle and for arranging all the HPT social events, Hans, being a teaching assistant in your SAD rocks course was a wonderful experience. I truly enjoyed your teaching style and your guidance in my own teaching endeavors, Suzanne, I still remember our relaxing and enjoyable coffee chat at Minnaert. I also thoroughly enjoyed our field trip to Maastricht, where we had many engaging conversations on various topics, Evangelos, thank you for assisting me in tackling numerous experimental and coding issues at the start of my PhD. Talking with you always puts me at ease, as you constantly wear a smile on your face, Luuk, my senior in friction at HPT, thank you for teaching and sharing all your knowledge on friction. I would also like to express my gratitude for having a coffee chat with me and sharing your career choices with me at Botanische Tuinen. Your thesis has been of tremendous help to me in completing my own thesis, Jianye, I want to extend my heartfelt thanks to you for your brilliant contributions to my research, teaching me how to operate the Shuttle apparatus, and for assisting me with modeling even during your busy time in China. Taka and Mark, I am grateful to both of you for serving as my paranymphs. It has been a pleasure to have fellow lab members who joined roughly around the same time, and we have created many enjoyable memories together. Taka, in particular, I have cherished our experiences running marathon, enjoying sashimi at your place, and attending international conferences together. I wish you the best of luck in completing your thesis and in your future endeavors, Thony, Floris,

and Gerard, I extend my sincere thanks for your invaluable technical support with various machine-related issues. Your assistance greatly facilitated the progress of my research. I would also like to express my gratitude to many former and current lab members: Casper, Mariska, Ronald, Loes, Hadi, Tim, Maartje Houben, Miao, Wen, Dawin, Jeroen, Aditya, Peter, Anastasia, Yuntao, Bart, Mike, Sahar, Johanna, Vangelis, Elisabeth, and Gaurav.

Furthermore, I would like to thank members from other groups or departments: Job, thank you for inviting me to go bouldering so I could realize that you are so damn good at it. Also thank you for helping me translate summary in Dutch. I really appreciate your help, Meng, besides Taka, we embarked on our PhD journeys at the same time. Your extensive knowledge and proficiency in learning different languages have been truly admirable. I wish you all the best in completing your thesis and in your post-doc endeavors as well, and also many others: Ylona, Martyn, Oliver, Maartje Hamers, Markus, Helen, Eric, Leonard, Henkjan, Ivan, Rens, as well as many visiting researchers to our lab: Weijia, Tanmaya, Bex, Lulu, Hanaya, Entela, Alexandros, Bowen, and all the individuals I had the pleasure of meeting during the DeepNL program. You are all wonderful people who have made my PhD journey unforgettable. I would also like to express my appreciation to Stefano, Elena, and Chiara for their discussions and technical support during my slip-pulse experiments when I visited INGV in Rome for two weeks. I particularly miss the taste of the espresso at the canteen and hope for the opportunity to visit you all again in the future.

Then, I would like to show my gratitude to all the friends that I have met here in the Netherlands for their company and support. Yu-Hsien, you were the first Taiwanese PhD student I met at Utrecht University and also one of my closest friend in the Netherlands, though you are in Austria now. Your sharing of useful and valuable PhD and life experiences was extremely helpful. We played numerous games of tennis and exchanged many playful remarks during that time. Those moments are unforgettable, and I am truly thankful for your support and encouragement during the ups and downs of my journey. Ash and Cindy, you two are also among my closest friends in the Netherlands, even if you might not agree with this! Haha. I always enjoy spending time with you both, chatting, and unwinding from the stresses of life. We have shared many wonderful and joyful moments, and I hope our friendship continues to thrive forever. Qingwu and

List of publications

Manuscripts in preparation:

Hung, C. C., Niemeijer, A. R., Effect of Pore Fluid Properties on Dynamic Slip in Fault Gouges Derived from the Groningen Gas Reservoir

Hung, C. C., Niemeijer, A. R., Aretusini, S., Spagnuolo E., Chen. J., Hamers M. Effects of Normal Stress and Slip Acceleration on Weakening in Sandstone-Derived Fault Gouges During Simulated Small-Magnitude Earthquakes

Manuscripts submitted:

Hung, C. C., Niemeijer, A. R., Vasconcelos, I. Strain Localization in Sandstone-Derived Fault Gouges Under Conditions Relevant to Earthquake Nucleation. *Submitted to Journal of Geophysical Research: Solid Earth.*

Manuscripts published:

Hung, C. C., Niemeijer, A. R., Raoof, A., & Sweijen, T. (2023). Investigation of strain localization in sheared granular layers using 3-D discrete element modeling. Tectonophysics, 862, 229974.

Kuo, L. W., **Hung, C. C.**, Li, H., Aretusini, S., Chen, J., Di Toro, G., ... & Sheu, H. S. (2022). Frictional Properties of the Longmenshan Fault Belt Gouges From WFSD-3 and Implications for Earthquake Rupture Propagation. Journal of Geophysical Research: Solid Earth, 127(5), e2022JB024081.

Hung, C. C., Kuo, L. W., Spagnuolo, E., Wang, C. C., Di Toro, G., Wu, W. J., ... & Hsieh, P. S. (2019). Grain fragmentation and frictional melting during initial experimental deformation and implications for seismic slip at shallow depths. Journal of Geophysical Research: Solid Earth, 124(11), 11150-11169.

Curriculum Vitae

Date of Birth: 3 May 1993
Place of Birth: Taichung, Taiwan
Email: cchung08a@gmail.com

Working Experience

2019.08.01 – present: PhD Candidate at High Pressure Temperature Laboratory, Utrecht University
2018.09.05 – 2019.07.19: Project assistant at National Central University (NCU), Taiwan

Education

2015.07 – 2017.07: Master, Department of Earth Sciences – division of Geophysics, National Central University, Taiwan
2011.09 – 2015.06: Bachelor, Department of Earth Sciences, National Central University, Taiwan